UNIVERSITY OF
LIVERPOOL

Kriging Regression in Digital Image Correlation for Error Reduction and Uncertainty Quantification

Thesis submitted in accordance with the requirements of the University of Liverpool
for the degree of Doctor in Philosophy

By

Dezhi Wang

September 2015

Abstract

Digital Image Correlation (DIC) is a widely used full-field measurement technique in the field of experimental mechanics because of its simplicity and ease of implementation. However, owing to the inherent complexity of DIC error sources, the problem of DIC error reduction and uncertainty quantification is still unsolved and has received considerable attention in recent years. The existing work on DIC error reduction is usually focused on specific error sources, e.g. local smoothing techniques are normally applied to reduce errors due to image acquisition noise. Moreover, DIC uncertainty quantification methods are usually derived from a subset-based DIC framework with an assumption of Gaussian image noise. Established methods are normally subject to an ad-hoc choice of parameterisation and might only be able to achieve a local optimum. On the other hand, originally developed in geo-statistics, Kriging is known as optimal interpolation to predict interpolated values using random variables as a realization of a Gaussian process. The Kriging technique has the excellent capability in global optimisation and uncertainty quantification. It is advisable to make an attempt to introduce the Kriging method to DIC to facilitate the solution of error and uncertainty issue.

The main purpose of this thesis is to offer a generic and global method that can reduce general DIC errors and quantify measurement uncertainty for displacement and strain results based on Kriging regression from Gaussian Process (GP) and Bayesian perspective.

Firstly, a new global DIC approach known as Kriging-DIC was developed through incorporating the Kriging regression model into the classical global DIC algorithm as a full-field shape function. The displacement field of the Region of Interest (RoI) is formulated as a best linear unbiased realisation that contains correlations between all the samples. The measurement errors of control points are accounted for through a global regularisation technique using a global error factor. With the aid of the Mean Squared Error (MSE) determined from the Kriging model, a self-adaptive updating strategy was developed to achieve an optimal control grid without artificial supervision. The developed Kriging DIC method was compared with subset-based DIC, FE-DIC and B-Spline DIC by using synthetic images and open-access experimental data. The effectiveness and robustness of Kriging DIC was verified by numerical examples and an experimental I-section beam test.

Secondly, a Kriging-based DIC uncertainty quantification method was proposed to quantify uncertainty of displacement and strain results of the subset-based DIC through a post-processing analysis based on Kriging regression. The subset-by-subset uncertainty was estimated through the subset-based DIC framework and derived as a function of the inverse of the Hessian matrix and residual of Sum of Squared Difference (SSD). This local subset-based uncertainty was then integrated into Kriging regression formula allowing uncertainty quantification of displacement field from a global sense. Based on Cholesky decomposition and covariance matrix solved by the Kriging formula, a multivariate normal sampling process was used to

quantify the strain uncertainty whereas displacement gradients were calculated by a Finite Difference technique. Both numerical case studies and an experimental cantilever beam test were employed to test the method, which was found to be able to improve the accuracy of displacement and strain results and quantify corresponding uncertainties. Furthermore, a new approach was developed to calculate strain results by means of Kriging gradients, which was also compared with a state-of-the-art PLS local fitting algorithm.

In summary, the main contribution of this thesis is the development of a global DIC algorithm (i.e. Kriging-DIC) and a Kriging-based DIC uncertainty quantification approach. These two methods provide great potential to globally improve DIC measurement accuracy and quantify uncertainties of displacement and strain results.

Acknowledgements

VI

Contents

Nomenclature

f , g	Reference and Deformed Images
$\mathbf{x}$, (x, y)	Pixel (Point) Coordinate in the Region of Interest (RoI)
∇	Gradient Operator
$\mathbf{u}$	Displacement field of the RoI
$u(x, y)$, $v(x, y)$	Displacements in x- and y-directions at (x, y)
$\mathbf{P}$, $\mathbf{p}$, p	Displacement Matrix, Vector and Scalar of Control Points
$\mathbf{p}^{e}$	Nodal Displacement Vector of One Finite Element
$\mathbf{G}^{e}$	Finite Element Nodal Assembly Matrix
$\boldsymbol{\rho}_{e}$, $(\boldsymbol{\rho}_{u}, \boldsymbol{\rho}_{v})$	Displacement Uncertainty Vector of Control Points (in X and Y)
$\tilde{\boldsymbol{\varepsilon}}_{e}$	Uncertainty of Displacement Field of the RoI
$\mu(\mathbf{x})$	Shape (Kernel) Functions (in general)
$\Phi(\mathbf{x})$	Q4-FE Shape (Kernel) Functions
$\varphi_{i,s}(\cdot)$, $\varphi_{j,t}(\cdot)$	B-Spline Shape (Kernel) Functions
$u_{0}, \mathrm{u}_{x}, \mathrm{u}_{y}, \mathrm{u}_{xx}, \mathrm{u}_{yy}, \mathrm{u}_{xy}$	X-direction Gradient Coefficients in Shape Function (2nd-order)
$v_{0}, v_{x}, v_{y}, v_{xx}, v_{yy}, v_{xy}$	Y-direction Gradient Coefficients in Shape Function (2nd-order)
$\mathcal{C}_{\mathcal{SSD}}$,	Sum of Squared Difference (SSD) Criterion
$\mathcal{C}_{\mathcal{CC}}$	Cross-correlation Coefficient (CC) Criterion
M , N	The Number of Pixels (Points)
ξ	Global (Local) Error Factor
ζ_{f}, ζ_{g}	Gaussian Image Noise (for Reference and Deformed Images)

σ_ζ^2	Variance of Gaussian Image Noise
$\mathrm{E}(\cdot)$, $\mathrm{Var}(\cdot)$, $\mathrm{Cov}(\cdot)$	Expectation, Variance, Covariance
$\mathbf{H}$	Hessian Matrix
ϑ_x, ϑ_y	Kriging Hyper-Parameters in Correlation Function
$\boldsymbol{\psi}$, ψ	Kernel Functions of Bi-cubic Interpolation Scheme
$w(x, y)$, $\hat{w}(x, y)$	True Displacement Field and Kriging Prediction
$\mathbf{w}_0$	Displacement Vector of Sample Points in Kriging Formula
$\hat{\mathbf{w}}$	Displacement Vector of Predicted Points in Kriging Formula
X	Matrix Including all the Locations of Sample Points
X^*	Matrix Including all the Locations of Predicted Points
$Z(x, y)$	Gaussian Stochastic Field with Zero Mean
$\mathbf{c}$, c	Kriging Regression Functions of An Untried Site
$\mathbf{r}$, r	Kriging Correlation Functions of An Untried Site
$\mathbf{C}$	Matrix of Kriging Regression Functions of Design Sites
$\mathbf{R}$	Matrix of Kriging Correlation Functions of Design Sites
$\boldsymbol{\kappa}$, κ	Kriging Weights (Kriging Shape Functions)
$\boldsymbol{\beta}$, $\hat{\boldsymbol{\beta}}$	Kriging Regression Parameters and the Estimate
σ^2, $\hat{\sigma}^2$	Kriging Field Variance and the Estimate
$\mathrm{MSE}(x, y)$	Kriging Mean Square Error
$\mathbf{J}$	Jacobian Matrix
$\mathcal{L}(\cdot)$	Likelihood Function
$\mathcal{N}(\bullet)$	Multivariate Normal Distribution
$\overline{\mathbf{w}}^*(\cdot)$	The Mean of Gaussian Process (Simple Kriging)
$\overline{\mathbf{w}}^{**}(\cdot)$, $\overline{\mathbf{w}}(\cdot)$, $\overline{w}(\cdot)$	The Mean of Gaussian Process (Universal Kriging)
$\mathbf{V}^*(\cdot,\cdot)$	The Covariance Matrix of Gaussian Process (Simple Kriging)
$\mathbf{V}^{**}(\cdot,\cdot)$, $\mathbf{V}(\cdot,\cdot)$, $V(\cdot,\cdot)$	The Covariance Matrix of Gaussian Process (Universal Kriging)
$\boldsymbol{\Lambda}$	The Lower Triangular Matrix After Cholesky Decomposition
$\mathbf{n}_s$	The Scalar in Standard Gaussian Distribution

Acronyms

DIC	Digital Image Correlation
SSD	Sum of Squared Difference
CC	Cross-correlation Coefficient
NSSD	Normalized Sum of Squared Differences
ZNSSD	Zero-Normalized Sum of Squared Difference
NR	Newton-Raphson
RoI	Region of Interest
DoF	Degrees of Freedom
FFT	Fast Fourier Transform
FE	Finite Element
NURBS	Non-Uniform Rational B-Spline
GP	Gaussian Process
BLUP	Best Linear Unbiased Prediction
MSE	Mean Square Error
GMSE	Global Mean Square Error
RMSE	Root Mean Square Error
STD	Standard Deviation
CI	Confidence Interval
GUM	Guide to the expression of Uncertainty in Measurement
UQ	Uncertainty Quantification
MCM	Monte Carlo Method
MCMC	Markov Chain Monte Carlo
MLE	Maximum Likelihood Estimation

UK	Universal Kriging
NIST	National Institute of Standards and Technology
ISO	International Standardization Organization

List of Figures

XXI

List of Tables

1

Introduction

In this chapter, the problem of DIC measurement error and uncertainty is considered in terms of DIC algorithms, DIC error sources and DIC uncertainty estimation methods. Then the characteristics of Kriging regression are introduced to highlight the advantage of applying this technique for DIC error reduction and uncertainty quantification. Finally, the outline and principal contributions of this thesis are presented.

In the field of experimental mechanics, full-field measurement techniques have been increasing in popularity during the past 30 years, for example, geometrical methods such as Digital Image Correlation (DIC) and interferometric methods such as holographic interferometry and speckle-pattern interferometry. Among these methods, DIC technique has become the most popular full-field measurement technique due to its simplicity in principle and implementation. The early development of DIC can be traced back to the work by researchers at the University of South Carolina in the early 1980s [1-4]. DIC principle was derived based on the

optical-flow theory [5] which enables the tracking of speckle patterns and image registration for quantitative measurements of the shape, displacement, and strain of test objects. Nowadays, DIC has been extended and widely applied in many areas of science and engineering thanks to the development of computer technology, digital cameras and white-light optics.

Even though DIC is a widely used measurement method, the problem of measurement error and uncertainty is still unsolved and needs further investigations. In the following sections, it is briefly addressed in the consideration of DIC algorithms, DIC measurement errors and DIC uncertainty estimation.

1.1 DIC algorithms

In general, DIC consists in maximising a correlation coefficient that is determined by the grey-intensity difference between reference and deformed images, which achieves a measurement of displacement field that is normally formulated by a deformation mapping function known as shape function. Depending on the type of shape function, DIC algorithms can be mainly classified into two categories [6]:

i. **Local DIC algorithm:** namely subset-based DIC [5], for which the shape function is only applied within a subset in the Region of Interest (RoI). The local approach is the most commonly used DIC algorithm with advantages of simplicity [5], flexibility, suitability for parallel computation [7] and so on. However, without inter-subset continuity, it is sensitive to grey-intensity noise and may yield large uncertainties in measurement results [8]. Further, its performance highly depends on the parameters input by the user, which also limits its efficiency.

ii. **Global DIC algorithm** [9-17]**:** known as full-field DIC, which applies the shape function to the entire RoI and the displacement field is solved at once. By imposing continuous constraints, the global approach is able to yield a smooth displacement field with good sub-pixel accuracy. However, the computational complexity can become significant when a large number of Degrees of Freedom (DoF) is considered. The performance can degrade at low spatial resolutions due to the smooth effect introduced by continuous constraints. Moreover, the measurement accuracy still relies on the user's choice for parameters in most global DIC algorithms.

Thus, both the local and global DIC algorithms have advantages and disadvantages. Generally for any DIC algorithm, a compromise has to be made between resolution (precision) that indicates the capability of measuring a minimum change in the measured quantity (e.g. displacement) and spatial resolution that represents the capability of measuring at closely-spaced locations. An ideal DIC algorithm is expected to be able to achieve an excellent resolution and an excellent spatial resolution at the same time [18, 19].

1.2 DIC error sources

Though the DIC principle and experimental setup are relatively simple compared to other techniques, DIC measurement results are not any less vulnerable to various kinds of error sources in the measurement process, which inevitably contain a certain level of uncertainty. Under ideal experimental conditions and using state-of-the-art DIC algorithm, DIC measurement is reported as having an accuracy of a hundredth of a pixel [20]. However, this kind of accuracy normally cannot be guaranteed in a practical DIC test and the actual measurement accuracy varies a lot

for different DIC setups. The error sources can be generally classified into two groups:

i. **Experimental errors:** The error sources occur in the image acquisition process, normally related to experimental setups. The experimental error sources consist of speckle-pattern quality [21-25], optical distortion [26-28] and focus error [29], image acquisition noise [30-32] and so on, which are fully contained in acquired digital images and will be propagated to final measurement results through DIC algorithms.

ii. **Algorithmic errors:** The error sources are introduced in the process of parameters measurement by applying DIC algorithms based on acquired digital images. The algorithmic error sources include DIC correlation criterion [20, 32-35], grey-intensity interpolation scheme [36, 37], shape-function reconstruction error [38, 39] and so on. Algorithmic errors can be significantly reduced by utilising a superior or more suitable DIC algorithm with respect to a specific application.

In addition, DIC error sources can also be briefly classified into systematic errors and random errors. Based on the investigation of DIC error sources, the works related to DIC error analysis lead in two directions: one is to estimate measurement uncertainty by quantifying the influence of error sources and the other is to increase measurement accuracy by improving DIC algorithms or experimental setups. For instance, local smoothing [32, 33, 40-42] techniques are normally applied in DIC algorithms to reduce measurement errors due to various kinds of random error sources. Generally these methods work effectively and are beneficial in terms of simplicity of implementation. However, they probably can only achieve a local optimum rather than a global optimum for the full-field measurement. Also they are

subject to the ad-hoc choice of parameterisation which results in inconvenience and time-consuming problems in practical applications.

1.3 DIC uncertainty estimation

On the other hand, as a measuring technique, DIC should not be limited to obtaining the measurement result but should also provide an estimate of measurement uncertainty to show how good the result is, which is crucial for DIC applications and still remains as an ongoing research topic. Because of intrinsic complexity of DIC error sources [43], a reliable uncertainty quantification (UQ) of DIC results under various experimental conditions is considered to be challenging. However, some advances have already been made on UQ of DIC measurement in the recent years, which can be briefly summarised as follows:

i. **For systematic errors:** For example, systematic error due to the use of under-fitting shape function can be conveniently estimated by approximating the shape function as a Savitzky-Golay low-pass filter based on the work of Schreier et al. [39]. As presented in [44], the uncertainty of the measurements (systematic and random errors) was predicted by using the numerically generated deformed synthetic images, whereas the confidence intervals of the identified material parameters were also simulated. A general procedure to numerically simulate the unnotched Iosipescu test was proposed in order to investigate the influence of DIC error factors such as spatial resolution, noise and interpolation on the identification results with virtual field method, Pierron et al. [45].

ii. **For random errors:** The measurement uncertainty caused by the most common random error i.e. image acquisition noise (e.g. read-out noise,

photon noise) was analysed by several researchers using self-correlated images with uncorrelated Gaussian intensity noise [5, 23, 46]. The results demonstrate that the measurement uncertainty is proportional to the standard deviation of image noise and inversely proportional to the average of the squared grey level gradients and the subset size.

iii. **Experimental analysis:** Influence of hardware, acquisition system, experimental condition and setup on DIC measurement uncertainty was experimentally studied by using tensile loading tests [47], translation experiments [48], the rigid-body-motion test [49] and so on.

iv. **Theoretical analysis:** Some efforts have also been made to theoretically analyse DIC measurement uncertainty. For instance, a theoretical model was derived by Pan et al [50] to indicate that the standard deviation error of displacement measurement is closely related to the quality of speckle patterns. Moreover, the effect of speckle size and density on the DIC measurement uncertainty was also investigated based on numerical experiments [21].

So far most studies that have been performed at DIC UQ consist in comparing DIC measurement results with known displacements (e.g. using synthetic images) or strains (e.g. obtained by strain gauges) and lead to very positive results [43], but those results only apply to specific DIC setups. Concerning the quantification of uncertainty due to various error sources under different DIC setups, a generic UQ method should be developed to evaluate the reliability and accuracy of DIC measurement results.

In an attempt to estimate measurement uncertainties in DIC in a general sense, an expression for uncertainty in the presence of Gaussian image noise was derived

analytically based on the framework of subset-based DIC and the sum of squared difference (SSD) DIC criterion [5, 23, 51]. Though this method is still restricted to Gaussian image noise, a potential possibility is provided to extend the method to handle uncertainty due to general DIC errors. In addition, there are also other attempts of trying to achieve a generic expression for DIC UQ, for example, a post-processing UQ method was proposed on the basis of the expected asymmetry of correlation peak [35] in the correlation map of matched subsets. However, all the above methods are derived from the subset-based DIC, which leads to a local uncertainty estimate. On the contrary, it is more preferable to develop an UQ method for DIC full-field measurement.

Inspired by existing approaches and related concerns, attempts were made to introduce Kriging regression to DIC in order to effectively reduce DIC measurement error and quantify the uncertainty for the full-field measurement.

1.4 Characteristics of Kriging regression

As widely used in the fields of spatial analysis and computer experiments [52, 53], Kriging is a method that provides a best linear unbiased prediction (BLUP) for a RoI based on observed values at design sites, which yields the most likely intermediate values as opposed to the most 'smooth' intermediate values optimised by a piecewise-polynomial spline. Moreover, if interpreted from a Bayesian framework [53, 54], Kriging is modelled by a Gaussian process governed by a prior covariance which straightforwardly provides the uncertainty estimate for predicted values. In addition, thanks to the estimated uncertainty across the RoI, a self-adaptive infill criterion can be employed to select new design locations required to achieve a realization of the true-value field with reasonable accuracy. The introduction of error

factors to the diagonal of Kriging correlation matrix [55, 56] enables the Kriging regression method to regularise the measurement errors at the design sites which further improves the accuracy of predicted values towards the 'true' values.

In light of potential applications in DIC for error reduction and uncertainty analysis, the main features of Kriging regression technique can be summarised as follows:

i. **Global:** Kriging method aims to optimise full-field prediction model based on observed data to achieve a best linear unbiased prediction, which is different from most other DIC techniques that only consider the local information or result in a local optimum.

ii. **Flexible:** Compared with shape functions used in other global DIC methods, Kriging model is capable of adapting to an irregular distribution of control points (as opposed to regular or uniform distributions) which provides the flexibility for global DIC analysis.

iii. **Automatic:** Instead of using the ad-hoc choice of parameterisation in classical DIC methods, the Kriging method can be used to achieve the parameter values through a global optimisation algorithm which is implemented automatically without user intervention. Furthermore, in the proposed Kriging DIC method, the optimal number of control points is also achieved automatically through a self-adaptive updating process.

iv. **Consideration of errors:** As aforementioned, measurement error of observed data can be considered and incorporated into the Kriging regression model, which significantly improves the accuracy of DIC results.

v. **Uncertainty quantification:** As a Gaussian process emulator, the Kriging method is conveniently used to quantify the uncertainty of estimated displacement field. Moreover, the uncertainty of the strain field can be

obtained through a multivariate normal sampling process based on the Kriging model.

1.5 Outline of the thesis

In the scope of applying the Kriging regression method to DIC for error reduction and uncertainty analysis, two promising methods were carried out, they are, (1) a new global DIC method named Kriging-DIC was developed by incorporating the Kriging regression model into global DIC algorithm to formulate the displacement field of the RoI as a global shape function with consideration of measurement error; (2) a post-processing technique based on Kriging regression with error estimate (in both global and local senses) was proposed to regularise the measurement error of subset-based DIC (to improve measurement accuracy) and quantify the measurement uncertainty of both displacement and strain results. The overall structure of the thesis is presented in Figure 1–1.

Chapter 2: This chapter reviews DIC local and global algorithms to identify the advantages and limitations of different kinds of DIC approaches. DIC objective functions, solution strategies and displacement resolution and spatial resolution are also considered.

Chapter 3: DIC errors and uncertainties are extensively reviewed. Concerning DIC uncertainty analysis, the standard uncertainty analysis approach is briefly introduced. Also a brief review of the Kriging regression method and Kriging-based uncertainty analysis is provided.

Chapter 4: The significance of error reduction and uncertainty quantification in DIC applications is briefly discussed first. A generic uncertainty estimation is

derived based on the subset-based DIC algorithm (SSD criterion) by considering an equivalent error variance due to common DIC error sources. Also the bias error in DIC sub-pixel registration caused by Gaussian image noise under uniform translation is estimated in the same framework. An error reduction method is proposed in regard to the bias errors in DIC sub-pixel registration.

Chapter 1: Introduction
problem overview and outline

Chapter 2 & 3: Literature Review
Part 1:local & global DIC algorithms
Part 2:DIC error sources/uncertainty
analysis/Kriging method

Chapter 4: DIC Error Reduction &
Uncertainty Quantification
theoretical derivations

Chapter 5: Kriging Regression
Theory in the DIC context

Chapter 6: Full-field DIC with
Kriging Regression
a global DIC algorithm

Chapter 7: Uncertainty
Quantification in DIC with
Kriging Regression
a post-processing technique

Chapter 8: Conclusions
& Future Studies

Figure 1–1. Outline of the thesis

Chapter 5: Kriging regression theory is briefly addressed in this chapter. The derivations of Kriging interpolation method are presented from both the framework of best linear unbiased prediction (BLUP) and the framework of Bayesian inference. Concerning measurement error of observed data, Kriging regression method is presented by regularising measurement error from both global and local senses. Furthermore, uncertainty analysis based on the Kriging regression method is also addressed.

Chapter 6: In this chapter, a global (full-field) DIC algorithm with integrated Kriging regression is proposed. Kriging regression model is employed as a full-field shape function to formulate the displacement field of RoI. The displacement errors of control points are quantified by introducing an error factor to the Kriging model. In addition, a self-adaptive control grid updating strategy is developed on the basis of the Mean Squared Error (MSE), which enables the proposed Kriging-DIC method to achieve the optimal control grid automatically. Both numerical and experimental case studies are used to verify the performance of Kriging-DIC method.

Chapter 7: The measurement uncertainty of subset-based DIC results is expressed as a function of inverse Hessian matrix and SSD residual. The Kriging regression method is developed as a post-processing technique including local error estimation, which is able to improve the accuracy of measured subset-based DIC displacement results and strain results. Uncertainty of the estimated displacement field is illustrated in terms of the root mean square error (RMSE). Furthermore, strain uncertainty is determined in terms of standard deviation (STD) by a multivariate normal sampling process based on Kriging regression model. Both numerical and experimental case studies are used to test the method.

Chapter 8: A review of key components of the research and main conclusions of this thesis are presented. The important contributions of this study are highlighted with suggestions for the future research which could be proceeded to extend current investigations.

1.6 Contribution by the author

This thesis addresses the error reduction and uncertainty quantification problem in Digital Image Correlation (DIC), which is crucial for DIC applications and remains unsolved. The principal contribution of this thesis is introducing the Kriging technique to DIC to deal with the measurement error and uncertainty from a new perspective i.e. in the sense of a Gaussian-process. A new global DIC method known as Kriging-DIC is developed to accurately measure the full-field displacement in DIC. Further, a post-processing technique based on the Kriging regression method with error estimation is also proposed to reduce the measurement error and quantify the measurement uncertainty.

The author has summarised the above research findings into two journal papers on Kriging-DIC method (J1) and Kriging-based DIC uncertainty quantification method (J2) respectively. Also there are two conference papers presented at international conferences. Paper C1 offers a good understanding of DIC error sources in the testing of composite materials and Paper C2 covers the study of how to integrate the estimated uncertainty of subset-based DIC into the Kriging regression model.

J1: **D.Z. Wang**, F.A. DiazDelaO, W.Z. Wang and J.E. Mottershead, 'Full-field digital image correlation with Kriging regression'. *Optics and Lasers in Engineering*, 67(2015) 105-115, doi: 10.1016/j.optlaseng.2014.11.004

J2: **D.Z. Wang**, F.A. DiazDelaO, W.Z. Wang, X.S. Lin, E.A. Patterson and J.E. Mottershead, 'Uncertainty Quantification in DIC with Kriging Regression'. Optics and Lasers in Engineering, doi: 10.1016/j.optlaseng.2015.09.006, In Press

C1: W.Z. Wang, **D.Z. Wang**, J.E. Mottershead and G. Lampeas, 'Identification of Composite Delamination Using the Krawtchouk Moment Descriptor', *Key Engineering Materials*, 569-570(2013) 33-40, doi: 10.4028/www.scientific.net-/KEM.569-570.33, (*10th International Conference on Damage Assessment of Structures (DAMAS 2013),* July 8-10, 2013, Dublin, Ireland)

C2: **D.Z. Wang**, J.E. Mottershead, F.A. DiazDelaO and W.Z. Wang, 'Kriging Regression in Full-field Digital Image Correlation based on the Global and Local Error Estimate', *the 16th International Conference on Experimental Mechanics*, July 7-11, 2014, Cambridge, UK

2

Literature Review

Part 1 – DIC Algorithms

DIC local and global algorithms are reviewed in this chapter. It aims to identify the advantages and disadvantages of these two types of DIC approaches. In addition, DIC objective functions and solution strategies are briefly considered while a discussion on DIC displacement resolution and spatial resolution is also presented.

2.1 Objective functions

Digital Image Correlation is a full-field, non-contact measurement technique which employs algorithms based on optical flow (which relates to the classic Lucas-Kanade tracker) to determine underlying deformation between images [57]. Since it is normally impossible to match individual pixels in different images, the area match is actually used to achieve a displacement field that consists of displacements of all

the pixels within the area. The Region of Interest (RoI) in the image may be divided into a large number of small areas so called 'subsets' normally with overlapping [18]. On the other hand, the whole RoI could also be treated as a large 'subset' for analysis. On that basis, algorithms in DIC could be categorized as either local methods (subset-based) or global methods.

The matching criterion is normally interpreted in two forms, they are, minimization of Sum of Squared Differences (SSD) [58] of grey intensities between an image pair and maximization of Cross-correlation Coefficient (CC) [58] between two images. Assuming intensity functions are continuous for the reason of simplicity, these two criteria can be written as:

$$
\begin{aligned}
C_{SSD} &= \arg \min \int_{\Theta} \left(g\left(x+u(x,y), y+v(x,y)\right) - f(x,y) \right)^2 d\Theta \\
C_{CC} &= \arg \max \int_{\Theta} \left(g\left(x+u(x,y), y+v(x,y)\right) \times f(x,y) \right) d\Theta
\end{aligned}
\tag{2-1}
$$

where Θ denotes the RoI in the first image. The displacement $\left(u(x,y), v(x,y)\right)$ may also be understood as the optical flow of the speckle-pattern intensity from a reference image $f(x,y)$ to its corresponding deformed image $g(x,y)$. It is noteworthy that there are also other types of DIC criteria applied including Sum of Absolute Difference (SAD) [59], Parametric Sum of Squared Difference (PSSD) [60] with additional unknown parameters and extended SSD and CC criteria [33, 61] e.g. Normalized Sum of Squared Differences (NSSD), Normalized Cross-correlation Coefficient (NCC), Zero-Normalized Sum of Squared Differences (ZNSSD) and Zero-Normalized Cross-Correlation Coefficient (ZNCC). Though the mathematical expressions of the correlation criteria are different, original and extended CC criteria are actually equivalent to and can also be deduced from the SSD criteria [33].

2.2 Solution strategies

In order to find a solution for the DIC correlation criterion, the displacement field of a subset or RoI should be formulated by a shape function with finite unknown parameters to be determined. These parameters act as Degrees of Freedom (DoF) and are used to allow images to distort. Generally the DIC solution is related to the framework of ill-posed inverse problems [62]. For both global and local DIC approaches, the displacement field $\left(u(x,y),v(x,y)\right)$ can be approximated as a linear combination of chosen basis functions of unknown parameters [8, 18, 63] with finite dimension n, expressed as

$$u(x,y) \approx \sum_{j=1}^{n} \mu_j(x,y) p_{u_j}$$
$$v(x,y) \approx \sum_{j=1}^{n} \mu_j(x,y) p_{v_j}$$

(2-2)

where $\mu_j(x,y); j=1,2,\ldots,n$ are kernel functions and $p_{u_j}, p_{v_j}; j=1,2,\ldots,n$ are combination coefficients. Since $g\left(x+u(x,y), y+v(x,y)\right)$ is an implicit function of $\left(u(x,y),v(x,y)\right)$, an iterative process is usually applied to solve the minimisation problem in Equation (2-1) (SSD criterion). Different types of algorithms e.g. genetic algorithms [64-66], Levenberg–Marquardt algorithm [17, 39], Newton–Raphson iteration [2, 36, 67-69], and multi-grid solver [10] may be used to solve the minimization problem. However among the above algorithms, a detailed examination [70] has shown that the spatial-domain Newton-Raphson algorithm provides the highest accuracy and the implementation of the NR algorithm is relatively simple as well.

Therefore, an approximate solution of the full-field displacement, $\left(u(x, y), v(x, y)\right)$, may be obtained by the NR iteration [10, 11, 71, 72]: (considered as the governing equation in ith iteration)

$$\mathbf{M}^i \left(\mathbf{p}^{i+1} - \mathbf{p}^i\right) = \mathbf{b}^i \tag{2-3}$$

where $\mathbf{p}^i = \begin{bmatrix} p_{u_1}^i & p_{v_1}^i & p_{u_2}^i & p_{v_2}^i & \cdots & p_{u_n}^i & p_{v_n}^i \end{bmatrix}^{\mathrm{T}}$ is a $2n \times 1$ vector, $\mathbf{M}^i$ are $2n \times 2n$ matrices and $\mathbf{b}^i$ are $2n \times 1$ vectors, with components given by

$$\left(M_{jk}\right)^i = \int_\Theta \Xi_j^i \times \Xi_k^i \mathrm{d}\Theta \tag{2-4}$$

and

$$\left(b_j\right)^i = \int_\Theta \Xi_j^i \times \left(f(x, y) - g(x + u^i, y + v^i)\right) \mathrm{d}\Theta \tag{2-5}$$

where

$$\Xi^i = \begin{bmatrix} \mu_1 \dfrac{\partial g(x + u^i, y + v^i)}{\partial x} \\[2mm] \mu_1 \dfrac{\partial g(x + u^i, y + v^i)}{\partial y} \\[2mm] \vdots \\[2mm] \mu_n \dfrac{\partial g(x + u^i, y + v^i)}{\partial x} \\[2mm] \mu_n \dfrac{\partial g(x + u^i, y + v^i)}{\partial y} \end{bmatrix}_{2n}^{\mathrm{T}} \quad \text{and } j, k = 1, 2, \ldots, 2n \tag{2-6}$$

The gradients $\dfrac{\partial g(x + u^i, y + v^i)}{\partial x}$ and $\dfrac{\partial g(x + u^i, y + v^i)}{\partial y}$ in equations (2-4) and (2-5) are in principle updated at each iteration. However, as proposed by Sutton [57, 73], the grey-level gradients may be calculated from the reference image rather than the deformed image without loss of accuracy.

Since the sub-pixel accuracy is normally required for DIC measurement, the objective function (correlation criterion) should be evaluated at non-integer locations. Therefore, an interpolation method has to be employed to approximate the grey values among pixels. A comprehensive catalogue of interpolation methods used in the field of image processing was presented [37], which also provides a general comparison and valuable comments for different interpolation approaches. The interpolation bias was studied through the analytical phase error of interpolation filters [36] and experimental validation [74] while high-number-tap interpolation filters were recommended for related applications in DIC [57]. Aiming to enhance the accuracy of B-spline interpolation used in DIC, a technique was proposed by employing a family of recursive interpolation schemes and its inverse gradient weighting form [75].

Besides spatial-domain iterative methods (like Newton iteration), there are also some other strategies which have been employed in order to achieve the displacement field with sub-pixel accuracy [20], including correlation coefficient curve-fitting [76, 77] or interpolation methods [78, 79] (so-called peak finding algorithms [29]), gradient-based methods [80-83], artificial neural network methods [84, 85] and so on. However, these methods can hardly be used to achieve more accurate measurement than the NR iteration method and are normally subject to the intrinsic lack of deformational DoF of the subset, namely the application of shape functions [29].

2.3 Displacement resolution and spatial resolution

The displacement resolution is defined as the smallest change of the displacement field that can be reliably measured and reflected in the measured displacement [18,

86]. In practice, it is quantified by the noise level of the measured displacement in terms of standard deviation and depends on various error sources and on the sampling resolution of the imaging system. In contrast to the displacement resolution, the spatial resolution is defined as the smallest distance between two independent data points [18, 86]. In practice, a more reasonable definition for the spatial resolution is one-half of the period of the highest frequency component contained in the frequency band of the displacement data [87]. The spatial resolution of subset-based DIC can be approximately considered as the subset size while the spatial resolution of global DIC depends on the number of measurements obtained within the RoI. It is desirable to have small values for both the displacement resolution and the spatial resolution, which indicates a more favourable measurement [19]. Fundamentally a compromise is generally made between the displacement and spatial resolutions for a DIC algorithm [57]. In [19], the spatial resolution was re-defined for both local and global DIC algorithms and evaluated with the help of deformed images with a unidirectional in-plane sinusoidal deformation field, which enables a fair comparison between different DIC algorithms by plotting displacement resolution versus spatial resolution in the same figure.

2.4 Local vs global DIC algorithms

There are the different ways applying DIC algorithms to the RoI, which belong to two general classes: local (subset-based) methods and global (full-field) methods, both of which have been well developed. The local approach is perhaps the better established of the two because of its simplicity [5], flexibility, and suitability to parallel computation [7]. However the lack of inter-subset continuity results in the

local method being more sensitive to measurement noise than the global approach and yields relatively larger uncertainties in the measured displacement [8]. Consequently, measured displacement field of the local method is unsmooth with discontinuities, for example, as shown in Figure 2–1. Thus a smoothing technique is normally applied as a post-processing operation especially for calculating strain results [88].
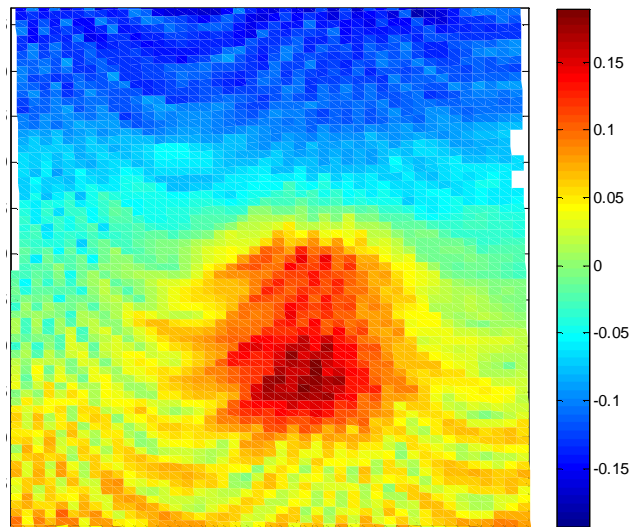
Figure 2–1. Discontinuities in the measured displacement field from a test of composite material based on a commercial DIC system (Dantec Q400)

Alternatively, the global approach imposes continuous constraints and treats the RoI as a whole, thereby enabling smooth displacement fields to be achieved together with good sub-pixel accuracy. However, there are also challenges for global method. Firstly, apart from the limited number of DoF involved in the local methods, the number of DoF that needs to be solved simultaneously increases quickly in global methods as the spatial resolution decreases. The associated computational complexity becomes significant [8, 72], which may result in failure to solve the inverse of the Hessian matrix during NR iteration. Secondly, the continuous constraint of global methods can become a disadvantage by degrading the spatial

resolution when localized phenomena occur (e.g. cracks, sliding and shear-bands) since discontinuities may be smoothed out or lead to non-convergence of the optimisation [10, 89].

2.5 Local DIC algorithms

By meshing the RoI with a set of evenly spaced grid points in the reference image, a local method may be applied on each of the subsets with the centres located at the grid points in order to find matched subsets in the deformed image as shown in Figure 2–2. According to the objective function shown in Equation (2-1), unknown parameters for each subset are solved by the aforementioned NR iteration. Normally the displacement field of one subset is formulated by a shape function (up to a second-order) around the centre point. For instance, a second-order Taylor expansion around the centre node at (x_0, y_0) is applied for the coordinate transformation as:

$$
\begin{aligned}
u(x_i, y_j) &= u_0 + u_x \Delta x + u_y \Delta y + \tfrac{1}{2} u_{xx} \Delta x^2 + \tfrac{1}{2} u_{yy} \Delta y^2 + u_{xy} \Delta x \Delta y \\
v(x_i, y_j) &= v_0 + v_x \Delta x + v_y \Delta y + \tfrac{1}{2} v_{xx} \Delta x^2 + \tfrac{1}{2} v_{yy} \Delta y^2 + v_{xy} \Delta x \Delta y
\end{aligned}
\tag{2-7}
$$

where $\Delta x = x_i - x_0$ and $\Delta y = y_j - y_0$. u_0, v_0 are the x- and y-directional displacement components of the centre node at (x_0, y_0), u_x, v_x, u_y, v_y are the components of the first-order displacement gradient and $u_{xx}, v_{xx}, u_{yy}, v_{yy}, u_{xy}, v_{xy}$ are the components of the second-order displacement gradient. Meanwhile, some of the typical deformations described by a second-order shape function are demonstrated in Figure 2–3. In general, the subsets are artificially designated as squares in the reference image for reasons of simplicity. However, instead of square subsets,

Gaussian weighted windows [90, 91] are also successfully applied in order to achieve an optimal compromise between the systematic errors and random errors.

Under the assumption of only pure translations existing in sufficiently small subset regions, displacement field could be approximated by a zero-order shape function which only contains the first term in Equation (2-7). This approximation was developed and applied in both physical space [4, 92] and Fourier space [76, 93] in the 1980s and 90s. Based on the requirement of detecting a complex spatial deformation, the first- and second-order shape functions [2, 94] are employed in local methods with a higher computational cost. Furthermore, a simplified form of Hessian matrix is also derived by ignoring the second-order partial derivatives without loss of accuracy [67, 94]. The initial values used to start the NR iteration can be calculated based on a fast cross-correlation technique using the zero-order shape function [67, 94].
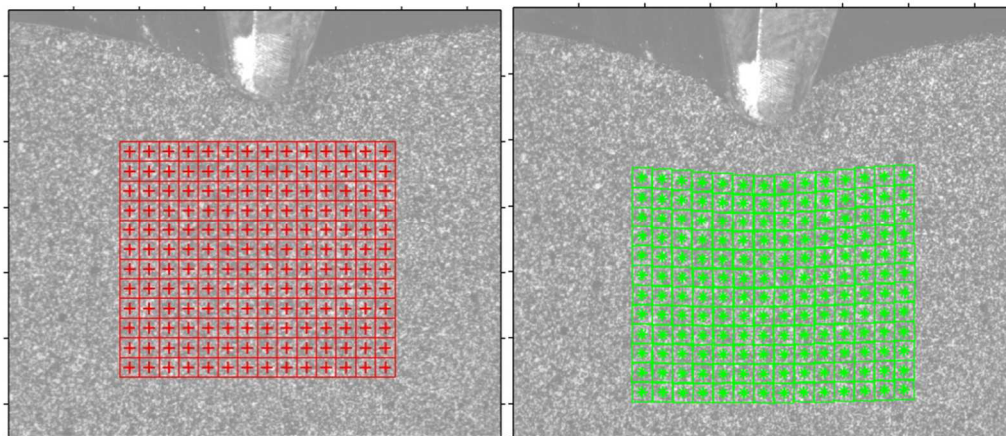
Figure 2–2. The illustration of subset-based DIC method (without overlapping subsets), the uniformly distributed square subsets (centre nodes marked in '+') are initialized in the reference image (left) while the matched deformed subsets (centre nodes marked in '*') are shown in the deformed image (right)
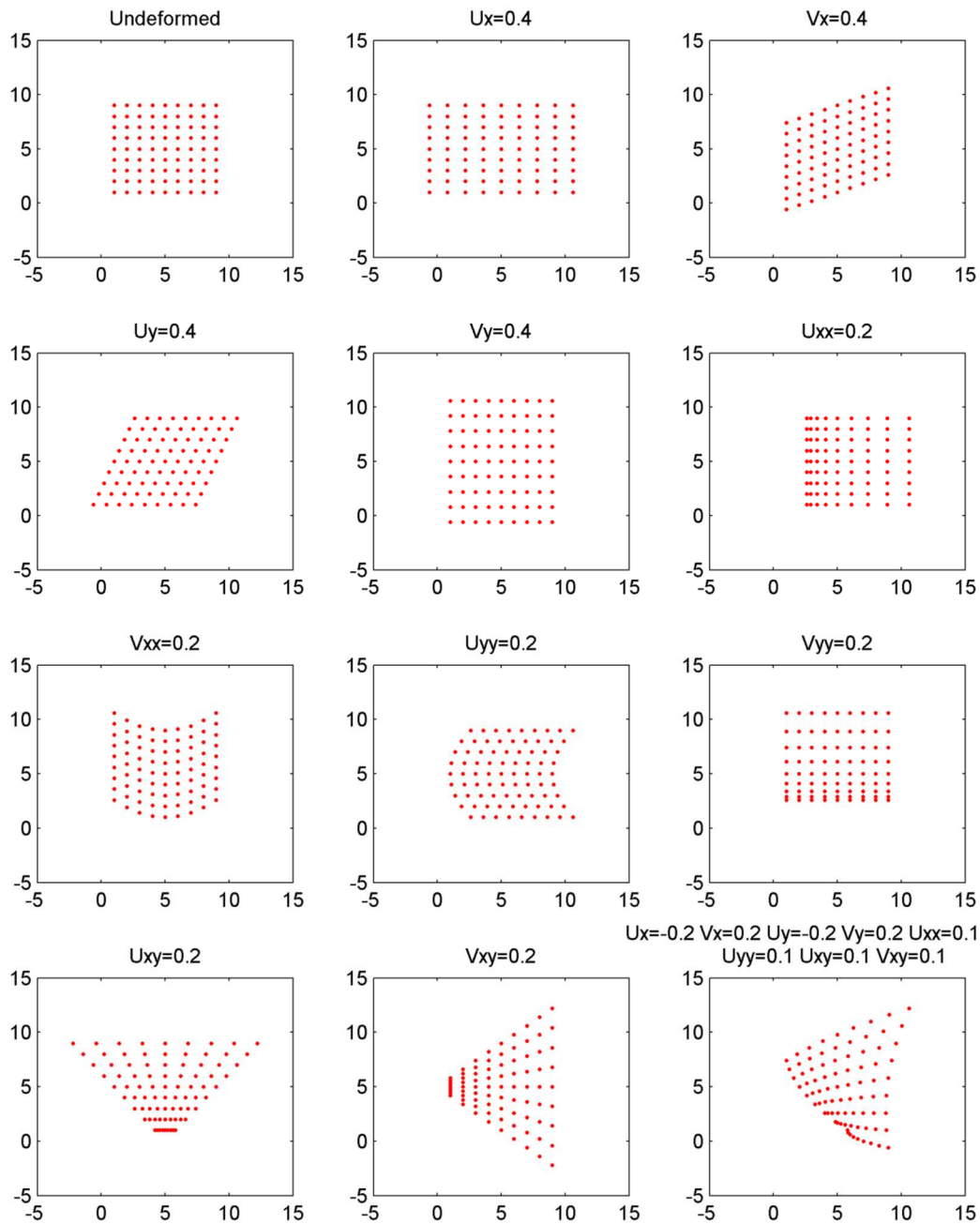
Figure 2–3. Deformations formulated by the 2nd-order shape function depending on different shape parameters

In addition, a so-called analytic propagation function was developed to produce accurate initialization for the NR iteration [95]. A method used with the multiple growing cracks is implemented by modifying the local method to allow the crack areas can be automatically identified and excluded from the analysis [96]. Another

improved local method was proposed in order to tackle discontinuities of the displacement field through splitting the subset into two sections where each of the sections is matched using independent deformation parameters [97]. On account of the possible error propagation of the general subset-based DIC method, a reliability-guided technique [98-101] was developed to optimise the calculation path of subsets to enhance the robustness in discontinuous and large-deformation areas.

2.6 Global DIC algorithms

Instead of calculating the displacement field of RoI based on a large number of independent subsets, a global framework was proposed to solve the minimization problem at once for the whole RoI. In the global approach, displacement field is formulated by a sophisticated shape function with a large number of DoF which is able to capture detailed deformation. The iteration process as shown in Equation (2-3) is essentially the same as in the local methods but works over the whole RoI. Various different types of full-field shape functions were studied. The full-field DIC methods are summarized in the following sections:

2.6.1 FE based DIC

Due to extensive DIC applications in experimental mechanics, Finite Element (FE) shape functions naturally became a popular choice to formulate the displacement field, which satisfies the requirement of displacement continuity among elements. For example, the bilinear rectangular elements (Q4-FE) introduced in [9-11] are used to mesh the RoI globally. The basic idea is shown as follows: (x, y) represents any single point in the RoI and $\mathbf{p}^e$ is the nodal displacement vector of the element where (x, y) is located. $\mathbf{p}$ denotes the global nodal displacement vector including

displacements of all the nodes on the meshed grid in the RoI. In order to assemble all the subsets together for a global analysis, $\mathbf{G}^e$ is employed as the nodal assembly matrix [9, 102] for the aforementioned element. Thus the displacements of the point (x, y) in terms of the Q4-FE [102] shape function are described as:

$$u(x, y) = \sum_{j=1}^{4} \Phi_j(x, y) p_{u_j}^e$$
$$\text{and } \mathbf{p}^e = \mathbf{G}^e \mathbf{p} \qquad (2\text{-}8)$$
$$v(x, y) = \sum_{j=1}^{4} \Phi_j(x, y) p_{v_j}^e$$

where $\Phi_j(x, y); j = 1, 2, \ldots, 4$ are the Q4-FE kernel functions. A new solution strategy known as the non-linear multi-grid solver [10] is integrated into the Newton iterative procedure to efficiently find the global minima of the correlation criteria. Apart from the Q4-FE elements, linear triangular (T3-FE) [103], higher-order FE shape functions like beam elements [104] and planar iso-parametric elements (with 24 DoF) [105] are also used through the same framework. Based on standard FE basis functions, a new method called PGD-DIC [72] employs a proper generalized decomposition technique to transform the 2D or 3D DIC problem into two 1D problem only involving 1D mesh. This method is able to significantly reduce the computational cost of traditional FE-DIC but is subject to separability of the displacement fields. On account of the connections between FE-DIC and the mechanical properties identification using FE Model Updating (FEMU), the nodal displacements measured by FE-DIC are easily integrated into the FEMU framework [106]. Furthermore, the introduction of parallel computation and the incorporation of a mixed optical/mechanical cost function [107] further improve the application of FE-DIC in mechanical properties identified by FEMU.

2.6.2 Extended FE-DIC

In the presence of discontinuities like cracks and shear bands, the aforementioned FE-DIC methods may become inappropriate for the application. A feasible approach is implemented to exclude the discontinuities from the RoI by using refined meshes in the vicinity [13]. However, the refined meshes are normally unfavourable on account of the accuracy and computational cost. In contrast to mesh refinements, eXtended FE method (XFEM) [10, 12] was introduced to the FE-DIC to add extra DoF with enriched elements and allow to measure irregular displacements due to various kinds of discontinuities [89]. Also a strategy of optimising the crack path configuration was proposed in [89]. An extended correlation technique by introducing discontinuous enrichment to FE shape functions was also proposed to allow the partition of FE elements when detecting shear-band like discontinuities [10]. Furthermore, an additional penalization is incorporated into the extended FE-DIC [108] to reduce measurement uncertainty, estimate crack tip locations and evaluate stress intensity factors [109].

2.6.3 P-DIC

In order to reduce the dependency of DIC measurement results on the user's choice of parameters and accurately measure high heterogeneous deformations, a new global DIC algorithm with a self-adaptive higher-order mesh was proposed based on p-adaptive finite element analysis [110], known as p-DIC [19]. When a p-adaptive mesh was used, degrees of freedom of the elements in the mesh could be adjusted to sufficiently represent the real deformation field. The mesh refinement was carried out according to a posterior residual error estimation based on an approach using multiple passes algorithms [111]. In contrast to the shape functions used in traditional finite element analysis, the shape functions of higher orders used in the p-

refinement will not influence lower-order shape functions. This independent property of shape functions leads to the characteristic that the calculated lower-order shape function parameters keep constant when introducing the higher orders. The performance of p-DIC was validated by plotting the measurand resolution against the spatial resolution [19].

2.6.4 Spectral DIC

In the sense of reconciling spatial flexibility and computational efficiency, the Fourier decomposition was also used in the approximation of displacement field [14], which shows high reconstruction capacities and relatively low computational costs benefiting from the FFT algorithm. However, this approach highly relied on the periodic nature of displacement fields and images which rarely occurs in the experimental situations [18]. In contrast to the original spectral DIC methods, an improved approach using a prior correction strategy to account for non-periodic displacement fields was developed [15, 16] and applied in the field of high-resolution strain measurement particularly in the composites tests at micro-scale [18]. In particular, the displacement field is expressed in terms of its inverse discrete Fourier transform (IDFT) as follows:

$$
\begin{aligned}
u(x, y) &= \sum_{r^*=-M}^{M-1} \sum_{s^*=-N}^{N-1} ff_u(i, j) \exp\left(\hat{\imath}\left(\frac{r^*\pi}{ll}x + \frac{s^*\pi}{ll}y \right) \right) \\
v(x, y) &= \sum_{r^*=-M}^{M-1} \sum_{s^*=-N}^{N-1} ff_v(i, j) \exp\left(\hat{\imath}\left(\frac{r^*\pi}{ll}x + \frac{s^*\pi}{ll}y \right) \right)
\end{aligned}
\tag{2-9}
$$

where ll denotes the half-width of RoI and $ff_u(r^*, s^*), ff_v(r^*, s^*)$ denote the Fourier transforms of $u(x, y)$, $v(x, y)$ respectively. Only Fourier coefficients within a rectangle of size $2M \times 2N$ were used to approximate the displacement field, which

requires $M, N \leq ll$. However, the displacement field is impossible to be exactly reconstructed in the extreme case when $M, N = ll$ due to the ill-posed problem. Consequently $M, N \ll l$ is normally needed for the accurate measurement [14]. Furthermore, on the basis of the spectral formulations, the components of governing equation shown in Equation (2-4) and (2-5) become the expressions in terms of Fourier transform [15, 16]. In addition, the forward and backward FFT was applied to improve the computational efficiency of the spectral based DIC [15].

2.6.5 B-Spline based DIC

B-Spline basis functions were firstly introduced to global DIC in [17] to formulate the entire displacement field with implicitly continuous positions and derivatives up to a specified order. Apart from the FE shape functions, B-Spline functions consist of piece-wise polynomials and are capable of efficiently representing smooth surfaces depending on displacements of the control points that are similar to the nodal points in EF-DIC. The B-Spline DIC can be referred to [17, 71] and interpreted as follows: firstly any pixel point in the RoI of the reference image can be linearly mapped into a unit square, with $0 \leq \alpha^*, \beta^* \leq 1$. The mapping is written in the following form (n_1 and n_2 are the number of pixels in x- and y-directions respectively).

$$\alpha^* = \frac{x}{n_1 - 1} \quad \beta^* = \frac{y}{n_2 - 1} \tag{2-10}$$

With this parameterization scheme, the B-Spline shape functions are written below to represent the displacements of any pixel point in the RoI:

$$u(\alpha^*, \beta^*) = \sum_{i=0}^{m_1} \sum_{j=0}^{m_2} \varphi_{i,s}(\alpha^*) \varphi_{j,t}(\beta^*) p_{u_{ij}}$$

$$v(\alpha^*, \beta^*) = \sum_{i=0}^{m_1} \sum_{j=0}^{m_2} \varphi_{i,s}(\alpha^*) \varphi_{j,t}(\beta^*) p_{v_{ij}}$$

(2-11)

where $p_{u_{ij}}, p_{v_{ij}}$ have the similar meanings as in Q4-FE DIC denoting the displacements of the control points. m_1 and m_2 are the numbers of control points in the RoI in x- and y-directions respectively. In addition, $\varphi_{i,s}(\cdot)$ and $\varphi_{j,t}(\cdot)$ denote the B-spline basis functions for a given order s and t (for cubic spline $s = t = 3$). Also they are defined recursively in the parametric space based on a knot vector shown as the following recursive formula [112]:

$$\varphi_{i,0}(\alpha^*) = \begin{cases} 1 & if \, \alpha_i^* \leq \alpha^* < \alpha_{i+1}^* \\ 0 & otherwise \end{cases}$$

$$\varphi_{i,p}(\alpha^*) = \frac{\alpha^* - \alpha_i^*}{\alpha_{i+p}^* - \alpha_i^*} \varphi_{i,p-1}(\alpha^*) + \frac{\alpha_{i+p+1}^* - \alpha^*}{\alpha_{i+p+1}^* - \alpha_{i+1}^*} \varphi_{i+1,p-1}(\alpha^*)$$

(2-12)

It is noted that the Levenberg-Marquardt approach [39] was employed to iteratively optimize the control-point variables and minimize the SSD criterion. A further development was published in [71] where the Non-Uniform Rational B-Spline (NURBS) functions were applied in DIC to improve the conditioning of the problem and reduce the uncertainty and noise levels. Moreover, in [71] a similar multi-scale strategy as demonstrated in [10] is used in the optimisation process.

2.7 Closure

A review of various kinds of DIC local and global algorithms has been presented. It sets the basis for research on the development of a new global DIC algorithm (i.e.

Kriging DIC) in Chapter 6. In the next chapter, DIC errors and uncertainties are reviewed in order to highlight the unsolved problems and the applicability of the Kriging technique to the problem of addressing DIC uncertainty.

3

Literature Review

Part 2 – DIC Uncertainties & Kriging

In this chapter, an extensive review of DIC error and uncertainty sources is presented first. A standard uncertainty analysis technique on image processing is briefly considered in relation to the DIC uncertainty analysis. Finally, a general review of the Kriging regression method and Kriging-based uncertainty analysis is provided.

Although DIC technique has been extensively used in various fields, the uncertainty quantification of DIC measurement is still an on-going research topic and is crucial for the wide acceptance of DIC as a standard measurement technology. In this sense, the main error sources in DIC technique are discussed and summarised in the following sections.

As an image-based measurement process, DIC consists of three main components [113], they are, (a) image acquisition; (b) image pre-processing; (c) parameters

measurement. Since the image pre-processing (e.g. filtering, edge detection) is normally not necessary in DIC, DIC uncertainty factors generally fall into two categories, namely, experimental factors in the image acquisition (including quality of speckle patterns) and algorithmic factors in the parameters measurement shown in Table 3–1. Furthermore, the main error sources are also briefly classified into the systematic errors and random errors as shown in Table 3-2.

Table 3–1: DIC error sources

Experimental (image acquisition)	I. Texture pattern
	  o Pattern Characterisation e.g. pattern shape, size and density
	II. Image acquisition
	  o Optics distortion, camera focus
	  o Out-of-plane motions (2D only)
	  o Image noise e.g. digitization, read-out noise, black current noise and photon noise
	  o Illumination variation
	  o 2D/3D Calibration
	  o Environment e.g. light reflections, air temperature, vibrations

Algorithmic (parameters measurement)	o Correlation criterion o Sub-pixel interpolation o Shape function (reconstruction error) o Conservation of optical flow (speckle patterns may be changed by large deformation) o Optimisation techniques

Table 3–2: DIC error classification

Systematic error sources	o Image noise o Texture pattern o 2D/3D Calibration o Sub-pixel interpolation o Shape function (reconstruction error) o Optics distortion o Out-of-plane motions o Illumination variation
Random error sources	o Image noise o Illumination variation o Camera vibration

3.1 Basic concepts

As a measuring technique, the DIC result generally should be expressed as a measurement quantity value together with a measurement uncertainty. The underlying concepts are clarified herein firstly in order to eliminate the ambiguity of the related usage in this thesis. The definitions shown below (in italic) are taken from [114-118] and Figure 3–1 [119] is used to illustrate the basic relationship among the concepts.

i. *True value: 'True' in the sense that it is the value of a quantity that is believed fully compatible with the definition of the measurand [117, 118]. Since the true value cannot be absolutely determined, in practice an accepted reference value is usually established by repeatedly measuring*

NIST or ISO traceable reference standards. It is worthwhile to note that true value is not the reference value that has errors associated with it and may not be totally representative of the specific sample being measured.

ii. Error: The difference between a measurement and the true value of the measurand. Error does not include mistakes that should be explained and excluded from the data set. Although it is not possible to completely eliminate error in a measurement, it can be controlled and characterized. The total error is usually a combination of systematic error and random error.

iii. Systematic error: The mean error resulting from an infinite number of measurements of the same measurand under repeatability conditions, systematic error represents the component of measurement error that consistently deviates from the true value of the measurand by a constant amount or varying in a predictable manner [117, 118]. It is not determined by chance but is introduced by an inaccuracy (known or unknown) inherent in the system, which is not reduced when observations are averaged. Systematic error can be corrected only when the true value is known.

iv. Random error: Random error is defined as the difference between a measurement and the mean resulting from an infinite number of measurements of the same measurand under repeatability conditions [117, 118]. It is also a component of the measurement error which varies in an inherently unpredictable way. Random errors can occur for a variety of reasons such as noise in the measurement and are impossible to be corrected.

v. Uncertainty: Uncertainty of a measurement reflects the lack of exact knowledge of the value of the measurand [118]. Uncertainty characterizes

the range of values within which the true value is asserted to lie. All possible error effects (both systematic and random) should be addressed by an uncertainty estimate that is the most appropriate means of expressing the accuracy of results and is consistent with ISO guidelines. In spite of this, the systematic error cannot be estimated in many measurement situations and only random error is included in the uncertainty estimate. When only random error is included, the uncertainty is actually a reflection of the precision [117] of the measurement.

vi. *Bias: It is the difference between the average value of a large series of measurements and the accepted true value. Bias is an estimate of the total systematic error in the measurement and a correction can be made by adjusting for the bias in order to reduce the systematic error.*

vii. *Accuracy, precision and trueness: Measurement accuracy means the closeness of agreement between a measured value and the true value and is not a quantity [117]. A measurement is said to be more accurate when its measurement error is smaller. Measurement precision refers to the closeness of agreement between different measured values obtained by replicate measurements and is normally regarded as the estimate of random error [119]. Measurement trueness is defined as closeness of agreement between the expectation of measured values and a reference true value and is normally treated as the estimate of systematic error [119].*

viii. *Standard uncertainty: According to the definition in the expression of uncertainty in measurement (GUM) [113, 117, 120], the standard uncertainty is the estimate of the standard deviation of measurement results once the correction of systematic effects has been applied including the*

uncertainty of correction. Standard uncertainty defines a confidence level of the corrected measurement results for the measurand.
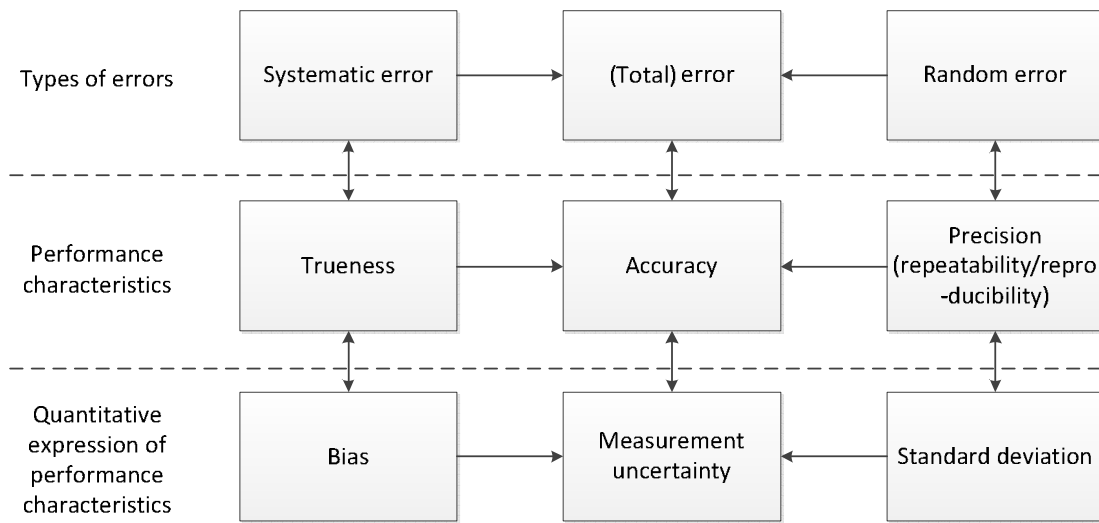
Figure 3–1. Relationship between different types of errors, qualitative and quantitative performances (taken from [119])

3.2 Experimental error sources

The error sources included in the experimental process can be generally classified into two procedures: speckle pattern preparation and image acquisition which are listed as follows.

3.2.1 Errors arising from speckle patterns

In DIC, random speckle patterns are applied to the surface of measuring object (specimen) to provide stochastic grey-value variations. The quality of speckle patterns is fundamental to the accuracy of DIC measurement. The variations of grey-intensity gradients (related to the image contrast) are found having a strong influence on the accuracy and reliability of DIC measurements (gradient-based), as noted in several speckle pattern assessment criteria [21], for example, the sum of squared subset intensity gradients [22, 23] and mean intensity gradient [24]. Apart

from the intensity gradients, concepts of subset entropy [121] and mean subset fluctuation [122] were also utilized to assess the quality of speckle patterns. In order to balance the measurement uncertainty (displacement resolution) and spatial resolution before a test, a method of texture evaluation was proposed, which consists of two a-priori criteria: the minimum grey-level standard deviation and representative speckle size [123].
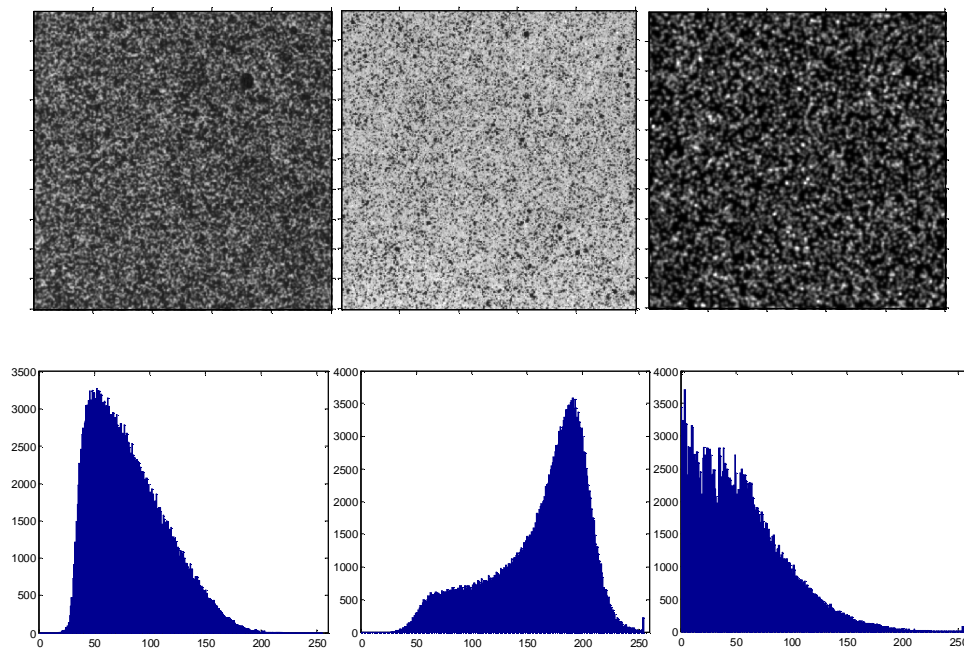
Figure 3–2. Grey level histograms (x-axis: grey scale, y-axis: number of pixels) of different types of speckle patterns, from left to right: airbrush, spray can, synthetic (Gaussian speckles)

Pattern Characteristics

Morphological approaches [21, 124, 125] have been introduced and used to analyse the pattern quality on account of the physical properties of speckle patterns like pattern size, shape, density and frequency components. Owing to the study in [21], it is shown that the way speckle patterns are made as shown in Figure 3–2, e.g. using a spray paint or an airbrush, making black speckles on a white background or making white speckles on a black background, has a non-trivial effect on the measurement

error. For the purpose of well controlling the quality of speckle patterns, a new technique called 'toner transfer' was proposed on the basis of a thermo-mechanical procedure by transferring melted toner from a printed paper to the surface of specimen [29]. An effective method was developed to generate stochastic patterns from metallic thin films at a sub-micron scale [126].

Rigid/deformable patterns

In general, there are two different types of pattern degradation: deformable patterns and rigid patterns. It was studied and presented in [25] involving the high tension rates and fatigue. It was shown that rigid patterns have an extra influence on the DIC uncertainty compared to deformable patterns and this effect is equivalent to an image noise imposed on deformable patterns. However, similar results were obtained on rigid and deformable patterns under large strains since the effect of pattern deformation becomes predominant [25]. Nevertheless, it should be noted that a relationship between the spatial scale and the size of rigid or deformable pattern was studied and an estimation method for the pattern size was also proposed on the basis of a 3-point 1D Gaussian fitting [35].

Synthetic (numerical) speckle patterns

Except natural speckle patterns used in tests, synthetic speckle patterns are often generated and applied to assess the performance of DIC algorithms due to the well-controlled speckle features and deformation information. Based on numerically-produced Gaussian speckles with uniformly distributed means, an efficient approach [20, 81, 95] was developed to simulate the real speckle patterns on the CCD target. Furthermore, an interpolation-based method was proposed to generate the deformed image by numerically deforming a piece of real speckle pattern using FE displacement fields [127]. With the purpose of producing realistic speckle patterns, a

framework was proposed consisting in using successive transformations of Perlin coherent noise functions [128].

3.2.2 Errors arising from image acquisition

Main error sources related to the image acquisition are introduced below, of which errors are also propagated through the process of parameters measurement to the final results.

Optics distortion and focus

In a practical DIC application, non-linearity is introduced to the image projection plane due to the lens distortion particularly the radial distortion [29] as shown in Figure 3–3. Radial lens distortion was modelled by considering the first two radial terms and model parameters were solved through the maximum likelihood estimation [26]. Alternatively a more complex lens-distortion model [27, 28] based on cubic and quantic radial terms of the camera was applied and solved by a Levenberg-Marquardt technique [129]. Once the distortion model is obtained, the effect of distortion can be easily compensated and removed. It is worth noting that the camera focus algorithm was studied in [29] for the purpose of acquiring the highest achievable focus, which can also be found in [130, 131].
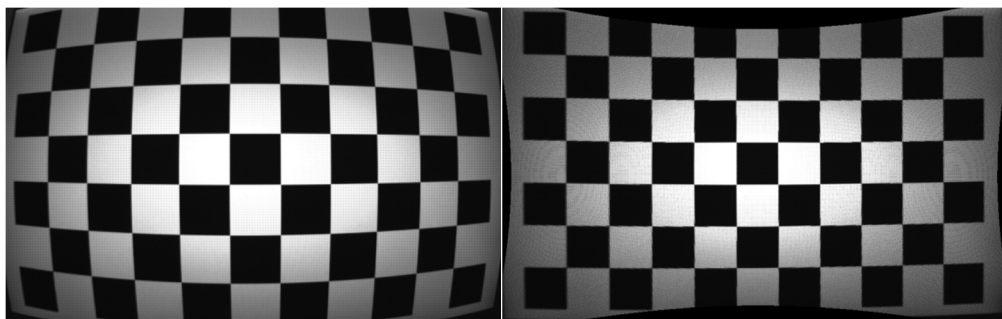
Figure 3–3. Positive and negative camera distortions (taken from [132])

Out-of-plane motion

The out-of-plane motion (or deformation) is normally unavoidable in the practical applications. The errors like fictitious strains [29] due to out-of-plane motion (rigid translation, rotation etc.) in 2D-DIC analysis were compensated by several different approaches [29, 57, 133-136]: for instance, directly measuring the out-of-plane strain error from a function of measured distance between the camera and the specimen based on a single-camera vision system [136], significantly increasing the imaging distance between the camera and the specimen by using a tele-centric lens [5], doing the correction using a knowledge of the specimen material properties [133]. However, based on analytical and experimental studies, it was shown that the in-plane displacement errors and strain errors are not introduced by the out-of-plane translation and rotation in a 3D-DIC measurement [136]. Three interesting compensation methods for the out-of-plane motions in 2D DIC measurements were presented in [137]: (1) misalignments of the camera and out-of-plane motions were avoided by a mechanical camera positioning tool; (2) the camera was aligned on the basis of the camera pinhole model and numerically deformed images; (3) A reference region method was applied for the related compensation.

3D calibration

For 2D-DIC, it is assumed that the motions of a planar object occur within the object plane, which requires the camera sensor to be nominally parallel to the object plane [5], e.g. with the help of a laser [139]. As 2D-DIC is normally vulnerable to the errors due to out-of-plane motions [136], 3D-DIC is highly recommended and extensively applied in practice. The accuracy of stereo-based DIC measurement strongly depends on the calibration process.
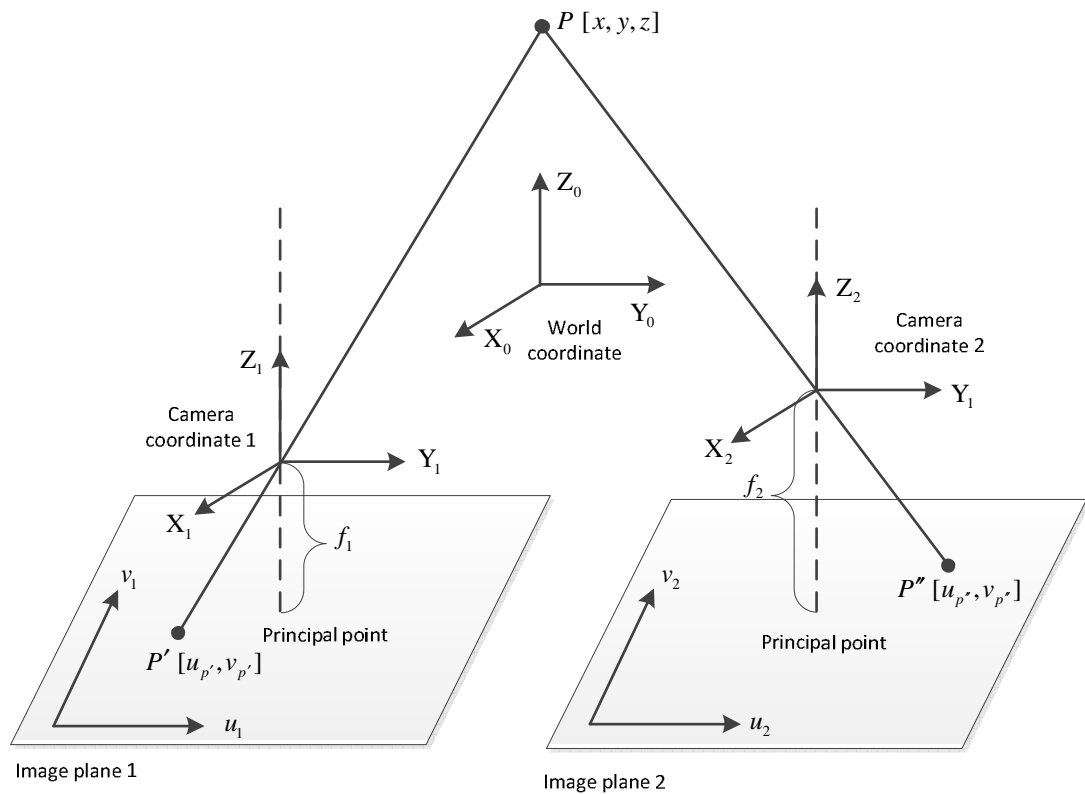
Figure 3–4. The 3D calibration procedure, a spatial point P is projected onto the image plane of the camera (pinhole model)

On the basis of error propagation equations [27, 140] and camera calibration technique [26], an analytical framework was developed for quantifying the measurement errors stemming from a stereo-vision calibration procedure [129]. In particular, by using a pinhole camera model, the errors of camera intrinsic and extrinsic parameters [129] under known distributions [141] are analysed during the calibration process and combined into a general formulae for assessing the expectation and variance of 3D measurement results. According to the developed formulae, experiments were also performed to validate biases and variances of 3D displacements and strains based on the theoretical predictions [51]. Moreover, a Monte Carlo approach was applied to obtain uncertainties of the calibration parameters by using experimental images [142].

As shown in Figure 3–4, the principal point is the mapping of the intersection of optical axis with the image plane. The principal point is ideally located in the centre of the image but is not always the case in practice due to tangential distortion and other manufacturing defects. The mapping between image coordinates and physical world coordinates is represented by a 3×3 camera intrinsic matrix, which is normally used to correct the deviation of principal point.

Image acquisition noise

Noises are inevitable in the image acquisition (e.g., digitization noise, read-out noise, photon noise [30]). For the sake of simplicity, the noise-induced errors are normally assessed by assuming the model of image noise as Gaussian, additive, independent at each pixel and independent of the grey intensity, which is generally consistent with the characteristics of real noise under a well-controlled experimental condition [31, 32]. On the basis of Gaussian assumption, analytical expressions of noise-induced bias and variance for planar translations were derived according to SSD criterion using error propagation principles [23, 31, 51, 57, 143]. It is shown that variance error is proportional to the variance of the Gaussian noise (zero mean) and inversely proportional to the sum of intensity gradients [5, 23]. If the sum of squared intensity gradients is interpreted as the information contained in the image, the variance error can be understood as the noise-to-signal ratio (NSR) [35, 46].

On the other hand, the error reduction methods were also developed in order to reduce or compensate the noise-induced uncertainties. Pan et al. proposed to employ a 5×5 pixels Gaussian low-pass filter to pre-smooth the speckle images before applying correlation analysis [32], which showed an appealing effectiveness and was further experimentally validated in [31]. Unlike the noise sensitivity was analysed locally based on subset DIC, noise-induced errors could be also quantified in global

approaches. In particular, based on Q4 FE-DIC method, an analytical expression was derived and illustrated for the sensitivity of the displacement measurement to noise [11]. The sensitivities to acquisition noise were compared for both local and global DIC methods by using 4-noded zones and 4-noded elements respectively and demonstrated in terms of the uncertainty levels of nodal displacements, mean displacements and mean strains [8].

Illumination variations

Even given ideal experimental conditions, illumination change is still an unavoidable error source which makes a contribution to intensity differences of images taken only at different times. In particular, these changes may have a localized and uneven effect on the whole image. The photometric transformations [5] were discussed for the offset and scale changes in the lighting and led to the optimization of DIC criterion, namely the ZNSSD criterion [32, 34, 144]. In practice, setting adequate illumination to minimize the camera gain was presented as a simple way to decrease the noise level, which was validated by a test using identical speckle patterns but with different illumination qualities [43]. In view of the normalized spatial cross-correlation approach used when illumination conditions change, a gradient-based sub-pixel registration method was proposed to yield the correlation coefficients which are only sensitive to the variations of illumination and noise [145].

3.3 Algorithmic error sources

3.3.1 Correlation criteria

Due to the fact that experimental conditions like illumination and noise may have significant influence on the intensity noise of acquired images, a robust and reliable

correlation criterion is required to be able to minimise or even eliminate the resulting displacement or strain errors [34]. In that case, the zero-mean normalized criteria are highly recommended [20, 32-35] for the sake of insensitivity to the linear scale and offset changes of intensities. Assuming a square reference RoI of $(2M+1)\times(2M+1)$ pixels is chosen, the ZNSSD and ZNCC criteria could be written in the following discrete expressions:

$$C_{ZNSSD} = \arg\min \sum_{i=-M}^{M} \sum_{j=-M}^{M} \left(\frac{g\left(x_i + u(x_i,y_j), y_j + v\left(x_i,y_j\right)\right) - g_m}{g_{std}} - \frac{f\left(x_i,y_j\right) - f_m}{f_{std}} \right)^2$$

$$C_{ZNCC} = \arg\max \sum_{i=-M}^{M} \sum_{j=-M}^{M} \left(\frac{g\left(x_i + u(x_i,y_j), y + v\left(x_i,y_j\right)\right) - g_m}{g_{std}} \times \frac{f\left(x_i,y_j\right) - f_m}{f_{std}} \right)$$

$$(3\text{-}1)$$

where

$$g = g\left(x_i + u(x_i,y_j), y_j + v(x_i,y_j)\right), \quad f = f\left(x_i,y_j\right)$$

$$g_m = \frac{1}{(2M+1)^2} \sum_{i=-M}^{M} \sum_{j=-M}^{M} g\left(x_i + u(x_i,y_j), y_j + v(x_i,y_j)\right),$$

$$f_m = \frac{1}{(2M+1)^2} \sum_{i=-M}^{M} \sum_{j=-M}^{M} f\left(x_i,y_j\right),$$

$$g_{std} = \sqrt{\sum_{i=-M}^{M} \sum_{j=-M}^{M} \left(g - g_m\right)^2}, \quad f_{std} = \sqrt{\sum_{i=-M}^{M} \sum_{j=-M}^{M} \left(f - f_m\right)^2}$$

g_m, f_m and g_{std}, f_{std} are the means and standard deviations of subset intensities in deformed and reference images respectively. It is a remarkable fact that the ZNSSD and ZNCC criteria are applicable not only in the local (subset-based) algorithms but also in the global algorithms.

3.3.2 Sub-pixel interpolation

As the correlation criterion must be evaluated at non-integer positions, a systematic bias is generated owing to the application of sub-pixel interpolation schemes [36]. A

comprehensive catalogue of interpolation methods used in the field of image processing was presented in [37], which also provides a general comparison and valuable comments for different interpolation approaches. The interpolation bias was studied through analytical phase error of interpolation filters [36] and experimental validation [74]. It was shown that the systematic bias in displacement measurement stems from the phase-shift error and depends on the sub-pixel displacement [5, 36].
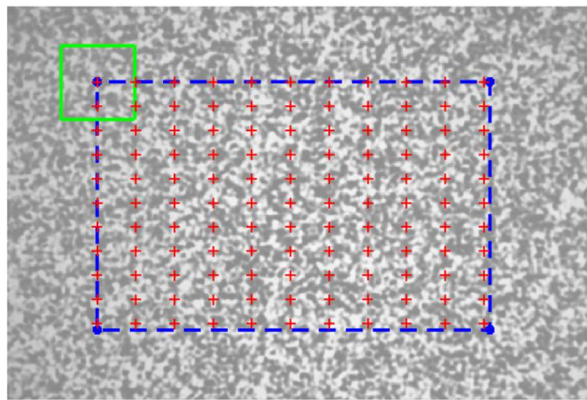
Figure 3–5. A region of interest (in blue square) is chosen from an experimental speckle image, 11×11 samples (in red plus) are uniformly selected and designed as the centres of subsets with a size of 11×11 pixels

Based on an experimental speckle image shown in Figure 3–5, typical bias errors and standard deviations on the usage of a 6×6 bi-cubic intensity interpolation scheme are presented as illustrated in Figure 3–6 on the basis of an experimental image applied by a sub-pixel translation from 0 to 1 pixel with an increment of 0.05 pixels in both x- and y-directions at the same time. High-order interpolation schemes were recommended in DIC [36, 57]. Aiming to enhance the accuracy of B-spline interpolation used in DIC, a technique was proposed by employing a family of recursive interpolation schemes and its inverse gradient weighting form [75].

Interpolation schemes may be used not only in interpolating the grey intensities to provide grey values for non-integer positions but also in interpolating the correlation coefficients in the neighbourhood of the correlation peak to solve the peak location with sub-pixel accuracy [20, 146].
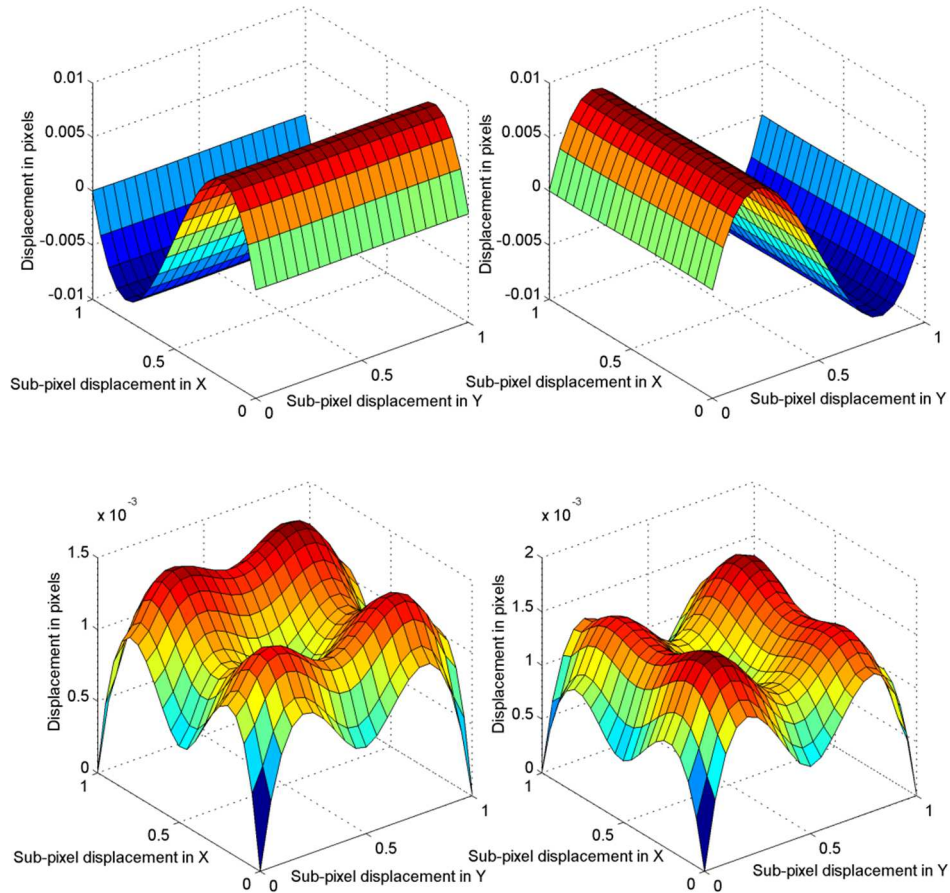
Figure 3–6. The distributions of mean errors and standard deviations of the samples with respect to the 2D sub-pixel translations

3.3.3 Iterative initial values

The iterative spatial correlation methods generally require a proper guess of initial values to guarantee the convergence of optimisation. Vendroux and Knauss [67] showed that the NR iteration method has a convergence radius of 7 pixels for initial values in DIC applications. In the case of small deformation between reference and

deformed images, a fast cross-correlation technique using the zero-order shape function [67, 94] is normally used to obtain the initial values with 1 pixel accuracy. Additionally, the coarse-fine search scheme [147] and frequency-domain technique [148] are applied to improve the accuracy and efficiency for the initialization. On the other hand, the modified coarse-fine search scheme [149], propagation function [95], genetic algorithm [150] or even manual initialization have to be employed when discontinuities or critical situations occur in the test.

3.3.4 Reconstruction error

As shown in Equation (2-7), the displacement field is normally formulated and approximated by shape functions in order to solve the inverse problem. Various kinds of shape functions are applied in both local and global DIC approaches, which is also the fundamental part to classify DIC methods into the local and global algorithms. It is generally not possible to design a shape function that perfectly matches the actual displacement field in a particular application. Meanwhile, a higher-order or more complex shape function generally does not guarantee a more accurate measurement as errors could be introduced with the extra DoF of shape functions and the computational cost could be raised as well. Given a certain spatial resolution, a shape function with higher DoF is necessarily applied in order to capture the detail of a complex deformation. However, the error due to imperfect (under-fitting or over-fitting) shape functions cannot be eliminated by decreasing the spatial resolution through e.g. choosing smaller subsets (subset-based DIC) and elements (FE-based DIC) and can only be quantified when the kinematic field is known a-priori [38, 39]. The proper parameters of shape function could be determined for DIC analysis in the case that a-priori knowledge about the

complexity of actual displacement field is obtained by means of simulated experiments such as FE analysis [151].

3.3.5 Spatial resolution

For a local approach, it is desirable to improve the spatial resolution by decreasing the size of subsets in the RoI [18]. However, it was shown that the chosen subset size must be large enough in the subset-based DIC for precise displacement measurement when subset shape functions match underlying deformation [121]. On account of the influence of image noise in actual applications, there is also a lower limit for the subset size in order to reduce the errors due to noise [5, 11, 38, 121, 123]. Since a compromise always needs to be determined between the spatial resolution and the measurement precision (resolution), a criterion based on the variance of image noise and Sum of Square of Subset Intensity Gradients (SSSIG) was deduced from the SSD cost function for the selection of subset size [22]. A concept of subset entropy is created to normalize the subset size in [121] and the influences of subset size were studied on both homogeneous and heterogeneous displacement fields. On the other hand, the number of control points is subject to the computational cost [72, 152] and ill-posed problem [72] in regard to improving the spatial resolution in global DIC approaches.

3.3.6 Discontinuities

Discontinuities such as cracks are the main error sources that can lead to DIC mismatch. The essential reason comes from the failure of shape function to capture the local discontinuities as shape functions are normally applied on an assumption of a continuous and smooth displacement field. There are normally two procedures for tackling the effects of discontinuities, namely identification and correction. The

identification consists in developing a penalty function (e.g. on the distance between the estimated displacement field and its projection [108] or using an equivalent strain [10] or directly using the poor correlation coefficients [97]) to detect the discontinuities once they occur. Secondly, the correction mainly lies in excluding the large-deformed or discontinuous areas from the RoI [96], adding extra DoF or independences to the shape function [108], splitting the related subset [97] or zone of interest [10] and so on.

3.3.7 Optimisation techniques

Given the correlation criterion used in both local and global DIC approaches, the minimisation problem in terms of least square solution is generally implemented by spatial-domain iterative strategies such as gradient descent method like Newton–Raphson (NR) iteration [2, 36, 67-69], damped least-squares method like Levenberg–Marquardt algorithm [17, 39], genetic algorithms [64-66] and multi-grid solver [10]. Among these methods the NR iteration is considered to be the most accurate and commonly used method [70]. Due to the fact that DIC problem is actually an inverse problem, the ill-posed problem and computational cost become significant as the increasing complexity of shape functions and increasing number of control points (or finer control grid). In this sense, various procedures may have to be chosen for regularization (e.g. dealing with the noise) such as Fourier filtering [10], a frequency filter based on Laplacian operator [72], a regularization term based on Dirichlet Energy functional [18] and so on. From a Bayesian point of view, many regularization techniques actually correspond to imposing certain prior distributions on model parameters.

3.4 Standard uncertainty estimation in DIC

Most work has been done on investigating the errors and uncertainties due to a specific source, e.g. imperfect sub-pixel interpolation algorithm, Gaussian image noise and so on. However, little work has been carried out to develop a generic method in order to quantify the uncertainties from different error sources in DIC. A general framework [113, 153] of uncertainty quantification in an image-based measuring system shown in Figure 3–7 may be employed to illustrate the basic UQ approaches in regard to uncertainties introduced to different parts of DIC. It is shown that the standard uncertainty (defined in Section 3.1) of DIC measurement results may be quantified through an evaluation process which consists of three steps.

Specify the influence factors and their uncertainties → Develop model for standard uncertainty: a) Black-box model b) Analytical model → Propagate standard uncertainty through uncertainty model
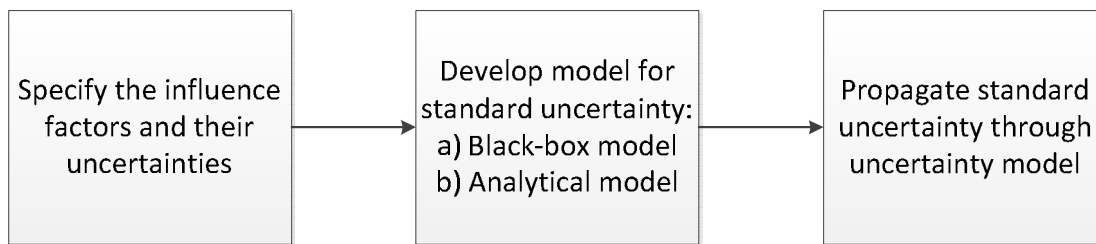
Figure 3–7. Standard uncertainty estimation in an image-based measuring system

3.4.1 Influence factors

The uncertainty of DIC measurement depends on a number of influence factors, e.g. the error factors shown in Table 3–1. The experimental errors in the image acquisition process result in intensity uncertainties in acquired images that can be propagated to the final DIC measurement result through DIC algorithms. Meanwhile the algorithmic errors also make a contribution to the uncertainty of the final DIC result.

3.4.2 Uncertainty modelling

In order to quantify the standard uncertainty of DIC measurement results, deterministic error effects (different from systematic errors) normally need to be estimated and corrected firstly [113, 120]. Once the correction ce has been estimated and applied, the standard uncertainty se of the measurement results is expressed as the combination of uncertainty of random errors se_s and uncertainty of the correction se_t as follows:

$$se^2 = se_s^2 + se_t^2 \qquad\qquad (3\text{-}2)$$

In general, there are two ways to evaluate the standard uncertainty, they are, black-box model (by statistical methods) and analytical model (white box) [154].

Black-box model

The black-box model is used to evaluate the standard uncertainty without the necessity of knowing the analytical relationship between the standard uncertainty and influence factors and is normally implemented through statistical methods (in a Monte Carlo manner). As shown in Figure 3–8, the deterministic errors may be experimentally evaluated through a comparison with a reference object or system yielding a correction ce and its corresponding uncertainty se_s [155]. In the meantime the standard deviation of measurement results se_t is obtained on the basis of a set of measurements keeping the measurand constant. However, the application of black-box method is subject to the number of influence factors and whether the measurand itself is controllable or not [155]. Based on a reference system of synthetic speckle images with spatially fluctuating sinusoidal displacement fields, the uncertainty of DIC measured displacements in terms of root-mean-square (RMS)

error was evaluated depending on a group of influence factors such as subset size, speckle size, shape function and sub-pixel interpolation scheme [38]. As discussed in [156], a calibration specimen called as reference material [157] was used to calibrate a DIC system to an acceptable uncertainty level according to the Standardisation Project for Optical Techniques of Strain measurement (SPOTS) [158] guideline.
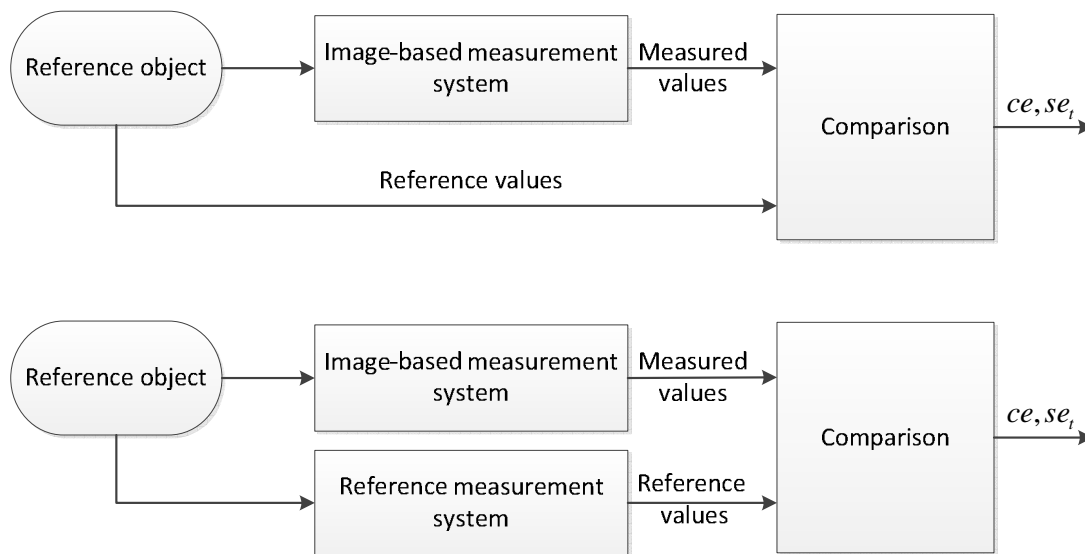
Figure 3–8. Estimation of deterministic errors by a black-box model (taken from [155])

White-box model

Apart from the black-box model, the analytical method works as an indirect approach to determine an analytical model for the uncertainty estimation, which requires the deterministic error and standard uncertainty to be known and analytically modelled.

Exact analytical model

The exact analytical model is normally expressed in an algebraic form for the measurement uncertainty (e.g. in terms of probability distribution) which can be

obtained without introducing any approximation. However it can be applied only in relatively simple cases. For example, a typical DIC systematic error due to intensity interpolation in a 1-D translation test was modelled by an analytical function of the phase error based on a Fourier shift theorem [36]. As shown in [23], the analytical expressions for DIC error expectation and variance due to Guassian image noise were derived according to DIC algorithm under uniform 1D and 2D translations.

Approximate model

In contrast to the accurate analytical model, approximation normally has to be employed to simplify the complex dependence relationship between influence factors and measurement uncertainty. A generic so-called GUM uncertainty framework [118, 153, 155, 159] may be applied to evaluate the standard uncertainty of DIC measurement results due to a number of influence factors under the assumption of linear dependence relationship and symmetric probability distribution of input and output quantities. By means of basic equations of stereo-vision, an analytical model for 3D DIC measurement was developed to estimate the 3D position bias and variability caused by stereo-vision parameters and image-plane matching procedures [129]. As opposed to these uncertainty models relying on DIC algorithms, a general post-processing uncertainty estimation model is presented in [35] by deriving the relationship between the standard deviation of intensity differences over a pair of matched subsets and the expected asymmetry of the correlation peak. Furthermore, the distribution of standard displacement uncertainty over a RoI induced by Gaussian image noise was analytically derived for the global FE DIC [8].

3.5 Uncertainty propagation

3.5.1 Uncertainty propagation law

Once an analytical expression for the standard uncertainty of DIC measurement is obtained, the uncertainty propagation law is applied to integrate the uncertainties of influence factors into the standard uncertainty of final measurement result. As presented in [23], the uncertainty due to Gaussian image noise in terms of intensity standard deviations was propagated to the uncertainty of measured displacement through DIC algorithm based on the uncertainty propagation law. The similar application of uncertainty propagation law is also observed in estimating the theoretical uncertainty of measured 3D positions in a 3D DIC system [129].

The application of uncertainty propagation law is generally developed for 3 types of uncertainty models including explicit model, implicit model and model involving complex quantities [159]. Taking an explicit multivariate model for example, a relationship specified between an output quantity $\tilde{\mathbf{h}} = (\tilde{h}_1, \cdots \tilde{h}_s)^{\mathrm{T}}$ and an input quantity $\tilde{\mathbf{d}} = (\tilde{d}_1, \cdots \tilde{d}_t)^{\mathrm{T}}$ is expressed as [159]:

$$\tilde{\mathbf{h}} = \Upsilon(\tilde{\mathbf{d}}), \quad \Upsilon = (\Upsilon_1, \cdots, \Upsilon_s)^{\mathrm{T}} \tag{3-3}$$

Given an estimate $\mathbf{d}$ of $\tilde{\mathbf{d}}$ and an estimate $\mathbf{h}$ of $\tilde{\mathbf{h}}$, it is obtained $\mathbf{h} \approx \Upsilon(\mathbf{d})$. According to the propagation law, the uncertainty covariance matrix related to $\mathbf{h}$ is given by (for random errors):

$$\mathbf{S_h} = \mathbf{D_d} \mathbf{S_d} \mathbf{D_d^{\mathrm{T}}} \text{ and } \mathbf{S_h} = \begin{bmatrix} \mathrm{cov}(h_1, h_1) & \cdots & \mathrm{cov}(h_1, h_s) \\ \vdots & \ddots & \vdots \\ \mathrm{cov}(h_s, h_1) & \cdots & \mathrm{cov}(h_s, h_s) \end{bmatrix}_{s \times s} \tag{3-4}$$

where $\text{cov}(h_j, h_j) = se^2(h_j)$ denotes the standard uncertainty of the output component h_j, $\mathbf{D_d}$ is the sensitivity matrix in the propagation and has the form:

$$\mathbf{D_d} = \begin{bmatrix} \dfrac{\partial \Upsilon_1}{\partial d_1} & \cdots & \dfrac{\partial \Upsilon_1}{\partial d_t} \\ \vdots & \ddots & \vdots \\ \dfrac{\partial \Upsilon_s}{\partial d_1} & \cdots & \dfrac{\partial \Upsilon_s}{\partial d_t} \end{bmatrix}_{s \times t} \tag{3-5}$$

3.5.2 Uncertainty propagation based on the Monte Carlo method

When an analytical model is not available (e.g. black-box model) or it is impossible to apply the uncertainty propagation law, Monte Carlo method (MCM) is a feasible way to approximate the distribution function (uncertainty) for the output quantities and is established numerically by making random draws from the probability distributions of input quantities [153]. Both a boot-strap Monte Carlo approach and a traditional Monte Carlo approach [142] were used to propagate the image correlation error and the calibration parameter variation through a triangulation process to the uncertainty of 3D-DIC measurement result. Along with an analytical uncertainty model, the Monte Carlo approach was also used to estimate the expectation and variance of 3D positions in DIC measurement in order to validate the theoretical results given by the analytical model [129].

3.6 Kriging regression method

Originally developed in geo-statistics [160], Kriging is also widely used in the fields of spatial analysis and computer experiments. The word "Kriging" is synonymous

with "optimal prediction" [161]. It is a method of interpolation which predicts unknown values from data observed at known locations. This method uses variogram to express the spatial variation and minimizes the error of predicted values which are estimated by spatial distribution of the predicted values. The development and applications of Kriging method was extensively overviewed in the work of Cressie [52, 53]. Different from a piecewise-polynomial spline that optimizes smoothness of the observed data, Kriging provides the best linear unbiased prediction (BLUP) [53] of intermediate values. Based on a Bayesian perspective [53, 54], Kriging models the intermediate values by using a Gaussian process governed by prior covariance, which further delivers uncertainty quantification (UQ) on the best linear unbiased prediction of the measurement.

Since the sample data is not measured with perfect accuracy and normally subject to measurement noise, an error factor can be introduced to the Kriging interpolation model to account for the measurement imprecision and allow the regression instead of interpolation on the sample points. The introduction of a regularization factor for the treatment of biased estimates in multiple regression was originally proposed in the work of Hoerl and Kennard [55] in 1970, who termed the technique 'ridge regression'. Aiming to filter out numerical noise, the same approach was applied to the design and analysis of 'noisy' computer experiments in the field of computer simulations by Forrester et al. [56]. If only a single regularization factor is introduced, it is deemed as a global approach by which the uniform uncertainty across the domain of interest [162] can be treated. In contrast, a local error estimate technique in the field of particle image velocimetry (PIV) was proposed by Jouke et al. [163] by means of developing an uncertainty model based on peak ratios [164] in

the cross-correlation map, which actually extended the error estimate from the global to the local sense.

3.7 Uncertainty analysis based on Kriging regression

The Monte Carlo Method (MCM) is a feasible way to analyse the uncertainty for output quantities, it can be computationally expensive and time consuming. In contrast, Kriging can be used as a surrogate model [165] to simulate the true output quantities with minimizing the computational cost and maximizing model accuracy, which further makes a contribution to the uncertainty quantification. The Kriging surrogate modelling strategy is also known as Gaussian process emulation based on the concepts of Bayesian statistics [166] and the analysis and design of computer experiments [167, 168]. Oakley [169] applied the Gaussian process emulation to analyse the uncertainty for computationally expensive computer models based on an inference about the observed sample data from a Bayesian perspective. Apart from the Monte Carlo analysis, an alternative general theory for uncertainty analysis with uncertain inputs was developed in the thesis of Haylock [170] by using the stochastic process models from a Bayesian context. Furthermore, F.A. DiazDelaO et al. [171] employed Bayesian emulator (Kriging) for the uncertainty analysis of the frequency response in a stochastic structural dynamic analysis.

3.8 Closure

A detailed survey of DIC error sources and standard uncertainty analysis in image processing is presented first in this chapter. In addition, a brief review is provided on the Kriging regression and the uncertainty quantification. It will be discussed in detail in Chapter 5. In the next chapter, the significance of and existing problems

concerning DIC error reduction and uncertainty quantification are addressed. The idea of applying the Kriging regression method to DIC is also introduced.

4

DIC Error Reduction and

Uncertainty Quantification

This chapter outlines the significance of error reduction and uncertainty quantification in DIC applications. The commonly used methods in DIC error reduction and uncertainty quantification are briefly reviewed first. A generic uncertainty quantification technique for the subset-based DIC is then derived according to the DIC SSD criterion. The bias error induced by Gaussian image noise under uniform translation is estimated for the application in DIC sub-pixel registration. Furthermore, a simple but effective error reduction approach is proposed with respect to the bias due to the grey-level interpolation and image noise. The Kriging regression method is applied to DIC, which aims at developing a superior and reliable technique to deal with DIC measurement errors and uncertainties from a global sense.

4.1 Introduction

4.1.1 DIC error reduction

The basic principle and implementation of DIC is relatively simple, but the effective reduction of the measurement error due to various error sources remains an unsolved problem. As discussed in Chapter 2, DIC error sources can be generally classified into two main categories: experimental and algorithmic errors. Each category includes a series of specific error sources, for example, the quality of experimental images is inevitably influenced by experimental setups like illumination, vibration and so on. In the existing work, some methods are proposed focusing on dealing with specific error sources, e.g. the imperfect grey-interpolation schemes [5, 36] and the limitation of shape functions (under- or over-fitting problems) [38, 39]. In contrast to the error reduction methods focusing on a certain error source, local smoothing [32, 33, 40-42] techniques are applied as a kind of generic method to reduce measurement errors due to various kinds of image acquisition noise. These methods have the advantage of simplicity and work well for most DIC applications but are subject to an ad-hoc choice of parameterisation, which probably only lead to a local optimum. In order to overcome such limitations, the Kriging regression techniques can be introduced to deal with these error sources in a global sense for a global improvement in the measurement accuracy, thanks to the excellent capability of Kriging in global optimisation. This is discussed in detail in Chapter 6 and 7.

In Section 4.3, a simple but effective error reduction approach developed by the author is presented. The method is proposed to tackle the sub-pixel registration bias in an algorithmic sense.

4.1.2 DIC uncertainty quantification

Along with increasing applications of DIC in various fields, there has been a growing interest in a reliable quantification for DIC measurement uncertainty, which is particularly important since DIC is extensively used as a full-field measurement technique and the measurement uncertainty will always be present whatever the level of precision. However, due to the intrinsic complexity of DIC error sources as discussed in Chapter 3, it is very difficult to analytically quantify the measurement uncertainty by means of a rigorous mathematical derivation especially when considering all the possible error sources. Aiming to quantify uncertainties due to various error sources, a generic UQ method should be developed. Very little work has been done in this field except for the following methods:

(i) An uncertainty quantification method derived based on Gaussian image noise and the DIC SSD criterion [5, 23, 51]: This method was originally developed by Sutton et al. [5] whereas the uncertainty estimation of a 1D DIC case with uniform translations was developed as a function of the variance of Gaussian image noise and sum of the grey-level intensity gradients. Furthermore, this method was extended to a 2D DIC case and the sum of grey-gradients was changed to the inverse of Hessian matrix [51]. However, this method only provides an approximate uncertainty estimation without considering the subset deformation and is limited to the presence of Gaussian image noise rather than various kinds of error sources.

(ii) A post-processing uncertainty quantification method developed based on the expected asymmetry of a correlation peak [35]: This post-processing uncertainty quantification method developed by Wieneke et al. [35] derived a relationship between the standard deviation of intensity differences of matched subsets and the

expected asymmetry of correlation peak in a post-processing correlation map. In fact, this kind of method was developed based on a second-order polynomial fitting for the expected correlation peak, which might not hold all the time. Also the subset deformation is still not taken into consideration for uncertainty quantification properly.

(iii) The temporal and spatial random errors in subset-based DIC measurement investigated by Wang [172]: The temporal and spatial random errors were defined to describe the repeatability of the DIC measurements due to the time varying image noise and the differences between subsets when they were subject to the same displacement respectively. Basically, these two types of errors focused on the repeatability of measurement rather than a specific measurement which is actually studied in this thesis. However, the derivation of the spatial random error was limited to the self-correlated or rigid-motion test, where the subset displacements were the same from location to location. Also the derivation of temporal random error was very similar to Sutton's work [5] except for considering the intensity-interpolation errors in a very complicated way. In addition, the intensity-interpolation error may be considered in a simple way by using SSD residual.

According to the above studies, a more general form of the DIC uncertainty estimation is derived in the sequel by considering an equivalent variance based on the SSD residual and the subset deformation in terms of a second-order shape function. This generic subset-based uncertainty estimation is also incorporated into a post-processing Kriging regression technique for a global uncertainty quantification, which is discussed in detail in Chapter 7.

4.2 Generic uncertainty estimation for subset-based DIC

In this section, a generic analysis for measurement error of the subset-based DIC is presented in order to obtain a mathematical expression for the measurement error due to various error sources. For simplicity, derivations start from a 2-dimensional case in the presence of Gaussian random additive noise with grey-intensity interpolation schemes [5, 23], which are also the most common error sources in DIC measurement. A point at coordinate $\mathbf{x}_c:(x_c, y_c)$ defines the central pixel of a reference grey-level image $f(x, y)$, which for convenience takes the form of a square subset consisting of $N \times N$ pixels. The central-node coordinate of the deformed grey-level image $g(\tilde{x}, \tilde{y})$ is given by $\tilde{\mathbf{x}}_c:(\tilde{x}_c, \tilde{y}_c)$.

The grey-level images $\overline{f}(x, y)$ and $\overline{g}(\tilde{x}, \tilde{y})$ consist of the true images, $f(x, y)$ and $g(\tilde{x}, \tilde{y})$, plus the grey-intensity error defined by $\zeta_f(x, y)$ and $\zeta_g(\tilde{x}, \tilde{y})$ respectively,

$$\overline{f}(x, y) = f(x, y) + \zeta_f(x, y) \tag{4-1}$$

$$\overline{g}(\tilde{x}, \tilde{y}) = g(\tilde{x}, \tilde{y}) + \zeta_g(\tilde{x}, \tilde{y}) \tag{4-2}$$

where $\zeta_f(x, y)$ and $\zeta_g(\tilde{x}, \tilde{y})$, to be estimated experimentally, are assumed to be Gaussian $\mathcal{N}(0, \sigma_\zeta^2)$, independent and identically distributed across the subset. Moreover, there is measurement error in the difference between the deformed- and the reference-image coordinates denoted by $\tilde{\boldsymbol{\varepsilon}}_e$. Then the measured coordinate

$\tilde{\mathbf{x}}_s : (\tilde{x}_s, \tilde{y}_s)$ takes the form of $\tilde{\mathbf{x}}_s = \boldsymbol{\tau}_s + \tilde{\boldsymbol{\varepsilon}}_e$ and $\boldsymbol{\tau}_s$ denotes the true coordinate of the deformed image.

The true coordinate, and therefore the displacement error is unknown. However, it is reasonable to assume that the error across each subset can be modelled using a shape function. This leads to the formulation of weighting terms that account for different levels of error in different regions of the full image. In this study the displacements error $\tilde{\boldsymbol{\varepsilon}}_e(\mathbf{x}_s)$ at an arbitrarily chosen pixel with coordinates (x_s, y_s) is modelled using a second-order shape function model,

$$\tilde{\boldsymbol{\varepsilon}}_e(\mathbf{x}_s) = \boldsymbol{\mu}^{\mathrm{T}}(\mathbf{x}_s)\boldsymbol{\rho}_e \tag{4-3}$$

where $\boldsymbol{\mu}(\mathbf{x}_s)$ denotes the shape function coefficients,

$$\boldsymbol{\mu}(\mathbf{x}_s) = [1 \quad \Delta x_s \quad \Delta y_s \quad \tfrac{1}{2}(\Delta x_s)^2 \quad \tfrac{1}{2}(\Delta y_s)^2 \quad \Delta x_s \Delta y_s]^{\mathrm{T}} \tag{4-4}$$

and $\boldsymbol{\rho}_e$ is the matrix of variables in the two directions x, y,

$$\boldsymbol{\rho}_e = \begin{bmatrix} \boldsymbol{\rho}_u & \boldsymbol{\rho}_v \end{bmatrix} = \begin{bmatrix} u_0 & u_x & u_y & u_{xx} & u_{yy} & u_{xy} \\ v_0 & v_x & v_y & v_{xx} & v_{yy} & v_{xy} \end{bmatrix}^{\mathrm{T}} \tag{4-5}$$

where Δx_s and Δy_s are the distances between the pixel point $\mathbf{x}_s$ and the centre node of the subset at $\mathbf{x}_c$. Alternative shape function models may also be used, for example, the first-order shape function, depending upon the shape function applied in the subset-based DIC algorithm.

The form of local error estimate is developed according to the most commonly used DIC criterion [33, 34] i.e. the SSD,

$$\mathcal{C}_{SSD} = \sum_{s=1}^{N \times N} \left[\overline{g}(\tilde{\mathbf{x}}_s) - \overline{f}(\mathbf{x}_s) \right]^2 \tag{4-6}$$

or, by equations (4-1), (4-2), (4-3) and (4-6),

$$\mathcal{C}_{SSD} = \sum_{s=1}^{N \times N} \left(g\left(\boldsymbol{\tau}_s + \boldsymbol{\mu}^{\mathrm{T}}(\mathbf{x}_s)\, \boldsymbol{\rho}_e \right) + \zeta_g\left(\boldsymbol{\tau}_s + \boldsymbol{\mu}^{\mathrm{T}}(\mathbf{x}_s)\, \boldsymbol{\rho}_e \right) - \left(f(\mathbf{x}_s) + \zeta_f(\mathbf{x}_s) \right) \right)^2 \tag{4-7}$$

Newton iteration is generally applied in the DIC calculation to determine the displacement error $\boldsymbol{\rho}_e$ that minimises $\mathcal{C}_{SSD}$, so that at the $(t+1)^{th}$ step [94],

$$\nabla\nabla\mathcal{C}_{SSD}\left({}_t\boldsymbol{\rho}_e \right)\left({}_{t+1}\boldsymbol{\rho}_e - {}_t\boldsymbol{\rho}_e \right) = -\nabla\mathcal{C}_{SSD}\left({}_t\boldsymbol{\rho}_e \right) \tag{4-8}$$

$\nabla\nabla\mathcal{C}_{SSD}$ is the second-order gradient of the correlation coefficient, also known as the Hessian matrix [2, 57, 94].

Alternatives to the SSD criterion include the normalized sum of squared differences (NSSD), zero-normalized sum of squared differences (ZNSSD) etc. The Cross Correlation (CC), which is related to and can also be deduced from the SSD criterion [33, 34], may also be used.

4.2.1 The Hessian matrix and determination of error variables

In Equation (4-7) the coordinate error $\boldsymbol{\mu}^{\mathrm{T}}(\mathbf{x}_s)\, \boldsymbol{\rho}_e$ may be considered to be small, in which case the first-order Taylor expansion with respect to $g(\bullet)$ and $\zeta_g(\bullet)$ leads to,

$$\begin{aligned}
\mathcal{C}_{SSD}(\boldsymbol{\rho}_e) = \sum_{s=1}^{N \times N} \Big(& g(\boldsymbol{\tau}_s) + \nabla g(\boldsymbol{\tau}_s) \cdot \boldsymbol{\mu}^{\mathrm{T}}(\mathbf{x}_s)\, \boldsymbol{\rho}_e + \zeta_g(\boldsymbol{\tau}_s) \\
& + \nabla\zeta_g(\boldsymbol{\tau}_s) \cdot \boldsymbol{\mu}^{\mathrm{T}}(\mathbf{x}_s)\, \boldsymbol{\rho}_e - f(\mathbf{x}_s) - \zeta_f(\mathbf{x}_s) \Big)^2
\end{aligned} \tag{4-9}$$

where $\nabla g (\boldsymbol{\tau}_s)$ represents the grey-level gradient. It is known that $g(\boldsymbol{\tau}_s) = f(\mathbf{x}_s)$ and $\nabla g (\boldsymbol{\tau}_s) + \nabla \zeta_g (\boldsymbol{\tau}_s) = \nabla \left(g(\boldsymbol{\tau}_s) + \zeta_g (\boldsymbol{\tau}_s) \right) = \nabla \overline{g} (\boldsymbol{\tau}_s)$, so that equation (4-9) may be simplified as,

$$\mathcal{C}_{SSD}(\boldsymbol{\rho}_e) = \sum_{s=1}^{N \times N} \left(\nabla \overline{g} (\boldsymbol{\tau}_s) \cdot \boldsymbol{\mu}^{\mathrm{T}} (\mathbf{x}_s) \boldsymbol{\rho}_e + \zeta_g (\boldsymbol{\tau}_s) - \zeta_f (\mathbf{x}_s) \right)^2 \qquad (4\text{-}10)$$

If the gradient terms in x- and y-directions are separated out, then

$$\mathcal{C}_{SSD}(\boldsymbol{\rho}_e) = \sum_{s=1}^{N \times N} \left(\nabla \overline{g}_x (\boldsymbol{\tau}_s) \cdot \boldsymbol{\mu}^{\mathrm{T}} (\mathbf{x}_s) \boldsymbol{\rho}_u + \nabla \overline{g}_y (\boldsymbol{\tau}_s) \cdot \boldsymbol{\mu}^{\mathrm{T}} (\mathbf{x}_s) \boldsymbol{\rho}_v \right.$$
$$\left. + \zeta_g (\boldsymbol{\tau}_s) - \zeta_f (\mathbf{x}_s) \right)^2 \qquad (4\text{-}11)$$

Minimisation of the SSD requires that, $d\mathcal{C}_{SSD}/d\boldsymbol{\rho}_u = d\mathcal{C}_{SSD}/d\boldsymbol{\rho}_v = 0$ which leads to the following expression for the determination of $\begin{pmatrix} \boldsymbol{\rho}_u^{\mathrm{T}} & \boldsymbol{\rho}_v^{\mathrm{T}} \end{pmatrix}$,

$$\mathbf{H} \begin{pmatrix} \boldsymbol{\rho}_u \\ \boldsymbol{\rho}_v \end{pmatrix} = \mathbf{b} \qquad (4\text{-}12)$$

where,

$$\mathbf{H} = \begin{bmatrix} \sum (\nabla \overline{g}_x \cdot \mu_1)^2 & \cdots & \sum (\nabla \overline{g}_x)^2 \mu_1 \mu_6 & \sum (\nabla \overline{g}_y \cdot \mu_1)(\nabla \overline{g}_x \cdot \mu_1) & \cdots & \sum (\nabla \overline{g}_y \cdot \mu_6)(\nabla \overline{g}_x \cdot \mu_1) \\ \vdots & & \vdots & \vdots & & \vdots \\ \sum (\nabla \overline{g}_x)^2 \mu_1 \mu_6 & \cdots & \sum (\nabla \overline{g}_x \cdot \mu_6)^2 & \sum (\nabla \overline{g}_y \cdot \mu_1)(\nabla \overline{g}_x \cdot \mu_6) & \cdots & \sum (\nabla \overline{g}_y \cdot \mu_6)(\nabla \overline{g}_x \cdot \mu_6) \\ \sum (\nabla \overline{g}_x \cdot \mu_1)(\nabla \overline{g}_y \cdot \mu_1) & \cdots & \sum (\nabla \overline{g}_x \cdot \mu_6)(\nabla \overline{g}_y \cdot \mu_1) & \sum (\nabla \overline{g}_y \cdot \mu_1)^2 & \cdots & \sum (\nabla \overline{g}_y)^2 \mu_1 \mu_6 \\ \vdots & & \vdots & \vdots & & \vdots \\ \sum (\nabla \overline{g}_x \cdot \mu_1)(\nabla \overline{g}_y \cdot \mu_6) & \cdots & \sum (\nabla \overline{g}_x \cdot \mu_6)(\nabla \overline{g}_y \cdot \mu_6) & \sum (\nabla \overline{g}_y)^2 \mu_1 \mu_6 & \cdots & \sum (\nabla \overline{g}_y \cdot \mu_6)^2 \end{bmatrix}$$
$$(4\text{-}13)$$

is an approximation to the Hessian matrix when the second-order partial derivatives are considered to be negligible [57, 94]. The terms $\nabla \overline{g}_x (\boldsymbol{\tau}_s)$, $\nabla \overline{g}_y (\boldsymbol{\tau}_s)$ and $\mu_i (\mathbf{x}_s)$

are abbreviated to $\nabla \overline{g}_x$, $\nabla \overline{g}_y$ and μ_i. The vector $\mathbf{b}$ in Equation (4-12) may be written as,

$$
\mathbf{b} = - \begin{pmatrix}
\sum_{s=1}^{N \times N} \left(\nabla \overline{g}_x (\boldsymbol{\tau}_s) \mu_1 (\mathbf{x}_s) \right) \cdot \left(\zeta_g (\boldsymbol{\tau}_s) - \zeta_f (\mathbf{x}_s) \right) \\
\vdots \\
\sum_{s=1}^{N \times N} \left(\nabla \overline{g}_x (\boldsymbol{\tau}_s) \mu_6 (\mathbf{x}_s) \right) \cdot \left(\zeta_g (\boldsymbol{\tau}_s) - \zeta_f (\mathbf{x}_s) \right) \\
\sum_{s=1}^{N \times N} \left(\nabla \overline{g}_y (\boldsymbol{\tau}_s) \mu_1 (\mathbf{x}_s) \right) \cdot \left(\zeta_g (\boldsymbol{\tau}_s) - \zeta_f (\mathbf{x}_s) \right) \\
\vdots \\
\sum_{s=1}^{N \times N} \left(\nabla \overline{g}_y (\boldsymbol{\tau}_s) \mu_6 (\mathbf{x}_s) \right) \cdot \left(\zeta_g (\boldsymbol{\tau}_s) - \zeta_f (\mathbf{x}_s) \right)
\end{pmatrix}
\tag{4-14}
$$

The vector of uncertainties is then given by,

$$
\begin{pmatrix} \boldsymbol{\rho}_u \\ \boldsymbol{\rho}_v \end{pmatrix} = \mathbf{H}^{-1} \mathbf{b}
\tag{4-15}
$$

4.2.2 Estimation of error variance in a general form

The grey-level error was defined as independent and identically distributed, satisfying a Gaussian distribution $\mathcal{N}\left(0, \sigma_\zeta^2\right)$, at each pixel. Therefore, by linearisation

$$
\mathrm{Cov} \begin{pmatrix} \boldsymbol{\rho}_u \\ \boldsymbol{\rho}_v \end{pmatrix} \cong \sigma_\zeta^2 \cdot \mathbf{J} \cdot \mathbf{J}^{\mathrm{T}}
\tag{4-16}
$$

where $\mathbf{J}$ is the Jacobian matrix, which from Equation (4-15) is given by

$$
\mathbf{J} = \mathbf{H}^{-1} \mathbf{b}'
\tag{4-17}
$$

where,

$$\mathbf{b}' = \left[\frac{\partial \mathbf{b}}{\partial \zeta_g(\boldsymbol{\tau}_{11})} \quad \cdots \quad \frac{\partial \mathbf{b}}{\partial \zeta_g(\boldsymbol{\tau}_{NN})} \quad \frac{\partial \mathbf{b}}{\partial \zeta_f(\boldsymbol{\tau}_{11})} \quad \cdots \quad \frac{\partial \mathbf{b}}{\partial \zeta_f(\boldsymbol{\tau}_{NN})} \right] \tag{4-18}$$

and,

$$\mathbf{b}'(\mathbf{b}')^{\mathrm{T}} = 2\mathbf{H} \tag{4-19}$$

Finally, from equations (4-16), (4-17) and (4-19) it is found that,

$$\mathrm{Cov}\begin{pmatrix} \boldsymbol{\rho}_u \\ \boldsymbol{\rho}_v \end{pmatrix} \cong 2\sigma_\zeta^2 \cdot \mathbf{H}^{-1} \tag{4-20}$$

The error at the centre node of the subset is the first term in each row of $\boldsymbol{\rho}_e$ as defined in Equation (4-5). The displacement variance at the centre node in one subset may then be approximated [5, 23] as,

$$\begin{cases} \mathrm{Var}(u_0) \cong 2\sigma_\zeta^2 \cdot \left(\mathbf{H}^{-1}\right)_{11} \\ \mathrm{Var}(v_0) \cong 2\sigma_\zeta^2 \cdot \left(\mathbf{H}^{-1}\right)_{77} \end{cases} \tag{4-21}$$

The above derivations are subject to the assumption of Gaussian errors and therefore provides only a lower-bound error estimate. A more general case may be derived from the residual $\mathcal{C}_{SSD}$ of the SSD criterion [35, 51] such that the $2\sigma_\zeta^2$ in Equation (4-21) is replaced by,

$$\frac{\mathcal{C}_{SSD}}{N^2} = \frac{\sum_{s=1}^{N \times N} \left[g(\tilde{\mathbf{x}}_s) - f(\mathbf{x}_s) \right]^2}{N \times N} \tag{4-22}$$

Since ideally the SSD criterion can be minimised close to zero under a perfect match of two subsets based on the optical flow theory, the non-zero SSD residual is actually caused by the combined effect of various error sources. Thus the

replacement of the $2\sigma_\zeta^2$ in Equation (4-21) by the Equation (4-22) enables the estimation of DIC measurement error due to different kinds of errors and results in a generic uncertainty quantification of DIC measurement.

4.2.3 Estimation of bias under the uniform translation

In practical applications, digital images are inevitably contaminated by noise. The influence of the noise-induced bias may become significant when high sub-pixel accuracy is demanded in the application such as DIC sub-pixel registration. Also the noise-induced bias is normally combined with the bias caused by the grey-intensity interpolation. The study in this section is limited to the Gaussian image noise and the uniform translation over a subset (or a RoI).

Depending on the error propagation theory [23] and the assumption of uniform translation, the bias error due to Gaussian image noise and imperfect grey-intensity interpolation may be expressed as:

$$\mathrm{E}\begin{pmatrix}\boldsymbol{\rho}_u\\\boldsymbol{\rho}_v\end{pmatrix}\approx\mathbf{H}^{-1}\mathrm{E}(\mathbf{b}) \tag{4-23}$$

Considering $\nabla\overline{g}_x\left(\boldsymbol{\tau}_s\right)=\nabla g_x\left(\boldsymbol{\tau}_s\right)+\nabla_x\zeta_g\left(\boldsymbol{\tau}_s\right)$ and $\zeta_f\left(\mathbf{x}_s\right)=\overline{f}\left(\mathbf{x}_s\right)-g\left(\boldsymbol{\tau}_s\right)$, the term of $\mathrm{E}(\mathbf{b})$ can be simplified by combining Equation (4-14) and (4-23) as:

$$\mathrm{E}(\mathbf{b})=\mathrm{E}\begin{pmatrix}\sum\left(\nabla\overline{g}_x\cdot\mu_1\cdot(\overline{f}-g)-\nabla g_x\cdot\mu_1\cdot\zeta_g-\nabla_x\zeta_g\cdot\mu_1\cdot\zeta_g\right)\\\vdots\\\sum\left(\nabla\overline{g}_x\cdot\mu_6\cdot(\overline{f}-g)-\nabla g_x\cdot\mu_6\cdot\zeta_g-\nabla_x\zeta_g\cdot\mu_6\cdot\zeta_g\right)\\\sum\left(\nabla\overline{g}_y\cdot\mu_1\cdot(\overline{f}-g)-\nabla g_y\cdot\mu_1\cdot\zeta_g-\nabla_y\zeta_g\cdot\mu_1\cdot\zeta_g\right)\\\vdots\\\sum\left(\nabla\overline{g}_y\cdot\mu_6\cdot(\overline{f}-g)-\nabla g_y\cdot\mu_6\cdot\zeta_g-\nabla_y\zeta_g\cdot\mu_6\cdot\zeta_g\right)\end{pmatrix} \tag{4-24}$$

The terms $\nabla \bar{g}_x(\boldsymbol{\tau}_s)$, $\nabla \bar{g}_y(\boldsymbol{\tau}_s)$, $\nabla g_x(\boldsymbol{\tau}_s)$, $\nabla g_y(\boldsymbol{\tau}_s)$, $\mu_i(\mathbf{x}_s)$, $\zeta_g(\boldsymbol{\tau}_s)$, $\nabla_x \zeta_g(\boldsymbol{\tau}_s)$, $\nabla_y \zeta_g(\boldsymbol{\tau}_s)$, $g(\boldsymbol{\tau}_s)$, $\bar{f}(\mathbf{x}_s)$ are abbreviated as $\nabla \bar{g}_x$, $\nabla \bar{g}_y$, ∇g_x, ∇g_y, μ_i, ζ_g, $\nabla_x \zeta_g$, $\nabla_y \zeta_g$, g, $\bar{f}$. In addition, the subscripts and superscripts on the summation are removed for simplicity. Since ζ_g, $\nabla g_\Omega (\Omega \in \{x, y\})$ and $\mu_i (i = 1, \cdots, 6)$ are independent by definition, it is straightforward to find that: $\mathrm{E}(\nabla g_\Omega \cdot \mu_i \cdot \zeta_g) = \mathrm{E}(\nabla g_\Omega) \cdot \mathrm{E}(\mu_i) \cdot \mathrm{E}(\zeta_g) = 0$. Thus the mathematical expectation can be simplified as:

$$\mathrm{E}(\mathbf{b}) = \mathrm{E}\begin{pmatrix} \sum\left(\nabla \bar{g}_x \cdot \mu_1 \cdot (\bar{f} - g) - \nabla_x \zeta_g \cdot \mu_1 \cdot \zeta_g\right) \\ \vdots \\ \sum\left(\nabla \bar{g}_x \cdot \mu_6 \cdot (\bar{f} - g) - \nabla_x \zeta_g \cdot \mu_6 \cdot \zeta_g\right) \\ \sum\left(\nabla \bar{g}_y \cdot \mu_1 \cdot (\bar{f} - g) - \nabla_y \zeta_g \cdot \mu_1 \cdot \zeta_g\right) \\ \vdots \\ \sum\left(\nabla \bar{g}_y \cdot \mu_6 \cdot (\bar{f} - g) - \nabla_y \zeta_g \cdot \mu_6 \cdot \zeta_g\right) \end{pmatrix} \tag{4-25}$$

Equation (4-25) can then be rearranged by incorporating an interpolation scheme (e.g. a 4×4 bi-cubic interpolation as discussed in Appendix A). According to the related derivations shown in Appendix A, the following equations are obtained:

$g(\boldsymbol{\tau}_s) = \boldsymbol{\psi}(\boldsymbol{\tau}_s^1) \cdot \mathbf{g}(\boldsymbol{\tau}_s^2)$, $\zeta_g(\boldsymbol{\tau}_s) = \boldsymbol{\psi}(\boldsymbol{\tau}_s^1) \cdot \hat{\boldsymbol{\zeta}}_\mathbf{g}(\boldsymbol{\tau}_s^2)$, $\nabla_x \zeta_g(\boldsymbol{\tau}_s) = \boldsymbol{\psi}'_x(\boldsymbol{\tau}_s^1) \cdot \hat{\boldsymbol{\zeta}}_\mathbf{g}(\boldsymbol{\tau}_s^2)$, and

$\nabla_y \zeta_g(\boldsymbol{\tau}_s) = \boldsymbol{\psi}'_y(\boldsymbol{\tau}_s^1) \cdot \hat{\boldsymbol{\zeta}}_\mathbf{g}(\boldsymbol{\tau}_s^2)$, where $\boldsymbol{\tau}_s^1$ and $\boldsymbol{\tau}_s^2$ are the fractional parts and integer parts of $\boldsymbol{\tau}_s$ respectively, $\boldsymbol{\psi}(\cdot)$ denotes the vector of interpolation kernel functions while $\boldsymbol{\psi}'_x(\cdot)$ and $\boldsymbol{\psi}'_y(\cdot)$ denote the vectors of corresponding derivative kernel functions of the grey-interpolation scheme. Thus Equation (4-25) may then be re-written as:

$$E(\mathbf{b}) = E \begin{pmatrix} \sum_{s=1}^{N \times N} \left(\nabla \overline{g}_x \cdot \mu_1 \cdot \left(\overline{f} - \psi(\boldsymbol{\tau}_s^1) \cdot \mathbf{g}\left(\boldsymbol{\tau}_s^2\right) \right) - \psi_x'(\boldsymbol{\tau}_s^1) \cdot \hat{\zeta}_{\mathbf{g}}\left(\boldsymbol{\tau}_s^2\right) \cdot \psi(\boldsymbol{\tau}_s^1) \cdot \hat{\zeta}_{\mathbf{g}}\left(\boldsymbol{\tau}_s^2\right) \cdot \mu_1 \right) \\ \vdots \\ \sum_{s=1}^{N \times N} \left(\nabla \overline{g}_x \cdot \mu_6 \cdot \left(\overline{f} - \psi(\boldsymbol{\tau}_s^1) \cdot \mathbf{g}\left(\boldsymbol{\tau}_s^2\right) \right) - \psi_x'(\boldsymbol{\tau}_s^1) \cdot \hat{\zeta}_{\mathbf{g}}\left(\boldsymbol{\tau}_s^2\right) \cdot \psi(\boldsymbol{\tau}_s^1) \cdot \hat{\zeta}_{\mathbf{g}}\left(\boldsymbol{\tau}_s^2\right) \cdot \mu_6 \right) \\ \sum_{s=1}^{N \times N} \left(\nabla \overline{g}_y \cdot \mu_1 \cdot \left(\overline{f} - \psi(\boldsymbol{\tau}_s^1) \cdot \mathbf{g}\left(\boldsymbol{\tau}_s^2\right) \right) - \psi_y'(\boldsymbol{\tau}_s^1) \cdot \hat{\zeta}_{\mathbf{g}}\left(\boldsymbol{\tau}_s^2\right) \cdot \psi(\boldsymbol{\tau}_s^1) \cdot \hat{\zeta}_{\mathbf{g}}\left(\boldsymbol{\tau}_s^2\right) \cdot \mu_1 \right) \\ \vdots \\ \sum_{s=1}^{N \times N} \left(\nabla \overline{g}_y \cdot \mu_6 \cdot \left(\overline{f} - \psi(\boldsymbol{\tau}_s^1) \cdot \mathbf{g}\left(\boldsymbol{\tau}_s^2\right) \right) - \psi_y'(\boldsymbol{\tau}_s^1) \cdot \hat{\zeta}_{\mathbf{g}}\left(\boldsymbol{\tau}_s^2\right) \cdot \psi(\boldsymbol{\tau}_s^1) \cdot \hat{\zeta}_{\mathbf{g}}\left(\boldsymbol{\tau}_s^2\right) \cdot \mu_6 \right) \end{pmatrix} \quad (4\text{-}26)$$

Under the assumption of uniform translation, $\boldsymbol{\tau}_s^1$ and $\boldsymbol{\tau}_s^2$ are constant from pixel to pixel across the region of interest, which further leads to the simplification of Equation (4-26),

$$E(\mathbf{b}) = \begin{pmatrix} \sum_{s=1}^{N \times N} \left(\nabla \overline{g}_x \cdot \mu_1 \cdot \left(\overline{f} - \psi(\boldsymbol{\tau}_s^1) \cdot \mathbf{g}\left(\boldsymbol{\tau}_s^2\right) \right) \right) - \eta_x(\boldsymbol{\tau}_s^1) \cdot N^2 \sigma_\zeta^2 \cdot \mu_1 \\ \vdots \\ \sum_{s=1}^{N \times N} \left(\nabla \overline{g}_x \cdot \mu_6 \cdot \left(\overline{f} - \psi(\boldsymbol{\tau}_s^1) \cdot \mathbf{g}\left(\boldsymbol{\tau}_s^2\right) \right) \right) - \eta_x(\boldsymbol{\tau}_s^1) \cdot N^2 \sigma_\zeta^2 \cdot \mu_6 \\ \sum_{s=1}^{N \times N} \left(\nabla \overline{g}_y \cdot \mu_1 \cdot \left(\overline{f} - \psi(\boldsymbol{\tau}_s^1) \cdot \mathbf{g}\left(\boldsymbol{\tau}_s^2\right) \right) \right) - \eta_y(\boldsymbol{\tau}_s^1) \cdot N^2 \sigma_\zeta^2 \cdot \mu_1 \\ \vdots \\ \sum_{s=1}^{N \times N} \left(\nabla \overline{g}_y \cdot \mu_6 \cdot \left(\overline{f} - \psi(\boldsymbol{\tau}_s^1) \cdot \mathbf{g}\left(\boldsymbol{\tau}_s^2\right) \right) \right) - \eta_y(\boldsymbol{\tau}_s^1) \cdot N^2 \sigma_\zeta^2 \cdot \mu_6 \end{pmatrix} \quad (4\text{-}27)$$

where $N^2 \sigma_\zeta^2$ represents the summation of Gaussian image noise (zero mean) while σ_ζ^2 represents the variance of the Gaussian image noise. $\eta_x(\boldsymbol{\tau}_s^1)$ and $\eta_y(\boldsymbol{\tau}_s^1)$ are interpolation coefficients. The terms $\eta_x(\boldsymbol{\tau}_s^1) \cdot N^2 \sigma_\zeta^2$ and $\eta_y(\boldsymbol{\tau}_s^1) \cdot N^2 \sigma_\zeta^2$ are obtained from Equation (A-7) in Appendix A. It should be noted that the derivation of Equation (4-27) is subject to the assumption of uniform translation. It may be only applicable in DIC sub-pixel registration where all the pixels within a subset are assumed to have the same displacement, namely under a uniform translation.

Depending on Equation (4-27) the expectation of the bias error E(**b**) has two terms for each component. The first term depends on the grey-intensity difference between the matched subsets, which indicates a portion of bias due to interpolation errors [57]. The second term describes the other portion of bias due to Gaussian image noise.

Thus under the assumption of uniform translation, the bias error of variables may be finally expressed as shown in Equation (4-28) which formulates the bias error of DIC sub-pixel registration. In Section, 4.3, a simple but effective approach is developed in order to significantly reduce this bias error.

$$
E\begin{pmatrix} \boldsymbol{\rho}_u \\ \boldsymbol{\rho}_v \end{pmatrix} \approx \mathbf{H}^{-1} \begin{pmatrix} \sum_{s=1}^{N \times N} \left(\nabla \overline{g}_x \cdot \mu_1 \cdot \left(\overline{f} - \boldsymbol{\psi}(\boldsymbol{\tau}_s^1) \cdot \mathbf{g}(\boldsymbol{\tau}_s^2) \right) \right) - \eta_x(\boldsymbol{\tau}_s^1) \cdot N^2 \sigma_\zeta^2 \cdot \mu_1 \\ \vdots \\ \sum_{s=1}^{N \times N} \left(\nabla \overline{g}_x \cdot \mu_6 \cdot \left(\overline{f} - \boldsymbol{\psi}(\boldsymbol{\tau}_s^1) \cdot \mathbf{g}(\boldsymbol{\tau}_s^2) \right) \right) - \eta_x(\boldsymbol{\tau}_s^1) \cdot N^2 \sigma_\zeta^2 \cdot \mu_6 \\ \sum_{s=1}^{N \times N} \left(\nabla \overline{g}_y \cdot \mu_1 \cdot \left(\overline{f} - \boldsymbol{\psi}(\boldsymbol{\tau}_s^1) \cdot \mathbf{g}(\boldsymbol{\tau}_s^2) \right) \right) - \eta_y(\boldsymbol{\tau}_s^1) \cdot N^2 \sigma_\zeta^2 \cdot \mu_1 \\ \vdots \\ \sum_{s=1}^{N \times N} \left(\nabla \overline{g}_y \cdot \mu_6 \cdot \left(\overline{f} - \boldsymbol{\psi}(\boldsymbol{\tau}_s^1) \cdot \mathbf{g}(\boldsymbol{\tau}_s^2) \right) \right) - \eta_y(\boldsymbol{\tau}_s^1) \cdot N^2 \sigma_\zeta^2 \cdot \mu_6 \end{pmatrix} \tag{4-28}
$$

4.3 Error Reduction based on an anti-symmetric feature of the sub-pixel registration bias

In this section an effective error reduction method is developed in an algorithmic sense based on the anti-symmetry feature of the bias in DIC sub-pixel registration due to the combined effect of the grey-intensity interpolation and random additive noise. The performance of the proposed method is verified by the statistical analysis of a numerical case with synthetic images.

As discussed in Section 4.2.3, the derivations of the bias due to the grey-intensity interpolation and Gaussian random noise under a uniform translation is actually applicable to the DIC sub-pixel registration bias since all the pixels within a subset can be assumed to be under a uniform translation in sub-pixel registration. Normally the DIC sub-pixel registration bias can be significantly reduced by using higher-order interpolation schemes [23, 36, 94, 173], specially designed noise filters [174], e.g. the Gaussian pre-filter [32] and images with low spatial frequencies [175]. In this section, an effective method is proposed based on an anti-symmetric feature of the DIC sub-pixel registration bias. Different types of interpolation schemes and different levels of Gaussian additive noise are investigated to test the performance of the proposed method.

A common anti-symmetric feature of DIC sub-pixel registration bias has been observed in the results of different researchers [5, 23, 32, 36, 176]. Figure 4–1 illustrates this anti-symmetric feature with different interpolation schemes [37] and Gaussian noise levels. It is shown to be in accordance with other published results [5, 36].

Specifically, the speckle patterns are obtained from an open-access DIC data set namely DIC challenge database [177]. The sub-pixel shift is implemented by applying the Fourier shift theorem [5, 36] to the reference speckle image (300×500 pixels) to generate a series of 10 translated speckle images with a shift of 0.1 pixels between successive images. Totally five sets of images are generated whereas the first two sets of images are generated by using the high-contrast speckle patterns as shown in Figure 4–1(a) and low-contrast speckle patterns as shown in Figure 4–1(b) respectively. The remaining three image sets are generated by using high-contrast speckles and adding three levels of Gaussian noise to each image set, as shown in

Figure 4–1(c). The added noise levels are 1.96%, 2.94% and 3.92% of the full 256 grayscales in terms of the standard deviation. In each image set, the displacements of each translated speckle pattern are computed using the subset-based DIC with a first-order shape function at regularly distributed 900 points with a subset size of 31×31 pixels. The calculated sub-pixel displacement error is the mean bias error. Also four different interpolation algorithms, i.e. 4×4 bi-cubic, 4×4 cubic-Spline, 4×4 Lagrange and 6×6 bi-cubic [37] are applied for bias evaluation.

According to Figure 4–1, the registration bias at a certain sub-pixel displacement (shift) is able to be counteracted by using the registration bias at the corresponding anti-symmetric sub-pixel displacement (shift). The detailed procedures are introduced in the following sections.
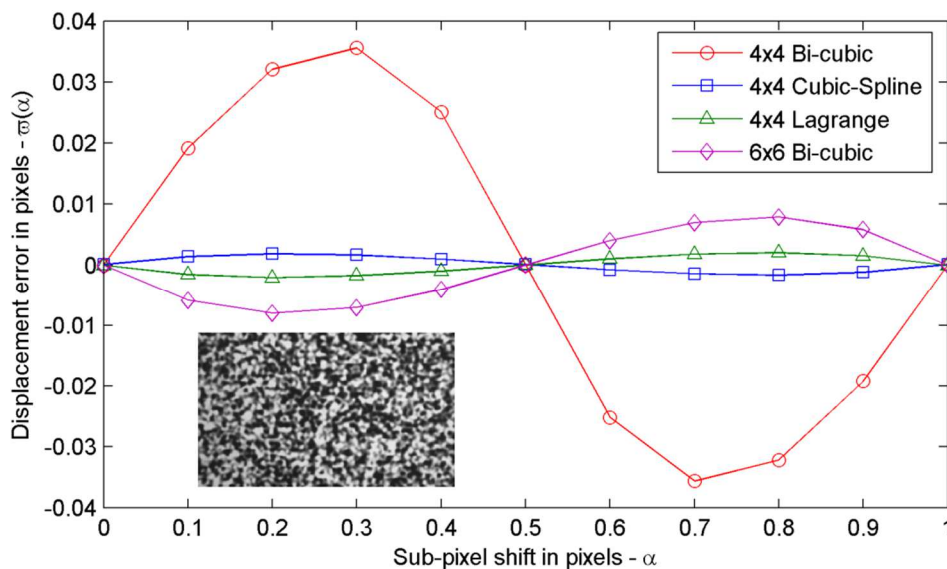
(a) high-contrast speckles with different interpolation schemes i.e. 4×4 Bi-cubic, 4×4 Cubic-Spline, 4×4 Lagrange and 6×6 Bi-cubic
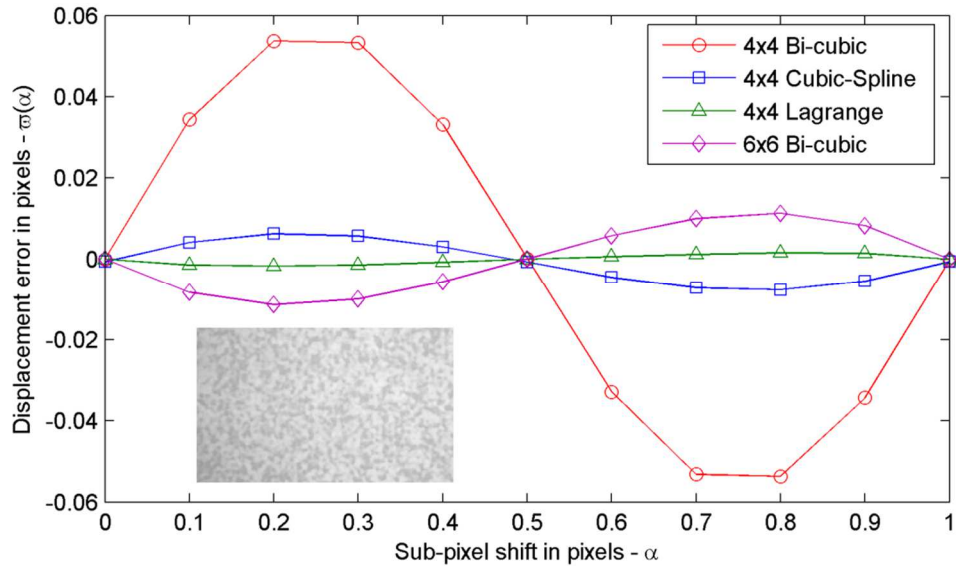
(b) low-contrast speckles with different interpolation schemes i.e. 4×4 Bi-cubic, 4×4
Cubic-Spline, 4×4 Lagrange and 6×6 Bi-cubic
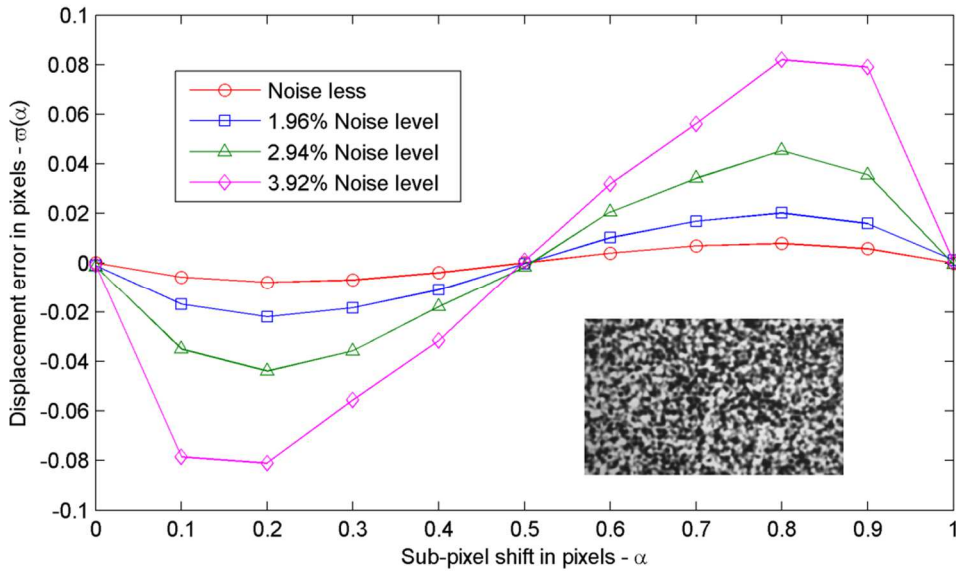
(c) high-contrast speckles with 6×6 Bi-cubic interpolation scheme under different
levels of noise

Figure 4–1. The anti-symmetric feature of sub-pixel registration bias due to
imperfect grey-intensity interpolation and additive Gaussian image noise

4.3.1 Method

According to the anti-symmetric feature of DIC sub-pixel registration bias, a simple but effective technique can be proposed to reduce or even eliminate the bias. As shown in Figure 4–1, the compensation of the bias at a certain sub-pixel displacement may be carried out by using the bias at the corresponding anti-symmetric sub-pixel displacement, since these two biases have the same amplitude but different signs. In practice, the true sub-pixel displacement shown on the x-axis of Figure 4–1 is unknown and may be approximated by the measured sub-pixel displacement with bias error. Thus the bias compensation method is actually implemented based on the measured displacement rather than the true displacement.

As illustrated in Figure 4–2 for a 1-D translation case, assuming α is the true sub-pixel displacement between the reference image Ref and deformed image Def, $\varpi(\alpha)$ denotes the sub-pixel registration bias (considering both the interpolation and noise-induced bias) with respect to the true displacement α. $\varpi(\alpha)$ has anti-symmetric and periodic features, which may be expressed as $\varpi(\alpha) = -\varpi(1-\alpha)$ (anti-symmetric) and $\varpi(\alpha) = \varpi(1+\alpha)$ (one period). If the measured displacement (between Ref and Def) is Γ_a ($\Gamma_a = \alpha + \varpi(\alpha)$) including the bias error $\varpi(\alpha)$, the corresponding anti-symmetric displacement $1-\Gamma_a$ contains a bias approximation to $-\varpi(\alpha)$. Thus the bias included in Γ_a may be approximately compensated by using the bias contained in $1-\Gamma_a$.

In order to obtain the displacement measurement $1-\Gamma_a$, an extra deformed image Def' may be generated by applying $1-2\Gamma_a$ translation to the original deformed image Def by using Fourier shift theorem. Then a new measurement Γ_b can be

carried out between the reference image Ref and the extra deformed image Def′.
Since no bias error is introduced by the Fourier shift, it actually gives
$\Gamma_b = \alpha + 1 - 2\Gamma_a \approx 1 - \Gamma_a$ where the approximation is due to the bias error.

Thus the bias may be approximately eliminated by summing Γ_a and Γ_b. Also the exact shift displacement $1 - 2\Gamma_a$ should be subtracted in order to calculate the improved displacement as shown in Figure 4–2. Then the displacement measurement between Ref and Def with reduced bias may be achieved as $\Gamma_c = \frac{1}{2} \times (\Gamma_a + \Gamma_b + 2\Gamma_a - 1)$. The above discussion is exemplified in the following analysis:

The measured displacement Γ_a may be expressed as:

$$\Gamma_a = \alpha + \varpi(\alpha) \tag{4-29}$$

Then the displacement Γ_b can be obtained as:

$$\begin{aligned}
\Gamma_b &= \alpha + 1 - 2\Gamma_a + \varpi(\alpha + 1 - 2\Gamma_a) \\
&= 1 - \alpha - 2\varpi(\alpha) + \varpi(1 - \alpha - 2\varpi(\alpha))
\end{aligned} \tag{4-30}$$

The displacement Γ_c with reduced bias becomes:

$$\begin{aligned}
\Gamma_c &= \frac{1}{2}(\Gamma_a + \Gamma_b + 2\Gamma_a - 1) \\
&= \alpha + \frac{1}{2}(\varpi(\alpha) + \varpi(1 - \alpha - 2\varpi(\alpha))) \\
&= \alpha + \frac{1}{2}(\varpi(\alpha) - \varpi(\alpha + 2\varpi(\alpha)))
\end{aligned} \tag{4-31}$$

Since $2\varpi(\alpha)$ is a very small quantity by definition, normally it gives $\left|\varpi(\alpha)-\varpi(\alpha+2\varpi(\alpha))\right|\ll\left|\varpi(\alpha)\right|$. Thus $\Gamma_c\approx\alpha$ is obtained, which indicates the registration bias has been reduced.

In some circumstances, applying the Fourier shift only once might not be good enough to approximate the true displacement when the image noise is relatively significant. In that case, the procedure can be repeated by applying a second Fourier shift to reduce the bias even further.
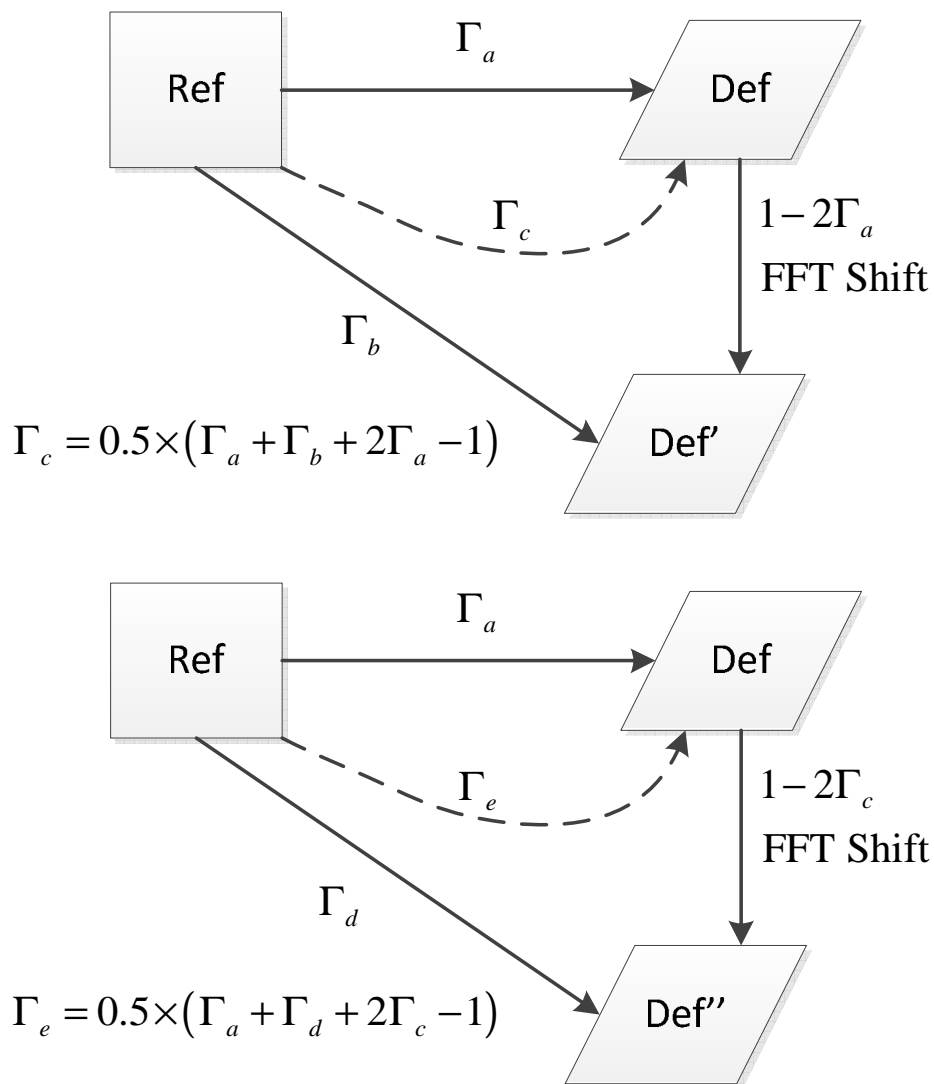
Figure 4–2. Bias reduction method based on the anti-symmetric feature of sub-pixel registration bias

An extra deformed image is generated through shifting the reference image by $1-2\Gamma_c$ (denoted as Def'') and the final result will become $\Gamma_e = \frac{1}{2} \times (\Gamma_a + \Gamma_d + 2\Gamma_c - 1)$. For the second Fourier shift, displacement Γ_d is calculated by:

$$\begin{aligned}\Gamma_d &= \alpha + 1 - 2\Gamma_c + \varpi(\alpha + 1 - 2\Gamma_c) \\ &= 1 - \alpha - \varpi(\alpha) + \varpi(\alpha + 2\varpi(\alpha)) + \varpi(1 - \alpha - \varpi(\alpha) + \varpi(\alpha + 2\varpi(\alpha)))\end{aligned} \tag{4-32}$$

Finally the measurement after a further bias reduction becomes:

$$\begin{aligned}\Gamma_e &= \frac{1}{2}(\Gamma_a + \Gamma_d + 2\Gamma_c - 1) \\ &= \alpha + \frac{1}{2}\Big[\varpi(\alpha) - \varpi\big(\alpha + (\varpi(\alpha) - \varpi(\alpha + 2\varpi(\alpha)))\big)\Big] \\ &\approx \alpha\end{aligned} \tag{4-33}$$

Compared with the term $\varpi(\alpha) - \varpi(\alpha + 2\varpi(\alpha))$ in the Equation (4-31), the error term $\varpi(\alpha) - \varpi\big(\alpha + (\varpi(\alpha) - \varpi(\alpha + 2\varpi(\alpha)))\big)$ in the above equation is much smaller. Thus it is found that the bias error has been further significantly reduced.
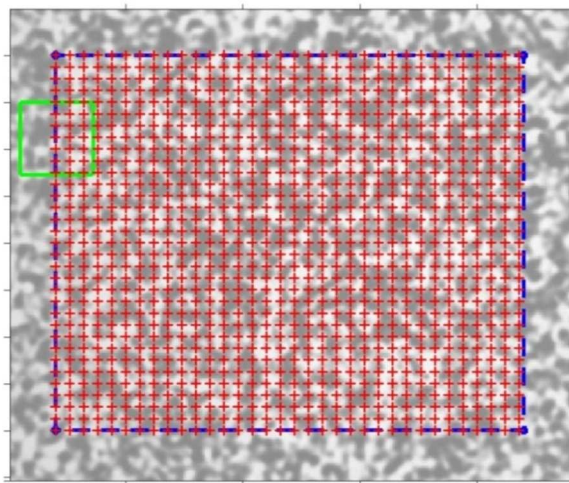
Figure 4–3. The distribution of sample points (centre points of subsets) shown in red crosses, subset size is illustrated by a green square

4.3.2 Case study

The performance of the proposed bias reduction method is verified by a numerical case study. Specifically, open-access speckle patterns from the DIC Challenge database [177] are applied to carry out the calculation for the purpose of isolating the errors due to imperfect imaging [178], loading [136] and so on. The image set consists of a reference image and 11 numerically translated counterparts according to Fourier shift theorem. The reference image is shown in Figure 4–3.

A shift increment of 0.1 pixels is used to generate the successive image counterparts from the reference image with a range from 0 to 1.0 pixels. Four different levels of white Gaussian noise are added to the original image set to generate other 4 sets of noisy images. The proposed method is applied to all the 5 sets of images in order to synthetically test its performance. The noise levels are 0%, 0.98%, 1.96%, 2.94% and 3.92% of full 255 greyscales respectively in terms of the standard deviation.

As shown in Figure 4–3, displacements between every two successive images are computed based on uniformly distributed 1024 points (centres of subsets) with a subset size of 31×31 pixels by using the subset-based DIC algorithm with a first-order shape function. The mean bias errors against sub-pixel shifts for various noise levels are demonstrated in Figure 4–4. It is observed that after the first bias reduction the bias of all noise levels are significantly reduced and after the second bias reduction all the bias are confined within a very narrow range from -0.004 to 0.004 pixels. The statistics of the registration bias in terms of standard deviation (STD) before and after the corrections are given in detail in Table 4-1.
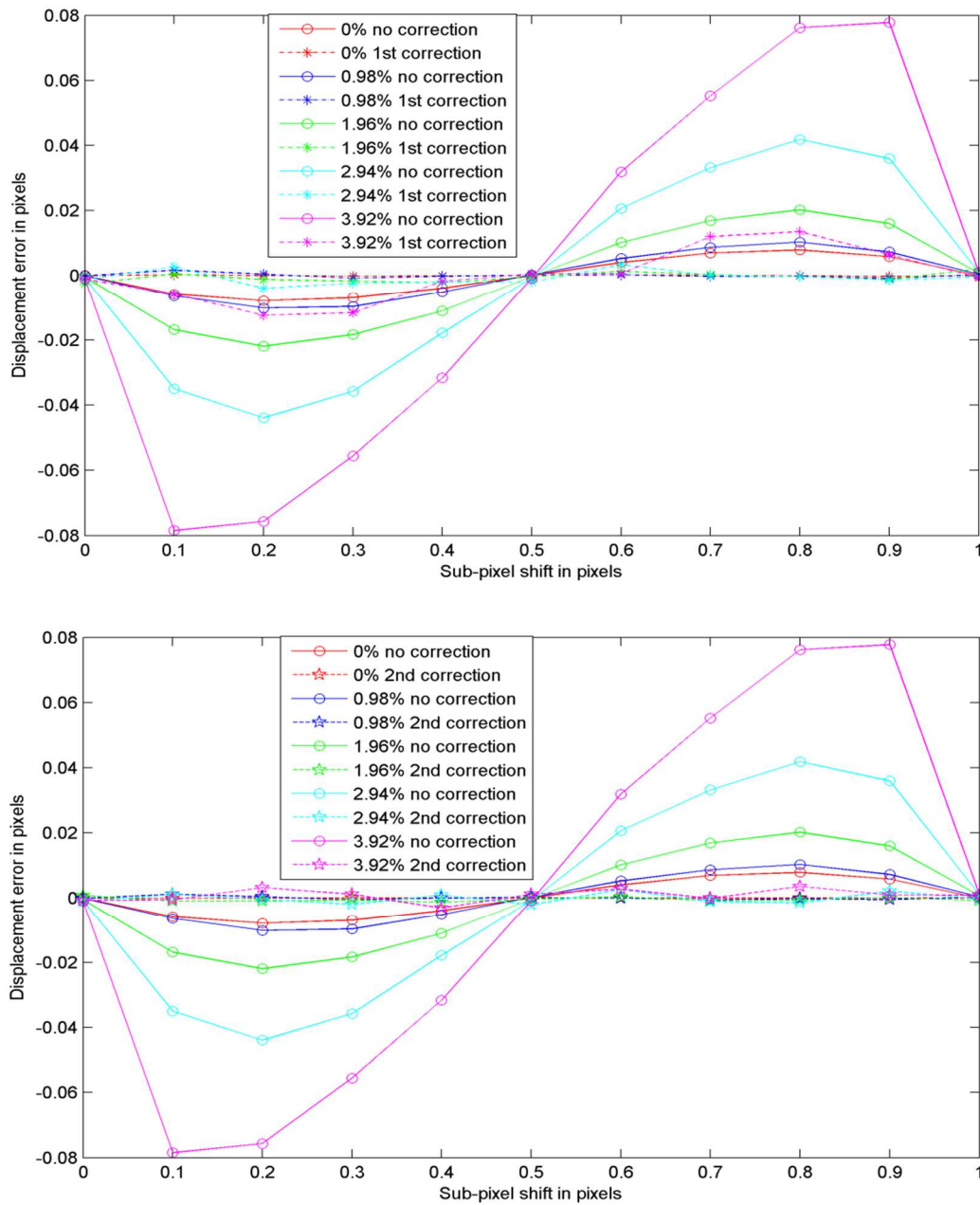
Figure 4–4. The reduction of sub-pixel registration bias based on its anti-symmetric feature, the x-axis denotes the sub-pixel increments while the y-axis denotes the mean bias based on 1024 samples.

Table 4–1: Statistics of the numerical results in terms of standard deviation STD

(in pixels)

Noise	No Correction - STD	1st Correction - STD	2nd Correction - STD
Original 0% noise	0.0057	0.0001	3e-5
0.98% noise	0.0073	0.0007	0.0005
1.96% noise	0.0151	0.0015	0.0006
2.94% noise	0.0305	0.0022	0.0016
3.98% noise	0.0565	0.0083	0.0019

4.4 Closure

Considering the limitations in existing uncertainty quantification methods, a generic subset-based uncertainty estimation is derived by using an equivalent error variance due to common DIC error sources. This local uncertainty estimation can be incorporated into the Kriging regression method to develop a post-processing technique to quantify the uncertainties of measured displacement and strain results, which is discussed in Chapter 7. Also the estimation of the bias error in DIC sub-pixel registration is derived under an assumption of Gaussian image noise and uniform translation. In addition, a simple but effective bias reduction method is developed from the algorithmic sense i.e. the reduction of DIC sub-pixel registration bias based on its anti-symmetric feature. Since most error reduction methods are normally proposed with respect to specific DIC error sources and generally lead to a local optimum, which highlights the significance of introducing the Kriging regression technique to improve the global accuracy of the measurement results, which is discussed in the Chapter 6 and 7.

5

Kriging Regression Theory

In this chapter, a brief introduction of Kriging regression theory is addressed with a view to potential applications in the field of DIC. A classical Kriging interpolation method is derived first through the framework of best linear unbiased prediction (BLUP). In regard to the measurement error of observed data, an error factor is introduced to Kriging interpolation in both global and local senses for the error regularisation, which actually enables the Kriging regression. As opposed to Kriging interpolation, Kriging regression accounts for the measurement errors of samples by regularising the Kriging correlation matrix. This allows regression instead of exact interpolation of the samples. Furthermore, the Kriging formula can also be derived and interpreted based on the Bayesian inference and it provides a practical way for uncertainty quantification.

5.1 Introduction

Originally developed in geo-statistics [160], Kriging is also known as a Gaussian process regression or Kolmogorov Wiener prediction, which is widely used in the fields of spatial analysis and computer experiments [168]. The complete history and extensive overview on the development of Kriging can be found in the work of Cressie [52, 53]. In the literature, Kriging is described as an interpolation (prediction) method to approximate unsampled points using random variables as a realization of a stochastic process. As opposed to a piecewise-polynomial spline that optimizes smoothness of the fitted data and is motivated by a minimum norm interpolation in Hilbert space, Kriging is a method that gives the best linear unbiased prediction (BLUP) [53] of intermediate values and is motivated by an expected squared error based on a stochastic model. Also Kriging can be interpreted from a Bayesian framework [53, 54], that is, the interpolated values are modelled by a Gaussian process governed by a prior covariance. Starting from a prior distribution over functions in terms of a Gaussian process, a value is predicted at any unsampled location by combining the prior with a Gaussian likelihood function and the resulting posterior distribution that is also Gaussian with a mean and covariance computed from the observed values.

Different types of Kriging [179] can be deducted on account of the stochastic properties of the random field and the various degrees of stationarity assumed, such as Simple Kriging with an assumption of a first-moment stationarity over the entire domain with a known mean, Ordinary Kriging assuming a constant unknown mean over the search neighbourhood of observed points, Universal Kriging (regression Kriging) formulating the unknown mean with a general polynomial trend model.

5.2 Kriging interpolation

The method applied in this study is the Universal Kriging, also known as 'Regression Kriging' or 'Kriging with External Drift' [180]. Specifically in DIC application, the true displacement field $w(x, y)$ is modelled using Kriging as a realisation of a random function $\hat{w}(x, y)$, which combines a deterministic regression model with a zero-mean stochastic field used to fit the residuals [168, 181] as,

$$\hat{w}(x, y) = \sum_{\ell=1}^{m} c_\ell(x, y)\beta_\ell + Z(x, y) \tag{5-1}$$

where $c_\ell(x, y)$, $\ell = 1, \ldots, m$, are regression functions, β_ℓ denotes the ℓth regression parameter and $Z(x, y)$ in the DIC algorithm will be modelled as a Gaussian stochastic field with zero mean and covariance between two arbitrary sample points j and k, assumed to take the form

$$\text{cov}\left(z(\mathbf{x}_j), z(\mathbf{x}_k)\right) = \sigma^2 r_{jk}\left(\mathbf{x}_j, \mathbf{x}_k, \vartheta_x, \vartheta_y\right); \quad \mathbf{x}_j = \left(x_j, y_j\right)^{\mathrm{T}}; \quad \mathbf{x}_k = \left(x_k, y_k\right)^{\mathrm{T}} \tag{5-2}$$

where $r_{jk}\left(\mathbf{x}_j, \mathbf{x}_k, \vartheta_x, \vartheta_y\right) = \text{corr}\left(z_j, z_k\right)$; $z_j = z(\mathbf{x}_j)$; $z_k = z(\mathbf{x}_k)$ is determined by the proximity of points j and k. The correlation parameters ϑ_x, ϑ_y and field variance σ^2 are described in detail in Section 5.3.3.

For the sake of convenience, only one-directional displacement response is considered and Kriging formula works exactly the same for the other directional displacement in DIC. If denoting $\mathbf{w}_0 = \left[w_1, \cdots, w_n\right]^{\mathrm{T}}$ as the vector of displacements calculated by DIC for a set of sample points (x_j, y_j), $j = 1, 2, \ldots, n$, , the matrix $\mathbf{R}$ of stochastic-process correlations between sample points may be defined as:

$$\mathbf{R} = \begin{bmatrix} r_{11}(\mathbf{x}_1, \mathbf{x}_1, \vartheta_x, \vartheta_y) & \cdots & r_{1n}(\mathbf{x}_1, \mathbf{x}_n, \vartheta_x, \vartheta_y) \\ \vdots & \ddots & \vdots \\ r_{n1}(\mathbf{x}_n, \mathbf{x}_1, \vartheta_x, \vartheta_y) & \cdots & r_{nn}(\mathbf{x}_n, \mathbf{x}_n, \vartheta_x, \vartheta_y) \end{bmatrix}_{n \times n} \tag{5-3}$$

where $r_{jk}(\mathbf{x}_j, \mathbf{x}_k, \vartheta_x, \vartheta_y)$, $i, j = 1, \cdots, n$ is the correlation function, the details of which are described in Section 5.2.5. For a untried point, $\mathbf{r}(x, y)$ is defined as the vector of stochastic-process correlations between the untried point (x, y) and each of the sample points (x_j, y_j), $j = 1, 2, \ldots, n,$:

$$\mathbf{r}(x, y) = \left[r(\mathbf{x}_1, \mathbf{x}, \vartheta_x, \vartheta_y) \quad \cdots \quad r(\mathbf{x}_n, \mathbf{x}, \vartheta_x, \vartheta_y) \right]_{1 \times n}^{\mathrm{T}}; \ \mathbf{x}_j = (x_j, y_j)^{\mathrm{T}}; \mathbf{x} = (x, y)^{\mathrm{T}} \tag{5-4}$$

Furthermore, $\mathbf{C}$ is defined as a matrix consisting of regression functions evaluated at the sample points:

$$\mathbf{C} = \begin{bmatrix} c_1(x_1, y_1) & c_2(x_1, y_1) & \cdots & c_m(x_1, y_1) \\ \vdots & \vdots & \ddots & \vdots \\ c_1(x_n, y_n) & c_2(x_n, y_n) & \cdots & c_m(x_n, y_n) \end{bmatrix}_{n \times m} \tag{5-5}$$

and $\mathbf{c}(x, y)$ is the vector of regression functions for the untried point (x, y):

$$\mathbf{c}(x, y) = \left[c_1(x, y) \quad \cdots \quad c_m(x, y) \right]_{1 \times m}^{\mathrm{T}} \tag{5-6}$$

5.2.1 Derivation of Kriging parameters

Based on the formulation of Kriging predictor, Kriging parameters can be derived through a framework of the best linear unbiased prediction, where 'best' means the Kriging predictor has a minimum mean square error; 'linear' indicates the Kriging predictor can be realised in linear mixed models for the estimation of random effects; 'unbiased' requires the expectation of the Kriging predicted values is equal to the true value under certain assumptions made, such as normality of the Gaussian

process. Basically, the Kriging predictor for an untried location (x, y) may be expressed in terms of a linear combination of the observed values as:

$$\hat{w}(x, y) = \sum_{j=1}^{n} \kappa_j(x, y) w_j = \mathbf{\kappa}^{\mathrm{T}}(x, y) \mathbf{w}_0 \qquad (5\text{-}7)$$

where $\mathbf{\kappa}(x, y) = \begin{pmatrix} \kappa_1 & \kappa_2 & \cdots & \kappa_n \end{pmatrix}^{\mathrm{T}}$ is a vector of linear coefficients. The prediction error can then be obtained:

$$\begin{aligned} \hat{w}(x, y) - w(x, y) &= \mathbf{\kappa}^{\mathrm{T}}(x, y) \cdot \mathbf{w}_0 - w(x, y) \\ &= \mathbf{\kappa}^{\mathrm{T}}(x, y)\big(\mathbf{C}\mathbf{\beta} + Z\big) - \big(\mathbf{c}^{\mathrm{T}}(x, y)\mathbf{\beta} + z(x, y)\big) \qquad (5\text{-}8) \\ &= \mathbf{\kappa}^{\mathrm{T}}(x, y)Z - z(x, y) + \big(\mathbf{C}^{\mathrm{T}}\mathbf{\kappa}(x, y) - \mathbf{c}(x, y)\big)^{\mathrm{T}} \mathbf{\beta} \end{aligned}$$

where $Z = \begin{bmatrix} z_1 & \cdots & z_n \end{bmatrix}^{\mathrm{T}}$ include the random errors at all the sample locations (design sites) and $z(x, y)$ represents the random error at the untried point (x, y). The Kriging model is obtained by the minimisation of mean squared error (MSE) subject to an unbiasedness condition,

$$\begin{aligned} &\underset{\kappa}{\arg\min.} \ \Big\{ \mathrm{E}\Big[\big(\hat{w}(x, y) - w(x, y)\big)^2 \Big] \Big\} \\ &\text{subject to } \mathrm{E}\big[\hat{w}(x, y) - w(x, y)\big] = 0 \end{aligned} \qquad (5\text{-}9)$$

where $\mathrm{E}[\bullet]$ denotes the mathematical expectation. The unbiasedness of Kriging predictor leads to:

$$\mathbf{C}^{\mathrm{T}}\mathbf{\kappa}(x, y) - \mathbf{c}(x, y) = 0 \qquad (5\text{-}10)$$

Thus under the unbiasedness condition, the mean squared error (MSE) of Kriging predictor is derived as:

$$\begin{aligned}
\mathrm{MSE}(x, y) &= \mathrm{E}\left[\left(\hat{w}(x, y) - w(x, y)\right)^2\right] \\
&= \mathrm{E}\left[\left(\boldsymbol{\kappa}^{\mathrm{T}}(x, y)Z - z(x, y)\right)^2\right] \\
&= \mathrm{E}\left[z^2(x, y) + \boldsymbol{\kappa}^{\mathrm{T}}(x, y)ZZ^{\mathrm{T}}\boldsymbol{\kappa}(x, y) - 2\boldsymbol{\kappa}^{\mathrm{T}}(x, y)Zz(x, y)\right] \\
&= \sigma^2\left(1 + \boldsymbol{\kappa}^{\mathrm{T}}(x, y)\mathbf{R}\boldsymbol{\kappa}(x, y) - 2\boldsymbol{\kappa}^{\mathrm{T}}(x, y)\mathbf{r}(x, y)\right)
\end{aligned}$$

(5-11)

The minimisation of the mean squared error (MSE) is achieved using a Lagrange multiplier function to enforce the constraint of unbiasedness:

$$\begin{aligned}
L(\boldsymbol{\kappa}(x, y), \boldsymbol{\lambda}) = {} & \sigma^2\left(1 + \boldsymbol{\kappa}^{\mathrm{T}}(x, y)\mathbf{R}\boldsymbol{\kappa}(x, y) - 2\boldsymbol{\kappa}^{\mathrm{T}}(x, y)\mathbf{r}(x, y)\right) \\
& - \boldsymbol{\lambda}^{\mathrm{T}}(\mathbf{C}^{\mathrm{T}}\boldsymbol{\kappa}(x, y) - \mathbf{c}(x, y))
\end{aligned}$$

(5-12)

The gradient of above function with respect to $\boldsymbol{\kappa}$ is:

$$L'(\boldsymbol{\kappa}(x, y), \boldsymbol{\lambda}) = 2\sigma^2\left(\mathbf{R}\boldsymbol{\kappa}(x, y) - \mathbf{r}(x, y)\right) - \mathbf{C}\boldsymbol{\lambda}$$

(5-13)

Concerning the necessary condition for the first-order optimality [182, 183], the Lagrangian function can be transformed to the solution of the following system of equations:

$$\begin{bmatrix} \mathbf{R} & \mathbf{C} \\ \mathbf{C}^{\mathrm{T}} & 0 \end{bmatrix} \begin{bmatrix} \boldsymbol{\kappa}(x, y) \\ \tilde{\boldsymbol{\lambda}} \end{bmatrix} = \begin{bmatrix} \mathbf{r}(x, y) \\ \mathbf{c}(x, y) \end{bmatrix}; \ \tilde{\boldsymbol{\lambda}} = -\frac{\boldsymbol{\lambda}}{2\sigma^2}$$

(5-14)

Finally, the Lagrange multiplier is obtained as:

$$\tilde{\boldsymbol{\lambda}} = (\mathbf{C}^{\mathrm{T}}\mathbf{R}^{-1}\mathbf{C})^{-1}(\mathbf{C}^{\mathrm{T}}\mathbf{R}^{-1}\mathbf{r}(x, y) - \mathbf{c}(x, y)) \ \text{ with } \ \boldsymbol{\kappa}(x, y) = \mathbf{R}^{-1}(\mathbf{r}(x, y) - \mathbf{C}\tilde{\boldsymbol{\lambda}})$$

(5-15)

Thus, the Kriging predictor is solved and expressed as:

$$\begin{aligned}
\hat{w}(x, y) &= \left((\mathbf{r}(x, y) - \mathbf{C}\tilde{\boldsymbol{\lambda}})^{\mathrm{T}}\mathbf{R}^{-1}\right)\mathbf{w}_0 \\
&= \left(\mathbf{r}^{\mathrm{T}}(x, y)\mathbf{R}^{-1} - (\mathbf{C}^{\mathrm{T}}\mathbf{R}^{-1}\mathbf{r}(x, y) - \mathbf{c}(x, y))^{\mathrm{T}}(\mathbf{C}^{\mathrm{T}}\mathbf{R}^{-1}\mathbf{C})^{-1}\mathbf{C}^{\mathrm{T}}\mathbf{R}^{-1}\right)\mathbf{w}_0
\end{aligned}$$

(5-16)

The estimated regression parameters $\hat{\boldsymbol{\beta}}$ may be estimated from the sample data by using the generalized least squares (GLS) method [53, 182], expressed as [182],

$$\hat{\boldsymbol{\beta}} = \left(\mathbf{C}^{\mathrm{T}}\mathbf{R}^{-1}\mathbf{C}\right)^{-1}\mathbf{C}^{\mathrm{T}}\mathbf{R}^{-1}\mathbf{w}_0 \tag{5-17}$$

Thus, a Best Linear Unbiased Prediction (BLUP) $\hat{w}(x, y)$ for arbitrary location (x, y) may be determined by Kriging interpolation as [182] (inserting Equation (5-17) to Equation (5-16)),

$$\hat{w}(x, y) = \mathbf{c}^{\mathrm{T}}(x, y)\hat{\boldsymbol{\beta}} + \mathbf{r}^{\mathrm{T}}(x, y)\mathbf{R}^{-1}\left(\mathbf{w}_0 - \mathbf{C}\hat{\boldsymbol{\beta}}\right) \tag{5-18}$$

5.2.2 Kriging weights

Since Kriging is derived as a Best Linear Unbiased Prediction (BLUP) for the true displacement field [160], the displacement response $\hat{w}(x, y)$ at an arbitrary untried location (x, y) can be formulated by the Kriging model in terms of a linear combination of the sample values and corresponding weights (as shown in Equation (5-7)):

$$\hat{w}(x, y) = \sum_{j=1}^{n} \kappa_j(x, y)w_j = \boldsymbol{\kappa}^{\mathrm{T}}\mathbf{w}_0\,(x, y) \tag{5-19}$$

where $\boldsymbol{\kappa}(x, y) = \left(\kappa_1 \quad \kappa_2 \quad \cdots \quad \kappa_n\right)^{\mathrm{T}}$ and $\kappa_j(x, y), j = 1, 2, \ldots, n,$ are actually the Kriging weights [184] obtained by the previously defined unbiasedness and minimisation of mean squared error (MSE). The Kriging weights may then be extracted from Equation (5-16) and written as [160],

$$\boldsymbol{\kappa}(x, y) = \mathbf{R}^{-1}\left(\mathbf{r}(x, y) - \mathbf{C}\left(\mathbf{C}^{\mathrm{T}}\mathbf{R}^{-1}\mathbf{C}\right)^{-1}\left(\mathbf{C}^{\mathrm{T}}\mathbf{R}^{-1}\mathbf{r}(x, y) - \mathbf{c}(x, y)\right)\right) \tag{5-20}$$

It can be easily verified that the sample-point displacements are exactly reproduced by the Kriging model based on (5-19) and (5-20). Let $\hat{w}(x, y) = w_j$, then $\mathbf{r}(x, y) = \mathbf{R}_{:,j}$ so that $\mathbf{R}^{-1}\mathbf{r}(x, y) = \mathbf{e}_j$. Also $\mathbf{c}(x, y) = \mathbf{C}^{\mathrm{T}}\mathbf{e}_j$ which causes the term $\left(\mathbf{C}^{\mathrm{T}}\mathbf{R}^{-1}\mathbf{r}(x, y) - \mathbf{c}(x, y)\right)$ to vanish. Then it is seen that $\boldsymbol{\kappa}(x, y) = \mathbf{e}_j$. In addition, according to the unbiased requirement and the stationary assumption, it requires that the sum of weights needs to be one:

$$\sum_{j=1}^{n} \kappa_j(x, y) = 1 \qquad (5\text{-}21)$$

5.2.3 Kriging gradients

With reference to strain calculation in DIC, how to accurately solve the gradients of displacement field becomes an important issue. In regard to Kriging application in DIC, it is appropriate to discuss the solution of gradients from the Kriging formula. According to Equation (5-18), the gradients at an arbitrary location in the region of interest formulated by Kriging model may be expressed as (only considering the displacement in one dimension):

$$\hat{\mathbf{w}}'(x, y) = \mathbf{J}_{\mathbf{c}}^{\mathrm{T}}(x, y)\hat{\boldsymbol{\beta}} + \mathbf{J}_{\mathbf{r}}^{\mathrm{T}}(x, y)\mathbf{R}^{-1}\left(\mathbf{w}_0 - \mathbf{C}\hat{\boldsymbol{\beta}}\right); \ \hat{\mathbf{w}}'(x, y) = \left[\frac{\partial \hat{w}(x, y)}{\partial x} \quad \frac{\partial \hat{w}(x, y)}{\partial y}\right]^{\mathrm{T}} \quad (5\text{-}22)$$

where $\mathbf{J}_{\mathbf{c}}(x, y)$ and $\mathbf{J}_{\mathbf{r}}(x, y)$ are the Jacobians of $\mathbf{c}(x, y)$ and $\mathbf{r}(x, y)$ respectively.

$$\left(\mathbf{J}_{\mathbf{c}}(x, y)\right)_i = \left[\frac{\partial c_i(x, y)}{\partial x} \quad \frac{\partial c_i(x, y)}{\partial y}\right]^{\mathrm{T}} \text{ and}$$

$$\left(\mathbf{J}_{\mathbf{r}}(x, y)\right)_i = \left[\frac{\partial r_i(\mathbf{x}_i, \mathbf{x}, \vartheta_x, \vartheta_y)}{\partial x} \quad \frac{\partial r_i(\mathbf{x}_i, \mathbf{x}, \vartheta_x, \vartheta_y)}{\partial y}\right]^{\mathrm{T}} \qquad (5\text{-}23)$$

Furthermore, if the displacement responses in both x- and y-directions are considered, the gradient matrix is expanded as ($\Omega \in \{x, y\}$)

$$\hat{\mathbf{w}}'_{\Omega}(x, y) = \begin{bmatrix} \hat{\mathbf{w}}'_x(x, y) & \hat{\mathbf{w}}'_y(x, y) \end{bmatrix} = \begin{bmatrix} \dfrac{\partial \hat{w}_x(x, y)}{\partial x} & \dfrac{\partial \hat{w}_y(x, y)}{\partial x} \\ \dfrac{\partial \hat{w}_x(x, y)}{\partial y} & \dfrac{\partial \hat{w}_y(x, y)}{\partial y} \end{bmatrix} \qquad (5\text{-}24)$$

5.2.4 Mean square error and infill criterion

The estimated Mean Squared Error (MSE) is easily obtained based on the optimised Kriging model, which normally provides a convenient infill criterion to determine the locations for new sample points to improve the Kriging model.

If substituting Equation (5-15) into Equation (5-11), the MSE at any location (x, y) may be derived and expressed as [182],

$$\text{MSE}(x, y) = \hat{\sigma}^2 \left(1 + \mathbf{v}^{\text{T}} \left(\mathbf{C}^{\text{T}} \mathbf{R}^{-1} \mathbf{C} \right)^{-1} \mathbf{v} - \mathbf{r}^{\text{T}}(x, y) \mathbf{R}^{-1} \mathbf{r}(x, y) \right) \qquad (5\text{-}25)$$

where $\mathbf{v} = \mathbf{C}^{\text{T}} \mathbf{R}^{-1} \mathbf{r}(\mathbf{x}) - \mathbf{c}(\mathbf{x})$, and $\hat{\sigma}^2$ is given by Equation (5-35). Adding the new sample point at the location where the Maximum Mean Square Error (MMSE) exists is a very commonly used infill criterion. However, it should be noted that adding new points imposes a compromise between accuracy and numerical stability. Even if the estimation improves due to the presence of more information carried by the data, having too many points may cause the columns of $\mathbf{R}$ to become numerically close and therefore linearly dependent for practical purposes.

Apart from the normally used MMSE criterion, Sacks et al. [168] introduced two other types of simple infill criteria in their study, they are, Integrated Mean Squared Error (IMSE) and Entropy [185]. In addition, other more sophisticated infill

strategies were also proposed based on placing the new sample point where the maximum likelihood of the predicted objective function value is highest and placing the new sample point where the expectation of the improvement of the objective function is highest. For example, an alternative infill criterion was proposed by Forrester et al. [56, 162, 186], in which the objective function is the Kriging output with a minimum at an unknown coordinate. This enables added control point to be chosen that have the greatest effect on reducing the objective function.

5.2.5 Regression and correlation functions

Referring to Equation (5-6), there are usually three types of regression functions applied in Kriging formula using 0, 1st and 2nd order polynomials respectively. The detailed expressions of regression functions are given as follows:

Constant, $m = 1$:

$$c_1(x, y) = 1 \tag{5-26}$$

Linear, $m = 3$:

$$c_1(x, y) = 1, \ c_2(x, y) = x, \ c_3(x, y) = y \tag{5-27}$$

Quadratic, $m = 6$:

$$c_1(x, y) = 1, \ c_2(x, y) = x, \ c_3(x, y) = y, \ c_4(x, y) = x^2,$$
$$c_5(x, y) = y^2, \ c_6(x, y) = xy \tag{5-28}$$

The corresponding Jacobians are (O denotes the null matrix and I is the identity matrix):

Constant: $\mathbf{J_c}(x, y) = \left[O_{2 \times 1} \right]$,

Linear: $\mathbf{J_c}(x, y) = \begin{bmatrix} O_{2\times 1} & I_{2\times 2} \end{bmatrix}$,

Quadratic: $\mathbf{J_c}(x, y) = \begin{bmatrix} O_{2\times 1} & I_{2\times 2} & H \end{bmatrix}$, where $H = \begin{bmatrix} 2x & y & 0 \\ 0 & x & 2y \end{bmatrix}$.

On the other hand, the correlation function is normally assumed exponential (also called Gaussian), expressed in the form,

$$r_{jk} = \exp(-\vartheta_x(x_j - x_k)^2 - \vartheta_y(y_j - y_k)^2) \tag{5-29}$$

The choice of this correlation function relies on the assumption of the response surface inferred by the Kriging regression to be smooth. This means that points close to each other have a higher correlation. The terms ϑ_x and ϑ_y determine how far apart both x_j and x_k and y_j and y_k need to be before differences in the estimate given by equation (5-29) become significant. Apart from the normally applied Gaussian correlation function, there are some other types of correlation functions shown in Table 5–1,which can be found in the literature [182].

Table 5–1: Correlation functions (only considering x- and y- directions)

Exponential (absolute)	$r_{jk} = \exp(-\vartheta_x\|x_j - x_k\| - \vartheta_y\|y_j - y_k\|)$
Generalized Exponential	$r_{jk} = \exp(-\vartheta_x\|x_j - x_k\|^{\vartheta_e} - \vartheta_y\|y_j - y_k\|^{\vartheta_e}), \ 0 < \vartheta_e \leq 2$
Linear	$r_{jk} = \max\{0, \ 1 - \vartheta_x\|x_j - x_k\|\} \cdot \max\{0, \ 1 - \vartheta_y\|y_j - y_k\|\}$

5.3 Kriging regression

In practical applications, the sample data are not measured with perfect accuracy, but are subject to measurement noise and imprecision. Kriging interpolation is incapable of tackling this measurement error. However, this limitation can be overcome by allowing the Kriging model to regress instead of exactly interpolating the sample data. Specifically, sample-data error can be accounted for by regularizing the diagonal elements of the Kriging correlation matrix $\mathbf{R}$ [55, 56, 163], which actually allows the Kriging model to pass through the small neighbourhoods of the samples rather than exactly through the samples themselves. This modified formulation introduces an additional parameter to be determined and is known as Kriging regression [162].

5.3.1 Kriging regression in a global sense

In a global sense, the measurement error is assumed independent and identically distributed across the entire RoI. Then the diagonal elements of the correlation matrix $\mathbf{R}$ can be modified by applying an unknown constant factor ξ [56, 63, 163]. It is implemented by perturbing the correlation matrix $\mathbf{R}$, which then becomes $\mathbf{R}+\xi\mathbf{I}$ where ξ predominantly represents measurement error (but also error induced by other sources such as numerical error) and the identity matrix in the added term $\xi\mathbf{I}$ corresponds to the independent and identically distributed error at each sample point.

5.3.2 Kriging regression in a local sense

However, the DIC error normally is not distributed uniformly over the RoI but varies from subset to subset and may be separately considered independent and identically distributed over a subset. If the local variations in the measurement

uncertainty can be quantified or estimated, then different error factors (rather than a constant factor) should be applied to the diagonal elements of **R** [54]. The modified diagonal elements of correlation matrix **R** can be expressed as:

$$\text{diag}(\mathbf{R}) = \varsigma_i \qquad (5\text{-}30)$$

where ς_i represents local measurement uncertainty. In order to reduce the computational complexity, only an unknown error parameter ξ is used and introduced to the optimisation process of Kriging model. Thus the element ς_i in the error vector can be formulated with the help of uncertainty ratios as:

$$\varsigma_i = \frac{\tilde{e}_i}{\tilde{e}_1} \xi \qquad (5\text{-}31)$$

where $\tilde{e}_i$ and $\tilde{e}_1$ denote the original local uncertainty estimates for the ith and 1st subset. $\tilde{e}_1$ is used as a normalising constant. In addition, the estimation for local measurement uncertainty of the subset-based DIC is given in detail in Section 4.2, and is further discussed in Chapter 7.

Compared with the Kriging interpolation model, the Kriging regression model introduces one more error parameter ξ to be determined in both global and local senses. Thus the Kriging interpolation prediction shown in Equation (5-18) is extended to the Kriging regression prediction by incorporating the error parameter ξ into the **R** matrix, as:

$$\hat{w}(x, y) = \mathbf{c}^{\mathrm{T}}(x, y)\hat{\boldsymbol{\beta}} + \mathbf{r}^{\mathrm{T}}(x, y)\mathbf{R}_\xi^{-1}\left(\mathbf{w}_0 - \mathbf{C}\hat{\boldsymbol{\beta}}\right) \qquad (5\text{-}32)$$

5.3.3 Solution of unknown parameters

The parameters of the Kriging regression model $\{\boldsymbol{\beta}, \sigma^2, \vartheta_x, \vartheta_y, \xi\}$ can be solved by maximizing the log likelihood of the observed data $\mathbf{w}_0$ under an assumed Gaussian distribution [187, 188], as given:

$$\mathcal{L}\left(\vartheta_x, \vartheta_y, \xi\right) = \frac{1}{(2\pi)^{\frac{n}{2}} (\sigma^2)^{\frac{n}{2}} \left|\mathbf{R}(\vartheta_x, \vartheta_y, \xi)\right|^{\frac{1}{2}}} \exp\left(\frac{-\left(\mathbf{w}_0 - \mathbf{C}\boldsymbol{\beta}\right)^{\mathrm{T}} \mathbf{R}^{-1}(\vartheta_x, \vartheta_y, \xi)\left(\mathbf{w}_0 - \mathbf{C}\boldsymbol{\beta}\right)}{2\sigma^2}\right) \quad (5\text{-}33)$$

By taking the natural logarithm and ignoring constant terms, it may be expressed as,

$$\ln \mathcal{L}\left(\vartheta_x, \vartheta_y, \xi\right) = -\frac{n}{2}\ln\left(\sigma^2\right) - \frac{1}{2}\ln\left(\left|\mathbf{R}(\vartheta_x, \vartheta_y, \xi)\right|\right) - \frac{\left(\mathbf{w}_0 - \mathbf{C}\boldsymbol{\beta}\right)^{\mathrm{T}} \mathbf{R}^{-1}(\vartheta_x, \vartheta_y, \xi)\left(\mathbf{w}_0 - \mathbf{C}\boldsymbol{\beta}\right)}{2\sigma^2} \\ + \text{ constant terms} \quad (5\text{-}34)$$

The estimate $\hat{\sigma}^2$ is obtained by setting the first derivative with respect to σ^2 to zero and then expressed by,

$$\hat{\sigma}^2 = \frac{1}{n}\left(\mathbf{w}_0 - \mathbf{C}\hat{\boldsymbol{\beta}}\right)^{\mathrm{T}} \mathbf{R}^{-1}\left(\vartheta_x, \vartheta_y, \xi\right)\left(\mathbf{w}_0 - \mathbf{C}\hat{\boldsymbol{\beta}}\right) \quad (5\text{-}35)$$

with regression coefficient $\hat{\boldsymbol{\beta}}$ is updated from Equation (5-17) by incorporating the error factor ξ:

$$\hat{\boldsymbol{\beta}} = \left(\mathbf{C}^{\mathrm{T}}\mathbf{R}^{-1}\left(\vartheta_x, \vartheta_y, \xi\right)\mathbf{C}\right)^{-1}\mathbf{C}^{\mathrm{T}}\mathbf{R}^{-1}\left(\vartheta_x, \vartheta_y, \xi\right)\mathbf{w}_0 \quad (5\text{-}36)$$

Substituting Equation (5-36) and (5-35) into Equation (5-34), the concentrated log likelihood function [187] is obtained and used in practice, given by,

$$\frac{n}{2}\ln(\hat{\sigma}^2) + \frac{1}{2}\ln\left(\left|\mathbf{R}(\vartheta_x, \vartheta_y, \xi)\right|\right) \quad (5\text{-}37)$$

The log likelihood function (5-37) is complex and generally multimodal. Thus, the computation of optimal values for $\vartheta_x, \vartheta_y, \xi$ usually requires specialised optimisation algorithms and heuristics like genetic algorithms [168, 189] or gradient-free methods such as the Hooke and Jeeve's algorithm [67], and the Nelder-Mead [190] simplex algorithm.

In the case of a large number of sample points Q, the computational cost of a conventional maximum likelihood estimate (MLE) could become significant. Two fast methods for estimating the unknown parameters of Kriging model were proposed in [191], they are, the frequency-domain maximum likelihood estimate (FMLE) for uniformly sampled data and the frequency-domain sample variogram (FSV) for non-uniformly sampled data. It is shown that a significant reduction in the computational complexity (related to the number of floating-point operations) from $O(Q^3)$ (MLE) to $O(Q \ln Q)$ is achieved while preserving the accuracy of the Kriging model.

In addition, it is necessary in above equations to invert the correlation matrix, which may be ill-conditioned while the introduction of ξ has the benefit of acting as a regularisation parameter [162] against ill-conditioning, which tends to prevail when large numbers of control points are introduced. Ranjan et al. [192] considered the classical Tikhonov regularisation of the form $\left(\mathbf{R} + \delta \mathbf{I} \right)$ where δ is the regularisation parameter or nugget. The optimised parameter ξ in Equation (5-31) has the same effect, though in a slightly different form. Regularisation introduces the smoothing required in DIC post-processing and results in a regressing, rather than an interpolating random function represented by the Kriging model. It is however necessary to test the condition of correlation matrix $\mathbf{R}$, which can be done by

simply determining the condition number. Ranjan et al. [192] developed a formula for the lower bound on delta, given by

$$\delta_{lb} = \max\left\{ \frac{\lambda_n^*\left(\kappa^*\left(\mathbf{R}\right) - e^a\right)}{\kappa^*\left(\mathbf{R}\right)\left(e^a - 1\right)}, 0 \right\}$$ (5-38)

where $\kappa^*\left(\bullet\right)$ denotes the condition number, λ_n^* is the highest eigenvalue of $\mathbf{R}$ and $a \approx 25$ (an empirical term obtained by a large number of numerical simulations). This point is further discussed in Chapter 7.

In the examples presented in this thesis the term $\left(\dfrac{\lambda_n^*\left(\kappa^*\left(\mathbf{R}\right) - e^a\right)}{\kappa^*\left(\mathbf{R}\right)\left(e^a - 1\right)}\right)$ was found in every case to be negative, so that the optimised ξ was able to reduce the measurement error without encountering problems in inverting the correlation matrix, $\mathbf{R}$.

5.4 Kriging formula based on Bayesian inference

In general, the Kriging formula may be derived in two equivalent ways: (i) based on the framework of best linear unbiased prediction (BLUP) [56, 182] as shown in Section 5.2; (ii) based on Bayesian inference [54, 169, 193]. In this section, the Kriging formula is derived from a Bayesian perspective whereas the uncertainty is also interpreted as a posterior covariance instead of the MSE. In order to keep consistent, the same notations shown in above sections are used in the following derivations. According to Equation (5-1), Kriging predictor $\hat{w}\left(x, y\right)$ is formulated as a combination of a regression model with regression parameters $\boldsymbol{\beta}$ and a zero-mean stochastic field with field variance σ^2.

Interpreted from the Bayesian framework, the Universal Kriging applied in this study is actually a Gaussian process with the prior assumption of constant variance σ^2, constant hyper parameters $\{\vartheta_x, \vartheta_y, \xi\}$ and non-informative prior distribution of regression parameters $\boldsymbol{\beta}$ [194]. Thus the prior distribution of the Kriging predictor depends on the observations $\mathbf{w}_0$ at a number of design locations (x_j, y_j), $j = 1, 2, \ldots, n$, is chosen as the following Gaussian process distribution for the sake of analytical convenience [171]. For the observations:

$$\mathbf{w}_0 \mid \boldsymbol{\beta} \sim \mathcal{N}\left(\mathbf{C}\boldsymbol{\beta},\ \sigma^2 \mathbf{R}_\xi\right) \tag{5-39}$$

where $\mathbf{C}$ is defined in Equation (5-5) and $\mathbf{R}_\xi$ denotes the correlation matrix at the sample points including the error factor ξ.

If $\hat{\mathbf{w}}$ is used to denote Kriging prediction at a number of predicted locations (x_j^*, y_j^*), $j = 1, 2, \ldots, m$, , new notations X and X^* are employed herein for the reason of simplicity to respectively represent all the design locations and predicted locations in the RoI, where $X = [\mathbf{x}_1 \quad \mathbf{x}_2 \quad \cdots \quad \mathbf{x}_j \quad \cdots \quad \mathbf{x}_n]$, $\mathbf{x}_j = \left(x_j, y_j\right)^{\mathrm{T}}$ and $X^* = [\mathbf{x}_1^* \quad \mathbf{x}_2^* \quad \cdots \quad \mathbf{x}_j^* \quad \cdots \quad \mathbf{x}_m^*]$, $\mathbf{x}_j^* = \left(x_j^*, y_j^*\right)^{\mathrm{T}}$.

Then the joint Bayesian prior distribution for the combination of Kriging prediction $\hat{\mathbf{w}}$ at a number of predicted locations X^* and observations $\mathbf{w}_0$ can be expressed as [195]:

$$\begin{bmatrix} \hat{\mathbf{w}} \\ \mathbf{w}_0 \end{bmatrix} \Bigg| \boldsymbol{\beta} \sim \mathcal{N}\left(\begin{bmatrix} \bar{\mathbf{w}} \\ \mathbf{C}\boldsymbol{\beta} \end{bmatrix},\ \sigma^2 \begin{bmatrix} \mathbf{R}(X^*, X^*) & \mathbf{R}(X^*, X) \\ \mathbf{R}(X, X^*) & \mathbf{R}_\xi \end{bmatrix} \right) \tag{5-40}$$

where $\bar{\mathbf{w}} = \mathbf{C}(X^*)\boldsymbol{\beta}$, $\mathbf{R}(X^*, X^*)$ denotes the correlation matrix of the predicted points while $\mathbf{R}(X^*, X)$ and $\mathbf{R}(X, X^*)$ denote the correlation matrix between the predicted locations and design locations, $\mathbf{C}(X^*)$ is the matrix including the regression functions evaluated at the predicted points X^*.

The above prior distribution is actually a multivariate normal distribution. In order to obtain the posterior distribution with the restriction that the observations must be retained, the theorem of conditional multivariate normal distribution is adopted based on the proof shown in books [196, 197]. The theorem can be briefly introduced as follows: Let $\dot{\mathbf{z}}_1$ and $\dot{\mathbf{z}}_2$ be jointly normal random vectors,

$$\begin{bmatrix} \dot{\mathbf{z}}_1 \\ \dot{\mathbf{z}}_2 \end{bmatrix} \sim \mathcal{N}\left(\begin{bmatrix} \boldsymbol{\omega}_1 \\ \boldsymbol{\omega}_2 \end{bmatrix}, \begin{bmatrix} \boldsymbol{\Sigma}_{11} & \boldsymbol{\Sigma}_{12} \\ \boldsymbol{\Sigma}_{21} & \boldsymbol{\Sigma}_{22} \end{bmatrix} \right) \tag{5-41}$$

The conditional distribution of $\dot{\mathbf{z}}_1$ given $\dot{\mathbf{z}}_2$ is then derived as:

$$\dot{\mathbf{z}}_1 \mid \dot{\mathbf{z}}_2 \sim \mathcal{N}\left(\boldsymbol{\omega}_1 + \boldsymbol{\Sigma}_{12}\boldsymbol{\Sigma}_{22}^{-1}(\dot{\mathbf{z}}_2 - \boldsymbol{\omega}_2), \ \boldsymbol{\Sigma}_{11} - \boldsymbol{\Sigma}_{12}\boldsymbol{\Sigma}_{22}^{-1}\boldsymbol{\Sigma}_{21} \right) \tag{5-42}$$

Thus, the conditional posterior distribution of $\hat{\mathbf{w}}$ (for Simple Kriging [194]) can be obtained as,

$$\hat{\mathbf{w}} \mid \boldsymbol{\beta}, \mathbf{w}_0 \sim \mathcal{N}\left(\bar{\mathbf{w}}^*(.), \ \sigma^2 \mathbf{V}^*(.,.) \right) \tag{5-43}$$

where

$$\bar{\mathbf{w}}^*(X^*) = \mathbf{C}(X^*)\boldsymbol{\beta} + \mathbf{R}(X^*, X)\mathbf{R}_{\xi}^{-1}(\mathbf{w}_0 - \mathbf{C}\boldsymbol{\beta}) \tag{5-44}$$

$$\mathbf{V}^*(X^*, X^*) = \mathbf{R}(X^*, X^*) - \mathbf{R}(X^*, X)\mathbf{R}_{\xi}^{-1}\mathbf{R}(X, X^*) \tag{5-45}$$

Due to the conjugate prior assumption [169, 193, 194], it is found that the conditional distribution of $\boldsymbol{\beta}$ given $\mathbf{w}_0$ was derived as a Gaussian distribution:

$$\boldsymbol{\beta} \mid \mathbf{w}_0 \sim \mathcal{N}\left(\hat{\boldsymbol{\beta}}, \ \hat{\sigma}^2(\mathbf{C}^{\mathrm{T}}\mathbf{R}_\xi^{-1}\mathbf{C})^{-1}\right) \tag{5-46}$$

where the $\hat{\sigma}^2$ and $\hat{\boldsymbol{\beta}}$ are evaluated from maximizing the likelihood function [194] and have the same expressions as shown in Equation (5-35) and (5-36) respectively

The posterior distribution shown in (5-43) can be updated by eliminating the conditioning on $\boldsymbol{\beta}$ based on a standard integration technique [171, 198]:

$$\hat{\mathbf{w}} \mid \mathbf{w}_0 \sim \mathcal{N}\left(\bar{\mathbf{w}}^{**}(.), \ \hat{\sigma}^2\mathbf{V}^{**}(.,.)\right) \tag{5-47}$$

where

$$\bar{\mathbf{w}}^{**}(X^*) = \mathbf{C}(X^*)\hat{\boldsymbol{\beta}} + \mathbf{R}(X^*, X)\mathbf{R}_\xi^{-1}(\mathbf{w}_0 - \mathbf{C}\hat{\boldsymbol{\beta}}) \tag{5-48}$$

$$\begin{aligned}\mathbf{V}^{**}(X^*, X^*) = \ &\mathbf{V}^*(X^*, X^*) + \\ &\left(\mathbf{C}(X^*) - \mathbf{R}(X^*, X)\mathbf{R}_\xi^{-1}\mathbf{C}\right)(\mathbf{C}^{\mathrm{T}}\mathbf{R}_\xi^{-1}\mathbf{C})^{-1}\left(\mathbf{C}(X^*) - \mathbf{R}(X^*, X)\mathbf{R}_\xi^{-1}\mathbf{C}\right)^{\mathrm{T}}\end{aligned} \tag{5-49}$$

It is found that the posterior distribution of Kriging prediction $\hat{\mathbf{w}}$ given the observed data $\mathbf{w}_0$ is subject to a multivariate Gaussian distribution. The predicted mean of Kriging regression model shown in Equation (5-48) is exactly the same as the Kriging regression prediction shown in Equation (5-32), except the latter only provides the prediction for a location (x, y) rather than all the locations. Further, the MSE of the Kriging regression model, incorporating the error factor ξ to Equation (5-25), actually stems from the diagonal elements of the covariance matrix $\mathbf{V}^{**}(X^*, X^*)$ shown in Equation (5-49). This point is further discussed in Chapter 7.

5.5 Uncertainty quantification based on Kriging

According to the Bayesian inference, Kriging can be utilized as an efficient surrogate model to analyse the uncertainty of DIC measurement results, which is specifically implemented through Gaussian process emulation. The displacement uncertainty of DIC measurement can be directly estimated by the MSE (variance terms of Equation (5-49)) provided by Kriging regression model. However, it is difficult to propagate the displacement uncertainty to the strain estimate for uncertainty quantification, since the strain results are actually computed from the displacement gradients. As the posterior distribution of Kriging model is indeed the multivariate Gaussian, it is possible to employ a sampling process of the displacement field to generate a large number of samples to estimate the strain uncertainty. A sampling from the multivariate Gaussian distribution is carried out based on the mean values (5-48) and corresponding covariance matrix (5-49) of the Kriging regression model. In order to generate samples $\hat{\mathbf{w}}_s$ from Kriging model, a scalar Gaussian generator is adopted and the whole process can be proceeded as follows:

Firstly, Cholesky decomposition is carried out for the covariance matrix (positive definite symmetric), i.e. $\mathbf{V}^{**} = \mathbf{\Lambda}\mathbf{\Lambda}^{\mathrm{T}}$, where $\mathbf{\Lambda}$ is a lower triangular matrix.

Secondly, the scalar Gaussian generator is used to generate a standard Gaussian scalar, $\mathbf{n}_s \sim \mathcal{N}(0, \mathbf{I})$.

Thirdly, random sample from the multivariate Gaussian distribution with desired mean and covariance can be computed as:

$$\hat{\mathbf{w}}_s = \mathbf{\Lambda}\mathbf{n}_s + \overline{\mathbf{w}}^{**} \tag{5-50}$$

Based on the random displacement samples, the uncertainties of strain results can be computed in terms of the standard deviation (STD) or the 95% confidence interval (CI) [199].

5.6 Closure

The Kriging regression theory is presented concisely in this chapter in view of the related applications in DIC in order to reduce measurement errors and quantify uncertainties. Based on the formulation of Kriging interpolation, Kriging regression method is introduced in terms of regularising the measurement error from both global and local senses. Additionally, the uncertainty analysis based on the Kriging regression method is addressed from the perspective of Bayesian inference. Two applications of Kriging regression in both a full-field DIC framework and a subset-based DIC framework are discussed respectively in Chapter 6 and Chapter 7.

6

Full-field DIC with Kriging Regression

A global DIC algorithm with integrated Kriging regression is presented in this chapter. The displacement field is formulated as a best linear unbiased model that includes the correlations between all the locations in the RoI. A global error factor is employed to extend conventional Kriging interpolation to Kriging regression to quantify displacement errors of the control points. An updating strategy for the self-adaptive control grid is developed on the basis of the Mean Squared Error (MSE) determined from the Kriging model. The performance of Kriging DIC is validated in terms of resolution and spatial resolution, compared to the classical subset-based DIC. In addition, Kriging DIC is shown to outperform several other full-field DIC methods when using open-access experimental data. Numerical examples are used to demonstrate the robustness of Kriging DIC to different choices of initial control points and to speckle pattern variability. Finally Kriging DIC is tested on an experimental example.

6.1 Problem overview

Over the past three decades different methods have been developed and successfully applied in DIC. These methods belong to two general classes: local (subset-based) methods and global (full-field) techniques, both of which have been used extensively in different applications. The local approach is perhaps the better established of the two because of its simplicity and suitability to parallel computation [7], but lacks inter-subset continuity and is more sensitive to measurement noise than the global approach. Consequently it is necessary to apply smoothing as a post-processing operation to measured displacements before computing strain results [88]. Alternatively, the global approach imposes certain constraints and treats the RoI as a whole, thereby enabling smooth displacement fields to be achieved together with good sub-pixel accuracy. The same level of sub-pixel accuracy is achievable by the global approach, more efficiently than the local approach, which requires subset overlapping [18] with multiple processing of the same data and increased computational cost.

As summarised in literature review, full-field DIC methods include: Finite Element (FE) based methods [9, 11, 72, 103, 105, 106]; the Extended FE method, known as XFEM, [12, 13, 89, 109]; p-DIC method [19]; B-Spline methods (NURBS) [17, 71] and Spectral methods based on spatial Fourier transforms [14-16]. DIC techniques aim to produce an accurate and reliable displacement field through the computed correlation of deformed speckle patterns with a reference image. This process requires the use of shape functions to describe the displacement field in terms of grey-scale values determined in terms of individual pixel intensities within a subset or RoI. Of course, it is generally not possible to design a shape function that perfectly matches the actual displacement field in a particular application. However,

the Kriging prediction has the advantage that is based not only upon regressing certain parameters on discrete measurements, but also on the correlation of neighbouring samples. The fitting residual is represented by a Gaussian random process resulting in a best linear unbiased prediction. This represents lack of knowledge of the true displacement field and is not related to measurement error. The choice of a Gaussian random process is analogous to the choice of a Gaussian random variable in statistics: it is analytically tractable, flexible and frequently correct.

In this chapter Kriging regression is integrated into the classical full-field DIC algorithm. The full-field displacement estimate is obtained by training the Kriging model using increasing numbers of sample (or control) points at each step until the MSE at untried sites (between the control points) is deemed to be acceptably small. At the end of this process the displacements at the untried sites are found in terms of the complete system of control-point displacements. Figure 6–1 illustrates the dependency relationship of an inner point on control points based on the shape function. In Figure 6–1(a), it is seen that the inner-point displacement is determined by only 4 nodal displacements when using the Q4-FE shape function [102], possibly resulting in abrupt ridges at the element boundaries. When using the B-spline method, the inner-point displacement, shown in Figure 6–1(b), is given in terms of a greater number of nodal displacements, but shape-function remains local to the inner point. The Kriging shape function is genuinely global, as shown in Figure 6–1(c) where the inner-point displacement is given in terms of control points distributed over the entire RoI.
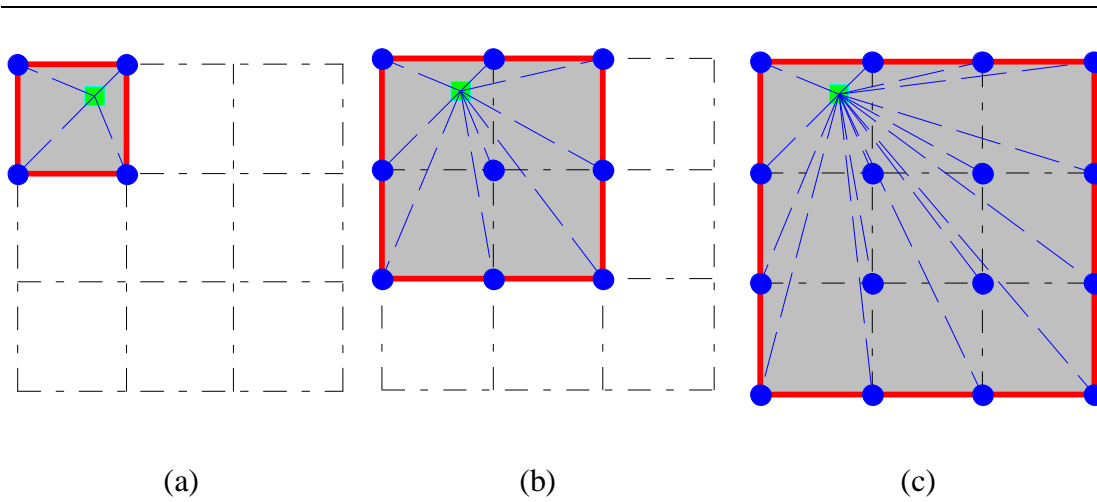
Figure 6–1. Dependency relationship of one inner point (green square): (a) Q4-FE, (b) Cubic Spline, (c) Kriging - control points shown as blue circles.

6.1.1 Review of the global DIC approach

Global DIC is considered for the case of a two-dimensional image where the unknown displacement field $(u(x, y), v(x, y))$ is to be determined at spatial coordinate (x, y). The displacement $(u(x, y), v(x, y))$ may also be understood as the optical flow from a reference image $f(x, y)$ of speckle-pattern intensity to its corresponding deformed image $g(x, y)$. Then the displacement field may be estimated by minimising the objective function,

$$\mathcal{C}_{SSD}(u, v) = \int_{\Theta} \left(g\left(x + u(x, y), y + v(x, y) \right) - f(x, y) \right)^2 d\Theta \qquad (6\text{-}1)$$

where Θ denotes the region of interest (RoI) in the reference image.

In practice, the continuous displacement field $(u(x, y), v(x, y))$ may be approximated by a linear combination of basis functions of finite dimension n, expressed as

$$u(x, y) \approx \sum_{j=1}^{n} \mu_j(x, y) p_{u_j}$$

$$v(x, y) \approx \sum_{j=1}^{n} \mu_j(x, y) p_{v_j}$$

$$(6\text{-}2)$$

where $\mu_j(x, y); j = 1, 2, \ldots, n$ are the kernel functions and $p_{u_j}, p_{v_j}; j = 1, 2, \ldots, n$ are the combination coefficients. Since $g\left(x + u(x, y), y + v(x, y)\right)$ is an implicit function of $\left(u(x, y), v(x, y)\right)$, the Newton method may be applied to solve the minimisation problem. Therefore, an approximate solution of the full-field displacement, $\left(u(x, y), v(x, y)\right)$, may be obtained by iteration [10, 11, 71, 72]

$$\mathbf{M}_\Omega^i \left(\mathbf{p}_\Omega^{i+1} - \mathbf{p}_\Omega^i \right) = \mathbf{b}_\Omega^i; \quad \Omega \in \{u, v\} \qquad (6\text{-}3)$$

where $\mathbf{M}_u^i, \mathbf{M}_v^i$ are $n \times n$ matrices and $\mathbf{b}_u^i, \mathbf{b}_v^i$ are $n \times 1$ vectors, with components given by

$$\left(M_{jk} \right)_\Omega^i = \int_\Theta \left(\mu_j(x, y) \frac{\partial g(x + u^i, y + v^i)}{\partial z} \right)$$
$$\times \left(\mu_k(x, y) \frac{\partial g(x + u^i, y + v^i)}{\partial z} \right) \mathrm{d}\Theta$$

$$(6\text{-}4)$$

and

$$\left(b_j \right)_\Omega^i = \int_\Theta \mu_j(x, y) \frac{\partial g(x + u^i, y + v^i)}{\partial z}$$
$$\times \left(f(x, y) - g(x + u^i, y + v^i) \right) \mathrm{d}\Theta$$

$$(6\text{-}5)$$

where $z \in \{x, y\}$ when $w \in \{u, v\}$ respectively and $j, k = 1, 2, \ldots, n$.

The gradient $\dfrac{\partial g(x+u^i, y+v^i)}{\partial z}$ in equations (6-4) and (6-5) is in principle updated

at each iteration. However, as proposed by Sutton [57, 73], the grey-level gradients

may be calculated from the reference image rather than the deformed image without

loss of accuracy i.e. $\dfrac{\partial g(x+u^i, y+v^i)}{\partial z} \approx \dfrac{\partial f(x, y)}{\partial z}$.

The interpolation functions in Equation (6-2) are generally local piecewise functions

[17, 184], e.g. cubic spline or finite element shape functions. The combination

coefficients then represent the displacements of a set of control points (or nodes). In

this study, a different linear modelling approach for the displacement field is

investigated, known as Kriging regression.

6.1.2 Kriging model

As discussed in Chapter 5, Kriging has originally been developed in the field of geo-

statistics [200] as a technique of interpolation which provides the Best Linear

Unbiased Prediction (BLUP) of intermediate values under suitable assumptions on

the priors. A Gaussian process governed by assumed prior variances is used to

model the interpolated field in Kriging formula. If interpreted from Bayesian view,

Kriging model can provide both mean values and estimated errors at the same time

for an arbitrary point in the RoI. This advantage enables Kriging to adaptively

achieve an optimal global model by infilling new sample points automatically. In

this proposal, Kriging model is integrated into a global DIC algorithm as a full-field

shape function for a more accurate full-field measurement.

6.2 Kriging-DIC

6.2.1 Algorithm

According to the derivations in Section 5.2, Kriging method can be utilized to obtain a BLUP for the true displacement field [160] $w(x, y)$ which then is modelled as a realisation of a random function which combines a deterministic regression model and a zero-mean stochastic field [168]. Denoting $\mathbf{w}_0 = \left[w_1, \cdots, w_n \right]^\mathrm{T}$ as displacements of a set of control points $\left(x_j, y_j \right)$, $j = 1, 2, \ldots, n,$, the displacement response $\hat{w}(x, y)$ at an arbitrary untried location (x, y) can be formulated by the Kriging model in terms of a linear combination of the sample values $\mathbf{w}_0$ and corresponding weights $\boldsymbol{\kappa}$:

$$\hat{w}(x, y) = \sum_{j=1}^{n} \kappa_j (x, y) w_j = \boldsymbol{\kappa}^\mathrm{T} \mathbf{w}_0 \tag{6-6}$$

As shown in Equation (5-20), the expression of Kriging weights can be written as [160],

$$\boldsymbol{\kappa}(x, y) = \mathbf{R}^{-1} \left(\mathbf{r}(x, y) - \mathbf{C} \left(\mathbf{C}^\mathrm{T} \mathbf{R}^{-1} \mathbf{C} \right)^{-1} \left(\mathbf{C}^\mathrm{T} \mathbf{R}^{-1} \mathbf{r}(x, y) - \mathbf{c}(x, y) \right) \right) \tag{6-7}$$

where $\boldsymbol{\kappa}(x, y) = \begin{pmatrix} \kappa_1 & \kappa_2 & \cdots & \kappa_n \end{pmatrix}^\mathrm{T}$ are the Kriging weights [184] obtained by the unbiasedness and minimisation of mean squared error (MSE). $\mathbf{R}$, $\mathbf{r}(x, y)$, $\mathbf{C}$ and $\mathbf{c}(x, y)$ are defined in Section 5.2. Thus under the framework of global DIC algorithm, Kriging DIC is actually implemented by applying Kriging shape function as shown in Equation (6-6) to replace the general form of global shape function shown in Equation (6-2).

6.2.2 Imprecise sample data

Generally DIC data is not measured with perfect accuracy, but is subject to measurement noise and imprecision [55, 56, 162, 201], the effect of which might be reduced by pre-filtering [32, 202]. However, in this study it can be accounted for in a global sense by perturbing the correlation matrix $\mathbf{R}$ which is replaced in Equation (6-7) (and in subsequent equations) by $\mathbf{R}+\xi\mathbf{I}$ (as shown in Equation (5-30)). ξ predominantly represents measurement error (but also error induced by other sources such as numerical error), considered to be independent and identically distributed at each sample point, hence the identity matrix in the added term $\xi\mathbf{I}$. This modified formulation is known as Kriging regression [162] (as opposed to Kriging interpolation, which is the conventional formulation that predicts the sample points exactly) and introduces an additional parameter ξ to be determined.

According to the discussion in Section 5.3.3, the parameters $\left\{\boldsymbol{\beta},\sigma^2,\vartheta_x,\vartheta_y,\xi\right\}$ can be optimised by maximizing the log likelihood of the observed data $\mathbf{w}_0$ by a Nelder-Mead [190] simplex algorithm. In addition, the introduction of ξ has the benefit of acting as a regularisation parameter [162] against ill-conditioning of the correlation matrix. In this study, a first-order regression function is chosen as shown in Equation (5-27). Also the exponential (also called Gaussian) correlation function is used, of which the expression is shown in Equation (5-29).

6.2.3 Implementation of Kriging-DIC

The Kriging-DIC can be implemented through the following procedures:

i.   Firstly, the displacement field of the RoI is formulated by a Kriging model using a certain number of randomly selected control points in the reference

image. A fast DIC subset method [57] was adopted to obtain approximate displacements for the control points. This fast DIC method employs square subsets of identical size in the reference and deformed images respectively to maximise correlation coefficients between them. The selected control points are assigned as centre points of the subsets in the reference image. When matched subsets (having maximum correlation) are found, initial displacements of control points are achieved as differences between subset centre points. This method generally obtains integer-pixel displacements with accuracy within 3 pixels, based on empirical evidence, which is close enough for initial values of Kriging-DIC method. Vendroux and Knauss [67] proved that the Newton iteration method has a convergence radius of 7 pixels for initial values. Zhao et al. [203] introduced a number of strategies to improve the robustness of DIC solutions to variability in initial estimates of displacements, especially for cases of large deformation.

ii. Secondly, an updating procedure was applied to add more control points to refine the initial Kriging model. This updating procedure will be introduced in the following section. However, it should be noted that this updating procedure is not necessary if sufficient control points are already artificially selected through a fixed control grid.

iii. Finally, on achieving an optimised Kriging model, Newton iteration is applied to calculate the final displacement field with a sub-pixel accuracy. Moreover, as grey values of non-integer pixels are required in this process, a 6×6 bi-cubic interpolation scheme (shown in Appendix A) was chosen in the examples presented in this chapter for reasons of simplicity.

6.3 Self-adaptive control grid updating

For DIC problems, it is desirable to have an algorithm that determines an optimal control grid. Generally, a finer control grid does not guarantee a more accurate measurement. However, a fine control grid is necessarily applied in the case of a complex deformation, when a coarse control grid would fail to capture the detail of local deformations.

Kriging provides the error estimations over the whole RoI and therefore it is possible to improve the control grid by adding new sample points. The estimated Mean Squared Error (MSE) of the Kriging model provides a criterion for achieving such an improvement. According to (5-25), the MSE at any location (x, y) may be expressed as [182],

$$\mathrm{MSE}(x, y) = \hat{\sigma}^2 \left(1 + \mathbf{v}^{\mathrm{T}} \left(\mathbf{C}^{\mathrm{T}} \mathbf{R}^{-1} \mathbf{C} \right)^{-1} \mathbf{v} - \mathbf{r}^{\mathrm{T}}(x, y) \mathbf{R}^{-1} \mathbf{r}(x, y) \right) \tag{6-8}$$

where $\mathbf{v} = \mathbf{C}^{\mathrm{T}} \mathbf{R}^{-1} \mathbf{r}(\mathbf{x}) - \mathbf{c}(\mathbf{x})$, and $\hat{\sigma}^2$ is given from Equation (5-35). It should be noted that adding new points imposes a compromise between resolution and spatial resolution. Even if the estimation improves due to the presence of more information carried by the data, having too many points may cause the columns of correlation matrix $\mathbf{R}$ to become numerically close and therefore linearly dependent for practical purposes.

As has been already stated, Kriging regression allows for the effect of measurement error at the sample points, determined according to the optimised term ξ. Of course this error is fully justified and has nothing to do with the lack of knowledge represented by the Gaussian process present in the Kriging model, which we seek to

reduce by adding new sample points at candidate locations where the MSE is greatest. The problem is that Equation (6-8) does not discriminate between the measurement error and lack of knowledge, and this inevitably leads to dense clusters of added points very close to the original control points and to the stalling of progress towards the desired Kriging model [56, 162]. This can be overcome by reformulation of the Kriging model as an interpolator (rather than a regressor) with the control-point error added to the coordinates of each control point.

Thus the infill criterion in the present study is the Maximum Mean Square Error (MMSE). An alternative infill criterion was proposed by Forrester et al. [56, 162, 186] in which the objective function is the Kriging output with a minimum at an unknown coordinate. This enables added control point to be chosen that have the greatest effect on reducing the objective function. In the present case, a constrained global objective function is defined by equation (6-1) and Forrester's criterion is therefore not applicable. This means that selecting a new control point based on the local MMSE does not necessarily lead to a reduction of the objective function. The Global Mean Square Error (GMSE), defined as the mean of the calculated MSE function over the region of interest, is used as the stopping criterion for control-grid updating.

The updating process can be briefly summarised as follows

i. Control points are selected on the edges of the RoI of the reference image, the threshold GMSE value, tol_{GMSE}, is set (user dependent) and the fast DIC algorithm (discussed previously) is used to obtain an approximate measurement of the control-point displacements (The choice of the points on the edges of the RoI is made due to a well-known property of Kriging: whilst

it delivers reliable interpolation given observed data, and such interpolation improves as more observations become available, it can perform poorly when extrapolating for training runs which are not in the neighbourhood of the available data samples).

ii. The Kriging regression model in Equation (6-7) is constructed (including optimised ξ) and displacements determined using Equation (6-6).

iii. Construct a new Kriging model with the measurement error ξ from (ii) added to the control point coordinates. Then set $\xi = 0$ and the new model becomes a Kriging interpolator. Compute the MSE and GMSE.

iv. $GMSE < \text{tol}_{GMSE}$? If not, add new control points at coordinates of greatest MSE (i.e. two new control points for x- and y-directions respectively) and return to step (ii). If so, the Kriging model is complete.

The self-adaptive control grid updating process is also illustrated in Figure 6–2.
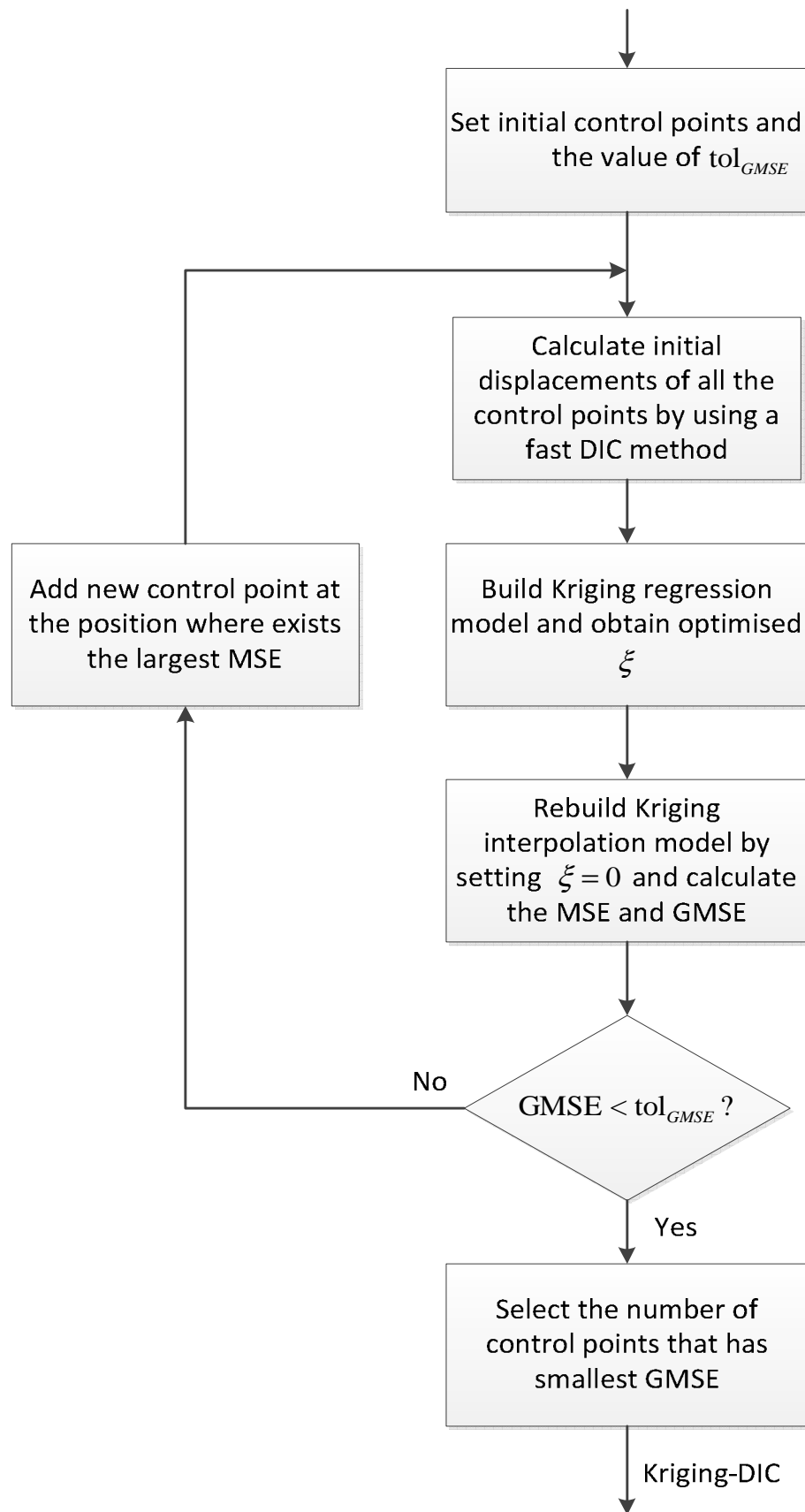
Figure 6–2. The self-adaptive control grid updating

6.4 Applications

Four case studies are included to illustrate the performance of Kriging-DIC. In the first of these, performance of the Kriging-DIC algorithm, in terms of resolution and spatial resolution, is verified through a comparison with the classical subset-based DIC algorithm. In the second case, experimental speckle-pattern images from the DIC Challenge 2D Dataset [177] are translated by 2.2 and 3.3 pixels in the *x*- and *y*-directions respectively. Kriging-DIC results are compared to those obtained by Q4-FE DIC and Cubic-Spline DIC methods. The third case study concerns a numerically-produced complex displacement field using grey-scale images generated by (a) interpolation from the FE model and (b) Gaussian speckles on the reference and deformed images. Finally, application of Kriging-DIC is demonstrated in an experimental example.

6.4.1 Case study 1: displacement resolution and spatial resolution of Kriging DIC

In order to validate the performance of different DIC algorithms, resolution is plotted against spatial resolution in one graph. This method was originally introduced by Wittevrongel et al. [19] and performance of DIC algorithms is indicated by a combination of the two quantities. Basically, a superior DIC algorithm should be able to achieve a lower value in both the resolution and the spatial resolution.

A series of sinusoidal surface deformation generated with various spatial frequencies and amplitudes [38] is used to assess the resolution and the spatial resolution. In this sense, different from the original definition given in Section 2.3, the spatial resolution is evaluated as the lowest period (i.e. the highest frequency) of a

sinusoidal deformation that can be reproduced by the algorithm while the loss of measured amplitude does not exceed a certain percentage of total amplitude. The displacement resolution may be understood as measurement precision. It can be defined as the change in displacement that causes a change in the corresponding measurement greater than one standard deviation of the measurement noise.
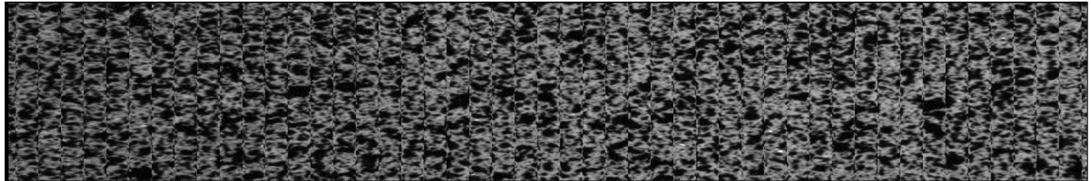

Figure 6–3. A deformed image with a sinusoidal displacement field with a period of 25 pixels

Obtained from the authors of the work in [19], a series of images with different sinusoidal deformation fields as shown in Figure 6–3 are used to calculate the displacement resolution and amplitude loss of both the subset-based DIC and the Kriging DIC at a series of spatial resolutions (in terms of sinusoidal periods). The reference image comes from an original speckle pattern, while the deformed images are generated by imposing a Gaussian noise and unidirectional sinusoidal displacement field on the original pattern. The related parameters of the deformed images and the DIC algorithms used are shown in Table 6–1 and Table 6–2 respectively.

At first, a region of interest was selected from the image which contains at least one period of the sinusoidal displacement field. Then the subset-based DIC with a subset-size of 21×21 pixels (with a second-order shape function and a 6×6 bi-cubic intensity interpolation scheme) is used to compute the displacement field of the region of interest (pixel by pixel) in order to find peak locations. In addition,

uniformly distributed sample points (centres of subsets) are further designed on the region of interest, which includes the identified peak locations. Both the subset-based DIC and Kriging DIC were applied to calculate the displacements of sample points and evaluate the amplitude loss. At the same time, the displacement resolution was quantified in terms of standard deviation of the measured displacement field [38]. The amplitude loss $\Delta\mathcal{D}$ is defined as [19],

$$\Delta\mathcal{D} = \frac{|\tilde{a} - \mu_{\tilde{a}}| + 3\sigma_{\tilde{a}}}{\tilde{a}} \cdot 100 \tag{6-9}$$

where $\tilde{a}$ is the amplitude of imposed sinusoidal displacement, $\mu_{\tilde{a}}$ and $\sigma_{\tilde{a}}$ are average mean and standard deviation of the measured peak displacements. $3\sigma_{\tilde{a}}$ indicates a 99.8% confidence interval on amplitude determination. It should be noted that for a fair comparison the self-adaptive grid updating of Kriging-DIC is deactivated, which enables the displacement data to be measured based on the exactly same sample points for both the subset-based DIC and Kriging-DIC.

Figure 6–4 and Figure 6–5 illustrate the curves of the amplitude loss and displacement resolution against the period of the deformation sine wave (indicating spatial resolution) for both the subset-based DIC and Kriging-DIC. As expected, the amplitude loss and displacement resolution decrease as the period of the deformation sine wave increases. The influence of noise and spatial frequency of the deformation on the measurement precision (displacement resolution) is reduced as the spatial resolution increases (deformation becomes more flat). Moreover, Figure 6–6 and Figure 6–7 demonstrate characteristics of the subset-based DIC and Kriging-DIC in terms of the displacement resolution against the spatial resolution under a 5% and a 1% amplitude loss respectively. When smaller subsets and higher

order regression models are chosen, the spatial resolution decreases and it enables a better deformation measurement (with high spatial frequency content). However, a cost is paid since the displacement resolution increases in the meantime.

As a global DIC algorithm, the Kriging-DIC method is observed as having an excellent displacement resolution compared with the subset-based DIC at the same spatial resolution. This is shown in Figure 6–5, where the Kriging-DIC curves are generally lower than the curves of the subset-based DIC. However, Kriging-DIC introduces relatively larger amplitude loss at smaller periods of the deformation sine wave (smaller spatial resolution) compared with the subset-based DIC. This is shown in Figure 6–4. The larger amplitude loss in Kriging DIC may be caused by a compromise between regularization and spatial resolution, i.e. the regularization normally reduces the high spatial frequency content.

Thus under the criterion of amplitude loss (5% or 1%), it is observed that the performance of Kiging-DIC in terms of displacement resolution is superior to that of the subset-based DIC at the same spatial resolutions. However, no result is shown at lower spatial resolutions because the amplitude loss has risen above the threshold (e.g. 5% or 1%). In general, it can be concluded that the Kriging-DIC method is capable of achieving excellent robustness to noise. It is best applied in applications with low spatial frequency content (high spatial resolution) for a better displacement resolution (precision). On the other hand, for applications with high spatial frequency content, the subset-based DIC is probably a compromise choice though its displacement resolution is not as good as that of Kriging-DIC. In practice, when there is a requirement to measure the high spatial frequency deformation with an excellent displacement resolution, Kriging-DIC is still a good choice and the

disadvantage related to the low spatial resolution may be overcome by increasing the resolution of imaging system (e.g. choosing high-resolution CCD cameras).

Table 6–1: Deformation parameters of the images

Parameter	value
Amplitude	5 pixels
Period	$25 \xrightarrow{\ 25\ } 250$ pixels
Gaussian noise (standard deviation)	1% (2 grey values)

Table 6–2: Parameters of DIC algorithms

	Subset-based DIC	Kriging DIC
Criterion	NSSD	NSSD
Sample (control) points	31×10	31×10
Subset size	$21 \xrightarrow{\ 10\ } 61$ (pixels)	
Regression order		0, 1st and 2nd
Shape function	2nd-order	
Intensity interpolation	6×6 bi-cubic	6×6 bi-cubic
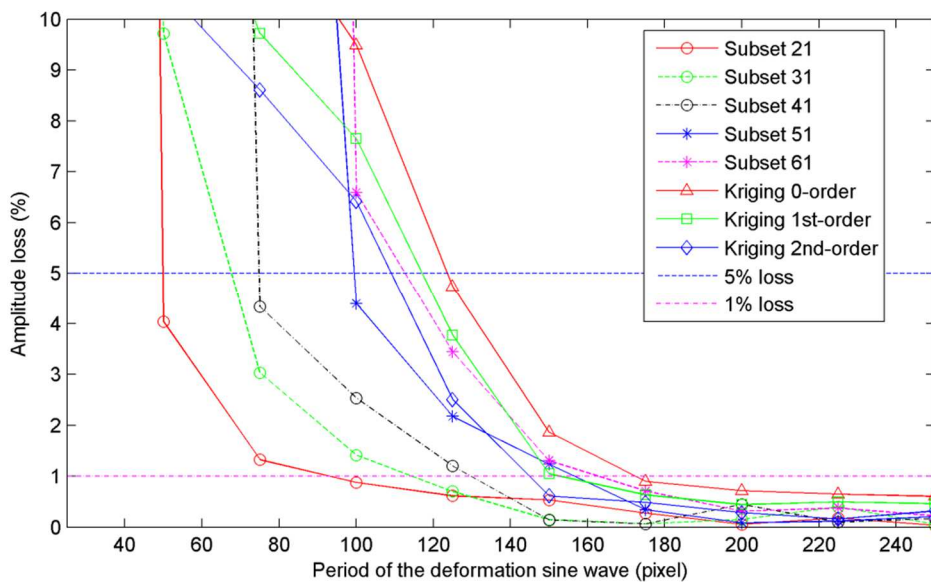
Figure 6–4. Amplitude loss vs period of the deformation sine wave for subset-based DIC and Kriging-DIC
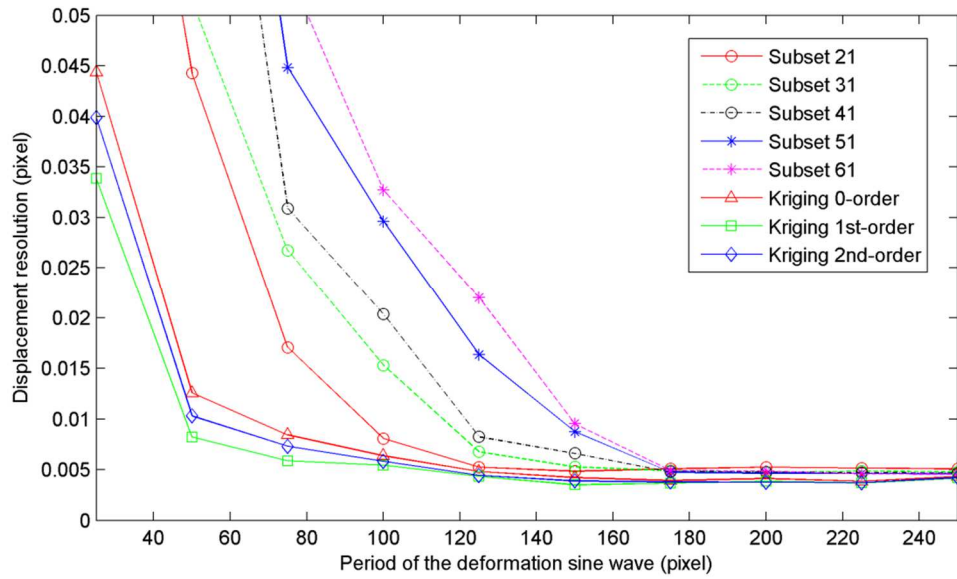
Figure 6–5. Displacement resolution vs period of the deformation sine wave for subset-based DIC and Kriging-DIC
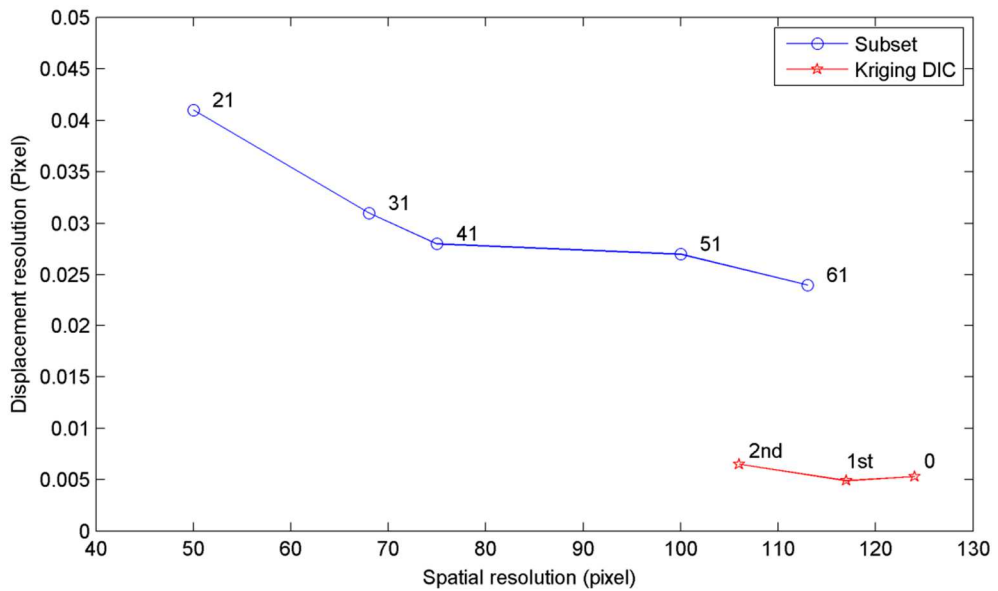

Figure 6–6. Displacement resolution vs spatial resolution under the criterion of 5% amplitude loss, a decrease in subset size and a increase in the order of regression function are adopted (from right to left) respectively in the subset-based DIC and Kriging DIC
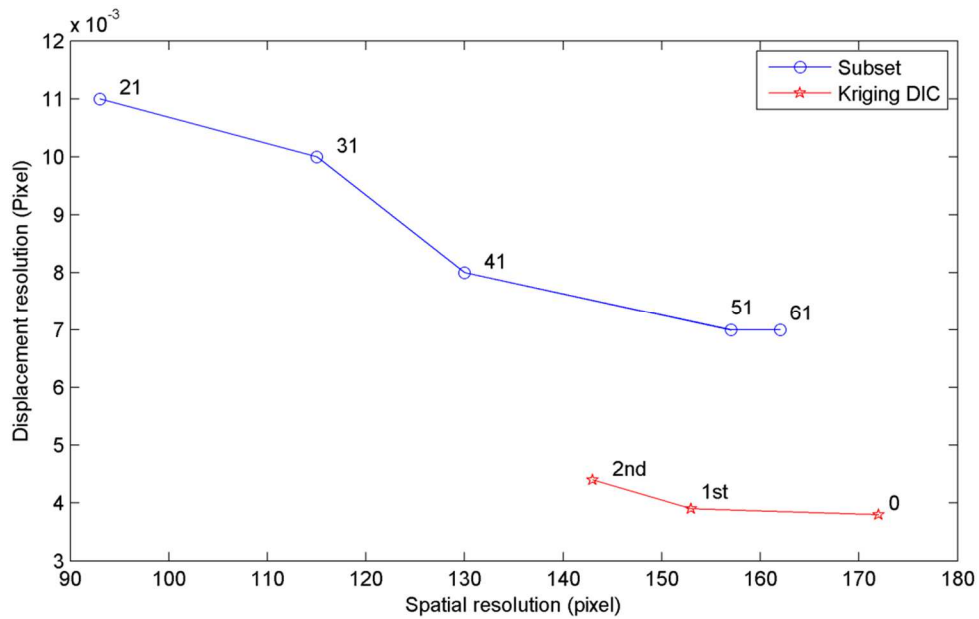
Figure 6–7. Displacement resolution vs spatial resolution under the criterion of 1% amplitude loss, a decrease in subset size and a increase in the order of regression function are adopted (from right to left) respectively in the subset-based DIC and Kriging DIC

6.4.2 Case study 2: DIC challenge data - rigid body displacement.

In this case study, the performance of three different global DIC algorithms is compared in terms of a full-field displacement measurement that provides more measurement details for comparison. Experimental speckle pattern images from DIC Challenge 2D Dataset [177] were translated by 2.2 and 3.3 pixels in the x- and y-directions respectively by Fourier transformation [36, 57], achieved by phase shifts without change of amplitude. The RoI, spanning 101×101 pixels, is uniformly meshed by 5×5 square elements, each of 21×21 pixels. This grid provides 6×6 control points (nodes) so that the full-field displacement is determined by the displacement of 36 control points, as shown in Figure 6–8.

The displacement field is calculated by three different global DIC methods, Kriging-DIC, Q4-FE DIC [9-11] and Cubic-spline DIC [17, 71] using B-spline basis functions. To ensure comparability, the number and location of the control points are fixed so that control-grid updating is not applied in the Kriging-DIC approach. Kriging regression was applied, but in this particular example it was found that $\xi = 0$, identical to the case of Kriging interpolation. This is to be expected since the true displacements of all the control points are the same (2.2 in x-direction, 3.3 in y-direction) and the initial displacements of all the control points calculated by the fast method are the same as well (2 in x-direction, 3 in y-direction). The number of degrees of freedom is the same for each of the three approaches.

It should be noted that due to the fixed regular grid, there is actually no grid updating process for this case. The Q4-FE DIC method [102] and Cubic-spline DIC method [17, 71] are briefly introduced in Section 2.6 and the corresponding shape functions are shown in Equation (2-8) and Equation (2-11) respectively, meanwhile Kriging DIC method can be referred to the Section 6.2.

Table 6–3: Details of the 3 DIC methods

|	Control points	Shape Function	Chosen Parameters
Kriging DIC	uniformly distributed 36 nodes shown in Figure 6–8	Equation (6-6)	1st order regression model and Gaussian correlation error model
Q4-FE DIC	The same as above	Equation (2-8)	4-node quadrangle FE shape function
Cubic-spline DIC	The same as above	Equation (2-11)	Uniformly spaced knot vector [0 0 0 0.25 0.5 0.75 1 1 1] and 3rd order B-spline basis functions
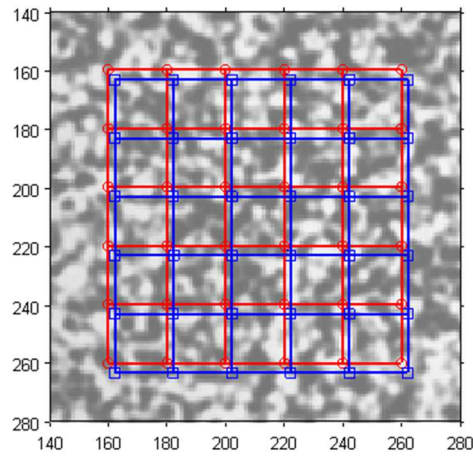
Figure 6–8. Reference and deformed grids shown as red and blue squares respectively.
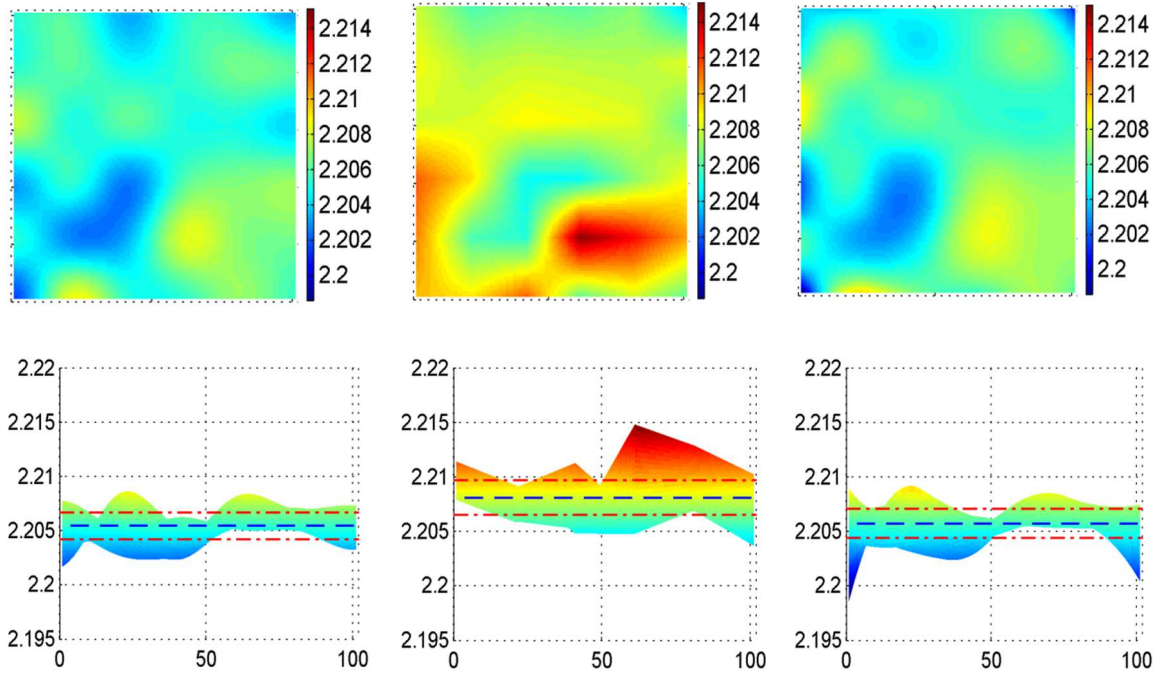

Figure 6–9. Calculated displacement fields in x-direction (real displacement 2.2 pixels), from left to right: Kriging DIC, Q4-FE DIC and Cubic Spline DIC, and '--' indicates the Mean while '-.' indicates the Standard Deviation.
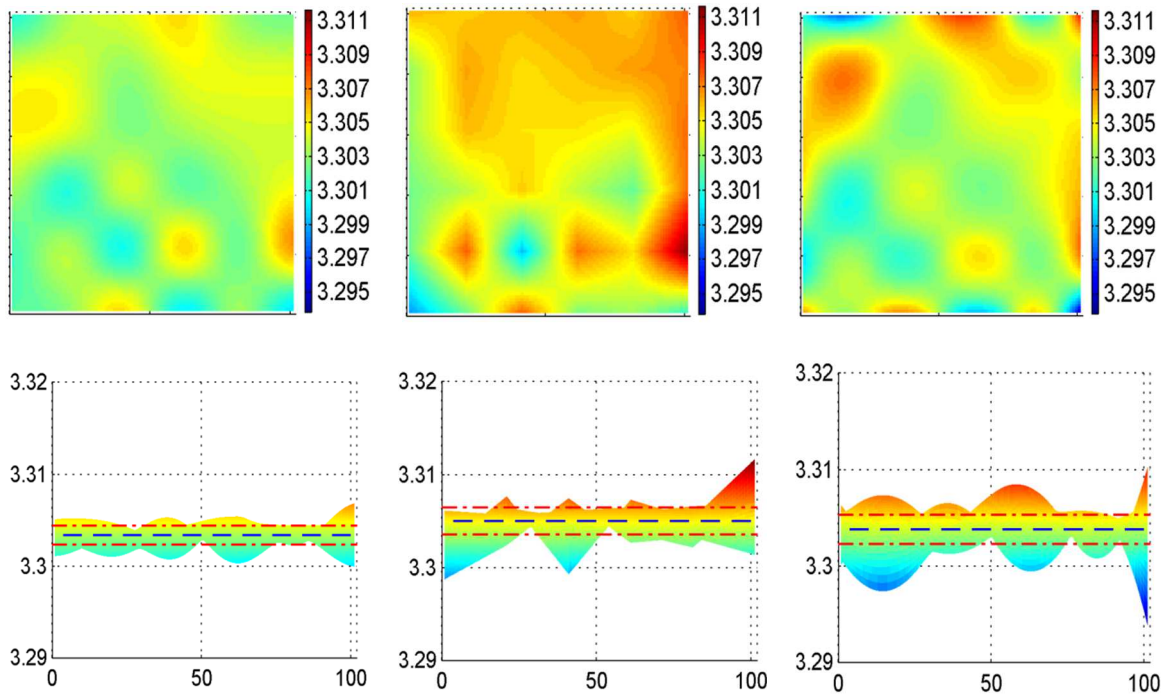
Figure 6–10. Calculated displacement fields in y-direction (real displacement 3.3 pixels), from left to right: Kriging DIC, Q4-FE DIC and Cubic Spline DIC, and '--' indicates the Mean while '-.' indicates the Standard Deviation

Table 6–4: Errors comparison (in pixels)

		Kriging	Q4-FE	Cubic Spline
X	Mean Error	5.44e-3	8.10e-3	5.72e-3
	STD	1.23e-3	1.57e-3	1.33e-3
Y	Mean Error	3.34e-3	4.98e-3	3.74e-3
	STD	1.04e-3	1.46e-3	1.50e-3

*Mean Error here is the difference between actual Mean and the theoritical values i.e. 2.2 &3.3 pixels

The chosen parameters for 3 methods are listed respectively in Table 6–3. The initial displacements of the 36 control points were obtained by the fast DIC method based on integer pixels and Newton iterations were subsequently carried out using 6x6

point bi-cubic interpolation [37] for sub-pixel grey values. Results are summarised in Table 6–4 and Figure 6–9 and Figure 6–10 where it can be seen that the displacement field produced by Kriging DIC is smoother than that produced by Q4-FE DIC, which shows some significant ridges at the element boundaries. The Kriging results are also better than those produced by Cubic Spline DIC, which shows some abrupt peaks and greater deviations than Kriging DIC. In this particular case, Kriging is seen to produce a full-field measurement with lower mean error and standard deviation (STD) than the other two methods. The small biases shown in Figure 6–9 and Figure 6–10 are due to the effect of bi-cubic grey-scale interpolation [23, 36, 57].

6.4.3 Case study 3: non-uniform displacement field with numerically produced speckles.

In this case study, two examples having same displacement field but using numerically-produced grey-scale images generated by different methods are presented. The displacement field is calculated from a FE model and used to test the performance of the Kriging-DIC method with control grid updating.

In the first approach, displacements at integer pixel locations are determined by FE shape-function interpolation. The deformed image is then generated by displacing the speckle pattern shown in Figure 6–13 (DIC Challenge 2D Dataset [177]) of the reference image pixel-by-pixel by the corresponding FE displacement. The second approach is based on numerically-produced Gaussian speckles [81, 95] (not directly related to the Gaussian process that forms part of the Kriging model) with means uniformly distributed over the RoI. In both cases, bi-cubic intensity interpolation is applied to determine the grey-scale images.

Finite Element model

In order to generate a displacement field to test the performance of the proposed Kriging-DIC method, a finite element model was built in MSC Patran. The FE model of the square plate (100×100×10 mm) in standard steel, with a central hole of radius of 20 mm, is composed of a very fine mesh of CQUAD4 elements with a total of 10,400 nodes. A 2-D shell structure (i.e. 2D plane stress element) is assigned to the FE model for the simplicity of analysis. The meshed FE grid and corresponding deformation of the model are shown in Figure 6–11, where the left hand side of the plate is clamped and a uniformly distributed tensile load on the right-hand edge produces an elastic extension of approximately 14 mm. The RoI consists of 250×250 pixels and the FE displacement field of RoI in the *x*- and *y*-directions are shown in Figure 6–12.
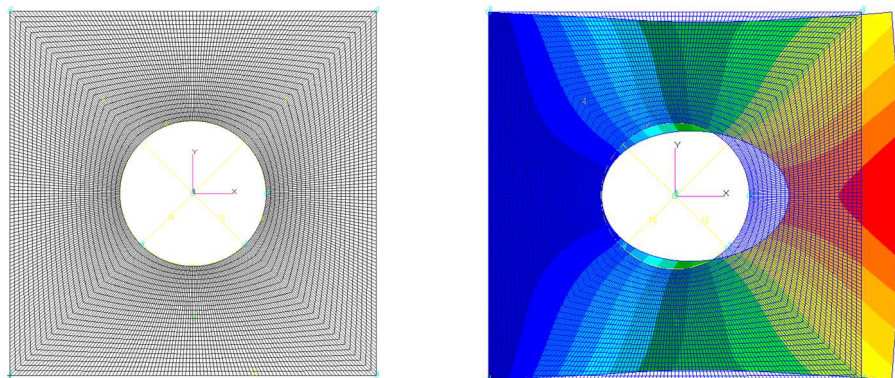

Figure 6–11. The mesh grid of FE model (left plot) and the deformation under tensile loading (right plot)
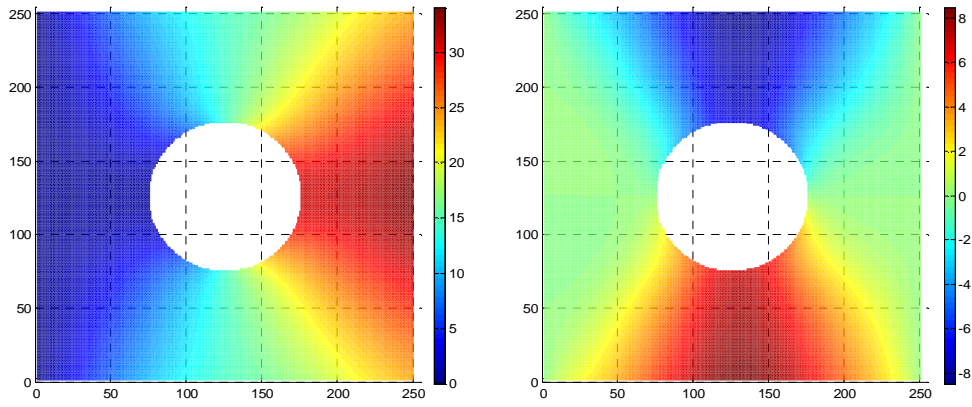
Figure 6–12. The interpolated FE displacement fields (in pixels) in x-direction (left) and y-direction (right)

Approach 1: using experimental speckles

The same speckle pattern used in the second case study (from DIC Challenge 2D Dataset [177]) is employed to as the source image from which the reference image is selected as indicated by the red square shown in Figure 6–13. The deformed image is achieved by interpolating grey intensities at integer positions after applying the FE displacements to pixels in the reference image. In regard to DIC, both the reference and deformed images are trimmed out along the outer edges and around the edge of the hole to avoid edge effects.
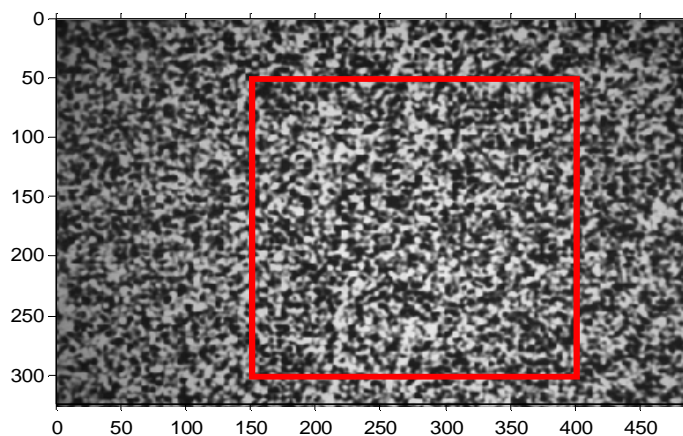

Figure 6–13. The selected region of interest (marked as a red rectangle) from a real experimental image (DIC Challenge 2D Dataset)
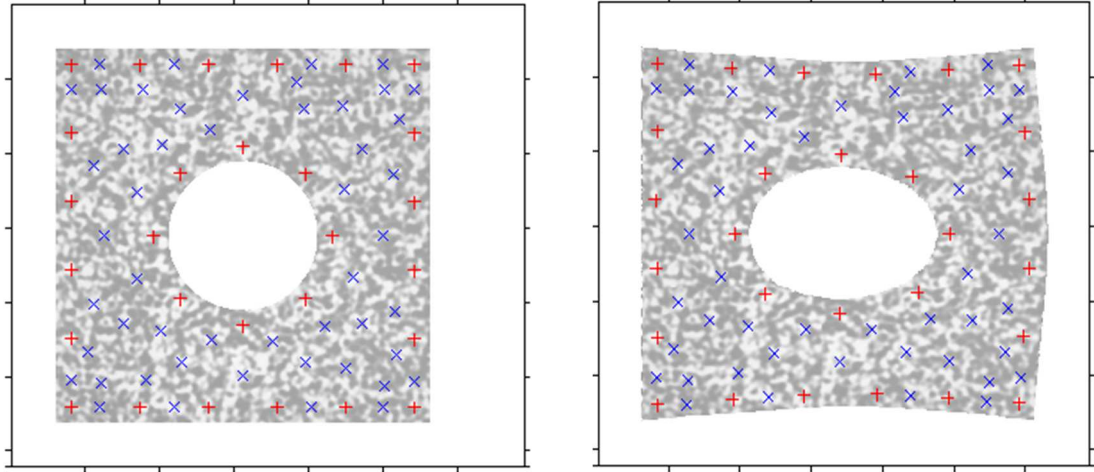
Figure 6–14. The distribution of 78 chosen control points (Approach 1, 28 initial points) on the reference image (left) and the deformed image (right).
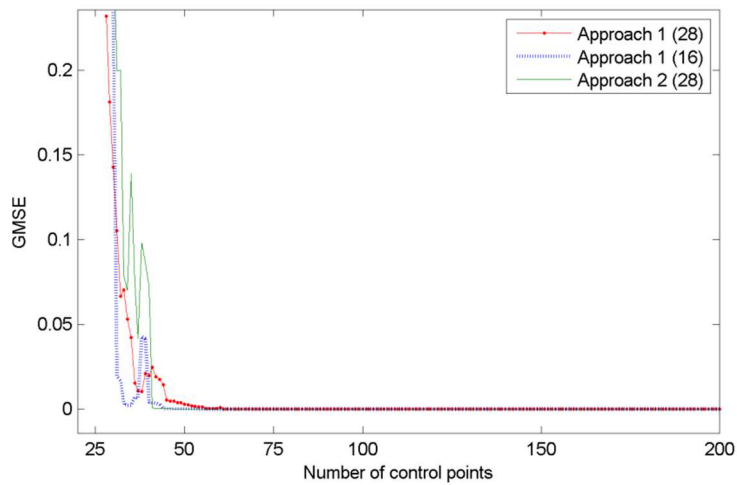

Figure 6–15. Evolution of GMSE: Approach 1 with 28 & 16 initial control points; Approach 2 with 28 initial points.

28 initial control points were firstly selected uniformly close to the outer and inner edges of the RoI denoted by the red '+' signs as shown in Figure 6–14. The control grid was updated adaptively as described in Section 6.3 using the fast DIC method (described previously). At each grid updating step two new control points were added having the greatest MSE in the x- and y-directions. Figure 6–14 shows the

added control points as blue '×' signs for the case of the first approach. Updating was continued until the GMSE was deemed sufficiently small according to a pre-set tolerance. Finally total 78 control points were used to formulate the Kriging model. It should be noted that this number was chosen as a compromise between the accuracy of the control grid and the efficiency of the computation.
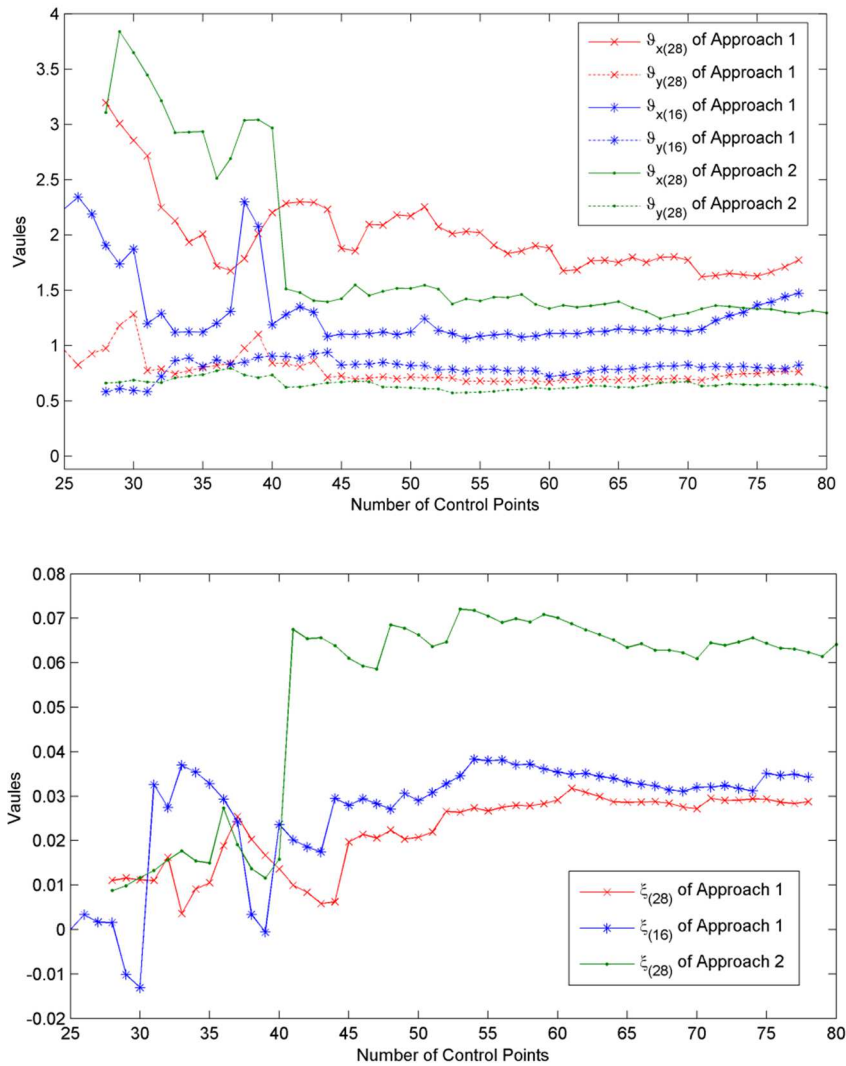

Figure 6–16. Evolution of optimization parameters with increasing numbers of control points.

Figure 6–18 illustrates the displacement errors (in pixels) in X and Y directions before the Newton iterative optimisation which are the absolute difference between the FE displacement field and the displacement field based on Kriging regression

model. Correspondingly Figure 6–19 shows the displacement residuals after the Newton interation. It can be seen that the displacement errors were significantly reduced.

On the other hand, with the purpose of testing the robustness of Kriging-DIC method, the calculation was repeated but using a different initial condition where 16 control points are arranged irregularly around the boundary shown in Figure 6–20. Also totally 78 control points were employed to build the Kriging model after the control-grid updating. Figure 6–21 and Figure 6–22 show displacement residual errors of the RoI before and after the iterative optimization respectively. According to the results, it can be seen that the measurement errors are hardly affected by the different settings of initial control points, which demonstrates the robustness and flexibility of Kriging DIC method. Moreover, a specific comparison can be found in Table 6–5.

The evolution of GMSE is shown in Figure 6–15 and optimisation parameters ϑ_x, ϑ_y and ξ in Figure 6–16. The fully converged Kriging model has 78 control points (approach 1, both 28 and 16 initial points) after adaptive control-grid updating. The objective function in Figure 6–17 is normalised by the sum of all the grey intensities in the reference image and is therefore unit-less. The evolution of the mean error and standard deviation is given in Figure 6–23.
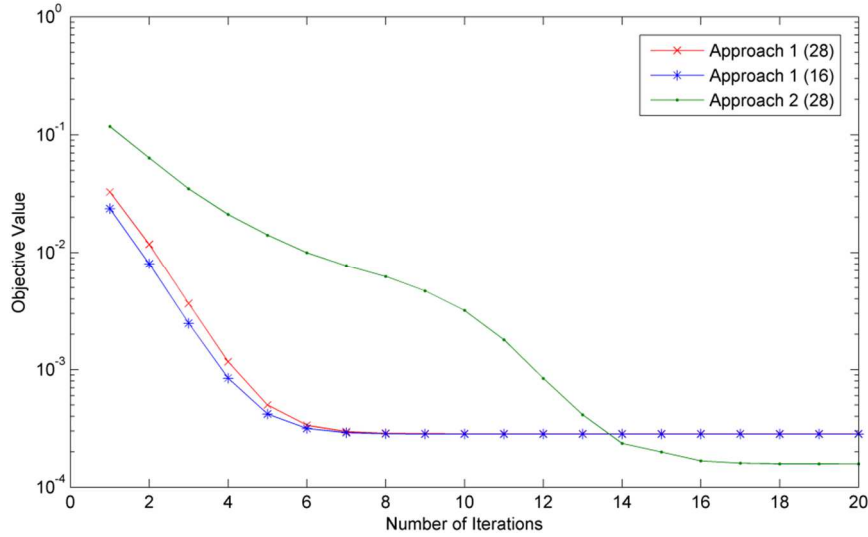
Figure 6–17. Convergence of the objective function – Newton iteration.

Approach 2: using Gaussian speckles

According to the work of Peng Zhou etc. [20, 81], speckle patterns on the CCD target before and after the deformation may be assumed to be the sum of individual Gaussian speckles. The Gaussian speckles are formulated as,

$$
\begin{aligned}
I(x,y) &= \sum_{k=1}^{M} A_k \exp\left(-\frac{(x-x_k)^2 + (y-y_k)^2}{\gamma^2}\right) \\
\tilde{I}(x,y) &= \sum_{k=1}^{M} A_k \exp\left(-\frac{(x-x_k-u(x,y))^2 + (y-y_k-v(x,y))^2}{\gamma^2}\right)
\end{aligned}
\tag{6-10}
$$

where I and $\tilde{I}$ represent the reference- and deformed-image speckle patterns respectively. M denotes the total number of speckle granules, γ is the size and A_k the peak intensity of each speckle granule and (x_k, y_k) represents the position of each speckle granule uniformly distributed over the RoI. In addition $u(x,y)$ and $v(x,y)$ denote the required displacement fields in x- and y-directions respectively which may be extracted from FE results.
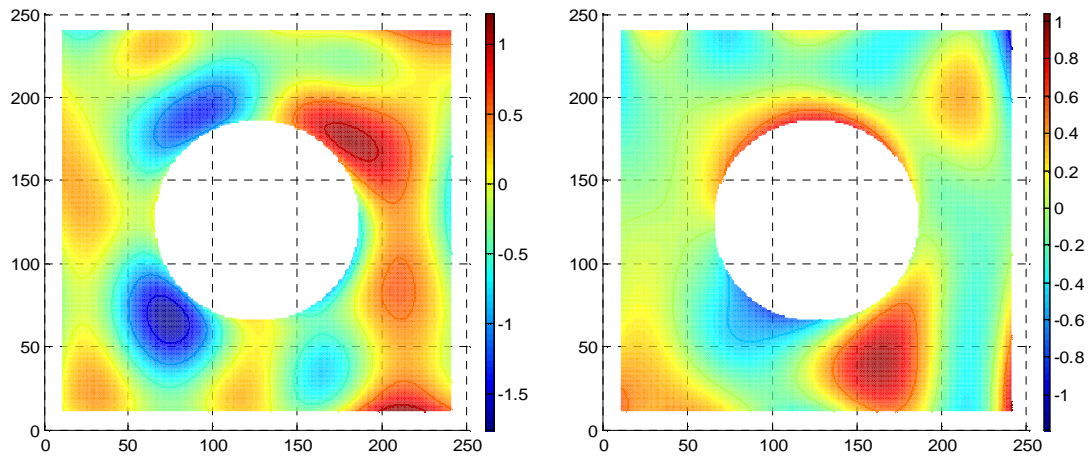
Figure 6–18. The displacement errors in pixels (Approach 1, 28 initial points) before
Newton iteration (difference with the FE displacement fields) in x-direction (left)
and y-direction (right)
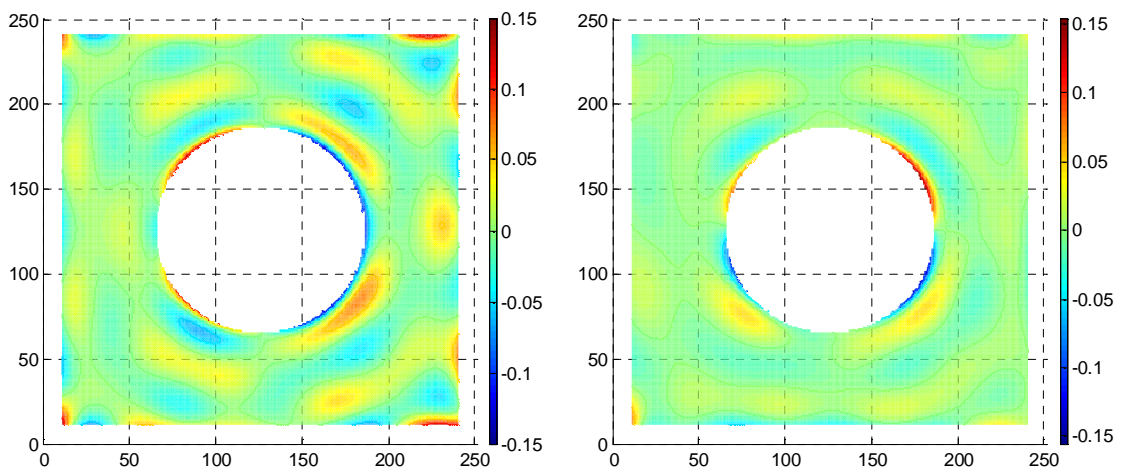
Figure 6–19. Displacement errors in pixels (Approach 1, 28 initial points) after
Newton iteration in x-direction (left) and y-direction (right)
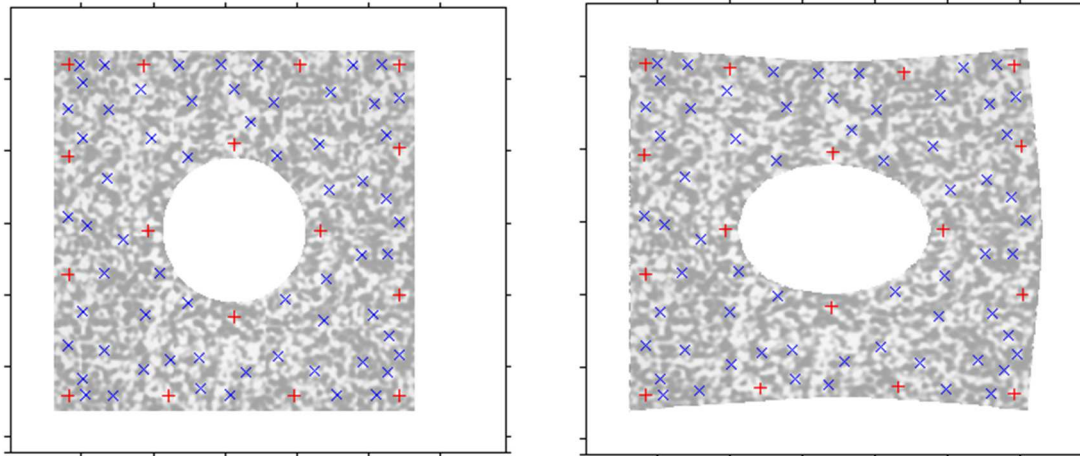
Figure 6–20. The distribution of 78 chosen control points (Approach 1, 16 initial points) on the reference image (left) and the deformed image (right), plus marks in red indicates initial control points while x-marks in blue are added control points through grid updating
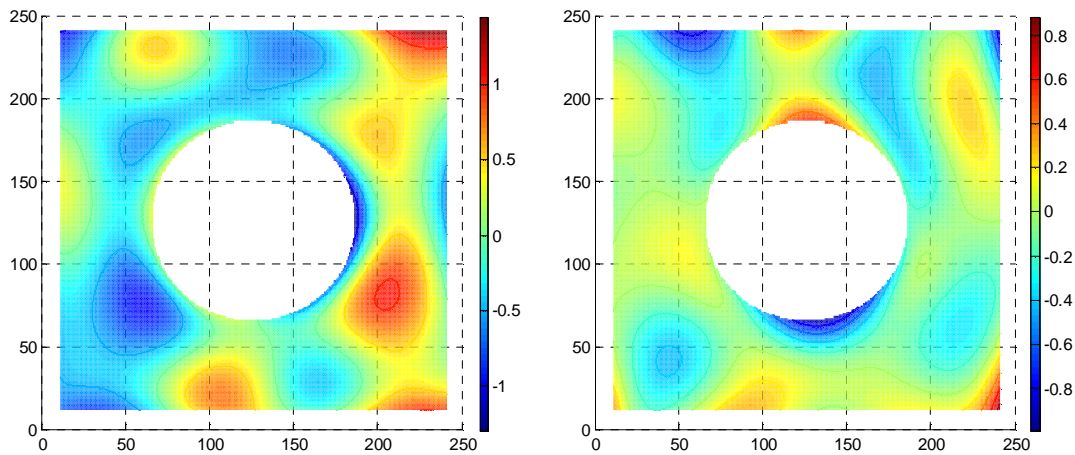

Figure 6–21. The displacement errors in pixels (Approach 1, 16 initial points) before Newton iteration (difference with the FE displacement fields) in x-direction (left) and y-direction (right)
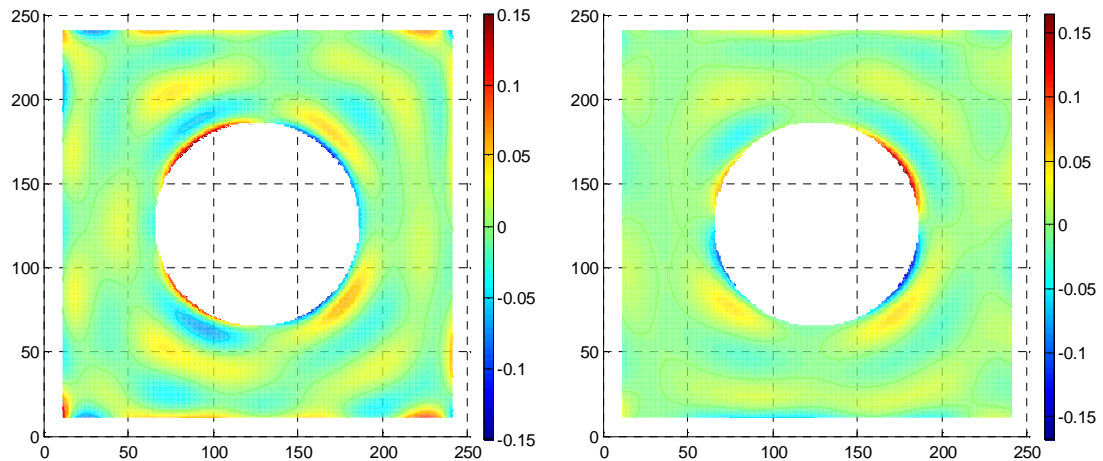
Figure 6–22. The displacement errors in pixels (Approach 1, 16 initial points) after Newton iteration (difference with the FE displacement fields) in x-direction (left) and y-direction (right)

The raw speckle images are generated using the numerical method based on Gaussian speckles. In the present case 7000 independent and identically distributed speckles are superimposed on the raw image of 250×300 pixels, each Gaussian speckle having a standard deviation of 2.5 pixels. The speckles of the deformed image are obtained by shifting the means (of the reference-image speckles) by the displacements determined from the FE model. The reference and deformed images are digitised using an 8-bit processor. Similar as the Approach 1, both the reference and deformed images are trimmed out from the raw speckle images shown in Figure 6–24.

The same 28 initial control points used in the first example of Approach 1 were arranged in the reference image indicated by the red '+' signs as shown in Figure 6–25. After the control grid was adaptively updated, the Kriging model finally reaches convergence when 88 control points were taken into consideration with 62 new added control points shown as blue '×' signs in Figure 6–25. Due to the fact that

measurement accuracy could be significantly improved through Newton iterative optimisation, the improvement was observed from the comparison between the residual displacement errors before and after the iteration, as shown in Figure 6–26 and Figure 6–27 respectively.
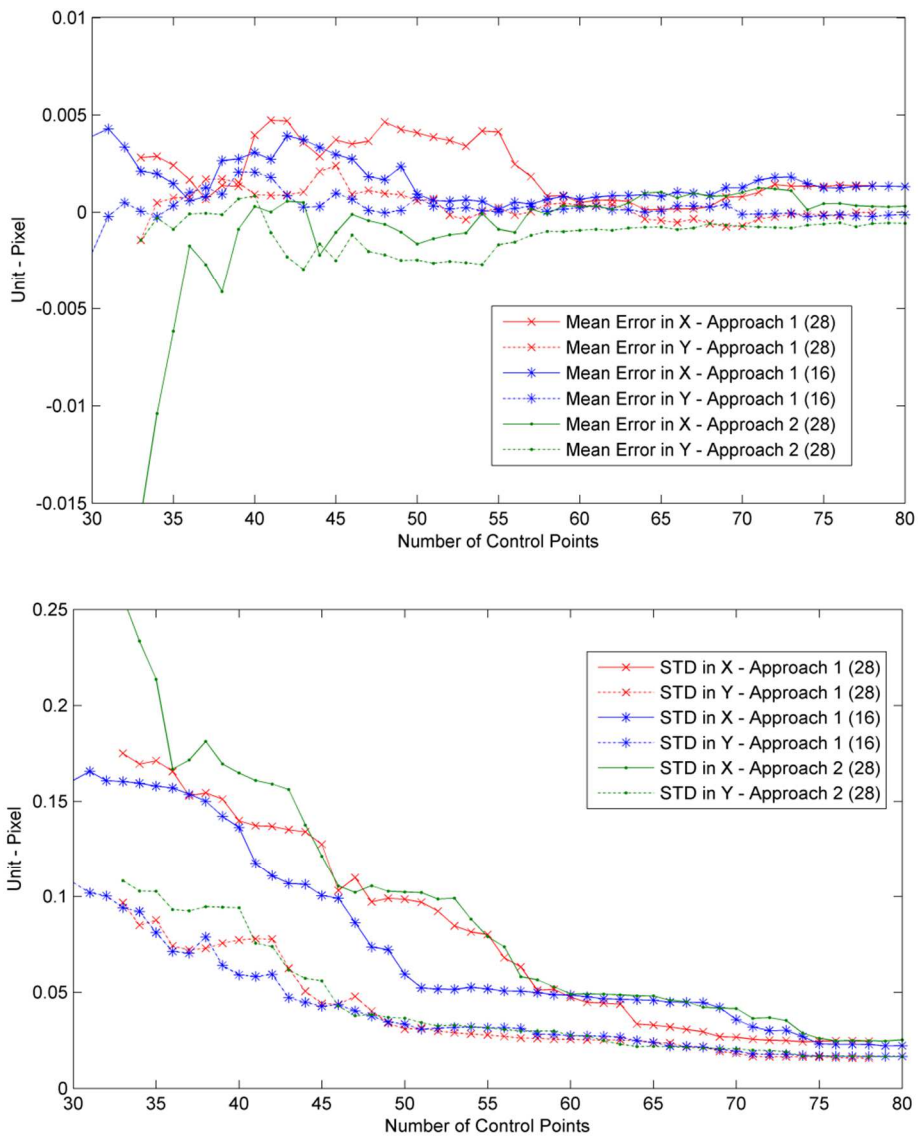
Figure 6–23. Evolution of Kriging-DIC measurement error statistics
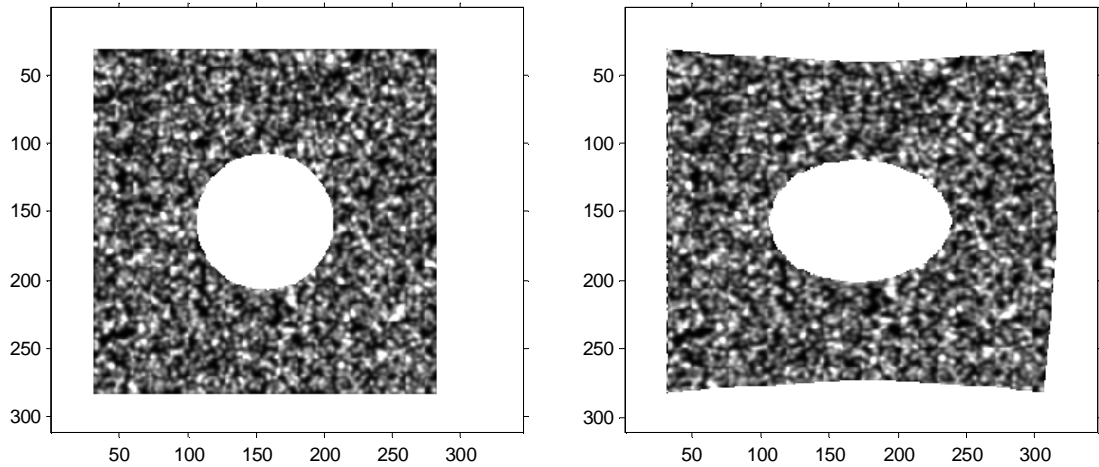
Figure 6–24. Trimmed speckle patterns, the reference image (left) and the deformed image (right)
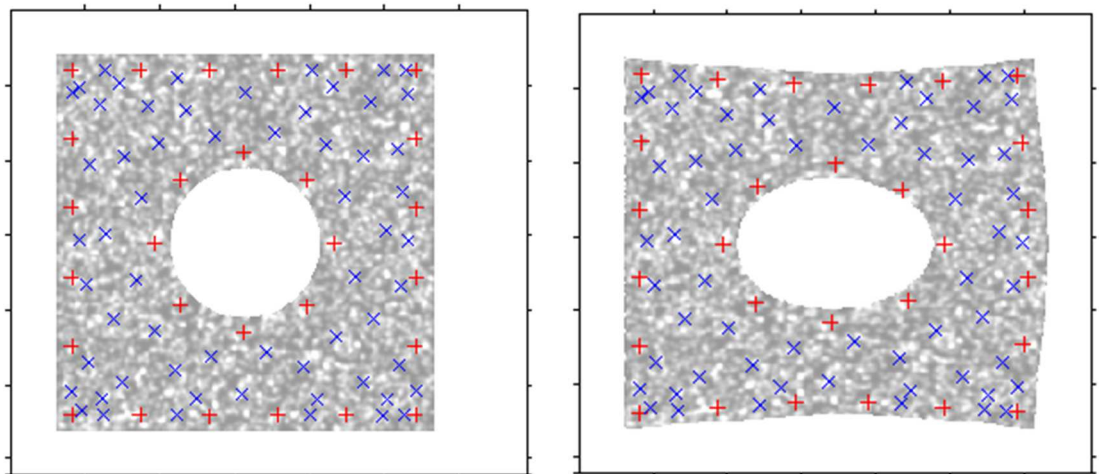
Figure 6–25. The distribution of 88 chosen control points (Approach 2, 28 initial points) on the reference image (left) and the deformed image (right), plus marks in red indicates initial control points while x-marks in blue are added control points through grid updating
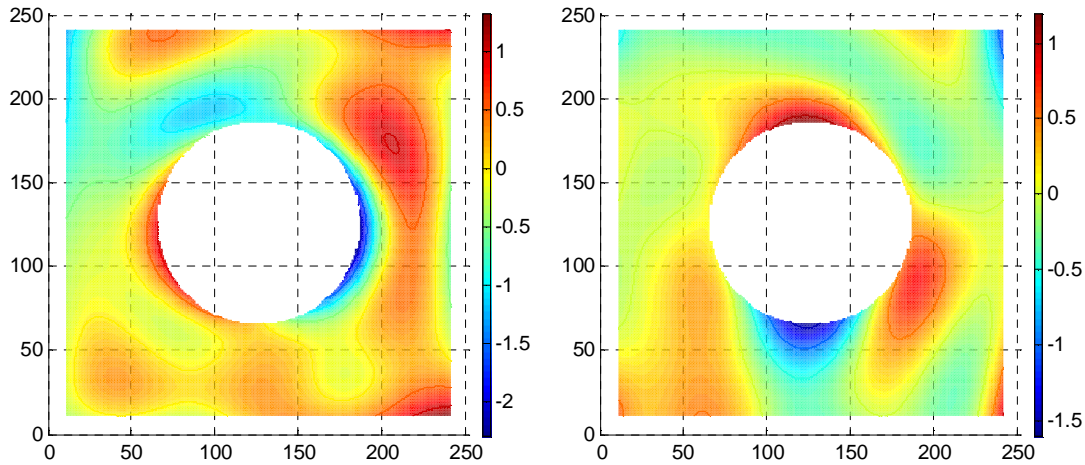
Figure 6–26. The displacement errors in pixels (Approach 2, 28 initial points) before Newton iteration (difference with the interpolated FE displacement fields) in x-direction (left) and y-direction (right)
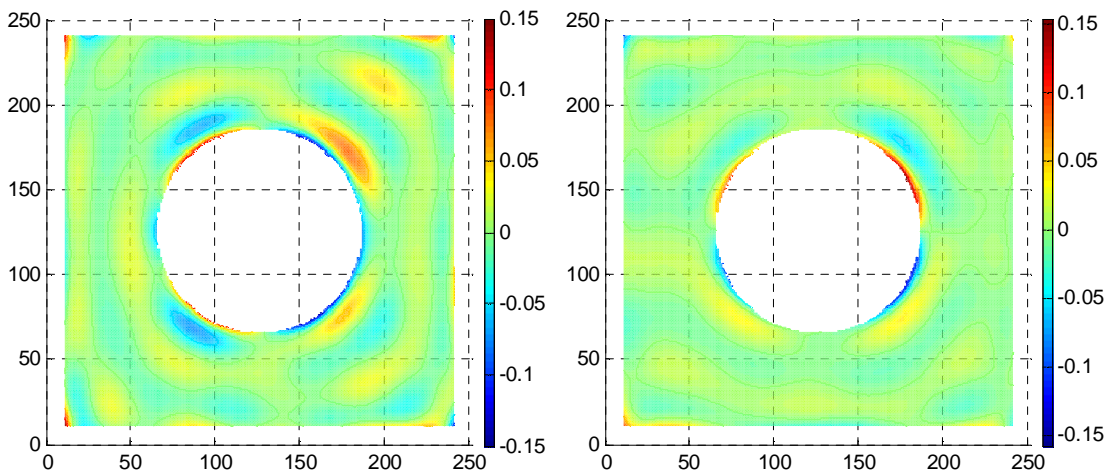
Figure 6–27. Displacement errors in pixels (Approach 2, 28 initial points) after Newton iteration in x-direction (left) and y-direction (right)

Figure 6–15 and Figure 6–16 show the evolution of GMSE and optimisation parameters ϑ_x, ϑ_y and ξ respectively compared with the corresponding parameters obtained in Approach 1. Similarly the unit-less normalised objective values were

presented in Figure 6–17. Further, the evolution of the mean error and standard deviation for the two approaches is given in Figure 6–23.

The optimisation parameters ϑ_x and ϑ_y from the two approaches were found to be similar, although there were differences in the values of ξ, presumably due to the different speckle patterns produced by the two methods. Convergence of the objective function was somewhat slower by the second approach, but the final estimated displacement fields were found to be almost identical from visual inspection of Figure 6–19, Figure 6–22 and Figure 6–27. The statistics of displacement fields are given in Table 6–5. The displacement fields from approach 1 were found to converge to almost identical statistics regardless of the number and location of the initial control points.

Table 6–5: Measurement error statistics (in pixels)

		Approach 1 (28 initial points & 78 in total)	Approach 1 (16 initial points & 78 in total)	Approach 2 (28 initial points & 88 in total)
X	Mean Error	0.00135	0.00134	2.60e-4
	STD	0.0244	0.0228	0.0209
Y	Mean Error	-1.51e-5	-2.25e-4	-4.93e-4
	STD	0.0157	0.0166	0.0151

6.4.4 Case study 4: experimental I-beam test

Application of the Kriging-DIC method is demonstrated on an experimental I-section beam with circular holes arranged symmetrically along the beam about its centre as shown in Figure 6–28. The overall dimensions of the cross section are 42 mm × 65 mm with 2.5 mm wall thickness. The distance between the supports is 450 mm. The test arrangement shown in the figure is designed to apply a mid-span

transverse point load, in the present case 2 kN. The experimental setup is described in detail by Labeas et al. [204].

The speckle-pattern reference image for a square RoI of 700×700 pixels is shown in Figure 6–29 with 12 initial control points denoted by red '+' signs and 30 added control points shown by blue '×' signs. The estimated displacement field determined by Newton iteration is shown in Figure 6–30 and for purpose of comparison results from a commercial DIC system (Dantec Q-400) using a local, subset-based DIC approach (41×41 pixel subsets and 30 pixel grid spacing) is provided in Figure 6–31. Figure 6–32 shows the absolute difference between the Kriging-DIC result and that produced by the commercial system, with the statistics of the difference summarised in Table 6–6. Results from the two systems appear to be similar although the displacement field produced by Kriging DIC seems smoother than that produced by the commercial system, which shows unexpected oscillations in the y-direction displacement field (Figure 6–31).

Figure 6–28. The experimental setup.
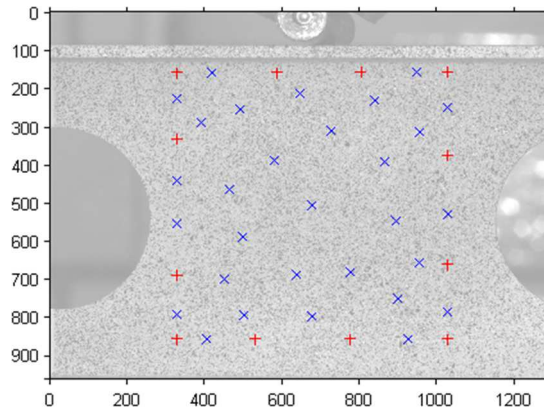
Figure 6–29. The distribution of initial control points (red '+' signs) and added control points (blue '×' signs) superimposed on the reference image.
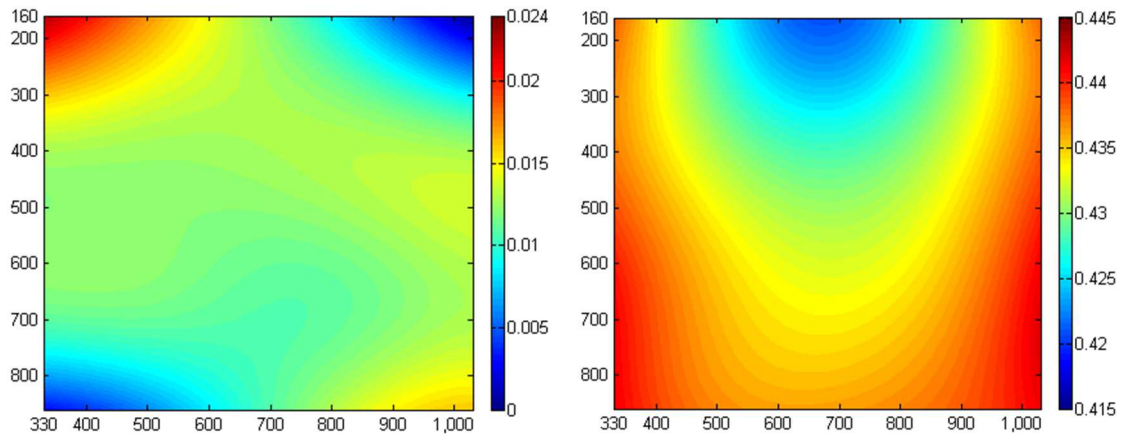
Figure 6–30. Displacement fields (mm) calculated by Kriging DIC method in x-direction (left) and y-direction (right).
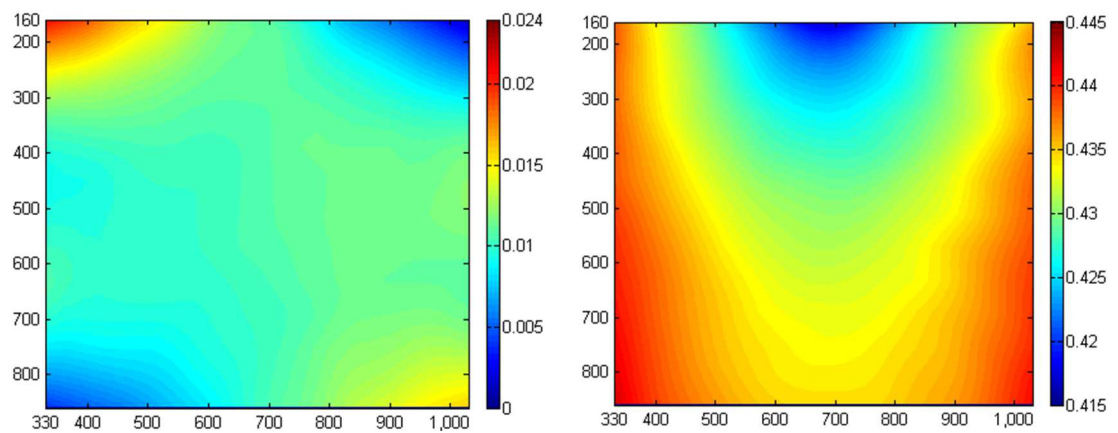
Figure 6–31. Displacement fields (mm) calculated by the commercial system in the x-direction (left) and y-direction (right)
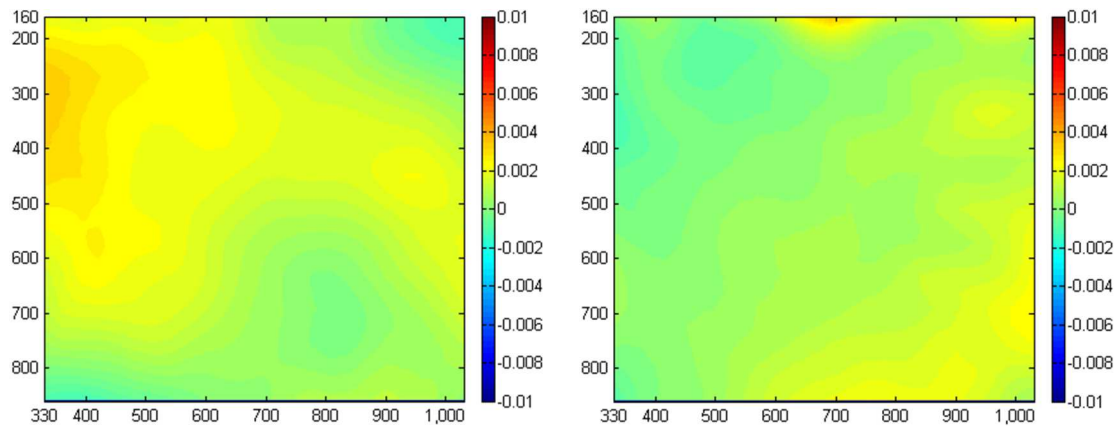
Figure 6–32. The absolute difference between the displacement fields (mm) calculated by Kriging DIC and the commercial system in the x-direction (left) and y-direction (right).

Table 6–6: Mean values and standard deviations of the absolute difference

Residual Disp		Unit: mm	Unit: pixel*
x	Mean	1.3472e-3	0.0182
	STD	9.1654e-4	0.0124
y	Mean	6.0095e-4	0.0081
	STD	7.3189e-4	0.0099

*1 pixel length ≈ 0.074 mm

6.5 Closure

A global DIC method based on Kriging regression with self-adaptive control grid updating is developed. The Kriging approach consists of two parts based on a regression model and the correlation between displacements at control points. The result is a minimum variance estimator with the error represented by a Gaussian process. Unlike FE DIC and Spline DIC, Kriging DIC is based on control points that are distributed fully throughout the region of interest. Since the control points are not measured with perfect accuracy, a regularization technique is employed to

extend Kriging interpolation model to a regression form to reduce the error effect. A self-adaptive updating technique is developed to optimise the control grid of Kriging model automatically.

The method is supported by four case studies, the first of which compares the performance of Kriging DIC and the classical subset-based DIC in terms of resolution and spatial resolution. It is found that Kriging DIC is able to achieve excellent displacement resolutions at high spatial resolutions and is very robust to image noise. However, it may need further adjustments for applications with high spatial frequency content. The second uses experimental data from the DIC Challenge 2D database. Using this data Kriging-DIC is shown to outperform Q4-FE DIC and Cubic Spline DIC. In the third case study Kriging DIC is shown to be robust to the number and location of initially-chosen control points and to speckle-pattern variations. The fourth case study is an experimental example where Kriging DIC is shown to perform favourably against a commercial subset-based DIC system.

7

Uncertainty Quantification in DIC

with Kriging Regression

A Kriging regression model is developed as a post-processing technique for the treatment of measurement uncertainty in the classical subset-based Digital Image Correlation (DIC). Regression is achieved by regularising the sample-point correlation matrix using a local, subset-based, assessment of the measurement error with assumed statistical normality and based on the Sum of Squared Difference (SSD) criterion. This leads to a Kriging-regression model in the form of a Gaussian process representing uncertainty on the Kriging estimate of the measured displacement field. The method is demonstrated using numerical and experimental examples. Kriging estimates of displacement fields are shown to be in excellent agreement with 'true' values for the numerical cases and in the experimental example uncertainty quantification is carried out using the Gaussian random process that forms part of the Kriging model. The root mean square error (RMSE) on the

estimated displacements is produced and standard deviations on local strain estimates are determined.

7.1 Problem overview

DIC is a well-developed and extensively applied technique in experimental mechanics while the subset-based DIC is probably the most commonly used approach because of its simplicity [5]. Inaccuracy, typically caused by camera noise, illumination variability, grey-scale interpolation and other sources, will always be present regardless of the level of precision of the DIC measurement. The resulting error in the measured data affects the accuracy of strain estimates [88] based on displacement data. A common way of dealing with this problem is to apply local smoothing [32, 33, 40], which has the advantage of simplicity but is subject to ad-hoc choice of order and parameterisation, possibly leading only to a local optimum. In the present study, a global improvement in measurement accuracy is sought by post-processing with a Kriging model that incorporates knowledge of error estimates determined from the classical subset-based DIC. Specifically, the measured data is regressed by utilizing an estimate of the measurement error built into the leading diagonal of the Kriging correlation matrix [55, 56, 163, 187].

Jouke et al. [163] proposed a local error estimate technique in particle image velocimetry (PIV) by using an uncertainty model based on peak ratios [164] in the cross-correlation map. This technique is not transferrable to DIC because of significant differences in the cross-correlation map of DIC data compared with PIV. Also DIC algorithms are usually based on the Sum of Squared Difference (SSD)

criterion and Newton iteration. Sutton et al. [23, 57] derived an estimate of displacement error due to the presence of Gaussian image noise, which is a function of the standard deviation of Gaussian noise and the sum of squared intensity gradients [24]. By considering the various error sources existing in the experiments, a more general form of error estimate was derived to approximate DIC error bounds as a function of the SSD residual and the inverse of Hessian matrix [35, 51], as discussed in Section 4.2.2. It is advantageous that the error estimate can be determined in the DIC process simultaneously with the displacement data without increasing the computational cost.

As discussed in Chapter 6, Kriging DIC considers the measurement uncertainty to be independent and identically distributed across the entire Region of Interest (RoI). Whilst this approach offers excellent error reduction properties, the resulting Gaussian-process estimate is limited by the assumption of measurement error that, within the RoI, remains the same from location to location. This limitation is addressed in this chapter whereby a local error estimate based on the inverse Hessian matrix and the residual of the SSD criterion is incorporated in Kriging regression. In Chapter 6, the Kriging model is used as a shape function in the full-field DIC Newton iteration, in this study Kriging regression is used as a post-processing technique to improve the accuracy of classical subset-based DIC measurement by including a local error estimate determined subset-by-subset. Numerical and experimental examples are used to test the performance of the proposed approach. One of the advantages of Kriging is that it provides not only a best linear unbiased prediction of the measurement, but also a Gaussian random process that delivers uncertainty quantification (UQ) on the prediction itself. Results show that Kriging regression with local error estimation is able to reduce the effect of measurement

errors and improve the accuracy of the estimated displacement field rather than just smoothing it. In an experimental example, the RMSE on the estimated displacement field and the standard deviations on locally estimated strains are presented. Post-processing with the Kriging model leads to a significant improvement in strain results obtained using an extensively used local linear fitting algorithm with a strain calculation window of various sizes [40]. The strain results determined directly from the gradients of the Kriging displacement field are also presented for comparison.

7.2 Uncertainty in the subset-based DIC

In order to obtain a mathematical expression for the local error estimate to be incorporated in the Kriging regression, a generic analysis for the measurement uncertainty of subset-based DIC is introduced first with the assumption of deformation continuity of a solid object and for reasons of simplicity a 2-dimensional case is considered. Detailed derivations for a general expression of the measurement uncertainty are given in Section 4.2.2.

The Kriging regression with local error estimate, described in the following section, is applied in the form of a non-parametric regression model and by including certain weighting terms, uncertainty in different parts of the full image may be represented probabilistically to develop an estimate of the true displacement field. Numerical and experimental examples show that the proposed approach is able to improve the measurement results of the classical subset-based method [63].

7.3 Kriging regression with local error estimate

Typically, DIC data are not measured with perfect accuracy, but are subject to measurement noise and imprecision [43, 55, 56, 162, 201], which might be reduced by pre-filtering [32, 41, 42]. However, in this study the Kriging regression approach accounts for measurement error in an overall way by regularizing the diagonal elements of the Kriging correlation matrix **R**. This means that the training points (or sample points) are not reproduced exactly but allow for error in the measured DIC image, thereby enabling the determination of an optimised displacement field represented by the Kriging model that represents the true displacement in the sense of a best linear unbiased prediction.

The method applied in this study is Kriging regression, also known as 'Universal Kriging' or 'Kriging with External Drift' [180]. Following the derivations of Kriging interpolation in Section 5.2, specifically in this study, Kriging is used to model the true displacement field $w(x, y)$ as a realisation of a random function $\hat{w}(x, y)$, which consists of a deterministic regression model and a zero-mean stochastic model [168, 181] as,

$$\hat{w}(x, y) = \sum_{\ell=1}^{m} c_\ell(x, y)\beta_\ell + Z(x, y) \tag{7-1}$$

where β_ℓ represents the ℓth regression coefficient based on regression functions $c_\ell(x, y)$, $\ell = 1, \ldots, m$, and The zero-mean Gaussian stochastic field is denoted by $Z(x, y)$, of which covariance between two arbitrary sample points j and k is formulated by,

$$\text{cov}\big(Z(\mathbf{x}_j), Z(\mathbf{x}_k)\big) = \sigma^2 r_{jk}\big(\mathbf{x}_j, \mathbf{x}_k, \vartheta_x, \vartheta_y, \xi\big); \quad \mathbf{x}_j = \big(x_j, y_j\big)^{\text{T}}; \quad \mathbf{x}_k = \big(x_k, y_k\big)^{\text{T}} \tag{7-2}$$

where $r_{jk}\big(\mathbf{x}_j, \mathbf{x}_k, \vartheta_x, \vartheta_y\big) = \text{corr}\big(Z(\mathbf{x}_j), Z(\mathbf{x}_k)\big)$ depends on the proximity of points j and k. Based on an optimisation procedure, the correlation parameters $\vartheta_x, \vartheta_y, \xi$ and field variance σ^2 are determined, as described in Section 5.2.

The regression parameters β_ℓ may be estimated from the sample by using the generalized least squares (GLS) method [53, 182]. Denoting $\mathbf{w}_0 = [w_1, \cdots, w_n]^{\text{T}}$ as the vector of displacements calculated by the subset-based DIC at a set of sample points (x_j, y_j), $j = 1, 2, \ldots, n$, , the estimated regression parameters $\hat{\boldsymbol{\beta}}$ are then expressed by [182] (as shown in Equation (5-36)):

$$\hat{\boldsymbol{\beta}} = \big(\mathbf{C}^{\text{T}} \mathbf{R}^{-1} \mathbf{C}\big)^{-1} \mathbf{C}^{\text{T}} \mathbf{R}^{-1} \mathbf{w}_0 \tag{7-3}$$

where the correlation matrix $\mathbf{R}$ is a function of the parameters $\vartheta_x, \vartheta_y, \xi$, i.e. $\mathbf{R}\big(\vartheta_x, \vartheta_y, \xi\big)$. Then, by minimising the mean-square prediction error under an unbiasedness constraint [182], the Kriging model at an arbitrarily chosen point $\mathbf{x}_p = (x_p, y_p)$ is obtained as,

$$\hat{w}(\mathbf{x}_p) \sim \mathcal{N}\big(\bar{w}(\mathbf{x}_p),\ \sigma^2 S(\mathbf{x}_p)\big) \tag{7-4}$$

where,

$$\bar{w}(\mathbf{x}_p) = \mathbf{c}^{\text{T}}(\mathbf{x}_p)\hat{\boldsymbol{\beta}} + \mathbf{r}^{\text{T}}(\mathbf{x}_p)\mathbf{R}^{-1}\big(\mathbf{w}_0 - \mathbf{C}\hat{\boldsymbol{\beta}}\big) \tag{7-5}$$

is the Best Linear Unbiased Prediction (BLUP) with the variance given by,

$$\hat{\sigma}^2 V\left(\mathbf{x}_p\right) = \hat{\sigma}^2 \left(1 - \mathbf{r}^{\mathrm{T}}(\mathbf{x}_p)\mathbf{R}^{-1}\mathbf{r}(\mathbf{x}_p) + \left(\mathbf{c}^{\mathrm{T}}(\mathbf{x}_p) - \mathbf{r}^{\mathrm{T}}(\mathbf{x}_p)\mathbf{R}^{-1}\mathbf{C}\right)\right.$$
$$\left. \times\left(\mathbf{C}^{\mathrm{T}}\mathbf{R}^{-1}\mathbf{C}\right)^{-1}\left(\mathbf{c}^{\mathrm{T}}(\mathbf{x}_p) - \mathbf{r}^{\mathrm{T}}(\mathbf{x}_p)\mathbf{R}^{-1}\mathbf{C}\right)^{\mathrm{T}}\right)$$

(7-6)

Covariance terms between two arbitrary locations $\mathbf{x}_p, \mathbf{x}_q$ may be expressed as,

$$\hat{\sigma}^2 V\left(\mathbf{x}_p, \mathbf{x}_q\right) = \hat{\sigma}^2 \left(r_{pq}\left(\mathbf{x}_p, \mathbf{x}_q\right) - \mathbf{r}^{\mathrm{T}}(\mathbf{x}_p)\mathbf{R}^{-1}\mathbf{r}(\mathbf{x}_q) + \left(\mathbf{c}^{\mathrm{T}}(\mathbf{x}_p) - \mathbf{r}^{\mathrm{T}}(\mathbf{x}_p)\mathbf{R}^{-1}\mathbf{C}\right)\right.$$
$$\left. \times\left(\mathbf{C}^{\mathrm{T}}\mathbf{R}^{-1}\mathbf{C}\right)^{-1}\left(\mathbf{c}^{\mathrm{T}}(\mathbf{x}_q) - \mathbf{r}^{\mathrm{T}}(\mathbf{x}_q)\mathbf{R}^{-1}\mathbf{C}\right)^{\mathrm{T}}\right)$$

(7-7)

where $\mathbf{x}_p, \mathbf{x}_q$ may be either sampled or unsampled points and $\left(\hat{\bullet}\right)$ denotes an estimate while $\hat{\sigma}^2$ is given by Equation (5-35). The variance and covariance terms given in Equation (7-6) and (7-7) respectively are equivalent to the corresponding diagonal and non-diagonal terms in the covariance matrix shown in Equation (5-49).

In the above expressions, $\mathbf{R}$ is the matrix of sample-point displacement correlation functions with terms $r_{jk}(\mathbf{x}_j, \mathbf{x}_k, \vartheta_x, \vartheta_y, \xi)$ described above; $\mathbf{r}(\mathbf{x}_{p(q)}, \vartheta_x, \vartheta_y)$ is the vector of displacement correlation functions between an arbitrarily chosen location $\left(\mathbf{x}_{p(q)}\right)$ and each of the sample points $\left(\mathbf{x}_j\right)$, $j = 1, 2, \ldots, n$; and $r_{pq}\left(\mathbf{x}_p, \mathbf{x}_q, \vartheta_x, \vartheta_y\right)$ denotes the correlation between two arbitrarily chosen points $\left(\mathbf{x}_p, \mathbf{x}_q\right)$. $\mathbf{C}$ is a matrix consisting of regression functions evaluated at the sample points, $C_{\ell j} = c_\ell\left(\mathbf{x}_j\right)$; and $\mathbf{c}(\mathbf{x}_{p(q)})$ is the vector of regression functions for an arbitrary location $\mathbf{x}_{p(q)}$, i.e. $c_\ell = c_\ell\left(\mathbf{x}_{p(q)}\right)$.

The correlation functions are generally assumed to be Gaussian [187] (as shown in Equation (5-29)), which relies on assuming the response surface inferred by Kriging regression is smooth. It can be expressed in the form:

$$r_{pq}(\mathbf{x}_p, \mathbf{x}_q, \vartheta_x, \vartheta_y) = \exp(-\vartheta_x(x_p - x_q)^2 - \vartheta_y(y_p - y_q)^2) \qquad (7\text{-}8)$$

where the terms ϑ_x and ϑ_y determine how significantly the distances between both x_p and x_q and y_p and y_q affect the correlation given by equation (7-8). It is seen that points close to each other have a higher correlation than those that are far away.

When measurement error is considered the diagonal elements of the correlation matrix $\mathbf{R}$ in the Kriging formula should be adjusted by the introduction of an error term (multiplicatively in the present work). This allows for regression instead of exact interpolation of the data samples. According to the correlation function (7-8), all the diagonal elements of matrix $\mathbf{R}$ are unity for Kriging interpolation which means that the Kriging model passes through all the samples exactly. In contrast, measurement error is taken into account by regularizing the diagonal elements of the correlation matrix $\mathbf{R}$, which allows regression of the Kriging model on the data samples. This modified formulation is known as Kriging regression [162] and introduces an additional parameter ξ.

7.3.1 Global error estimate

If the error is assumed independent and identically distributed across the entire region of interest then an unknown constant factor ξ may be applied [56, 63, 163] to modify the diagonal elements of the correlation matrix $\mathbf{R}$ according to Equation (7-8),

$$r_{jj}^* = \exp(\xi); \quad j = 1, 2, \ldots, n \qquad (7\text{-}9)$$

where n denotes the number of sample points.

7.3.2 Local error estimate

In many cases, the error is not constant over the entire domain but may separately be considered independent and identically distributed over a subset of the reference image. An estimate of displacement error for each subset due to the presence of Gaussian image noise was derived [23, 57] as a function of the standard deviation of Gaussian noise and the sum of squared intensity gradients [24]. As discussed in Section 4.2.2, a more general form of error estimate is derived to approximate the DIC error bound for each subset as a function of the SSD residual and the inverse of Hessian matrix [35, 51]. The multiple error sources in DIC measurement are included in a general way. By combining the Equation (4-21) and Equation (4-22), this general form of error estimate for each subset may be expressed as,

$$
\begin{aligned}
m_{xj}^* &= \frac{C_{SSDj}}{N^2} \cdot \left(\mathbf{H}^{-1}\right)_{11} \\
m_{yj}^* &= \frac{C_{SSDj}}{N^2} \cdot \left(\mathbf{H}^{-1}\right)_{77}
\end{aligned}
\tag{7-10}
$$

where m_{xj}^* and m_{yj}^* are approximations to the error variances associated with x- and y-direction displacements for the jth subset of $N \times N$ pixels, having a single sample point at its centre. C_{SSDj} denotes the SSD residual for the jth subset. $\mathbf{H}$ is the calculated Hessian matrix while subscripts 11 and 77 indicate the diagonal elements of $\mathbf{H}^{-1}$ that corresponds to the x- and y-direction displacements of the subset centre point.

If the different error for each subset is taken into account, equation (7-9) then may be expressed in modified form,

$$r_{jj}^* = \exp\left(\xi\left(\frac{-\vartheta_x m_{xj}^* - \vartheta_y m_{yj}^*}{\sqrt{(m_{x1}^*)^2 + (m_{y1}^*)^2}}\right)\right) \qquad (7\text{-}11)$$

where the term $\sqrt{(m_{x1}^*)^2 + (m_{y1}^*)^2}$ is a normalising constant.

The derivation of m_{xj}^* and m_{yj}^*, given in Equation (7-10), is achieved under the following conditions on the measurement error:

i. Assumed to be Gaussian with zero mean, independent and identically distributed over a subset of $N \times N$ pixels.

ii. Approximated using shape functions based on a second-order Taylor series expansion (may be first- or higher-order) about a sample point at a subset centre.

iii. Linearised at $N \times N$ pixels to relate field uncertainties to shape function variables.

iv. Pixel grey-intensity variances approximated using the SSD between the deformed and reference images.

As discussed in Section 5.3.3, the solution of unknown Kriging parameters $\{\vartheta_x, \vartheta_y, \xi, \sigma^2\}$ is carried out based on the maximum likelihood estimation by using a Nelder-Mead optimisation algorithm with a first-order regression function chosen for $\mathbf{c}(x, y)$ [182].

7.3.3 Strain calculation

Two different methods were applied to determine the strains. Firstly, a local fitting technique [40] based on the point-wise least squares algorithm (PLS), within a chosen strain calculation window, was utilized to estimate the strain result from the measured displacement data. Linear functions are fitted to approximate the gradients

at the centre point of each local strain window. It is known [40] that there might be an insufficient number of valid data points within the strain calculation window at the boundaries or where there are discontinuities. In order to solve this problem, a displacement continuity assumption may be used to extend the displacement field [78] or alternatively the invalid points may be identified and excluded from the local PLS fitting [40]. The latter was applied in this study, as was post-processing by the Kriging local method, which has a similar effect.

Secondly, the strain results were calculated directly from the gradients of the Kriging displacement model. This second approach is applied in an experimental case study, where estimated strains are compared to those produced by the PLS method. The Kriging gradients are calculated from the Jacobian of the vector of regression functions $\mathbf{c}(\mathbf{x}_p)$ and the vector of correlation functions $\mathbf{r}(\mathbf{x}_p)$ as discussed in Section 5.2.3.

Although the displacement field is Gaussian, the strain field is generally non-Gaussian. According to Section 5.5, a sampling method based on Cholesky decomposition was employed to sample the displacement field from the multivariate Gaussian distribution [195, 205] with the purpose of quantifying the uncertainty on the estimated strain field. Given the Cholesky decomposition of the correlation matrix $\mathbf{V} = \mathbf{\Lambda}\mathbf{\Lambda}^{\mathrm{T}}$ (equations (7-6) and (7-7)) where $\mathbf{\Lambda}$ is a lower triangular matrix, samples of the displacement field, across the region of interest, were generated from,

$$\hat{\mathbf{w}} = \mathbf{\Lambda}\mathbf{n}_s + \overline{\mathbf{w}} \tag{7-12}$$

by sampling from $\mathbf{n}_s \sim \mathcal{N}(0, \mathbf{I})$ which is subject to a multivariate standard normal distribution. Classical finite differences may then be applied to calculate the

gradients and generate the strain results. This requires dense sampling of displacement field (local sampling) to determine the uncertainty on the estimated strains.

7.4 Case studies

Numerical and experimental case studies are presented to illustrate the application of Kriging regression with local error estimation. Two sets of numerical simulation examples were carried out first so that possible errors introduced by the image acquisition system were excluded. In the first numerical example, the effectiveness of the proposed Kriging method in displacement estimation is investigated using numerically generated Gaussian speckles with uniform translations, affine deformation and Gaussian image noise. The second numerical example has the same numerically generated Gaussian speckles but a uniaxial tensile deformation with a constant strain. Gaussian image noise is employed to verify the performance of proposed Kriging method in strain measurement. In the experimental example, a cantilever beam test is chosen to investigate the performance of Kriging method in a practical DIC application, since it has a simple analytical solution for comparison with DIC results.

7.4.1 Numerical case study 1: verification of the Kriging method for displacement measurement

A 2-dimensional numerical example is illustrated, using numerically-produced Gaussian speckles [81, 95] with means uniformly distributed over the RoI. Gaussian speckles are formulated as shown in Equation (6-10) but the displacements $u(x, y)$ and $v(x, y)$ are represented in the form of first-order shape functions as:

$$u(x, y) = u_0 + u_x x + u_y y$$
$$v(x, y) = v_0 + v_x x + v_y y$$

<div align="right">(7-13)</div>

In the present case, 8000 independent and identically distributed speckles were superimposed on an image consisting of 500×500 pixels, each Gaussian speckle having a size of 3 pixels and a peak intensity of 60. In order to test the proposed method, several deformed images were produced with a combination of (a) rigid-body translation in x- and y-directions, (b) affine deformation, and (c) Gaussian image noise. The reference and deformed images were digitised using an 8-bit processor. As the grey values of non-integer locations are required in the DIC process, a grey-value interpolation scheme is needed and for reasons of simplicity a cubic spline intensity interpolation scheme was chosen.
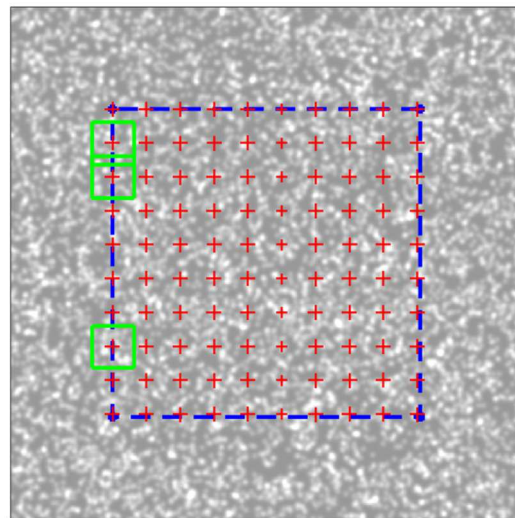

Figure 7–1. Numerically generated speckles and the distribution of sample points (red crosses) - 3 subsets are shown in green squares

The RoI was divided into 100 uniformly distributed sample points, each of which was defined as the centre node of a subset of 41×41 pixels, as shown in Figure 7–1. The subset-based DIC, based on a Newton-Raphson scheme, was applied to assess

the measurement error at all the sample points. Since only a linear deformation (affine transformation) was applied, a first-order Taylor-expansion shape function was chosen in order to avoid possible over-fitting. On the basis of this measurement, both Kriging regression with global and local error estimation were employed to regularize the measured data and achieve an estimate of the displacement at each centre node.

As the true displacements of the sample points are easily derivable, the residual errors of subset-based DIC, Kriging global and Kriging local methods are shown and may be compared in Figure 7–2 to Figure 7–5. The results shown for Kriging are the mean values of the Gaussian Process that represents the Kriging model. It is observed that the residual errors are significantly reduced after the application of Kriging regression with local error estimation. There is a very tiny difference in the residual errors of Figure 7–2 between the Kriging global and local methods, which is to be expected because uniform translation was applied to the whole RoI. The Kriging global method performs less well in the case of an affine deformation as shown in Figure 7–3, because the local deformations differ from subset to subset. Both the Kriging global and local methods demonstrate effective reduction of measurement errors due to Gaussian image noise as shown in Figure 7–4. In Figure 7–5 under the effect of combined error sources, the Kriging local method considerably out-performs the Kriging global method.

x-direction   (b) y-direction
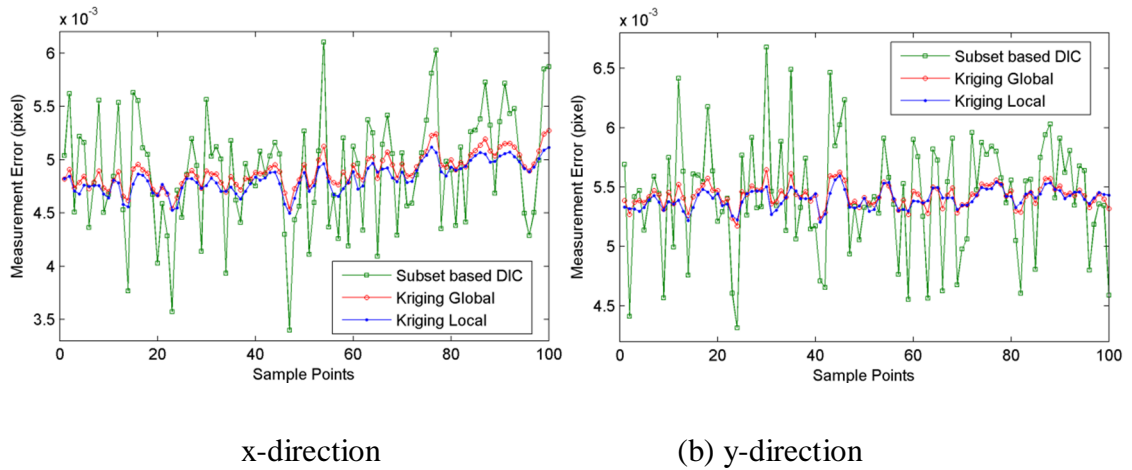
Figure 7–2. Numerical case study 1: residual error comparison for a rigid-body

translation $u_0 = 0.2,\ v_0 = 0.3$ pixels.

(a) x-direction   (b) y-direction
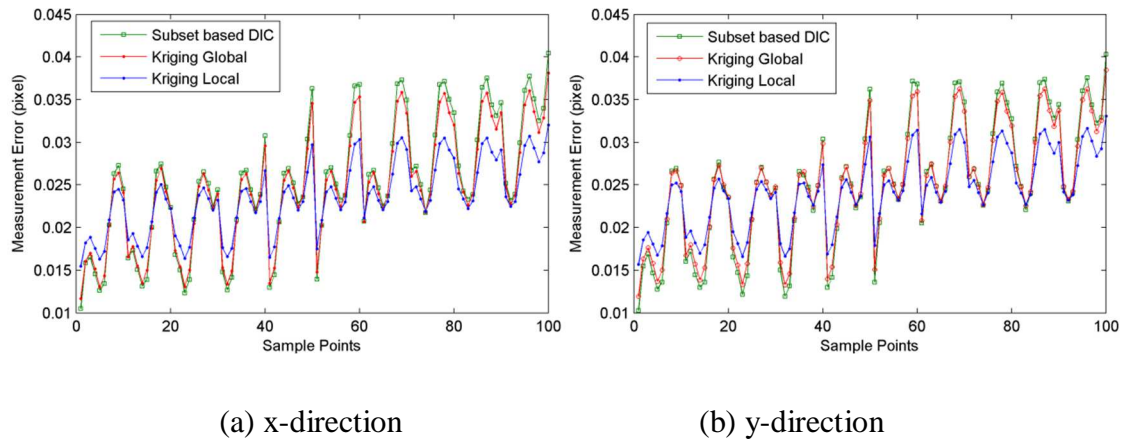
Figure 7–3. Numerical case study 1: residual error comparison for an affine

deformation $u_x = 0.005,\ u_y = 0.005,\ v_x = 0.005,\ v_y = 0.005$ pixels.

(a) x-direction   (b) y-direction
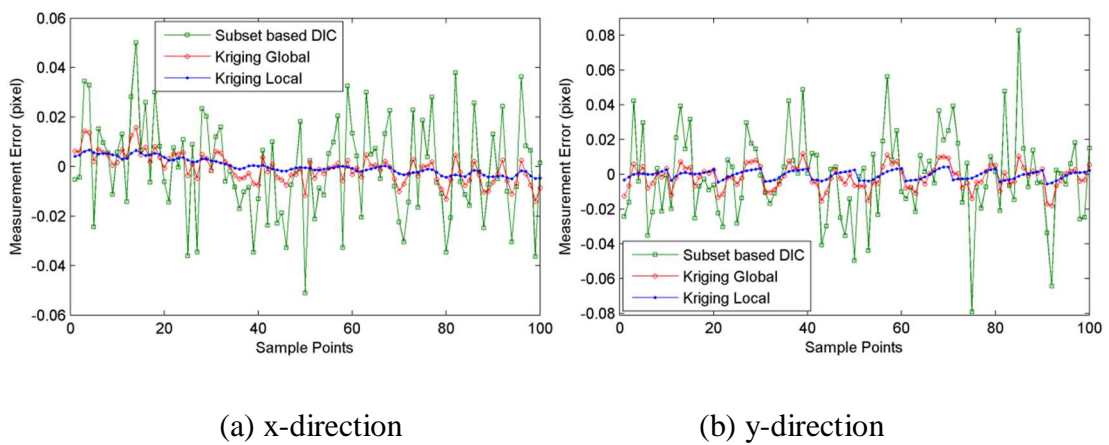
Figure 7–4. Numerical case study 1: residual error comparison for Gaussian image

noise, zero mean, $\sigma = 5$ grey-levels.

| (a) x-direction | (b) y-direction |
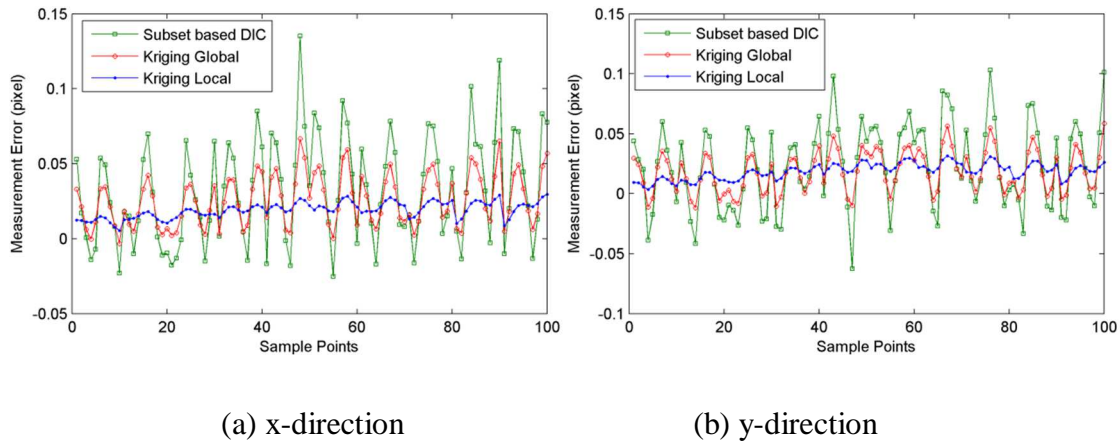
Figure 7–5. Numerical case study 1: residual error comparison for the combination of translation $u_0 = 0.2$, $v_0 = 0.3$ pixels, affine deformation $u_x = 0.005, u_y = 0.005, v_x = 0.005, v_y = 0.005$ pixels and Gaussian image noise, zero mean, $\sigma = 5$ grey-levels.

7.4.2 Numerical case study 2: verification of the Kriging method for strain measurement.

A uniaxial tensile deformation was applied to investigate the performance of proposed Kriging method in strain measurement. The pre-assigned homogenous strain was 5000 $\mu\varepsilon$ in the x-direction i.e. $u_x = 0.005, u_y = 0, v_x = 0, v_y = 0$. The same numerically generated Gaussian speckles as in Case Study 1 were used. Gaussian image noise with zero mean and $\sigma = 3$ grey-levels was added to the numerical images to simulate a practical noise condition. A central-area uniform grid 33×33 with a grid spacing of 13 pixels was superimposed upon the simulated image of 500 $\times$ 500 pixels. The displacement at the 1089 grid points was computed by the subset-based DIC using a Newton-Raphson scheme and a first-order Taylor-expansion shape function using subsets of 41×41 pixels.
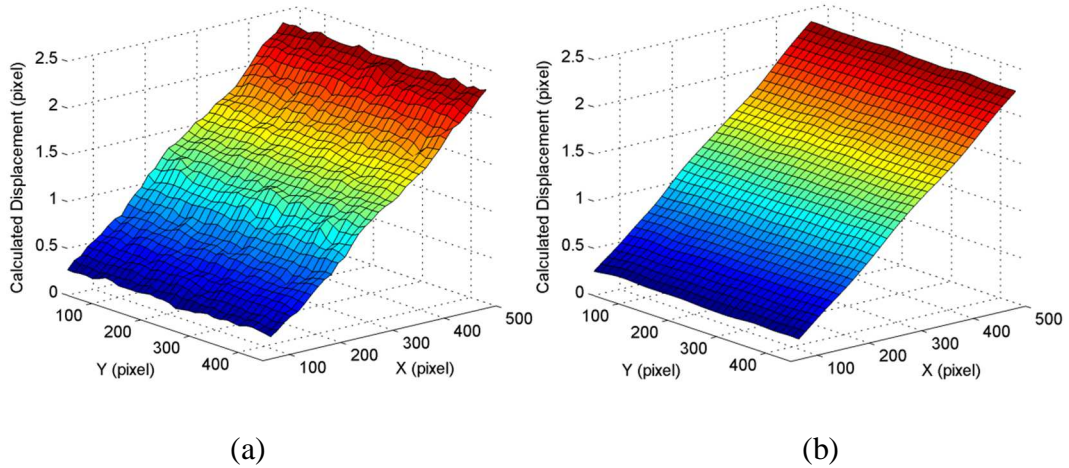
Figure 7–6. Numerical case study 2: calculated displacement fields, (a) by subset-based DIC using Newton-Raphson scheme, (b) by Kriging regression with local error estimate

Figure 7–6 (a) shows the displacement field calculated by the subset-based DIC where small fluctuations due to the Gaussian image noise can be observed. The regularized displacement field obtained by the Kriging local method is demonstrated in Figure 7–6 (b), where the error in the displacement field, due to Gaussian noise, has been significantly reduced. The strain results calculated by the PLS algorithm for different methods are illustrated in Figure 7–7. For this simple example, it is shown that based on the same size of strain calculation window, the Kriging local method is able to achieve superior strain results especially in the vicinity of the boundaries. The Kriging global and local methods were not significantly affected by the deficiency of valid data points at the boundaries of the strain window, since the displacement noise had already been substantially removed by the Kriging method. The boundary effect could also be reduced by extending of displacement field outside the calculation area boundaries [78], but might not be reliable in the case of complex deformations when additional errors might be introduced inadvertently.
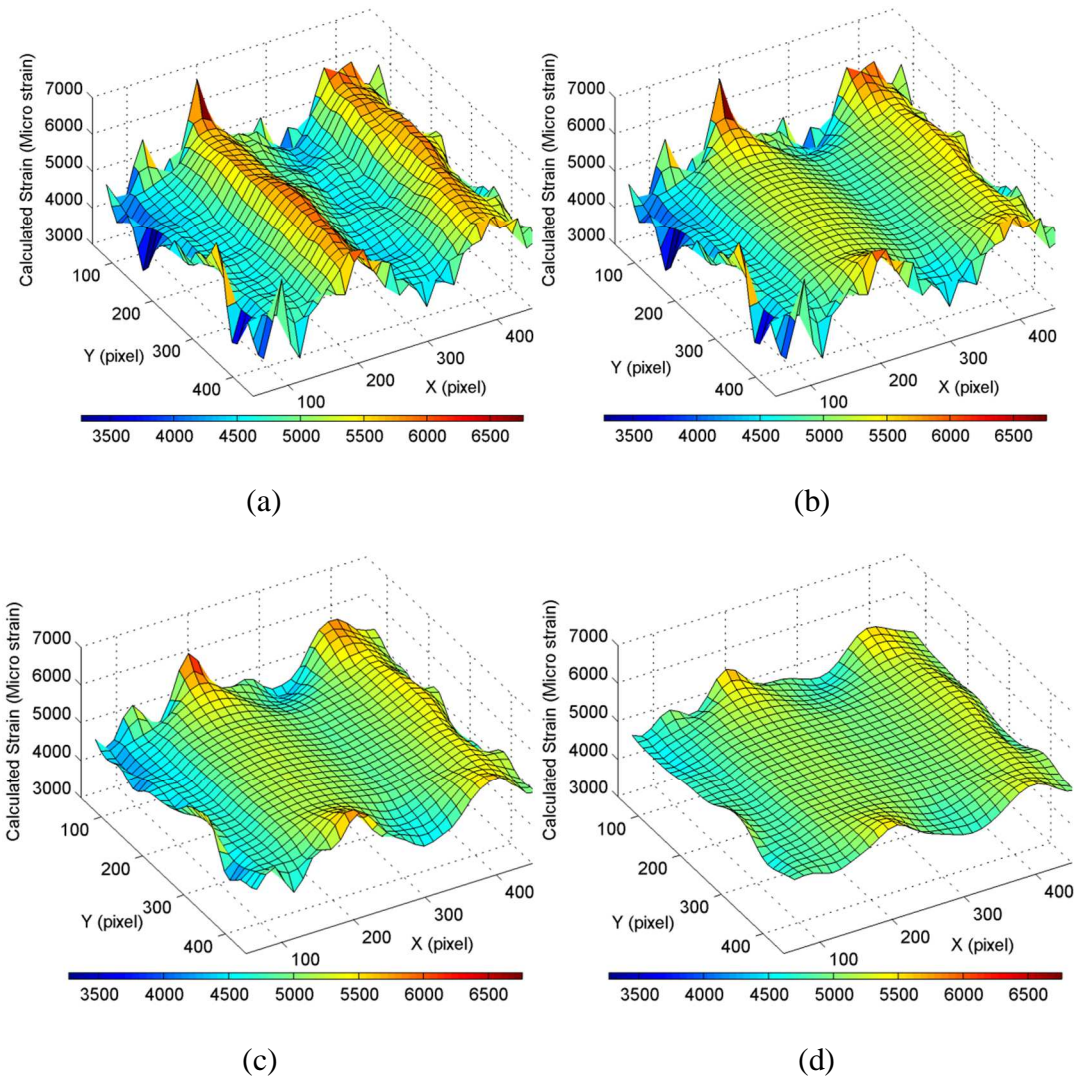
Figure 7–7. Numerical case study 2: calculated strain fields, (a) by subset-based DIC using 7×7 strain window, (b) by subset-based DIC using 15×15 strain window (c) by Kriging global method using 15×15 strain window (d) by Kriging local method using 15×15 strain window.

7.4.3 Experimental case study: cantilever beam test with UQ

The proposed Kriging regression technique was validated by using experimental data from an aluminium cantilever beam of dimensions 160 mm × 40mm × 4 mm thick. A thin coat of quick-drying white paint (Matt Super White 1107, Plasti-kote, UK) was sprayed onto the surfaces of the cantilever beam using an aerosol can, on top of which speckles were sprayed using black paint (Matt Super Black 1102,

Plastikote, UK). The beam was securely clamped to an optical table as shown in Figure 7–8 and, in order to avoid errors caused by relative motions, the DIC system was also clamped to the table with the camera perpendicular to the face-plane of the cantilever. Perpendicularity was checked in the present case by using a protractor, though more sophisticated techniques are available [137, 206]. A vertical load, generated by a dead-weight of 51 kg was applied at the tip, also shown in Figure 7–8. Two experiments (Test 1 and Test 2) were carried out using two different cantilever beams. The illumination intensity was slightly higher in Test 2 than in Test 1 as shown in Figure 7–9, while the speckles used in two tests were applied at different times and by different operatives. The CCD camera (Allied, Model F-125B/C) has a resolution of 1292 pixels × 964 pixels with a Schneider Xenoplan lens of f-number 1.4 and 12 mm focal length. This combination provides resultant scales of 7.298 pixels/mm for Test 1 and 7.326 pixels/mm for Test 2. The average speckle diameter in both Test 1 and 2 was estimated to be 5 pixels. The experimental setup is also described in detail in [207].
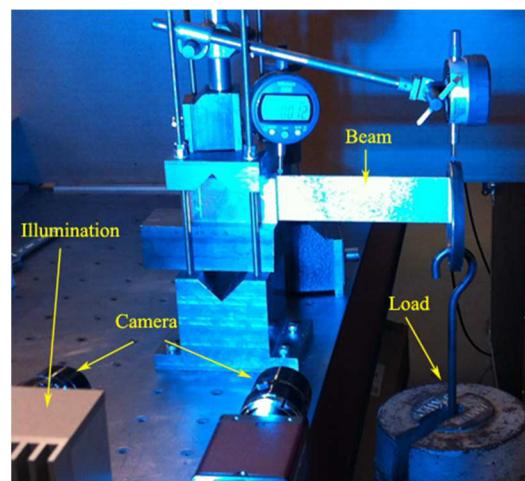

Figure 7–8. Experimental setup

A uniform grid of sample points (16×64) was selected as indicated by the red '+' signs shown in the reference images of Figure 7–9. The subset-based DIC method based on a Newton-Raphson scheme, a shape function in the form of a second-order Taylor expansion (subset size: 41×41 pixels, grid spacing: 15 pixels) and a 6×6 intensity interpolation scheme was then employed to calculate the displacements of the subset centre nodes while the PLS algorithm was applied to calculate the strain results. Analytical displacement and strain results were calculated based on the Timoshenko's beam theory according to [208] and shown in Figure 7–10. The diagonal elements of the optimised correlation matrix **R** may be used to indicate the relative magnitude of quantified DIC measurement error, which differs from subset to subset. The fractional part of the diagonal element represents the extent to which the regularized sample point deviates from the original sample point. It is seen in Figure 7–11 that the measurement error generally increases towards to free end of the cantilever where the loading is applied. The diagonal element of matrix **R** (same for each subset) by using the Kriging global method is presented in Table 7–1.
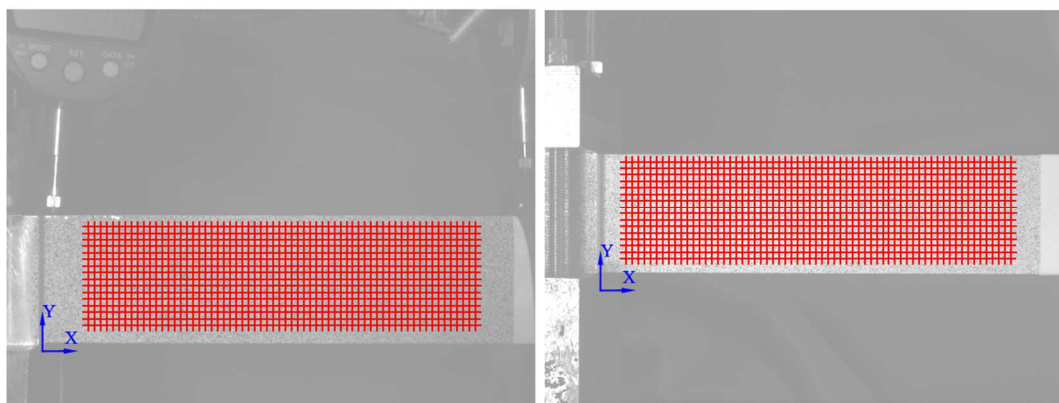
(a)   (b)

Figure 7–9. Distribution of sample points (16×64) in the reference image of the cantilever beam for Test 1 (a) and Test 2 (b)
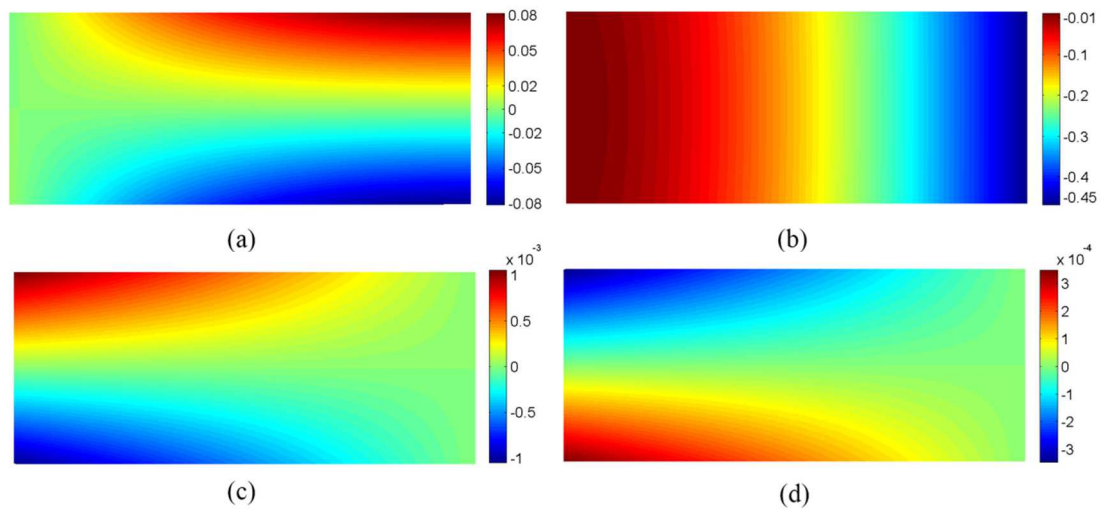
Figure 7–10. Analytical displacement fields (mm): (a) *x*- and (b) *y*-directions and strain distributions: (c) *x-x* and (d) *y-y* strains.

Table 7–1: Optimized diagonal elements with global error estimate

Test 1	Test 2
1.0035	1.0092

Figure 7–12 shows the RMSE on the *y*-direction mean Kriging estimate. Similar results were found for the x-direction, though the displacements are of course greater in the *y*-direction. The tiny error is an indicator of very significant confidence in the estimate. The increase in the RMSE at the boundaries is inherent to the Kriging method since there is less data available. The Gaussian process deals well with interpolation (in the sense of predicting values within the convex hull of the training runs), but, as with most other meta models, it suffers with extrapolation. The reason is that there is no information outside the bounds so the covariance function does not have a way to interpret the relationship between the outermost point and the nearest neighbors.

For reasons of simplicity and to avoid an excessive number of figures, only the *x-x* strain results for different methods applied to both the specimens are shown for comparison in Figure 7–13 and Figure 7–14, i.e. (1) subset-based DIC using 21×21 strain window, (2) Kriging global method using 21×21 strain window, (3) Kriging local method using 21×21 strain window and (4) Kriging local method using the gradients from Kriging model, calculated from the Jacobian of the vector of regression functions $\mathbf{c}(x, y)$ and the vector of correlation functions $\mathbf{r}(x, y)$ as discussed in [182]. It should be noted that the strain fields shown in Figure 7–13 and Figure 7–14 are linearly interpolated from the original discrete strain data (16×64) only for the purpose of visualisation. In order to quantify the similarity between post-processing results and analytical results, an image decomposition technique based on Tchebichef polynomials [209, 210] was used to represent each dataset and the concordance correlation coefficient [211] employed to compare the resultant moments. Specifically, 400 Tchebichef moments were used and the corresponding concordance correlation coefficients are listed in Table 7-2 where it is seen that Kriging regression with error estimation shows superior correlation with the analytical solution than does the subset-based DIC method. From the results in Figure 7–13 and Figure 7–14 and Table 7-2, it can be seen that superior results are achieved using Kriging regression with local error estimation, reducing the difference between the estimated strain field and the analytical solution. The DIC measurement error is reduced by post-processing with local Kriging regression.
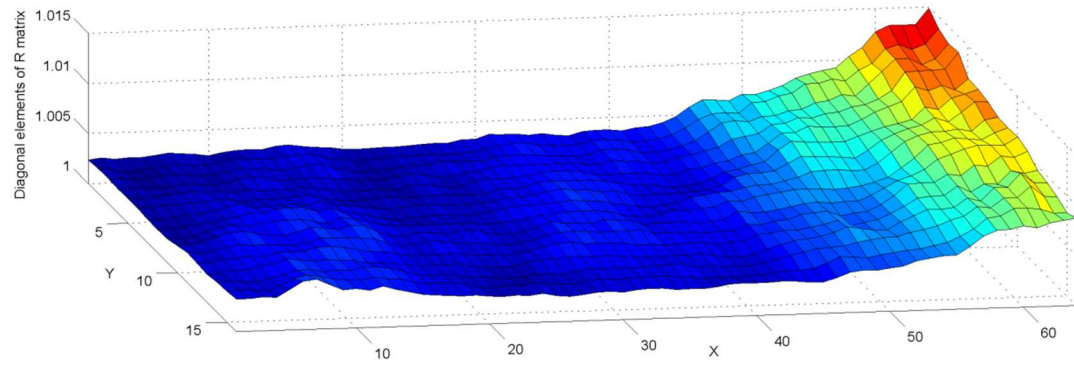
(a) Test 1
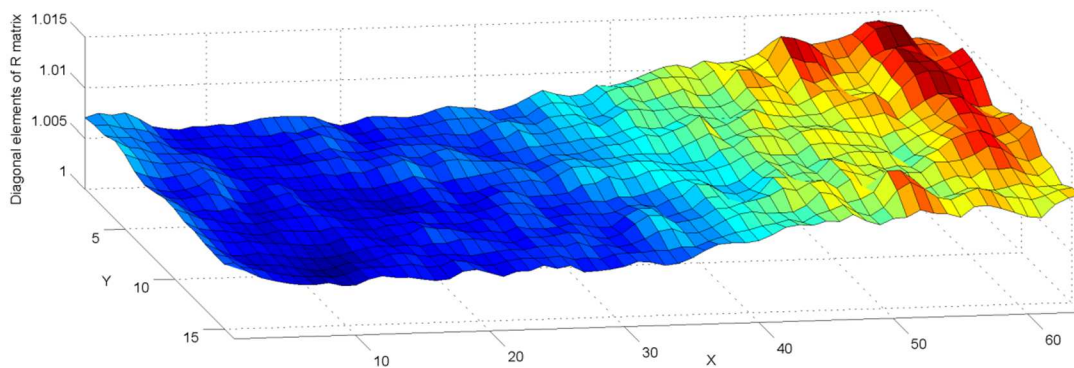
(b) Test 2

Figure 7–11. Diagonal elements of the optimized R matrix (16×64 centre nodes) in (a) Test 1, (b) Test 2

In order to quantify the uncertainty on strain results, a multivariate Gaussian sampling technique [212] described in Section 5.5 can be applied based on the Kriging mean values and covariance matrix [182] to generate a series of random samples of the displacement field. For reasons of reducing the computational cost, 3 local regions were selected on the cantilever beam labelled A, B and C in Figure 7–15. Each region contains 6×6 sample point and a further 1030 uniformly distributed new untried points. 10,000 displacement fields were generated and the corresponding strain fields calculated by the finite difference method which was also used to compute the gradients of the densely sampled displacement field. Finally the

strain field uncertainty in the local region was determined in terms of the standard deviation.

Figure 7–16 illustrates the standard deviation of the strain results of the 3 chosen local regions. In Figure 7–17 the estimated probability densities and the corresponding 95% confidence intervals of the strains are illustrated at 3 chosen points (labelled a, b and c, one each in the 3 local regions as shown in Figure 7–15). It is found that the greatest uncertainty appears at point c, close to the loading point. The strain at point b at mid-span and on the neutral axis is the most confidently predicted.

7.5 Discussion

As shown in Figure 7–13 and Figure 7–14, applying the proposed local Kriging regression method to the displacement data obtained by the classical subset-based DIC significantly improves the accuracy of the estimated displacement and strain fields. Also, the Gaussian process, which forms part of the Kriging model, allows for UQ on estimated displacement and strain fields. There is, however, a penalty to be paid for such improvements, in terms of computational cost. This might be reduced by using the two fast algorithms, FMLE and FSV [191] as discussed in Section 5.3.3, to accelerate the optimisation process in the Kriging local method without loss of accuracy.
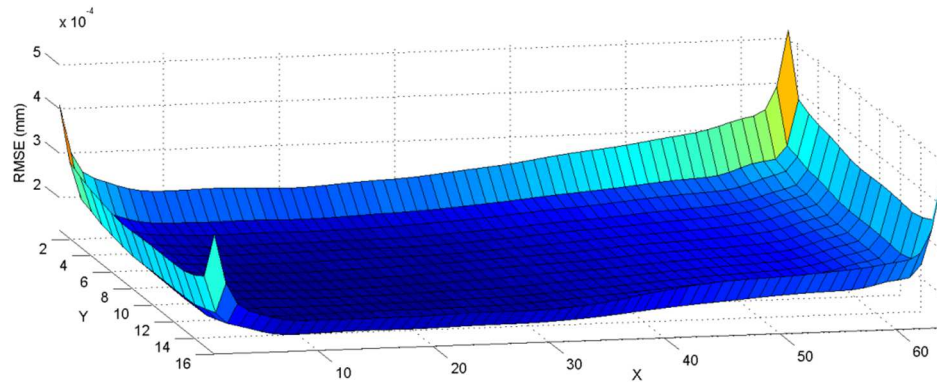
(a) Test 1
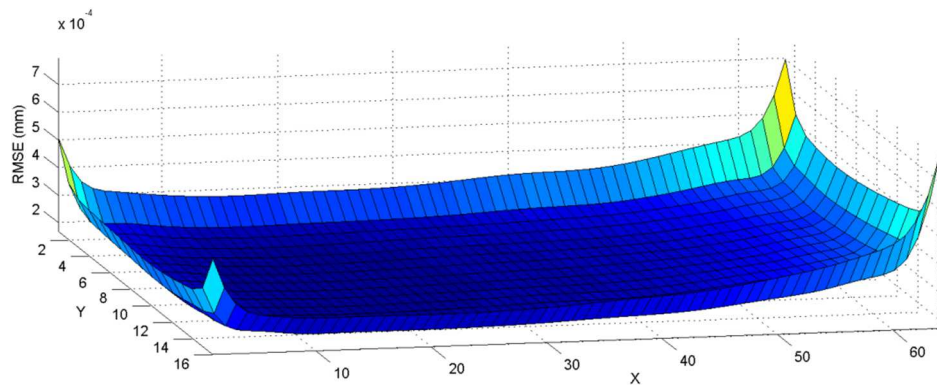
(b) Test 2

Figure 7–12. RMSE on the mean Kriging estimate of the displacement field (*y*-direction): (a) Test 1; (b) Test 2.

For the second case study (constant strain and Gaussian noise), the calculated strain results based on the Kriging gradients were found to be better than the strain results based on local-fitting gradients when a small strain calculation window, smaller than 9×9, was chosen, but slightly worse for large strain calculation windows greater than 9×9. There were found to be small, not very significant differences observed in the strain results calculated by Kriging gradients and locally fitted gradients for the experimental cantilever-beam case study (Figure 7–13(c) and (d) and Figure 7–14(c) and (d)).

Table 7–2: Concordance correlation coefficient based on Tchebichef shape decomposition for the strain fields in *x-x*

	Test 1	Test 2
Subset-based DIC PLS 21×21 strain window	0.9131	0.9327
Kriging global method PLS 21×21 strain window	0.9579	0.9520
Kriging local method PLS 21×21 strain window	0.9733	0.9783
Kriging local method using Kriging gradients	0.9703	0.9795

(a)　　　　　　　　　　　　　　(b)

(c)　　　　　　　　　　　　　　(d)
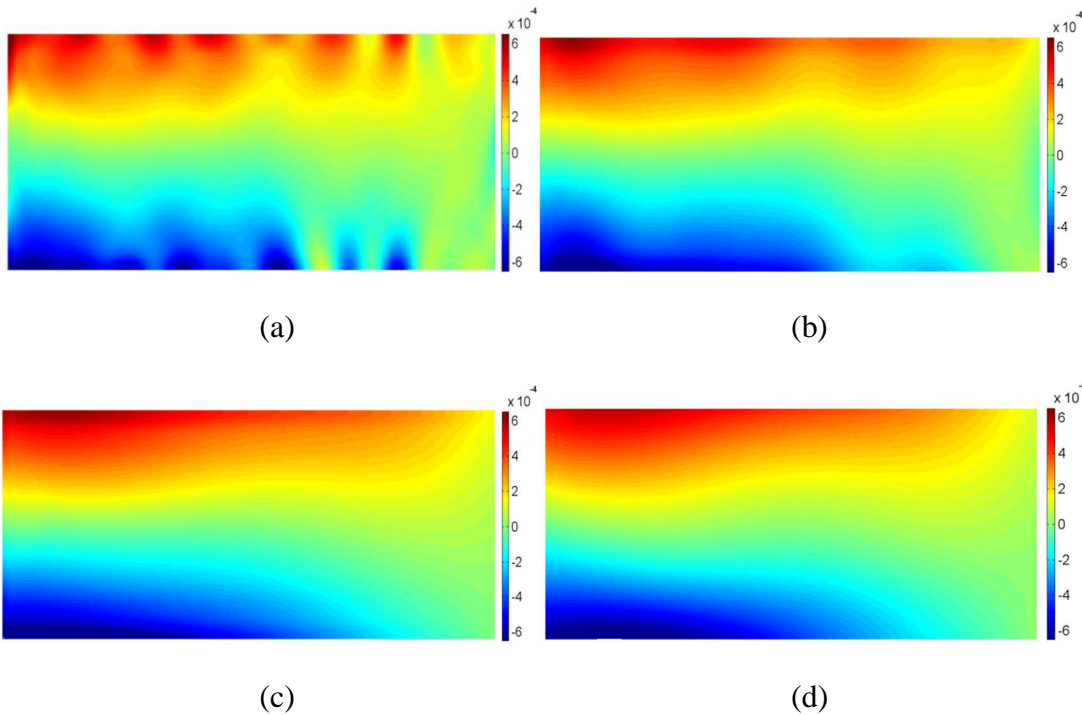
Figure 7–13. Test 1 *x-x* strain field: (a) subset-based DIC using 21×21 strain window; (b) Kriging global method using 21×21 strain window; (c) Kriging local method using 21×21 strain window. (d) Kriging local method using Kriging gradients
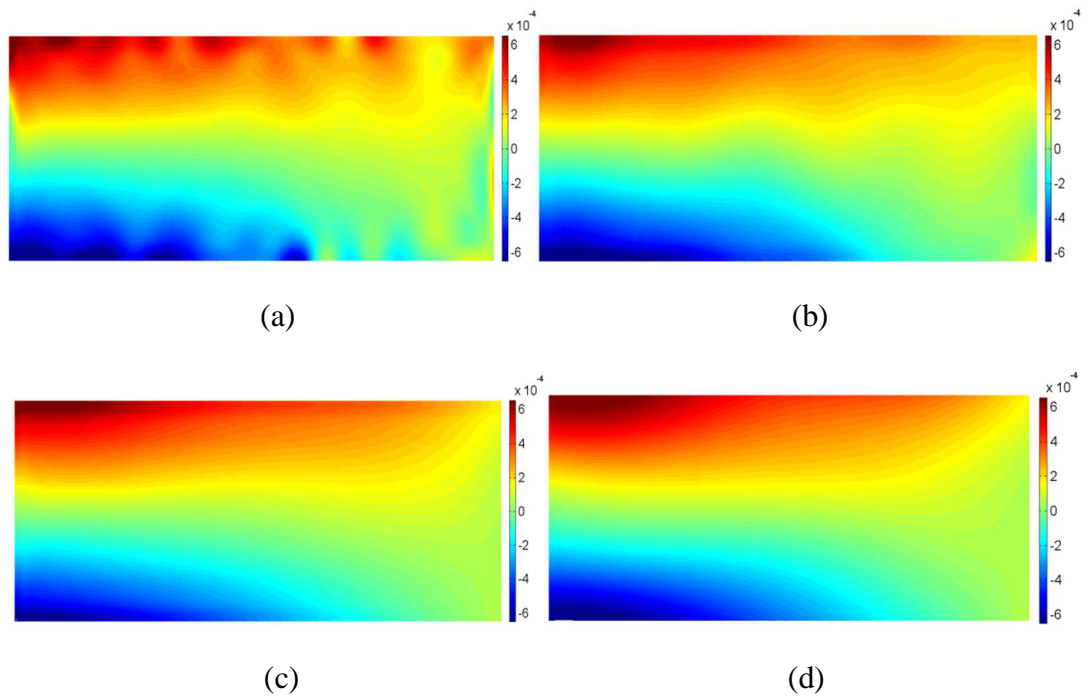
Figure 7–14. Test 2 *x-x* strain field: (a) subset-based DIC using 21×21 strain window; (b) Kriging global method using 21×21 strain window; (c) Kriging local method using 21×21 strain window. (d) Kriging local method using Kriging gradients
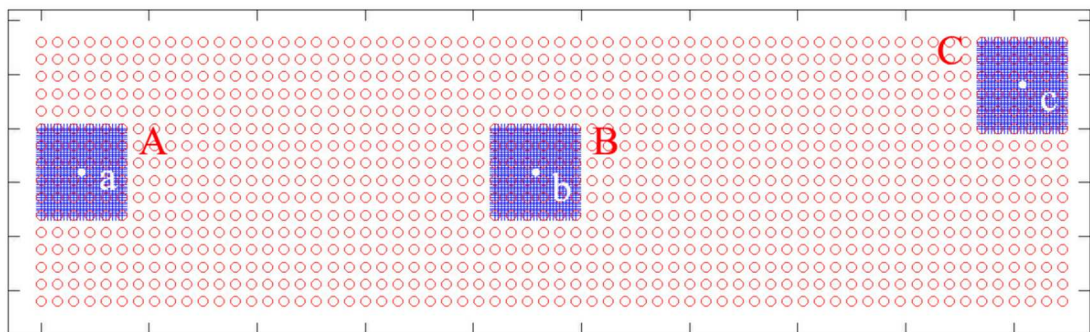
Figure 7–15. 3 local regions (A, B and C) are chosen on the beam in Test 2; each region contains 6×6 sample points shown as red 'o' markers and other 1030 uniformly distributed new predicted points shown as blue '+' markers; a, b and c are the points chosen from the same location of the 3 regions
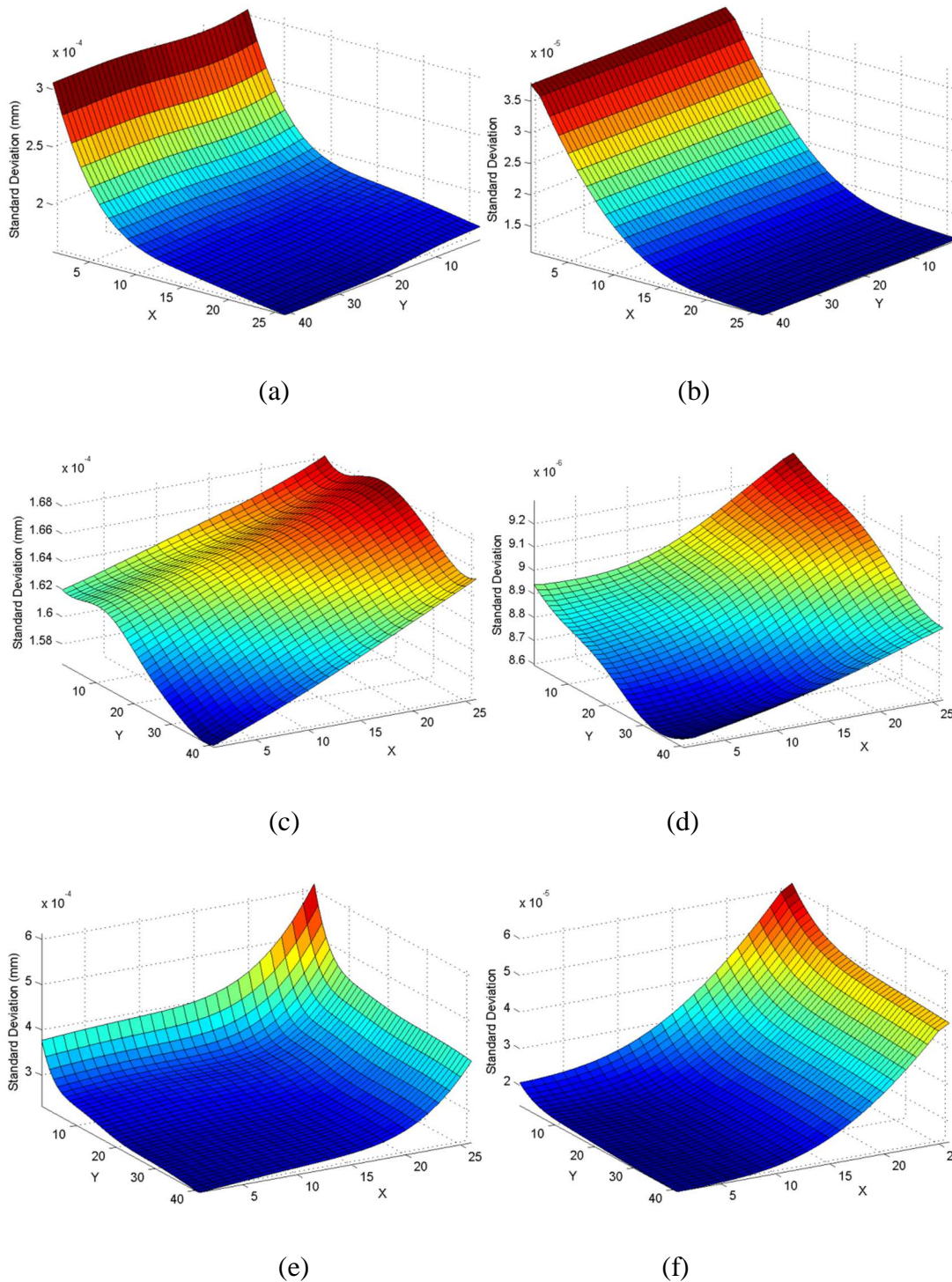
Figure 7–16. Displacement STD (x direction) shown in (a), (c) and (e) and Strain STD (x-x direction) shown in (b), (d) and (f) based on 10,000 random samples of the displacement field in Test 2, from top to bottom: Region A, Region B and Region C
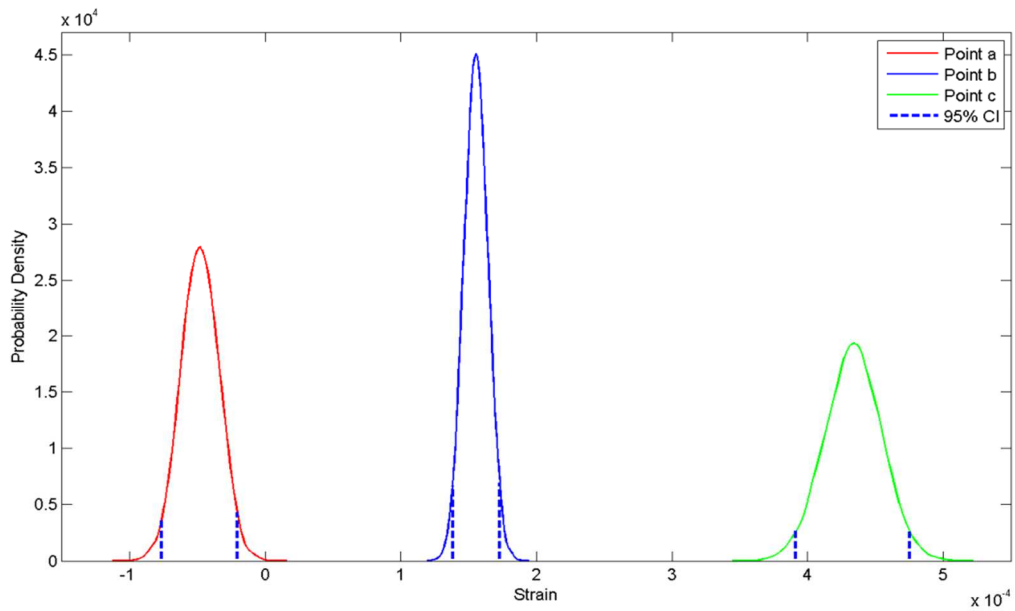
Figure 7–17. The probability density for the strains and 95% confidence interval of the 3 chosen points in the 3 regions respectively

7.6 Closure

A subset-by-subset approximation of DIC measurement error is derived and introduced into the leading-diagonal terms of the Kriging correlation matrix. This leads to a Kriging regression with local error estimation based on diagonal elements of the inverse Hessian matrix and SSD residual, for the post-processing of measured data produced by the subset-based DIC. Unlike spline or other interpolation methods, the proposed approach not only allows for regression of the model upon the measured data, but also incorporates a Gaussian process that enables RMSEs and STDs to be determined on the estimated displacement and strain fields. The methodology is supported by both numerical and experimental case studies. All the case studies show that the proposed Kriging local method out-performs the Kriging

global method and is able to improve the accuracy of measured subset-based DIC data and achieve more accurate strain results.

8

Conclusions and Future Studies

8.1 Conclusions

In this thesis, the problem of DIC error reduction and uncertainty quantification is addressed. As a non-contact optical full-field measurement technique, DIC measurement accuracy is subject to various kinds of error sources and experimental setups. The research presented in this thesis attempts to apply the Kriging regression method to deal with DIC measurement errors. It aims to develop methods that are capable of including measurement errors for a global optimum and quantifying measurement uncertainty. Accordingly, two useful applications of Kriging regression method in DIC are developed, they are, a new global DIC algorithm known as Kriging-DIC and a Kriging-based method for uncertainty quantification of the subset-based DIC measurement.

i. **Kriging-DIC method:** In order to formulate full-field displacement in a more accurate realisation of unknown true displacement field, a Kriging regression model is integrated into the global DIC framework as a full-field

shape function. The lack of knowledge of true displacement field is actually modelled by a Gaussian random process resulting in a Kriging model as a best linear unbiased prediction. Considering the measurement errors of control points, a regularisation technique in a global sense is utilized to further improve the accuracy of Kriging model, which also yields an approximation method to quantify displacement errors of control points. In addition, a strategy of self-adaptive control grid updating was developed based on the estimated MSE produced by the Kriging formula for properly distributing control points and causing the control grid to converge to an optimal density. This self-adaptive strategy also enables the Kriging-DIC method to become an unsupervised and versatile method, which eliminates the need to select DIC parameters (e.g. subset size, number of control points). Compared with other global DIC methods (e.g. FE-DIC and Spline-DIC), Kriging-DIC applies a more flexible control grid that is not necessarily regular or uniform, which gives Kriging-DIC greater adaptability for measurement on complex geometries.

The robustness of Kriging DIC is demonstrated using experimental and numerically-produced data in four case studies. In the first case study, a comparison is made between Kriging DIC and the classical subset-based DIC in terms of displacement resolution and spatial resolution. It is found that Kriging DIC achieves superior displacement resolution than subset-based DIC for the same spatial resolution. It is particularly well suited to low spatial frequency deformation where good displacement resolution is required. For higher spatial frequencies, the resolution of the imaging system (camera resolution) should be improved. By using experimental data from

DIC Challenge 2D database in the second case study, Kriging-DIC is shown to outperform Q4-FE DIC and Cubic Spline DIC in a full-field displacement measurement. In the third case study Kriging DIC is found to be robust to the number and location of initially-chosen control points and to speckle-pattern variations. Furthermore, Kriging DIC is shown to be favourably superior to a commercial subset-based DIC system through an experimental example based on an I-section beam test.

ii. **Kriging-based uncertainty quantification method:** The global error regularisation technique adopted in Kriging-DIC method accounts for the measurement error that is assumed to be independent and identically distributed across the entire RoI, which offers excellent error reduction properties but is still limited in respect to the fact that measurement errors are generally different from location to location. This limitation is then overcome by developing a more sophisticated local error regularisation technique incorporating Kriging regression in a post-processing approach using a local error estimate derived from the DIC algorithm. Inspired by the studies of subset-based error estimate due to Gaussian image noise, a more general expression for the local error estimate due to various error sources is derived as a function of the inverse of the Hessian matrix and the residual of SSD criterion. Based on the subset-based DIC measurement, the Kriging regression method was developed to account for the local error estimate and further quantify the uncertainty of the measured displacement field and strain field. The local error regularisation technique is implemented by using an error factor to formulate the measurement error in a local sense (subset by

subset) and introducing an error factor into the leading diagonal terms of Kriging correlation matrix. The results of numerical studies show that displacement accuracy has been significantly improved based on the proposed method.

In regard to strain calculations, a method is proposed by using the gradients calculated directly from the Kriging regression model known as Kriging gradients. It is shown that strain results computed by the Kriging gradients are comparable to those computed by a state-of-the-art local fitting algorithm, namely the PLS algorithm, with an optimal size of strain window.

The displacement field uncertainty can be directly quantified as the root mean square error (RMSE) based on the Kriging regression model. However, the quantified displacement uncertainty is difficult to be propagated in order to determine the strain uncertainty, since strain results are calculated from displacement gradients. As the Kriging regression model can be deemed as a multivariate Gaussian process, it is possible to carry out a sampling process of the displacement field to estimate the strain uncertainty, which was developed based on Cholesky decomposition of the covariance matrix extracted from the Kriging formula. Additional uncertainty may be introduced by the gradient calculation, and is reduced by using a classical Finite Difference (FD) technique that can be justified scientifically. Finally the standard deviation (STD) and 95% confidence interval (CI) are determined to illustrate the strain uncertainty. The performance of the proposed method is verified by both numerical and experimental case studies. All the case studies show that the proposed Kriging regression method with local error estimate out-performs the Kriging method with global error

estimate and is able to improve the accuracy of displacement and strain results of the subset-based DIC and quantify the corresponding displacement and strain uncertainties.

In summary, the Kriging-DIC method is a promising global DIC algorithm incorporating the regularisation of measurement error and a self-adaptive grid updating strategy. It is able to achieve an excellent performance in noise robustness and error reduction. On the other hand, Kriging-based uncertainty quantification method offers a new way to integrate the local measurement error of subset-based DIC into a global uncertainty quantification model. This post-processing technique not only improves the measurement accuracy of subset-based DIC but also quantifies the corresponding displacement and strain uncertainties.

8.2 Future studies

Although the proposed methods in this thesis have shown the effectiveness to reduce DIC measurement errors and quantify the uncertainties, there are still some deficiencies that restrain the methods to be used for a wide range of applications. Therefore, a further study into the limitations of the proposed methods could lead to an improvement in prospective applications. In the following, three main complements to the existing study in this thesis might be recommended and should be beneficial for further research:

i. **Extension to 3D DIC and Digital Volume Correlation (DVC):** So far, the developed Kriging-DIC method and Kriging-based uncertainty quantification method are still limited to 2D-DIC. However, there is no difficulty to extend the current methods to three dimensions since basic concepts and algorithms

are exactly the same in 3D-DIC. Digital images of a common object region in 3D-DIC are recorded from two or more viewpoints by a typical stereo-vision system that employs two or more cameras. The Kriging-DIC method can be used to perform cross-camera subset matching under a stereo-vision calibration procedure. However, it is noted that extra uncertainty introduced by 3D calibration should be quantified and combined with the uncertainty quantified by the Kriging-based method in the application of 3D-DIC.

Similarly, the Kriging methods can also be developed to Digital Volume Correlation (DVC). DVC primarily requires an imaging system capable of acquiring 3D digital images of a specimen. For this purpose, X-ray tomography, Confocal Microscopy (CM), and Scattered Light are normally popular techniques used in the literature [213]. However, problems related to image acquisition, image storage and computation in DVC have non-trivial effect on the DIC accuracy [18]. Thus further research needs to be carried out to fully consider these above practical issues in order to successfully extend the Kriging methods to DVC.

ii. **Adaptation to discontinuities and high spatial frequency deformations:**

The developed Kriging-DIC approach was based on a continuous formulation for the measuring displacement field. In addition, the correlation function applied in the Kriging regression is Gaussian in this thesis, which relies on the assumption that the displacement field to be measured is smooth without significant discontinuities e.g. fractures and cracks. Thus the resulting displacement measurements are not reliable in the vicinity of a discontinuity. In practical applications, extra criterion could be added to

Kriging-DIC to identify discontinuities and allow the control grid to be accordingly adjusted. Penalty functions can be employed to detect discontinuities, for example, (1) by measuring the distance between the estimated displacement field and its projection [108]; (2) by using an equivalent strain [10] on the detection of intense shear; (3) by utilising the poor correlation coefficients [97]. On the other hand, adjustments can be conducted to account for the discontinuous displacement field once some discontinuities are identified. Specifically, it might be implemented by separating the control grid at discontinuous locations to exclude the discontinuous areas and adding extra DoF to Kriging shape function.

Moreover, high spatial frequency displacement fields are challenging for Kriging-DIC. For example, in the testing of carbon-fibre-reinforced composite material, the displacement field normally is not smooth but significantly irregular. In that case, other types of correlation functions instead of Gaussian might be applied to adapt to this specific displacement behaviour.

iii. **Extension of the Kriging uncertainty quantification method through Bayesian framework**: Kriging regression method applied in this thesis stems from Universal Kriging (UK) obtained by an optimisation process and equivalent to a Bayesian formulation with non-informative priors and Gaussian posterior [194]. Though this assumption is generally reasonable for most cases and frequently correct, it may slightly underestimate the uncertainty of measurement results for some cases. However, other types of prior distributions can also be employed, whereas the Bayesian Kriging [169,

194] is actually utilized to carry out a more sophisticated uncertainty analysis. In this sense, improvement could be made through choosing proper priors for Kriging parameters with respect to a specific application, by which measurement uncertainty might be quantified more accurately. Also it normally requires a Markov Chain Monte Carlo (MCMC) simulation to sample the posterior distributions of all Kriging parameters, which however inevitably increases the computational cost compared with the usage of Universal Kriging.

To summarise, the introduction of Kriging regression to DIC turns out to be a meaningful attempt to deal with DIC measurement error and uncertainty especially in both global and local senses. Future developments of this application should continue to focus on improving its performance in challenging applications and adaptability for a wide range of practical problems.

Appendix A

Intensity Interpolation Scheme

Since the grey values at the non-integer locations are normally required in the DIC process, it is necessary to utilise a grey-intensity interpolation method. In this part, the classical 4×4 bi-cubic interpolation algorithm is introduced. Alternatively more sophisticated interpolation schemes may be found in [37].

With the purpose of reconstructing a continuous 2-D grey signal $\lambda_*(x, y)$ ($\lambda_*, x, y \in \mathbb{R}$) based on its discrete samples at integer locations $\lambda_*(s,t)$ ($s,t \in \mathbb{N}$), image interpolation may be implemented through the convolution [37, 74] of the discrete image samples with the continuous 2-D impulse response $_{2D}\psi(x, y)$ of a reconstruction filter [37].

$$\lambda_*(x, y) = \sum_s \sum_t {}_{2D}\psi(x - s, y - t) \cdot \lambda_*(s,t) \qquad \text{(A-1)}$$

In order to reduce the computational complexity, symmetrical and separable interpolation kernels are applied, resulting in:

$$_{2D}\psi(x, y) = \psi(x) \cdot \psi(y) \qquad \text{(A-2)}$$

The 4×4 bi-cubic interpolation is implemented by interpolating the point (x, y) in a 4×4 neighbourhood. The following 1-D kernel functions $\psi(b_0)$ and derivative kernel functions $\psi'(b_0)$ are actually employed:

$$\psi(b_0) = \begin{cases} (a_0 + 2)|b_0|^3 - (a_0 + 3)|b_0|^2 + 1 & for \ |b_0| \le 1 \\ a_0|b_0|^3 - 5a_0|b_0|^2 + 8a_0|b_0| - 4a_0 & for \ 1 < |b_0| \le 2 \\ 0 & otherwise \end{cases} \quad \text{(A-3)}$$

$$\psi'(b_0) = \begin{cases} -3a_0 b_0^2 + 10a_0 b_0 - 8a_0 & for \ -2 \le b_0 < -1 \\ -3(a_0 + 2)b_0^2 + 2(a_0 + 3)b_0 & for \ -1 \le b_0 < 0 \\ 3(a_0 + 2)b_0^2 - 2(a_0 + 3)b_0 & for \ 0 \le b_0 \le 1 \\ 3a_0 b_0^2 - 10a_0 b_0 + 8a_0 & for \ 1 < b_0 \le 2 \\ 0 & otherwise \end{cases} \quad \text{(A-4)}$$

where b_0 denotes the location coordinate in x- or y-direction within the 4×4 neighbourhood. Also it has been shown that cubic interpolation with $a_0 = -0.5$ can reconstruct any second-degree polynomial [37], which is optimal for most digital images [214]. Thus $a_0 = -0.5$ is used in this application.

As explained in Section 4.2.3, $\boldsymbol{\tau}_s^2 = [u_s \quad v_s]$ and $\boldsymbol{\tau}_s^1 = [u_d \quad v_d]$ respectively represent the integer parts and the fractional parts of the interpolated location $\boldsymbol{\tau}_s$ including both x- and y-directional components. $\lambda_*(\boldsymbol{\tau}_s)$ denotes the interpolated displacement value at $\boldsymbol{\tau}_s$ while $\lambda_*(\boldsymbol{\tau}_s^2)$ is the vector including grey values of the pixels at the neighbouring 4×4 integer locations. Then the 4×4 bi-cubic interpolation can be expressed in terms of the convolution kernels $\boldsymbol{\psi}_x = [\psi_{1x} \quad \psi_{2x} \quad \psi_{3x} \quad \psi_{4x}]$ and $\boldsymbol{\psi}_y = [\psi_{1y} \quad \psi_{2y} \quad \psi_{3y} \quad \psi_{4y}]$ in x- and y-directions respectively:

$$\lambda_*(\boldsymbol{\tau}_s) = \boldsymbol{\psi}_x(\boldsymbol{\tau}_s^1)\begin{bmatrix} \lambda_*(u_s-1,v_s-1) & \lambda_*(u_s,v_s-1) & \cdots & \lambda_*(u_s+2,v_s-1) \\ \lambda_*(u_s-1,v_s) & & & \vdots \\ \vdots & & \ddots & \\ \lambda_*(u_s-1,v_s+2) & \cdots & & \lambda_*(u_s+2,v_s+2) \end{bmatrix}_{4\times4} \cdot \boldsymbol{\psi}_y^T(\boldsymbol{\tau}_s^1)$$

$$= \begin{bmatrix} \psi_{1x}\psi_{1y} & \psi_{1x}\psi_{2y} & \psi_{1x}\psi_{3y} & \cdots & \psi_{2x}\psi_{1y} & \cdots & \psi_{4x}\psi_{4y} \end{bmatrix} \begin{bmatrix} \lambda_*(u_s-1,v_s-1) \\ \lambda_*(u_s-1,v_s) \\ \lambda_*(u_s-1,v_s+1) \\ \vdots \\ \lambda_*(u_s,v_s-1) \\ \vdots \\ \lambda_*(u_s+2,v_s+2) \end{bmatrix} \qquad \text{(A-5)}$$

$$= \boldsymbol{\psi}(\boldsymbol{\tau}_s^1)\cdot\boldsymbol{\lambda}_*(\boldsymbol{\tau}_s^2)$$

where
$$\begin{aligned}
\psi_{1x} &= \psi(u_d+1) & \psi_{1y} &= \psi(v_d+1) \\
\psi_{2x} &= \psi(u_d) & \psi_{2y} &= \psi(v_d) \\
\psi_{3x} &= \psi(u_d-1) & \psi_{3y} &= \psi(v_d-1) \\
\psi_{4x} &= \psi(u_d-2) & \psi_{4y} &= \psi(v_d-2)
\end{aligned}.$$

Similarly the grey gradients $\lambda_*'(\boldsymbol{\tau}_s)$ at $\boldsymbol{\tau}_s$ in x- and y-directions can be derived by using the derivative kernel functions as:

$$\lambda_*'(\boldsymbol{\tau}_s) = \begin{cases} \boldsymbol{\psi}_x'(\boldsymbol{\tau}_s^1)\cdot\boldsymbol{\lambda}_*(\boldsymbol{\tau}_s^2) \\ \boldsymbol{\psi}_y'(\boldsymbol{\tau}_s^1)\cdot\boldsymbol{\lambda}_*(\boldsymbol{\tau}_s^2) \end{cases} \qquad \text{(A-6)}$$

where
$$\begin{cases} \boldsymbol{\psi}_x'(\boldsymbol{\tau}_s^1) = \begin{bmatrix} \psi_{1x}'\psi_{1y} & \psi_{1x}'\psi_{2y} & \psi_{1x}'\psi_{3y} & \cdots & \psi_{2x}'\psi_{1y} & \cdots & \psi_{4x}'\psi_{4y} \end{bmatrix} \\ \boldsymbol{\psi}_y'(\boldsymbol{\tau}_s^1) = \begin{bmatrix} \psi_{1x}\psi_{1y}' & \psi_{1x}\psi_{2y}' & \psi_{1x}\psi_{3y}' & \cdots & \psi_{2x}\psi_{1y}' & \cdots & \psi_{4x}\psi_{4y}' \end{bmatrix} \end{cases} \text{with}$$

$$\begin{aligned}
\psi_{1x}' &= \psi'(u_d+1) & \psi_{1y}' &= \psi'(v_d+1) \\
\psi_{2x}' &= \psi'(u_d) & \psi_{2y}' &= \psi'(v_d) \\
\psi_{3x}' &= \psi'(u_d-1) & \psi_{3y}' &= \psi'(v_d-1) \\
\psi_{4x}' &= \psi'(u_d-2) & \psi_{4y}' &= \psi'(v_d-2)
\end{aligned}.$$

According to Equation (A-5) and (A-6), the terms $\eta_x(\boldsymbol{\tau}_s^1) \cdot N^2 \sigma_\zeta^2$ and $\eta_y(\boldsymbol{\tau}_s^1) \cdot N^2 \sigma_\zeta^2$

shown in Equation (4-27) can be derived from the related terms shown in Equation

(4-26). For the sake of simplicity, only the necessary terms are extracted from

Equation (4-26) to produce the derivation expressed as:

$$
\begin{aligned}
& \mathrm{E}\begin{pmatrix} \displaystyle\sum_{s=1}^{N\times N} \boldsymbol{\psi}_x'(\boldsymbol{\tau}_s^1) \cdot \hat{\boldsymbol{\zeta}}_\mathbf{g}\left(\boldsymbol{\tau}_s^2\right) \cdot \boldsymbol{\psi}(\boldsymbol{\tau}_s^1) \cdot \hat{\boldsymbol{\zeta}}_\mathbf{g}\left(\boldsymbol{\tau}_s^2\right) \\ \displaystyle\sum_{s=1}^{N\times N} \boldsymbol{\psi}_y'(\boldsymbol{\tau}_s^1) \cdot \hat{\boldsymbol{\zeta}}_\mathbf{g}\left(\boldsymbol{\tau}_s^2\right) \cdot \boldsymbol{\psi}(\boldsymbol{\tau}_s^1) \cdot \hat{\boldsymbol{\zeta}}_\mathbf{g}\left(\boldsymbol{\tau}_s^2\right) \end{pmatrix} \\
& \cong \mathrm{E}\begin{pmatrix} \boldsymbol{\psi}_x'(\boldsymbol{\tau}_s^1) \cdot \left(\boldsymbol{\psi}(\boldsymbol{\tau}_s^1)\right)^{\mathrm{T}} \cdot \displaystyle\sum_{s=1}^{N\times N}\left(\hat{\boldsymbol{\zeta}}_\mathbf{g}\left(\boldsymbol{\tau}_s^2\right)\right)^2 \\ \boldsymbol{\psi}_y'(\boldsymbol{\tau}_s^1) \cdot \left(\boldsymbol{\psi}(\boldsymbol{\tau}_s^1)\right)^{\mathrm{T}} \cdot \displaystyle\sum_{s=1}^{N\times N}\left(\hat{\boldsymbol{\zeta}}_\mathbf{g}\left(\boldsymbol{\tau}_s^2\right)\right)^2 \end{pmatrix} \qquad (\text{A-7}) \\
& \cong \begin{pmatrix} \eta_x(\boldsymbol{\tau}_s^1) \cdot N^2 \sigma_\zeta^2 \\ \eta_y(\boldsymbol{\tau}_s^1) \cdot N^2 \sigma_\zeta^2 \end{pmatrix}
\end{aligned}
$$

where

$$
\begin{cases}
\eta_x(\boldsymbol{\tau}_s^1) \cong \boldsymbol{\psi}_x'(\boldsymbol{\tau}_s^1) \cdot \left(\boldsymbol{\psi}(\boldsymbol{\tau}_s^1)\right)^{\mathrm{T}} \\
\qquad = \left(\psi_{1x}\psi_{1y}\psi_{1x}'\psi_{1y} + \psi_{1x}\psi_{2y}\psi_{1x}'\psi_{2y} + \psi_{1x}\psi_{3y}\psi_{1x}'\psi_{3y} + \cdots \psi_{2x}\psi_{1y}\psi_{2x}'\psi_{1y} + \cdots \psi_{4x}\psi_{4y}\psi_{4x}'\psi_{4y}\right) \\
\eta_y(\boldsymbol{\tau}_s^1) \cong \boldsymbol{\psi}_y'(\boldsymbol{\tau}_s^1) \cdot \left(\boldsymbol{\psi}(\boldsymbol{\tau}_s^1)\right)^{\mathrm{T}} \\
\qquad = \left(\psi_{1x}\psi_{1y}\psi_{1x}\psi_{1y}' + \psi_{1x}\psi_{2y}\psi_{1x}\psi_{2y}' + \psi_{1x}\psi_{3y}\psi_{1x}\psi_{3y}' + \cdots \psi_{2x}\psi_{1y}\psi_{2x}\psi_{1y}' + \cdots \psi_{4x}\psi_{4y}\psi_{4x}\psi_{4y}'\right)
\end{cases}
$$

Reference

[1]   Chu TC, Ranson WF, Sutton MA, Peters WH. Applications of Digital-Image-Correlation Techniques to Experimental Mechanics. Experimental Mechanics 1985; 25(3): 232-244.

[2]   Bruck HA, McNeill SR, Sutton MA, Peters WH. Digital Image Correlation Using Newton-Raphson Method of Partial-Differential Correction. Experimental Mechanics 1989; 29(3): 261-267.

[3]   Peters WH, Ranson WF. Digital Imaging Techniques in Experimental Stress-Analysis. Optical Engineering 1982; 21(3): 427-431.

[4]   Sutton MA, Wolters WJ, Peters WH, Ranson WF, McNeill SR. Determination of displacements using an improved digital correlation method. Image Vision Computatin 1983; 1(3): 133-139.

[5]   Sutton MA, Orteu JJ, Schreier HW. Image correlation for shape, motion and deformation measurements : basic concepts, theory and applications. New York, N.Y.: Springer; 2009.

[6]   Passieux JC, Bugarin F, David C, Perie JN, Robert L. Multiscale Displacement Field Measurement Using Digital Image Correlation: Application to the Identification of Elastic Properties. Experimental Mechanics 2015; 55(1): 121-137.

[7]   Gates M, Lambros J, Heath MT. Towards High Performance Digital Volume Correlation. Experimental Mechanics 2011; 51(4): 491-507.

[8]   Hild F, Roux S. Comparison of Local and Global Approaches to Digital Image Correlation. Experimental Mechanics 2012; 52(9): 1503-1519.

[9]   Sun YF, Pang JHL, Wong CK, Su F. Finite element formulation for a digital image correlation method. Applied Optics 2005; 44(34): 7357-7363.

[10]   Rethore J, Hild F, Roux S. Shear-band capturing using a multiscale extended digital image correlation technique. Computer Methods in Applied Mechanics and Engineering 2007; 196(49-52): 5016-5030.

[11]   Besnard G, Hild F, Roux S. "Finite-Element" displacement fields analysis from digital images: Application to portevin-le chatelier bands. Experimental Mechanics 2006; 46(6): 789-803.

[12]   Moes N, Dolbow J, Belytschko T. A finite element method for crack growth without remeshing. International Journal for Numerical Methods in Engineering 1999; 46(1): 131-150.

[13]   Rethore J, Gravouil A, Morestin E, Combescure A. Estimation of mixed-mode stress intensity factors using digital image correlation and an interaction integral. International Journal of Fracture 2005; 132(1): 65-79.

[14]   Wagne B, Roux S, Hild F. Spectral approach to displacement evaluation from image analysis. European Physical Journal-Applied Physics 2002; 17(3): 247-252.

[15]   Mortazavi F, Levesque M, Villemure I. Image-based Continuous Displacement Measurements Using an Improved Spectral Approach. Strain 2013; 49(3): 233-248.

[16]   Roux S, Hild F, Berthaud Y. Correlation image velocimetry: a spectral approach. Applied Optics 2002; 41(1): 108-115.

[17]   Cheng P, Sutton MA, Schreier HW, McNeill SR. Full-field speckle pattern image correlation with B-spline deformation function. Experimental Mechanics 2002; 42(3): 344-352.

[18]   Mortazavi F. Development of a global digital image correlation approach for fast high-resolution displacement measurements. 2013, École Polytechnique de Montréal, : Montreal.

[19]   Wittevrongel L, Lava P, Lomov SV, Debruyne D. A Self Adaptive Global Digital Image Correlation Algorithm. Experimental Mechanics 2015; 55(2): 361-378.

[20]   Pan B, Xie HM, Xu BQ, Dai FL. Performance of sub-pixel registration algorithms in digital image correlation. Measurement Science & Technology 2006; 17(6): 1615-1621.

[21]   Crammond G, Boyd SW, Dulieu-Barton JM. Speckle pattern quality assessment for digital image correlation. Optics and Lasers in Engineering 2013; 51(12): 1368-1378.

[22]   Pan B, Xie HM, Wang ZY, Qian KM, Wang ZY. Study on subset size selection in digital image correlation for speckle patterns. Optics Express 2008; 16(10): 7037-7048.

[23]   Wang YQ, Sutton MA, Bruck HA, Schreier HW. Quantitative Error Assessment in Pattern Matching: Effects of Intensity Pattern Noise, Interpolation, Strain and Image Contrast on Motion Measurements. Strain 2009; 45(2): 160-178.

[24]   Pan B, Lu ZX, Xie HM. Mean intensity gradient: An effective global parameter for quality assessment of the speckle patterns used in digital image correlation. Optics and Lasers in Engineering 2010; 48(4): 469-477.

[25]   Barranger Y, Doumalin P, Dupre JC, Germaneau A. Strain Measurement by Digital Image Correlation: Influence of Two Types of Speckle Patterns Made from Rigid or Deformable Marks. Strain 2012; 48(5): 357-365.

[26]   Zhang ZY. A flexible new technique for camera calibration. Ieee Transactions on Pattern Analysis and Machine Intelligence 2000; 22(11): 1330-1334.

[27]   Slama CC, Theurer C, Henriksen SW. Manual of photogrammetry. 4th ed. Falls Church, Va.: American Society of Photogrammetry; 1980.

[28]   Weng JY, Cohen P, Herniou M. Camera Calibration with Distortion Models and Accuracy Evaluation. Ieee Transactions on Pattern Analysis and Machine Intelligence 1992; 14(10): 965-980.

[29]   Mazzoleni P. Uncertainty estimation and reduction in digital image correlation measurements. in Department of Mechanical Engineering. 2013, Politecnico Di Milano.

[30]   Holst GC. CCD arrays, cameras, and displays. 2nd ed. Bellingham, Wash., USA: SPIE Optical Engineering; 1998.

[31]   Mazzoleni P, Matta F, Zappa E, Sutton MA, Cigada A. Gaussian pre-filtering for uncertainty minimization in digital image correlation using numerically-designed speckle patterns. Optics and Lasers in Engineering 2015; 66(0): 19-33.

[32]   Pan B. Bias error reduction of digital image correlation using Gaussian pre-filtering. Optics and Lasers in Engineering 2013; 51(10): 1161-1167.

[33]   Pan B, Qian KM, Xie HM, Asundi A. Two-dimensional digital image correlation for in-plane displacement and strain measurement: a review. Measurement Science & Technology 2009; 20(6).

[34] Tong W. An evaluation of digital image correlation criteria for strain mapping applications. Strain 2005; 41(4): 167-175.

[35] Wieneke B, Prevost R. DIC Uncertainty Estimation from Statistical Analysis of Correlation Values. Advancement of Optical Methods in Experimental Mechanics 2014.

[36] Schreier HW, Braasch JR, Sutton MA. Systematic errors in digital image correlation caused by intensity interpolation. Optical Engineering 2000; 39(11): 2915-2921.

[37] Lehmann TM, Gonner C, Spitzer K. Survey: Interpolation methods in medical image processing. Ieee Transactions on Medical Imaging 1999; 18(11): 1049-1075.

[38] Bornert M, Bremand F, Doumalin P, Dupre JC, Fazzini M, Grediac M, et al. Assessment of Digital Image Correlation Measurement Errors: Methodology and Results. Experimental Mechanics 2009; 49(3): 353-370.

[39] Schreier HW, Sutton MA. Systematic errors in digital image correlation due to undermatched subset shape functions. Experimental Mechanics 2002; 42(3): 303-310.

[40] Pan B, Asundi A, Xie HM, Gao JX. Digital image correlation using iterative least squares and pointwise least squares for displacement field and strain field measurements. Optics and Lasers in Engineering 2009; 47(7-8): 865-874.

[41] Zhou YH, Sun C, Song YT, Chen JB. Image pre-filtering for measurement error reduction in digital image correlation. Optics and Lasers in Engineering 2015; 65: 46-56.

[42] Mazzoleni P, Matta F, Zappa E, Sutton MA, Cigada A. Gaussian pre-filtering for uncertainty minimization in digital image correlation using numerically-designed speckle patterns. Optics and Lasers in Engineering 2015; 66: 19-33.

[43] Reu PL, Sutton MA, Wang Y, Miller TJ. Uncertainty quantification for digital image correlation. in Proceedings of the SEM Annual Conference. 2009: Albuquerque New Mexico USA.

[44] Wang P, Pierron F, Thomsen OT, Rossi M, Lava P, *Uncertainty Quantification in VFM Identification*, in *Experimental and Applied Mechanics, Volume 6*, Sottos,Rowlands, Editors. 2015, Springer International Publishing. p. 137-142.

[45]   Rossi M, Lava P, Pierron F, Debruyne D, Sasso M. Effect of DIC Spatial Resolution, Noise and Interpolation Error on Identification Results with the VFM. Strain 2015; 51(3): 206-222.

[46]   Wang ZY, Li HQ, Tong JW, Ruan JT. Statistical analysis of the effect of intensity pattern noise on the displacement measurement precision of digital image correlation using self-correlated images. Experimental Mechanics 2007; 47(5): 701-707.

[47]   Um GJ, Kim HJ. Experimental error assessment for image correlation analysis on a paper tensile specimen. Journal of Industrial and Engineering Chemistry 2007; 13(2): 214-218.

[48]   Tiwari V, Sutton MA, McNeill SR. Assessment of high speed imaging systems for 2D and 3D deformation measurements: Methodology development and validation. Experimental Mechanics 2007; 47(4): 561-579.

[49]   Haddadi H, Belhabib S. Use of rigid-body motion for the investigation and estimation of the measurement errors related to digital image correlation technique. Optics and Lasers in Engineering 2008; 46(2): 185-196.

[50]   Pan B, Qian K, Xie H, Asundi A. On errors of digital image correlation due to speckle patterns. in Proceedings of the international conference on experimental mechanics. 2008. p. z1:z7.

[51]   Ke XD, Schreier HW, Sutton MA, Wang YQ. Error Assessment in Stereo-based Deformation Measurements Part II: Experimental Validation of Uncertainty and Bias Estimates. Experimental Mechanics 2011; 51(4): 423-441.

[52]   Cressie N. The Origins of Kriging. Mathematical Geology 1990; 22(3): 239-252.

[53]   Cressie N. Statistics for spatial data. Rev. ed. Wiley series in probability and mathematical statistics Applied probability and statistics. New York: Wiley; 1993.

[54]   Wikle CK, Berliner LM. A Bayesian tutorial for data assimilation. Physica D-Nonlinear Phenomena 2007; 230(1-2): 1-16.

[55]   Banerjee KS, Carr RN. Ridge Regression - Biased Estimation for Non-Orthogonal Problems. Technometrics 1971; 13(4): 895-&.

[56]   Forrester AIJ, Keane AJ, Bressloff NW. Design and analysis of "Noisy" computer experiments. Aiaa Journal 2006; 44(10): 2331-2339.

[57]   Sutton MA, Orteu J-J, Schreier HW. Image correlation for shape, motion and deformation measurements : basic concepts, theory and applications. New York, N.Y.: Springer; 2009.

[58]   Chen DJ, Chiang FP, Tan YS, Don HS. Digital Speckle-Displacement Measurement Using a Complex Spectrum Method. Applied Optics 1993; 32(11): 1839-1849.

[59]   Antonini M, Barlaud M, Mathieu P, Daubechies I. Image coding using wavelet transform. Ieee Transactions on Image Processing 1992; 1(2): 205-220.

[60]   Bishop CM. Neural networks for pattern recognition. Oxford New York: Oxford University Press; 1995.

[61]   Pan B. Recent Progress in Digital Image Correlation. Experimental Mechanics 2011; 51(7): 1223-1235.

[62]   Aster RC, Borchers B, Thurber CH. Parameter Estimation and Inverse Problems. Parameter Estimation and Inverse Problems 2005; 90: 1-303.

[63]   Wang DZ, DiazDelaO FA, Wang WZ, Mottershead JE. Full-field digital image correlation with Kriging regression. Optics and Lasers in Engineering 2015; 67: 105-115.

[64]   Pilch A, Mahajan A, Chu T. Measurement of whole-field surface displacements and strain using a genetic algorithm based intelligent image correlation method. Journal of Dynamic Systems Measurement and Control-Transactions of the Asme 2004; 126(3): 479-488.

[65]   Jin H, Bruck HA. Pointwise digital image correlation using genetic algorithms. Experimental Techniques 2005; 29(1): 36-39.

[66]   Jin HQ, Bruck HA. Theoretical development for pointwise digital image correlation. Optical Engineering 2005; 44(6).

[67]   Vendroux G, Knauss WG. Submicron deformation field measurements: Part 2. Improved digital image correlation. Experimental Mechanics 1998; 38(2): 86-92.

[68]   Lyons JS, Liu J, Sutton MA. High-temperature deformation measurements using digital-image correlation. Experimental Mechanics 1996; 36(1): 64-70.

[69]   Yoneyama S, Morimoto Y. Accurate displacement measurement by correlation of colored random patterns. Jsme International Journal Series a-Solid Mechanics and Material Engineering 2003; 46(2): 178-184.

[70]   Li XD, Xu WJ, Sutton MA, Mello M. In situ nanoscale in-plane deformation studies of ultrathin polymeric films during tensile deformation using atomic

force microscopy and digital image correlation techniques. Ieee Transactions on Nanotechnology 2007; 6(1): 4-12.

[71]   Rethore J, Elguedj T, Simon P, Coret M. On the Use of NURBS Functions for Displacement Derivatives Measurement by Digital Image Correlation. Experimental Mechanics 2010; 50(7): 1099-1116.

[72]   Passieux JC, Perie JN. High resolution digital image correlation using proper generalized decomposition: PGD-DIC. International Journal for Numerical Methods in Engineering 2012; 92(6): 531-550.

[73]   Baker S, Matthews I. Lucas-Kanade 20 years on: A unifying framework. International Journal of Computer Vision 2004; 56(3): 221-255.

[74]   Baldi A, Bertolino F. Systematic errors due to polynomial interpolation in Digital Image Correlation. Analysis of some interpolating kernels and experimental validation. Speckle 2012: V International Conference on Speckle Metrology 2012; 8413.

[75]   Luu L, Wang ZY, Vo M, Hoang T, Ma J. Accuracy enhancement of digital image correlation with B-spline interpolation. Optics Letters 2011; 36(16): 3070-3072.

[76]   Chen DJ, Chiang FP, Tan YS, Don HS. Digital speckle-displacement measurement using a complex spectrum method. Applied Optics 1993; 32: 1839-1849.

[77]   Sjodahl M, Benckert LR. Electronic Speckle Photography - Analysis of an Algorithm Giving the Displacement with Subpixel Accuracy. Applied Optics 1993; 32(13): 2278-2284.

[78]   Wattrisse B, Chrysochoos A, Muracciole JM, Nemoz-Gaillard M. Analysis of strain localization during tensile tests by digital image correlation. Experimental Mechanics 2001; 41(1): 29-39.

[79]   Jin GC, Yao XF, Bao NK. Applications of speckle metrology to vibration and deformation measurements of electronic devices. Itherm 2000: Seventh Intersociety Conference on Thermal and Thermomechanical Phenomena in Electronic Systems, Vol 2, Proceedings 2000: 253-255.

[80]   Davis CQ, Freeman DM. Statistics of subpixel registration algorithms based on spatiotemporal gradients or block matching. Optical Engineering 1998; 37(4): 1290-1298.

[81]   Zhou P, Goodson KE. Subpixel displacement and deformation gradient measurement using digital image/speckle correlation (DISC). Optical Engineering 2001; 40(8): 1613-1620.

[82]   Zhang J, Jin GC, Ma SP, Meng LB. Application of an improved subpixel registration algorithm on digital speckle correlation measurement. Optics and Laser Technology 2003; 35(7): 533-542.

[83]   Zhang J, Jin GC, Meng LB, Jian LH, Wang AY, Lu SB. Strain and mechanical behavior measurements of soft tissues with digital speckle method. Journal of Biomedical Optics 2005; 10(3).

[84]   Pitter MC, See CW, Somekh MG. Fast subpixel digital image correlation using artificial neural networks. 2001 International Conference on Image Processing, Vol Ii, Proceedings 2001: 901-904.

[85]   Pitter MC, See CW, Somekh MG. Subpixel microscopic deformation analysis using correlation and artificial neural networks. Optics Express 2001; 8(6): 322-327.

[86]   De Bievre P. The 2007 International Vocabulary of Metrology (VIM), JCGM 200:2008 [ISO/IEC Guide 99]: Meeting the need for intercontinentally understood concepts and their associated intercontinentally agreed terms. Clin Biochem 2009; 42(4-5): 246-8.

[87]   Sutton MA. ASTM E2208 Standard Guide for Evaluating Non-Contacting Optical Strain Measurement Systems. 2010.

[88]   Zhao JQ, Zeng P, Pan B, Lei LP, Du HF, He WB, et al. Improved Hermite finite element smoothing method for full-field strain measurement over arbitrary region of interest in digital image correlation. Optics and Lasers in Engineering 2012; 50(11): 1662-1671.

[89]   Rethore J, Hild F, Roux S. Extended digital image correlation with crack shape optimization. International Journal for Numerical Methods in Engineering 2008; 73(2): 248-272.

[90]   Huang J, Pan X, Peng X, Yuan Y, Xiong C, Fang J, et al. Digital Image Correlation with Self-Adaptive Gaussian Windows. Experimental Mechanics 2013; 53(3): 505-512.

[91]   Yuan Y, Huang JY, Fang J, Yuan F, Xiong CY. A self-adaptive sampling digital image correlation algorithm for accurate displacement measurement. Optics and Lasers in Engineering 2015; 65: 57-63.

[92]   Burt PJ YC, Xu X. Local correlation measures for motion analysis: a comparative study. . in Proceedings of IEEE conference on pattern recognition and image processing. 1982. p. 269-274.

[93]   Chiang FP, Wang Q, Lehman F. New developments in full-field strain measurements using speckles. in Nontraditional methods of sensing stress,

strain and damage in materials and structures, STP 1318. 1997, ASTM: Philadelphia, USA. p. 156-169.

[94]   Lu H, Cary PD. Deformation measurements by digital image correlation: Implementation of a second-order displacement gradient. Experimental Mechanics 2000; 40(4): 393-400.

[95]   Zhou YH, Chen YQ. Propagation function for accurate initialization and efficiency enhancement of digital image correlation. Optics and Lasers in Engineering 2012; 50(12): 1789-1797.

[96]   Helm JD. Digital Image Correlation for Specimens with Multiple Growing Cracks. Experimental Mechanics 2008; 48(6): 753-762.

[97]   Poissant J, Barthelat F. A Novel "Subset Splitting" Procedure for Digital Image Correlation on Discontinuous Displacement Fields. Experimental Mechanics 2010; 50(3): 353-364.

[98]   Pan B. Reliability-guided digital image correlation for image deformation measurement. Applied Optics 2009; 48(8): 1535-1542.

[99]   Pan B, Wang ZY, Lu ZX. Genuine full-field deformation measurement of an object with complex shape using reliability-guided digital image correlation. Optics Express 2010; 18(2): 1011-1023.

[100]   Pan B, Wu DF, Xia Y. High-temperature deformation field measurement by combining transient aerodynamic heating simulation system and reliability-guided digital image correlation. Optics and Lasers in Engineering 2010; 48(9): 841-848.

[101]   Pan B, Wu DF, Xia Y. Incremental calculation for large deformation measurement using reliability-guided digital image correlation. Optics and Lasers in Engineering 2012; 50(4): 586-592.

[102]   Zienkiewicz OC, Taylor RL. The finite element method. 5th ed. Oxford ; Boston: Butterworth-Heinemann; 2000.

[103]   Leclerc H, Perie JN, Roux S, Hild F. Integrated Digital Image Correlation for the Identification of Mechanical Properties. Computer Vision/Computer Graphics Collaboration Techniques, Proceedings 2009; 5496: 161-171.

[104]   Hild F, Roux S, Gras R, Guerrero N, Marante ME, Florez-Lopez J. Displacement measurement technique for beam kinematics. Optics and Lasers in Engineering 2009; 47(3-4): 495-503.

[105]   Langerholc M, Slavic J, Boltezar M. Absolute Nodal Coordinates in Digital Image Correlation. Experimental Mechanics 2013; 53(5): 807-818.

[106] Avril S, Bonnet M, Bretelle AS, Grediac M, Hild F, Ienny P, et al. Overview of identification methods of mechanical parameters based on full-field measurements. Experimental Mechanics 2008; 48(4): 381-402.

[107] Rethore J. A fully integrated noise robust strategy for the identification of constitutive laws from digital images. International Journal for Numerical Methods in Engineering 2010; 84(6): 631-660.

[108] Rethore J, Roux S, Hild F. An extended and integrated digital image correlation technique applied to the analysis of fractured samples. European Journal of Computational Mechanics 2009(18): 285-306.

[109] Roux S, Hild F. Stress intensity factor measurements from digital image correlation: post-processing and integrated approaches. International Journal of Fracture 2006; 140(1-4): 141-157.

[110] Szabó B, Düster A, Rank E, *The p-Version of the Finite Element Method*, in *Encyclopedia of Computational Mechanics*. 2004, John Wiley & Sons, Ltd.

[111] Gratsch T, Bathe KJ. A posteriori error estimation techniques in practical finite element analysis. Computers & Structures 2005; 83(4-5): 235-265.

[112] Lee ETY. A Simplified B-Spline Computation Routine. Computing 1982; 29(4): 365-371.

[113] De Santo M, Liguori C, Paolillo A, Pietrosanto A. Standard uncertainty evaluation in image-based measurements. Measurement 2004; 36(3-4): 347-358.

[114] International Bureau of Weights and Measures., International Organization for Standardization. Guide to the expression of uncertainty in measurement. 1st ed. Genève, Switzerland: International Organization for Standardization; 1993.

[115] *NIST/SEMATECH e-Handbook of Statistical Methods*. 2012 [cited 2014 November]; Available from: http://www.itl.nist.gov/div898/handbook/.

[116] Ellison S, Williams A. Eurachem/CITAC guide: Quantifying Uncertainty in Analytical Measurement. Third edition ed.; 2012.

[117] JCGM 200: International vocabulary of metrology - Basic and general concepts and associated terms (VIM). Third Eidtion ed.; 2012.

[118] BIPM. JCGM 100: GUM 1995 with minor corrections, Evaluation of measurement data - Guide to the expression of uncertainty in measurement. 2008, Bureau International des Poids et Mesures.

[119] Menditto A, Patriarca M, Magnusson B. Understanding the meaning of accuracy, trueness and precision. Accreditation and Quality Assurance 2007; 12(1): 45-47.

[120] BIPM, IEC, ISO, IFCC, OIML. Guide to the expression of uncertainty in measurement. 1993.

[121] Sun Y, Pang J. Study of optimal subset size in digital image correlation of speckle pattern images. Optics and Lasers in Engineering 2007; 45(9): 967-974.

[122] Hua T, Xie HM, Wang SM, Hu ZX, Chen PW, Zhang QM. Evaluation of the quality of a speckle pattern in the digital image correlation method by mean subset fluctuation. Optics and Laser Technology 2011; 43(1): 9-13.

[123] Triconnet K, Derrien K, Hild F, Baptiste D. Parameter choice for optimized digital image correlation. Optics and Lasers in Engineering 2009; 47(6): 728-737.

[124] Lecompte D, Smits A, Bossuyt S, Sol H, Vantomme J, Van Hemelrijck D, et al. Quality assessment of speckle patterns for digital image correlation. Optics and Lasers in Engineering 2006; 44(11): 1132-1145.

[125] Hung P-C, Voloshin AS. In-plane strain measurement by digital image correlation. Journal of the Brazilian Society of Mechanical Sciences and Engineering 2003; 25: 215-221.

[126] Scrivens WA, Luo Y, Sutton MA, Collette SA, Myrick ML, Miney P, et al. Development of patterns for digital image correlation measurements at reduced length scales. Experimental Mechanics 2007; 47(1): 63-77.

[127] Lava P, Cooreman S, Coppieters S, De Strycker M, Debruyne D. Assessment of measuring errors in DIC using deformation fields generated by plastic FEA. Optics and Lasers in Engineering 2009; 47(7-8): 747-753.

[128] Orteu JJ, Garcia D, Robert L, Bugarin F. A speckle-texture image generator. SPECKLE06: Speckles, From Grains to Flowers 2006; 6341: U110-U115.

[129] Wang YQ, Sutton MA, Ke XD, Schreier HW, Reu PL, Miller TJ. On Error Assessment in Stereo-based Deformation Measurements Part I: Theoretical Developments for Quantitative Estimates. Experimental Mechanics 2011; 51(4): 405-422.

[130] Yang G, Nelson BJ. Wavelet-based autofocusing and unsupervised segmentation of microscopic images. Iros 2003: Proceedings of the 2003 Ieee/Rsj International Conference on Intelligent Robots and Systems, Vols 1-4 2003: 2143-2148.

[131] Lee SY, Kumar Y, Cho JM, Lee SW, Kim SW. Enhanced Autofocus Algorithm Using Robust Focus Measure and Fuzzy Reasoning. Ieee Transactions on Circuits and Systems for Video Technology 2008; 18(9): 1237-1246.

[132] *Doc-Ok. org*. 2014; Available from: http://doc-ok.org/?p=1095.

[133] Hoult NA, Take WA, Lee C, Dutton M. Experimental accuracy of two dimensional strain measurements using Digital Image Correlation. Engineering Structures 2013; 46: 718-726.

[134] Wang YG, Tong W. A high resolution DIC technique for measuring small thermal expansion of film specimens. Optics and Lasers in Engineering 2013; 51(1): 30-33.

[135] Tay CJ, Quan C, Huang YH, Fu Y. Digital image correlation for whole field out-of-plane displacement measurement using a single camera. Optics Communications 2005; 251(1-3): 23-36.

[136] Sutton MA, Yan JH, Tiwari V, Schreier HW, Orteu JJ. The effect of out-of-plane motion on 2D and 3D digital image correlation measurements. Optics and Lasers in Engineering 2008; 46(10): 746-757.

[137] Wittevrongel L, Badaloni M, Balcaen R, Lava P, Debruyne D. Evaluation of Methodologies for Compensation of Out of Plane Motions in a 2D Digital Image Correlation Setup. Strain 2015; 51(5): 357-369.

[138] Tan XH, Kang YL, Patterson EA. Calibration of a 3-D Digital Image Correlation system for large deformation contact problems. Modern Practice in Stress and Vibration Analysis 2012 (Mpsva 2012) 2012; 382.

[139] Cofaru C, Philips W, Van Paepegem W. A novel speckle pattern-Adaptive digital image correlation approach with robust strain calculation. Optics and Lasers in Engineering 2012; 50(2): 187-198.

[140] Liu XF, Kanungo T, Haralick RM. On the use of error propagation for statistical validation of computer vision software. Ieee Transactions on Pattern Analysis and Machine Intelligence 2005; 27(10): 1603-1614.

[141] Sanders-Reed J. Error propagation in two-sensor three-dimensional position. Optical Engineering 2001; 40(4): 627-636.

[142] Reu PL. Uncertainty Quantification for 3D Digital Image Correlation. in Imaging Methods for Novel Materials and Challenging Applications, Conference Proceedings of the Society for Experimental Mechanics Series 35, Jin, Editor. 2013, The Society for Experimental Mechanics.

[143] Reu PL. Experimental Validation of 2D Uncertainty Quantification for Digital Image Correlation. Icem 14: 14th International Conference on Experimental Mechanics, Vol 6 2010; 6.

[144] Pan B, Xie HM, Wang ZY. Equivalence of digital image correlation criteria for pattern matching. Applied Optics 2010; 49(28): 5501-5509.

[145] Chen YN, Jin WQ, Zhao L, Li FW. A subpixel motion estimation algorithm based on digital correlation for illumination variant and noise image sequences. Optik 2009; 120(16): 835-844.

[146] Riha L, Fischer J, Smid R, Docekal A. New interpolation methods for image-based sub-pixel displacement measurement based on correlation. 2007 Ieee Instrumentation & Measurement Technology Conference, Vols 1-5 2007: 1253-1257.

[147] Zhang ZF, Kang YL, Wang HW, Qin QH, Qiu Y, Li XQ. A novel coarse-fine search scheme for digital image correlation method. Measurement 2006; 39(8): 710-718.

[148] Hild F, Raka B, Baudequin M, Roux S, Cantelaube F. Multiscale displacement field measurements of compressed mineral-wool samples by digital image correlation. Applied Optics 2002; 41(32): 6815-6828.

[149] Pan B, Xie H, Xia Y, Wang Q. Large-deformation measurement based on reliable initial guess in digital image correlation method. Guangxue Xuebao/Acta Optica Sinica 2009; 29: 400-406.

[150] Pan B, Xie H. Digital image correlation method with differential evolution. Guangdianzi Jiguang/Journal of Optoelectronics Laser 2007; 18: 100-103.

[151] Canal LP, Gonzalez C, Molina-Aldareguia JM, Segurado J, LLorca J. Application of digital image correlation at the microscale in fiber-reinforced composites. Composites Part a-Applied Science and Manufacturing 2012; 43(10): 1630-1638.

[152] Leclerc H, Perie JN, Roux S, Hild F. Voxel-Scale Digital Volume Correlation. Experimental Mechanics 2011; 51(4): 479-490.

[153] BIPM. JCGM 104: 2009 Evaluation of measurement data - An introduction to the 'Guide to the expression of uncertainty in measurement' and related documents. 2009.

[154] Betta G, Liguori C, Pietrosanto A. A structured approach to estimate the measurement uncertainty in digital signal elaboration algorithms. in IEEE Proceedings on Science, Measurement and Technology. 1999. p. 21-26.

[155]   Massimo De Santo CL, Alfredo Paolillo, Antonio Pietrosanto. Standard uncertainty evaluation in image-based measurements. Measurement 2004; 36: 347-358.

[156]   Sebastian C, Patterson EA. Calibration of a Digital Image Correlation System. Experimental Techniques 2015; 39(1): 21-29.

[157]   Patterson EA, Hack E, Brailly P, Burguete RL, Saleem Q, Siebert T, et al. Calibration and evaluation of optical systems for full-field strain measurement. Optics and Lasers in Engineering 2007; 45(5): 550-564.

[158]   *Standardised Project for Optical Techniques of Strain Measurement (SPOTS)*. Guidelines for the Calibration and Evaluation of Optical Systems for Strain Measurement 2010   [cited 2014; Available from: www.opticalstrain.org.

[159]   BIPM. JCGM 102: 2011 Evaluation of measurement data - Supplement 2 to the 'Guide to the expression of uncertainty in measurement' - Extension to any number of output quantities. 2011.

[160]   Matheron G. Principles of geostatistics. Econimic Geology 1963; 58: 1246-1266.

[161]   Debenedetti A. Mining Geostatistics - Journel,Ag, Huijbregts,Cj. Scientia 1981; 116(1-4): 162-164.

[162]   Forrester AIJ, Sóbester A, Keane AJ. Engineering design via surrogate modelling : a practical guide. Chichester, West Sussex, England ; Hoboken, NJ: J. Wiley; 2008.

[163]   De Baar JHS, Percin M, Dwight RP, van Oudheusden BW, Bijl H. Kriging regression of PIV data using a local error estimate. Experiments in Fluids 2014; 55(1).

[164]   Charonko JJ, Vlachos PP. Estimation of uncertainty bounds for individual particle image velocimetry measurements from cross-correlation peak ratio. Measurement Science & Technology 2013; 24(6).

[165]   Kleijnen JPC. Kriging metamodeling in simulation: A review. European Journal of Operational Research 2009; 192(3): 707-716.

[166]   O'Hagan A. Bayesian analysis of computer code outputs: A tutorial. Reliability Engineering & System Safety 2006; 91(10-11): 1290-1300.

[167]   Santner TJ, Williams BJ, Notz W. The Design and analysis of computer experiments. Springer series in statistics. New York: Springer; 2003.

[168]   Sacks J, Welch WJ, Mitchell TJ, Wynn HP. Design and Analysis of Computer Experiments. Statistical Science, 1989; 4(4): 409-435.

[169] Oakley J. Bayesian uncertainty analysis for complex computer codes. in Department of Probability and Statistics, School of Mathematics and Statistics. 1999, the University of Sheffield.

[170] Haylock RGE. Bayesian inference about outputs of computationally expensive algorithms with uncertainty on the inputs. 1997, the University of Nottingham.

[171] DiazDelaO FA, Adhikari S, Flores EIS, Friswell MI. Stochastic structural dynamic analysis using Bayesian emulators. Computers & Structures 2013; 120: 24-32.

[172] Wang Y. Uncertainty quantification of digital image correlation and the impact on material identification. in Faculty of engineering science. 2015, KU Leuven: Heverlee, Belgium.

[173] Tong W, Yao H, Xuan Y. An Improved Error Evaluation in One-Dimensional Deformation Measurements by Linear Digital Image Correlation. Experimental Mechanics 2011; 51(7): 1019-1031.

[174] Robinson D, Milanfar P. Bias minimizing filter design for gradient-based image registration. Signal Processing-Image Communication 2005; 20(6): 554-568.

[175] Bailey DG, Gilman A, Browne R. Bias characteristics of bilinear interpolation based registration. Tencon 2005 - 2005 Ieee Region 10 Conference, Vols 1-5 2006: 978-983.

[176] Tong W. Reduction of Noise-Induced Bias in Displacement Estimation by Linear Off-Pixel Digital Image Correlation. Strain 2013; 49(2): 158-166.

[177] *DIC Challenge 2D Dataset*. 2002 [cited 2014; Available from: http://www.sem.org/dic-challenge/.

[178] Pan B, Yu LP, Wu DF, Tang LQ. Systematic errors in two-dimensional digital image correlation due to lens distortion. Optics and Lasers in Engineering 2013; 51(2): 140-147.

[179] Bohling G. *Kriging*. 2005 [cited 2014; Available from: http://people.ku.edu/~gbohling/cpe940/.

[180] Hengl T, Heuvelink GBM, Rossiter DG. About regression-kriging: From equations to case studies. Computers & Geosciences 2007; 33(10): 1301-1315.

[181] Hengl T, Heuvelink GBM, Stein A. A generic framework for spatial prediction of soil variables based on regression-kriging. Geoderma 2004; 120(1-2): 75-93.

[182] Lophaven SN, Nielsen HB. DACE A Matlab Kriging Toolbox. Denmark, Editor. 2002.

[183] Nocedal J, Wright SJ. Numerical optimization. 2nd ed. Springer series in operations research. New York: Springer; 2006.

[184] Press WH. Numerical recipes : the art of scientific computing. 3rd ed. Cambridge, UK ; New York: Cambridge University Press; 2007.

[185] Lindley DV. On a Measure of the Information Provided by an Experiment. Annals of Mathematical Statistics 1956; 27(4): 986-1005.

[186] Forrester AIJ, Sobester A, Keane AJ. Multi-fidelity optimization via surrogate modelling. Proceedings of the Royal Society a-Mathematical Physical and Engineering Sciences 2007; 463(2088): 3251-3269.

[187] Jones DR. A taxonomy of global optimization methods based on response surfaces. Journal of Global Optimization 2001; 21(4): 345-383.

[188] Schonlau M. Computer Experiments and Global Optimization. 1997, University of Waterloo: Waterloo, Ontario, Canada.

[189] Keane AJ, Nair PB. Computational Approaches for Aerospace Design: The Pursuit of Excellence. 2005: 1-582.

[190] Lagarias JC, Reeds JA, Wright MH, Wright PE. Convergence properties of the Nelder-Mead simplex method in low dimensions. Siam Journal on Optimization 1998; 9(1): 112-147.

[191] De Baar JHS, Dwight RP, Bijl H. Speeding up Kriging through fast estimation of the hyperparameters in the frequency-domain. Computers & Geosciences 2013; 54: 99-106.

[192] Ranjan P, Haynes R, Karsten R. A Computationally Stable Approach to Gaussian Process Interpolation of Deterministic Computer Simulation Data. Technometrics 2011; 53(4): 366-378.

[193] O'Hagan A. Bayes Hermite Quadrature. Journal of Statistical Planning and Inference 1991; 29(3): 245-260.

[194] Helbert C, Dupuy D, Carraro L. Assessment of uncertainty in computer experiments from Universal to Bayesian Kriging. Applied Stochastic Models in Business and Industry 2009; 25(2): 99-113.

[195] Rasmussen CE, Williams CKI. Gaussian processes for machine learning. Adaptive computation and machine learning. Cambridge, Mass.: MIT Press; 2006.

[196] Krzanowski WJ. Principles of multivariate analysis : a user's perspective. Rev. ed. Oxford statistical science series. Oxford Oxfordshire ; New York: Oxford University Press; 2000.

[197] Von Mises R. Mathematical theory of probability and statistics. New York,: Academic Press; 1964.

[198] Oakley J, O'Hagan A. Bayesian inference for the uncertainty distribution of computer model outputs. Biometrika 2002; 89(4): 769-784.

[199] Kenney JF, Keeping ES. Mathematics of statistics. 3d ed. New York,: Van Nostrand company; 1954.

[200] Mosammam AM. Geostatistics: modeling spatial uncertainty, 2nd edition. Journal of Applied Statistics 2013; 40(4): 923-923.

[201] Tikhonov AN. Numerical methods for the solution of ill-posed problems. Mathematics and its applications. Dordrecht ; Boston: Kluwer Academic Publishers; 1995.

[202] Zhou Y, Sun C, Song Y, Chen J. Image pre-filtering for measurement error reduction in digital image correlation. Optics and Lasers in Engineering 2014; in press.

[203] Zhao JQ, Zeng P, Lei LP, Ma Y. Initial guess by improved population-based intelligent algorithms for large inter-frame deformation measurement using digital image correlation. Optics and Lasers in Engineering 2012; 50(3): 473-490.

[204] Labeas G, Pasialis, V., Lin, X., Patterson, E.A. On the validation of solid mechanics models using optical measurements and data decomposition. Journal of Simulation Modelling Practice and Theory in press.

[205] Thomas DB, Luk W. Sampling from the Multivariate Gaussian distribution using reconfigurable hardware. Fccm 2007: 15th Annual Ieee Symposium on Field-Programmable Custom Computing Machines, Proceedings 2007: 3-12.

[206] Felipe-Sese L, Siegmann P, Diaz FA, Patterson EA. Simultaneous in-and-out-of-plane displacement measurements using fringe projection and digital image correlation. Optics and Lasers in Engineering 2014; 52: 66-74.

[207] Hack E, Lin X, Patterson EA, Sebastian CM. A reference material for establishing uncertainties in full-field displacement measurements. Measurement Science & Technology 2015; 26(7).

[208] Timoshenko S, Goodier JN. Theory of elasticity. 3d ed. Engineering societies monographs. New York,: McGraw-Hill; 1969.

[209] Wang WZ, Mottershead JE, Sebastian CM, Patterson EA. Shape features and finite element model updating from full-field strain data. International Journal of Solids and Structures 2011; 48(11-12): 1644-1657.

[210] Wang WZ, Mottershead JE. Adaptive moment descriptors for full-field strain and displacement measurements. Journal of Strain Analysis for Engineering Design 2013; 48(1): 16-35.

[211] Labeas G, Pasialis, V.P., Lin, X. & Patterson, E.A. On the validation of solid mechanics models using optical measurements and data decomposition. Simulation Modelling Practice & Theory 2015; 52: 92-107.

[212] Sandor Z, Andras P. Alternative sampling methods for estimating multivariate normal probabilities. Journal of Econometrics 2004; 120(2): 207-234.

[213] Germaneau A, Doumalin P, Dupre JC. Comparison between X-ray micro-computed tomography and optical scanning tomography for full 3D strain measurement by digital volume correlation. Ndt & E International 2008; 41(6): 407-415.

[214] Park SK, Schowengerdt RA. Image-Reconstruction by Parametric Cubic Convolution. Computer Vision Graphics and Image Processing 1983; 23(3): 258-272.